Biomechanical Comparison of Two Total Ankle Replacement Designs: Micromotion and Kinematic Patterns

by

KURTIS ANTHONY MCINNES

B.Eng. McGill University, 2009

A THESIS SUBMITTED IN PARTIAL FULFILMENT OF
THE REQUIREMENTS FOR THE DEGREE OF

MASTER OF APPLIED SCIENCE

in

THE FACULTY OF GRADUATE STUDIES
(Mechanical Engineering)

THE UNIVERSITY OF BRITISH COLUMBIA
July 2012

ABSTRACT

Introduction: Arthritis is a degenerative disease that causes irreversible damage to a joint's articular cartilage. Despite having high failure rates in early total ankle arthroplasty (TAA) models, recent improvements have increased the success of this procedure, providing end-stage ankle arthritis patients a viable alternative to fusion with better functional outcomes. Currently, the most prevalent cause of failure is aseptic loosening, which is believed to be affected by motion at the bone-implant interface. The objective of this study was to compare micromotion and kinematic patterns of two TAA designs.

Methods: A mechanical simulator was designed to apply compressive loads and bending moments to human cadaveric ankles, intact and replaced. It induced a maximal range of motion in the ankle about 3 orthogonal axes: plantarflexion-dorsiflexion (PF-DF), inversion-eversion (INV-EV), and internal-external rotation (IR-ER). Six ankle pairs were tested and compared. The implants analyzed were the Agility™ and the Scandinavian Total Ankle Replacement (S.T.A.R.®). Using an optical motion capture system, tibiocalcaneal kinematics and the relative bone-implant motion for each implant were recorded and analyzed.

Results: The Agility exhibited a greater amount of micromotion between the bone and prosthesis than the STAR for the tibial component in INV-EV ($p=0.037$), and for the talar component in PF-DF ($p=0.002$) and IR-ER ($p=0.038$). Micromotion magnitudes were affected by loading direction and compression. Kinematic changes were observed following replacement of the ankle joint. There were decreases in the amount of motion coupling for both implants when loaded in INV-EV and IR-ER. There were increases in joint translation for both implants in the medial/lateral direction under INV-EV loading, and for the STAR in the anterior/posterior and compression/distraction directions under PF-DF loading. No significant ROM differences were found.

Discussion: Increased micromotion in the Agility supports the hypothesis that higher aseptic loosening rates are correlated with reduced initial post-op fixation. The effect of loading direction on micromotion magnitude confirms the need to apply a variety of loading conditions to obtain a comprehensive micromotion analysis. Kinematic differences between implanted and intact ankles show that there is still room for improvement towards an ankle replacement design that replicates the performance of a healthy ankle.

PREFACE

UBC Research Ethics Board Approval:

Clinical Research Ethics Board

Certificate Number: H10-02860

TABLE OF CONTENTS

LIST OF TABLES

LIST OF FIGURES

ACKNOWLEDGEMENTS

I have so much respect and appreciation for Dr. Tom Oxland, who was a great supervisor that not only provided mentorship, support, and guidance, but also funded this project and my stipend through his personal research grant money.

I would like to thank Dr. Alastair Younger for providing crucial insight in the clinical aspect and implications of this research as well as performing the ankle replacement surgeries.

I would also like to thank my family, friends, and fellow lab mates at the Orthopaedic Injury Biomechanics Laboratory who were always there to provide support and encouragement when I needed it.

Without the help of all these people, none of this would have been possible. I consider myself truly blessed to have had the opportunity to perform this research.

1 INTRODUCTION

1.1 OVERVIEW

Arthritis is a leading cause of disability in Canada and is among the top three most common chronic conditions. Across the country, nearly 4 million people suffer from arthritis and approximately 100,000 more Canadians are diagnosed each year. In 1998, the cost of arthritis to Canadians was $4.4 billion, of which $908.9 million were direct co sts such as hospital stays, physician services, and medications, and the other $3.5 billion were incurred from indirect costs like loss of productivity [1]. Even though the prevalence of ankle arthritis is much lower than hip and knee, at 4.4 percent of the total demographic [2], the costs related to ankle arthritis approach $200 million per year.

Arthritis is a degenerative joint disease affecting all joints in the body that causes pain and stiffness, limits mobility, and decreases quality of life. When the ankle is affected by end stage arthritis, there are two main surgical options. The more recent but less common treatment is total ankle arthroplasty (TAA) [3], where joint articulation surfaces are replaced with metal and polyethylene components (sometimes ceramic). The other option is ankle arthrodesis, which addresses the pain by fusing the tibiotalar joint (and occasionally other adjacent joints) with pins and screws, eliminating all relative motion between the tibia and talus. Arthrodesis is a simpler and quicker procedure while TAA is more invasive, complex and costly. Recently, TAAs have been shown to offer equivalent pain relief with a comparable reoperation rate, while additionally providing better function [4,5]. Although subject to similar reoperation rates, the complexity of revision in TAA is much higher and in some cases not possible, making it a slightly riskier operation in the short term.

A large number of contraindications for TAA exist, which result in a high risk of failure from receiving an ankle replacement and reduce eligibility for the operation. Absolute contraindications include avascular necrosis, active or recent infection, neuropathy, and severe deformity or malalignment of the ankle. There are also relative contraindications, in which it is subject to the surgeon's discretion whether or not to perform a TAA on younger patients, extremely active or heavy-labour individuals, those with prior infection in the ankle, or patients with osteoporosis/osteopenia [6]. Even though success rates of TAA's are continuing to increase, the history of inadequacy continues to impact the reputation of this procedure, making it a somewhat controversial treatment option [7], which may influence some patients who would be good candidates to opt for ankle fusions instead. Currently, fusion is still viewed as the standard treatment for end-stage ankle arthritis [7], despite the reduction in mobility/function of the joint and high future complication rate in adjacent joints of the foot.

Based on statistics from a US healthcare database, the expected number of procedures performed treating ankle arthritis in 2012 is approximately 20,000 [3]. Only one fifth (3,925) of these will be TAAs (including revisions) and the rest will be ankle fusions [3]. This corresponds to an incidence of 1.25 per 10^5 people, which is of a similar magnitude to incidence rates reported in Sweden ($.8/10^5$)[8] and Finland ($1.5/10^5$)[9]. Assuming a similar demographic in Canada as in the US, there would be approximately 435 total ankle replacement (TAR) and 1757 arthrodesis procedures performed in Canada this year addressing the problem of end-stage ankle arthritis.

Success rates of current ankle replacements are under 85% when looking at short to mid-term results in national joint registers (non-designer surgeons) [9-12]. This is still quite low when compared to the survival rates of hip and knee replacement. A recent collation of data from joint registers across the world shows that the revision rate of ankles is more than 2.5 times greater than either hip or knee. This study used a metric of revisions per 100 observed component years, which

normalizes for follow-up period. Ankles were found to have a revision rate of 3.29, while hips and knees had rates of 1.29 and 1.26 respectively [13]. This corresponds to revision rates of 32.9%, 12.9%, and 12.6% at ten years. Historically, success rates for hip/knee devices have improved due to a greater number of clinical and biomechanical studies compared to ankle replacement. Similar benefits could be achieved for ankle replacements and comparable success rates will be reached as appropriate research is performed. As designs and success rates improve, it is expected that patient candidacy will also expand and those with end-stage ankle arthritis will receive a higher level of care and experience a greatly improved quality of life.

The most prevalent cause of TAA failure is currently aseptic loosening (Appendix A). Aseptic loosening results when bonding at the bone-implant interface fails. Successful bonding relies on osseointegration, which is bone ingrowth into the porous surface of the implant. When excessive micromotion occurs between the bone and implant, it prevents osseointegration and leads to TAA failure via aseptic loosening.

The objective for this thesis was to analyze the biomechanical behaviour of two current ankle replacement designs. Specific focus was given to measuring the micromotion between the implant components and their respective bone surfaces, and quantifying three-dimensional kinematic patterns.

1.2 Foot and Ankle Anatomy

The ankle joint complex consists of the talocrural and inferior tibiofibular joints, and sometimes includes the subtalar joint as well. These joints involve the tibia, fibula, talus, and calcaneus (refer to

figure 1). Because of its shape, the superior portion of the talocrural joint is commonly referred to as the ankle 'mortise'. Although it may appear to be just a simple hinge-joint at first glance, it is actually one of our most intricate joints, which involves coordination with numerous other joints in the forefoot in order to provide a balanced and stable foundation for all bipedal locomotion. Its particular architecture enables it to withstand and transmit the largest loads of any joint in the body. Loads up to as high as 13.3 times body weight (BW) have been predicted [14]. During daily activities such as gait, it is common for ankle loads to double the magnitude of those in the hip and knee while only having one-third of the contact area [15]. Despite experiencing much higher stresses, ankles are only accountable for approximately 7.5 percent of all lower extremity arthritis cases [16].

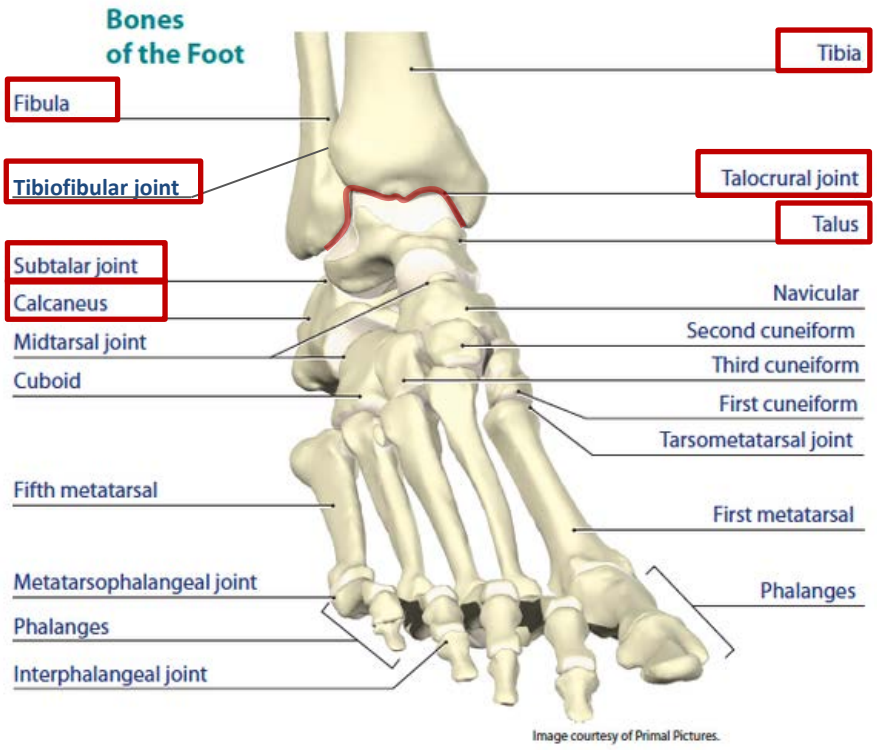

Figure 1: Bones and joints of the foot and ankle. ***Anatomy image courtesy and copyright of Primal Pictures Ltd – www.primalpictures.com***

1.2.1 *BONES*

The tibia acts as the main weight-bearing long bone of the lower leg. Its diaphysis has a cross-section that is roughly triangular in shape with posterior, medial, and lateral surfaces. It flares out at its superior aspect forming the tibial plateau which articulates with the femur at the knee. At its inferior aspect called the tibial plafond, its cross-sectional area also increases and forms a concave surface with the medial maleolus extending beyond it to form the superior and medial portions of the ankle mortise.

The fibula is a long bone located laterally to the tibia and bears relatively little weight in comparison. Its primary function is to provide attachment for muscles. It has the most slender aspect ratio of all long bones. The fibular head articulates with the tibia superiorly at the posterior aspect of the lateral condyle in an arthrodial (plane) synovial joint. Inferiorly, it articulates with the tibia and extends past the tibia distally to articulate with the talus, forming the lateral portion of the ankle mortise.

The talus is the most superior bone of the foot. The talus is unique in having a large surface area of articular cartilage and having no muscle origins and insertions. It is at risk of losing its blood supply in excessive dissection or after fracture. It can be subdivided into three parts: the head, neck, and body. The head is the most anterior portion of the talus and it articulates with the navicular bone. The neck is a rough, non-articulating segment that connects the head and body. On the superior aspect of the body is the trochlea, which articulates superiorly with the tibia and fibula at the talocrural joint. It has an articular surface that is convex in the sagittal plane and quasi-rectangular (anterior aspect is slightly wider than posterior) in the frontal plane with medial and lateral articulate facets for the two malleoli. The radius of curvature of the trochlea is longer on its posterior than its anterior articular surface [17]. The body of the talus also articulates inferiorly with the calcaneus at three locations forming the subtalar joint. The posterior calcaneal articular

surface is separated from the middle and anterior calcaneal articular surfaces by a deep groove called the sulcus tali. The talus is the insertion point for the anterior talofibular ligament, the posterior talofibular ligament and the deep deltoid ligament that act as the main stabilizers of the ankle joint.

The calcaneus is the bone most commonly known as the heel. It is the largest bone in the foot, and it is located directly beneath the ankle joint and extends out posterior to it. The posterior half of it is called the tuber calcanei, providing attachment of the achilles tendon and the plantar fascia. The achilles tendon is the main plantar flexor of the ankle. The calcaneal fibular ligament inserts into the lateral aspect of the body and the sustentaculum tali has the deltoid ligament insertion. Both stabilize the ankle joint. It articulates superiorly with the talus at the 3 locations previously mentioned, and it also articulates anteriorly with the cuboid.

The navicular articulates with the anterior aspect of the talus and forms part of the medial column of the foot. It provides the attachment for the tibialis posterior tendon and is the insertion of the majority of the deltoid ligaments supporting the arch. It also articulates with the three cuneiforms anteriorly and occasionally with the cuboid laterally. The 3 cuneiforms are situated anteriorly to the navicular and connected to the first, second, and third metatarsals. The metatarsals make up the largest portion of the forefoot and are numbered one through five from medial to lateral. The fourth and fifth metatarsals are anterior to the cuboid. The phalanges (or toes) project off the anterior aspect of the metatarsals.

1.2.2 *JOINTS*

While the number of joints in the foot and ankle number over 30, the predominant three providing ankle motion and included in the ankle joint proper are those of the inferior tibiofibular, talocrural (tibiotalar and talofibular), and subtalar joints (refer to figure 1).

The inferior tibiofibular joint (aka: tibiofibular syndesmosis) is a slightly movable joint where the fibula connects to the tibia at its most inferior aspect. At this location the convex fibula articulates with a concave groove on the lateral surface of the tibia. The fibula is attached to the tibia via fibrous tissues such as the interosseus membrane and ligaments spanning the gap between the tibia and fibula immediately proximal to this articulation. This syndesmosis holds the fibula in place next to the tibia to provide lateral stability to the ankle and form the lateral border of the ankle mortise.

The talocrural joint is the primary joint of the ankle complex and is formed by the articulation of the talus with the tibia and fibula. The superior part of this joint makes up the ankle mortise and consists of the concave distal end of the tibia, the medial malleolus of the tibia, and the fibula extending distally from the inferior tibiofibular joint as the lateral malleolus. The talus comprises the inferior portion of this joint, fitting inside the mortise. The talocrural joint acts primarily as a hinge and accounts for the majority of the foot's plantar- and dorsi-flexion range of motion; however, this is a gross over-simplification. This joint also allows small amounts of inversion-eversion (INV-EV) [18] and internal-external rotation (IR-ER) [19]. Additionally, calling it a hinge joint is inaccurate because the flexion axis changes location as the ankle flexes [20]. In the sagittal plane, the motion of the ankle is largely governed by the deltoid (especially tibiocalcaneal) and calcaneofibular ligaments. A four-bar linkage geometrical model of the ankle quite accurately predicts its motion patterns and surface geometries, including that the instantaneous centre of rotation moves from a posterior-inferior to an antero-superior position as the foot moves from plantar-flexion to dorsiflexion [21].

The subtalar joint is formed between the talus and calcaneus, and it articulates at three locations as previously mentioned. The posterior calcaneal articular surface is concave in the direction along its long axis, while the middle and anterior articular surfaces are slightly convex. The shapes of these joints primarily enable rotation in the frontal plane. The subtalar joint, along with the transverse tarsal joint (talonavicular and calcaneocuboid joint), accounts for the majority of INV-EV experienced by the foot.

1.2.3 *Articular Cartilage*

Articular cartilage is a form of hyaline cartilage found on the ends of bones in joints. Its function is to act as a bearing surface between the bones that move relative to each other. Its structure is perfectly suited to its purpose, which gives the joint an extremely low friction surface that is very resistant to wear and compliant structure that will minimize stresses and absorb shock (see fig. 2 for a breakdown of its hierarchical structure). Its molecular makeup facilitates ideal lubrication interaction with the synovial fluid and its molecular constituents, namely hyaluronic acid and numerous proteoglycans. The biphasic nature of this tissue creates a highly compliant material that will expel water when compressed and reabsorb when decompressed. Its compliance works to increase the contact area between bones and absorb shocks from impacts. This highly effective bearing surface can withstand many millions of cycles over the course of a person's life without breaking down for most healthy people. However, it is an avascular tissue with a very low cell division rate, resulting in a very limited ability to repair/regenerate damaged tissue.

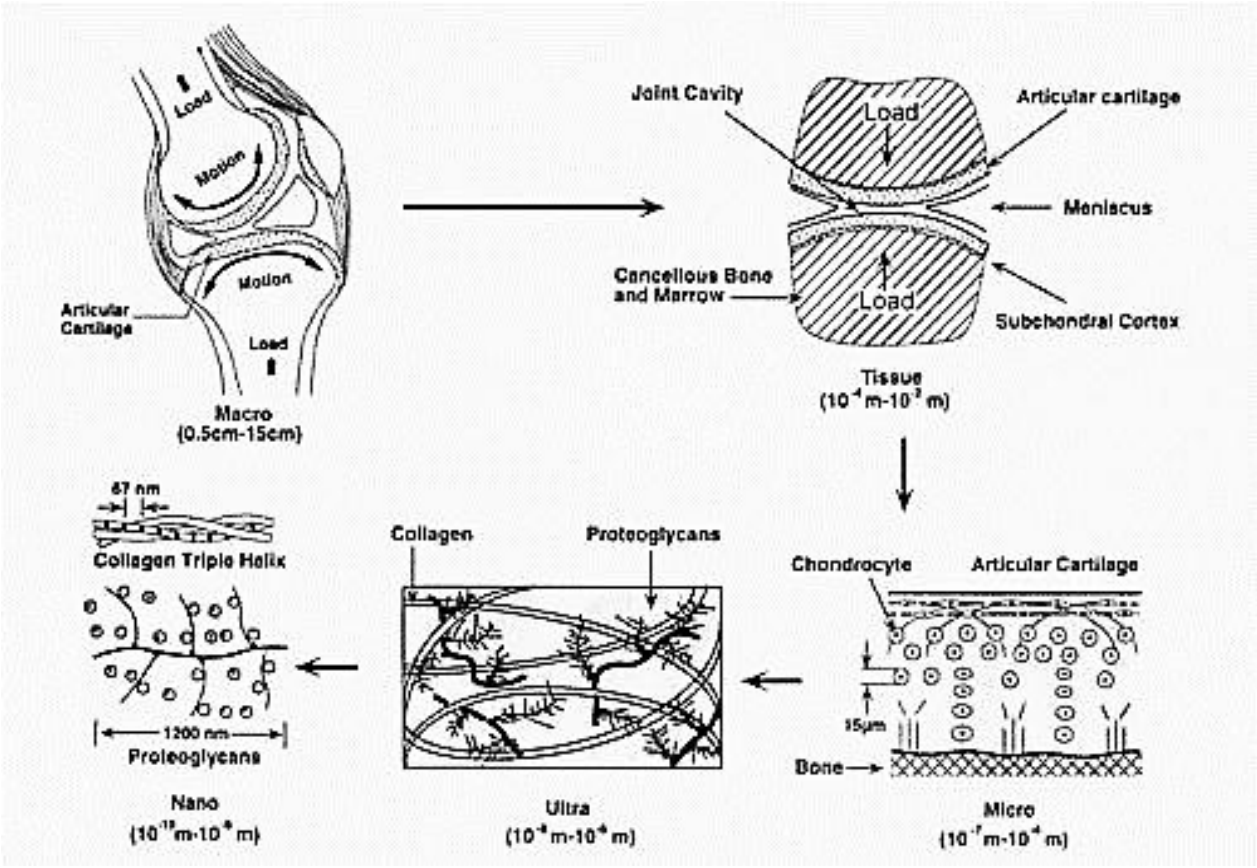

Figure 2: Articular cartilage and its hierarchical structure and components. Reprinted with permission from Elsevier via Copyright Clearance Center (source: Mow VC et al. 1992[22])

Articular cartilage is composed mainly of water (60-70% of wet weight), collagen (10-30% of wet weight), proteoglycans (3-10% of wet weight), and chondrocytes (<10% of tissue volume). Water is the fluid phase of cartilage that flows throughout the matrix and is absorbed or expelled depending on external loads. Collagen occurs primarily in the type II form, and it is the main structural component that gives cartilage its shape and attachment to the subchondral bone. It is responsible for cartilage's tensile strength and resistance to swelling with water. Proteoglycans are hyaluronate aggregates with numerous chains of glycosaminoglycans (mostly chondroitin sulfate and keratan sulfate). They are responsible for the hydrophilicity of articular cartilage, which gives it resiliency by decreasing its permeability. Finally, chondrocytes are the cells that govern the maintenance of

the cartilage. They synthesize the macromolecules of the matrix. They receive nutrients by diffusion and rarely divide/reproduce.

The thickness and mechanical properties of articular cartilage vary slightly between different joints. Of the lower extremities, the ankle's cartilage is the thinnest and the knee's is the thickest. Mean thicknesses were found to range from 1.0 to 1.62 mm and 1.69 to 2.55 mm for the ankle and knee respectively. The compressive modulus was also found to be inversely related to the thickness of the cartilage in all joints. [23]

1.3 ARTHRITIS

Arthritis is literally defined as joint inflammation and typically refers to a number of diseases where joint pain is the primary ailment. Arthritis is a blanket term that covers over 100 maladies, but the main classifications where joint pain is primary include: osteoarthritis, rheumatoid arthritis, ankylosing spondylitis, gout/pseudo-gout, juvenile idiopathic arthritis, septic arthritis, and Still's disease. Post-traumatic arthritis (PTA), rheumatoid arthritis (RA), and primary osteoarthritis (POA) are the types most commonly treated by TAA at 40.6%, 29.6%, and 26.9% respectively (see appendix B for details).

While POA is the most frequent diagnosis for patients receiving hip and knee replacements [16,24], it is much less common for it to affect the ankle. The low incidence of POA most likely plays a significant role in why the overall incidence of ankle replacements is so much lower than hip/knee. Even though obesity, certain occupations, genetics, and a few other risk factors have been identified with its occurrence, POA is generally idiopathic and the underlying cause remains unknown. PTA is

when osteoarthritis occurs secondary to traumatic injuries such as dislocations and fractures, especially a fracture transecting an articular surface. While POA and PTA differ in origin, the end result of both forms is essentially the same.

Osteoarthritis, whether primary or post-traumatic, is a degenerative process that is very difficult to treat even if it is caught at an early stage. It is defined by mechanical breakdown or fibrillation of the articular cartilage (see fig. 3), which initiates at a small localized area on the surface that expands to affect broader and deeper areas eventually to the point where bone on bone articulation occurs. It is accompanied by a breakdown of the collagen framework, decrease in proteoglycan aggregation, and an increase in water content. In turn, this decreases the compressive stiffness and increases the permeability of the cartilage, hindering its ability to absorb shock and distribute loads across the joint.

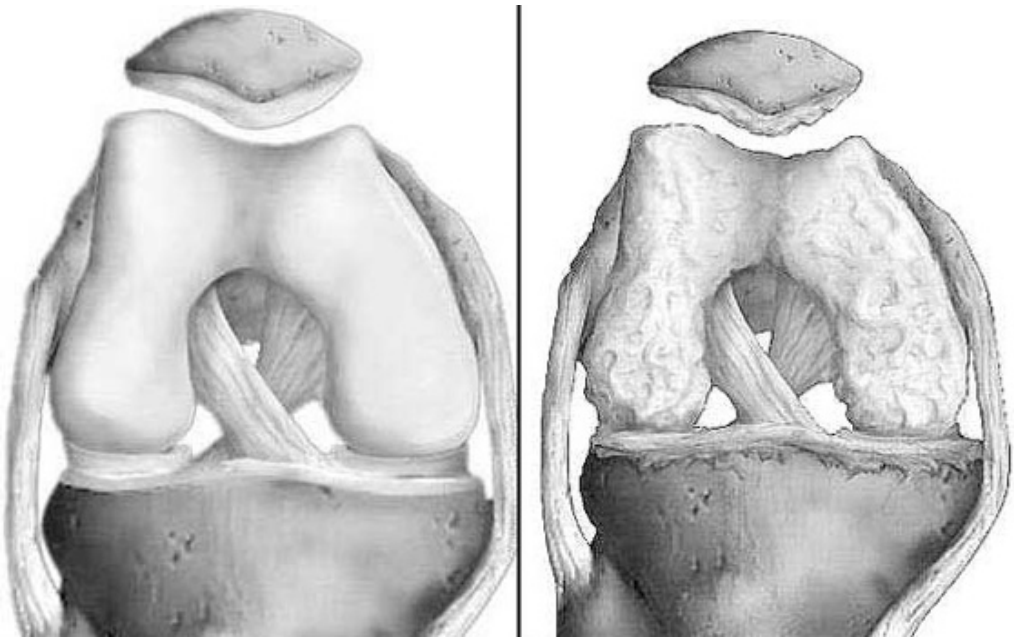

Figure 3: Normal knee articular cartilage with healthy, smooth surfaces (left) contrasted with osteoarthritic knee cartilage with rough, damaged surfaces (right). ***Image courtesy and copyright of Media Partners, Inc. from the patient education booklet "Total Knee Replacement: A Patient and Family Guide for Surgery and Recovery." (Source:*** **http://healthpages.org/health-a-z/osteoarthritis-degenerative-joint-disease/)**

RA, while entirely different in its mechanism, can result in similar consequences as the joint surfaces become eroded. RA is an autoimmune disease that primarily causes the body's immune system to attack its synovial joints. Because it is a systemic problem, it will usually end up affecting multiple joints and will even damage other organs on occasion. It is usually accompanied by symptoms of swollen, tender, warm, and stiff joints that are most painful in the morning or after extended periods of inactivity.

Since arthritis is a degenerative disease by nature, the severity of a patient's condition could lie anywhere along the continuum from initial onset to end-stage arthritis. Conservative treatments are available for the milder cases including a number of natural treatments, medications, joint injections, and even some less aggressive surgical procedures. Unfortunately, these conservative treatments focus mainly on pain management and slowing the process of degeneration, and their effectiveness at this is still suspect. We have yet to discover a treatment that can reverse the damage accumulated in the articular cartilage, leading most patients inevitably to end-stage arthritis. Once the disease has progressed to this point, conservative treatments are rendered completely ineffective and more aggressive surgical options are required.

For those with end-stage ankle arthritis, two options are available: arthrodesis and arthroplasty. Arthrodesis is the surgical procedure commonly referred to as joint fusion. Surgeons use any combination of plates, screws, pins, wires, and rods to immobilize the joint until it eventually fuses together. The end result of this operation is the elimination of all relative motion between the previously articulating surfaces, which allows weight bearing with effective pain relief at the cost of flexibility and motion at the fused joint. Despite its obvious functional limitations and risk of provoking arthritis in the adjacent joints, it is still the standard treatment for ankle arthritis because of its long track record of proven pain management and perception as a safer procedure.

However, total ankle arthroplasty has shown to be a comparably safe procedure in recent years with the added benefit of improved function [4].

1.4 TOTAL ANKLE ARTHROPLASTY

Total ankle arthroplasty (TAA) refers to the surgical replacement of degenerated/diseased ankle joint. As with arthrodesis, the main objective is to eliminate the pain caused by arthritis, but in addition it also aims to restore joint function. This procedure removes the damaged articular surfaces and inserts prosthesis components to replace them, which allow for relative motion. Current TAA designs are generally successful at eliminating pain and enabling patients to regain most of their ankle function [25,26]. Although this procedure might not restore ankle ROM to that of a normal ankle, patients can typically expect increases in ROM of between 5 to 10 degrees depending on implant type, which results in a post-op ROM of between 25 and 35 degrees depending on preoperative condition [27-29]. However, this procedure's major drawbacks are its limited longevity due to bearing wear and relatively low success rates [13].

The first generation of TAA designs emerged in the 1970's following the successes of hip and knee replacements. However, the ankle's complexity and its requirements for a successful joint replacement design were underestimated. The resulting first generation of TAA designs released were not anatomically accurate and produced disappointing outcomes. Even the most successful design of this generation, the Mayo total ankle arthroplasty, was reported to have a failure rate of 36% [30], while other designs' failure rates were as high as 90% [31]. This generation was typified by cemented designs that were either: over-constrained and susceptible to early loosening at the bone-cement interface, or under-constrained and prone to instability and displacement. By the

early 1980's, these designs were removed from circulation and the concept of total ankle replacements had been all but abandoned for the more reliable arthrodesis.

It wasn't until the second generation of TAA designs started showing improved mid-term outcomes in the late 90's and early 2000's that people began to view TAA as an acceptable, albeit slightly more risky, alternative to fusion. Second generation designs included implants such as the Agility, STAR, TNK, and Buechel-Pappas, some of which are still used today in their original or slightly modified form. Further attention to natural ankle kinematics [20] and attempts to replicate them with the new devices has yielded considerable improvements in these second generation implants. Third generation TAA designs seem to be showing further improvements in success rates [8,26], although more mid- and long-term follow-ups would be required to confirm this. Joint register data for all total ankle arthroplasties currently in circulation worldwide reveals a 10 year survivorship of around 70% [13]. This is a vast improvement on the previous designs and promotes optimism for even greater success rates with future generations of implants.

Every ankle replacement design has a different technique and uses its own set of specialized equipment. The similarities in surgical technique that can be drawn across the spectrum of designs are the following:

1. Incision to the anterior of the ankle joint to expose the bone/joint
2. Resurfacing cut(s) on the tibia
3. Resurfacing cut(s) on the talus
4. Cuts to facilitate fixation stems
5. Installation of metal (usually Ti or CoCr alloys) implants into tibia and talus
6. Insertion of polyethylene component (3-component designs)

Each different TAA system has also been designed with a unique combination of material selection, implant geometry, and fixation method. The design features of the two TAA prostheses examined in this study, the Agility™ Total Ankle Replacement Sytem and the Scandinavian Total Ankle Replacement (STAR™ Ankle), are described in detail in the following section.

1.5 TOTAL ANKLE ARTHROPLASTY DESIGNS

1.5.1 *AGILITY TOTAL ANKLE REPLACEMENT SYSTEM*

The Agility™ Total Ankle Replacement System was designed by Dr F.G. Alvine and is manufactured by DePuy Orthopaedics, (Warsaw, Indiana, USA). It was granted FDA approval in the USA in 1992 and was used in Canada from 1999 until 2006.

The Agility is a two-component semi-constrained total ankle prosthesis with a titanium tibial component and a cobalt chromium talar component. A polyethylene (PE) liner is attached to the tibial component. An arthrodesis of the syndesmosis allows load sharing through the fibula and the tibia, to stabilize the tibial component and simplify the ankle to a hinge joint by eliminating tibio-fibular motion. The talar component is tapered in the aagility nterior-posterior direction with its widest edge anterior with the aim of maximising stability in stance.

Both components have a sintered bead surface (POROCOAT) intended to allow osseointegration at the prosthesis/bone interface. POROCOAT has been used extensively for hip replacements, in the AML stem, with excellent long term function and bonding [32-34]. The Agility has flat bone interface surfaces on both the talus and the tibia, and fins are included to aid stability and increase surface area for bone ingrowth.

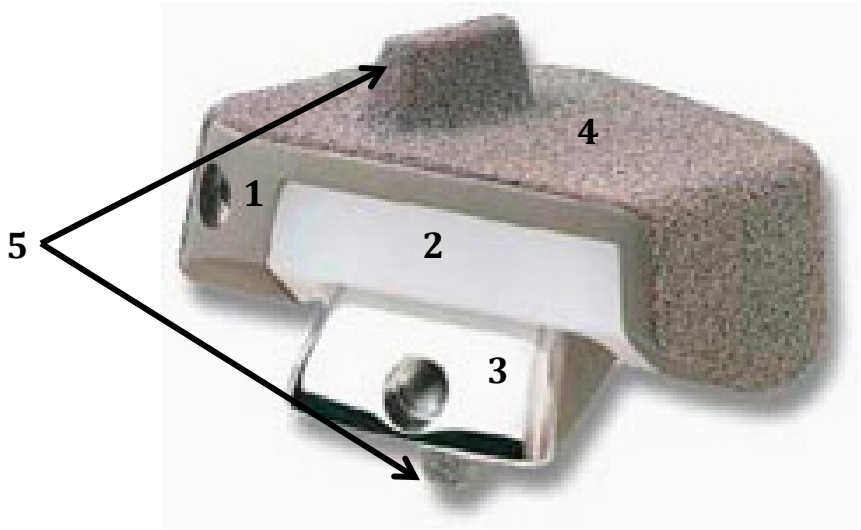

Figure 4: Agility ankle replacement prosthesis: 1) titanium tibial component 2) polyethylene bearing fixed to tibial component 3) CoCr talar component 4) POROCOAT sintered bead ingrowth surface 5) stabilization fins

1.5.2 *SCANDINAVIAN TOTAL ANKLE REPLACEMENT SYSTEM*

The Scandinavian Total Ankle Replacement (STAR®) is an unconstrained, three-component ankle arthroplasty implant manufactured by Small Bone Innovations (SBi , New Jersey). It has been used for more than 19 years and in over 15,200 patients worldwide, and just received FDA approval in 2009. The STAR is the only FDA-approved total ankle replacement system for uncemented use.

The STAR's tibial component is made from a cobalt-chromium-molybdenum (CoCrMo) alloy that has a titanium plasma spray coating on the proximal side for bone-ingrowth. It has a flat articulation surface and two cylindrical fixation barrels on the superior side to anchor the implant in the subchondral bone. It uses an ultra-high molecular weight polyethylene (UHMWPE) mobile bearing, which has a flat surface articulating with the tibial component and a concave surface with a

groove for articulation with talar component. Similarly to the tibial component, the talar component is made from the CoCrMo alloy and has a titanium plasma spray ingrowth surface. Its ingrowth surface has 5 flat surfaces combining to form a concave structure that cups the talus with a stabilization fin in the middle. It has a convex shaped proximal articulating surface with a ridge to match the groove on the bearing.

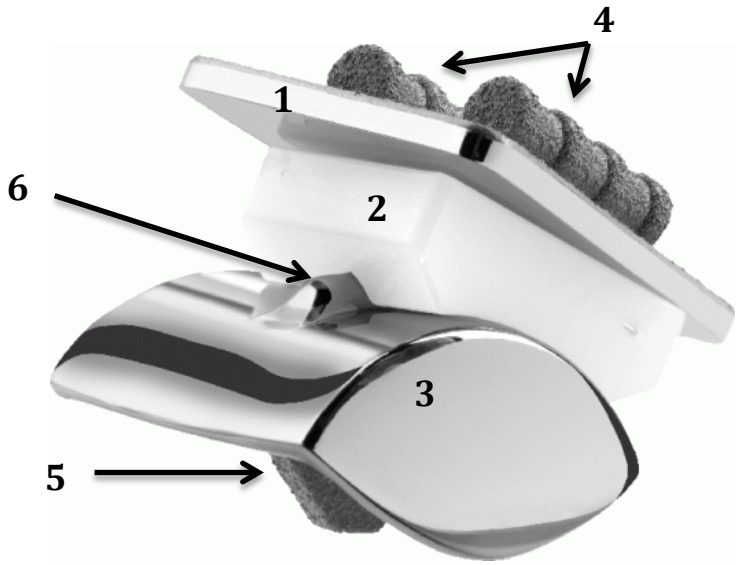

Figure 5: STAR prosthesis: 1) flat CoCrMo tibial component 2) polyethylene mobile bearing insert 3) convex CoCrMo talar component 4) tibial fixation barrels with Ti plasma spray coating 5) talar interface surface with stabilization fin and Ti plasma spray coating 6) groove and ridge to guide mobile bearing and prevent M/L dislocation

1.5.3 *Other Ankle Replacements*

Including the Agility and STAR, there are 20 TAA designs currently in use [35], and several of the other designs are shown in figures 6 through 13.

Figure 6: Salto Talaris

Figure 8: Inbone

Figure 10: AES

Figure 12: BOX

Figure 7: Buechel-Pappas

Figure 9: Hintegra

Figure 11: Eclipse

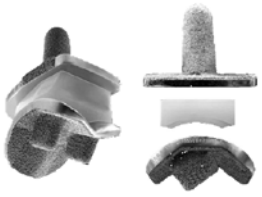

Figure 13: Mobility

As one will notice from a quick examination of these TAA models, there are a number of different geometries employed at both the articular level and bone-interface. This fact indicates that further investigation is still required to consolidate these implants and agree on the most effective designs.

1.6 CLINICAL OUTCOMES OF TAA

The implants selected for this study, the Agility and STAR, are two of the five most prevalent ankle replacement systems currently in use. Along with the notion that a larger population has interest in these results, this grants us the advantage that there is a wider range of background information on them to provide context for the results. A number of clinical studies have reported on the short- and mid-term outcomes of these implants. Examination of these clinical results can show us trends in which implants are failing, when they failing, and how they are failing. This will eventually lead to studies of a more fundamental nature in order to determine failure mechanisms and how to prevent these failures.

One major challenge with comparing or collating data from studies originating from different research groups is dealing with variation in data collection and reporting methodology. It is important to be conscientious with the data to ensure it is all taken within the same context. In this particular case, we have to be careful to maintain a consistent definition of key terms like failure rates and aseptic loosening, as well as considering the follow-up period for each patient. Slight variations to the implants and the surgical procedure have also occurred over the time frames of these studies, which cannot be accounted for. Unfortunately, some of these discrepancies cannot be reconciled and we have to accept them as a limitation. However, a benefit to be gained from synthesizing multi-study data is obtaining information from a wider demographic of surgeons and patients, which would give us a more comprehensive view of what would be occurring in practice. The following data should be considered with this in mind.

Failure of a TAA procedure is typically defined as when the patient requires a revision, arthrodesis, or below-knee amputation. Replacement of implant components, removal of one implant in exchange for another, and realignment of one or both component(s) are examples of revision,

whereas débridement and extra-articular procedures would not be included. There are several mechanisms for any type of joint replacement to fail or require some type of reoperation. The most common include aseptic loosening, instability, improper implant alignment, infection, polyethylene fracture, bone fracture, and persisting pain. A number of follow-up studies show that aseptic loosening is the predominant mode of failure (46%), followed by instability (14%), mal-alignment (11%), infection (9%), polyethylene failure (8%), pain with unknown origin (8%), and periprosthetic bone fracture (4%). (see Appendix A for details)

The failure rates of the ankle replacements in total along with those due to aseptic loosening vary a great deal across studies, due to the infrequent nature of this procedure and large variations between patients and surgeons. If we collate the data reported in all the different clinical outcome studies, we can achieve a respectable sample size that includes a range of surgeon skill levels and patients from across the globe. The following tables summarize the outcomes of several different STAR and Agility follow-up studies:

Table 1: STAR clinical aseptic loosening rates

Author	Year	N	Failures/ Revisions	Loosening Failures	Loosening Failure Rate
Anderson et al.[36]	2003	51	12	7	13.7
Skyttä et al.[9]	2010	217	31	16	7.4
Henricson et al.[10]	2007	303	71	27	8.9
Karantana et al.[37]	2010	52	8	2	3.8
Wood et al.[38]	2008	200	24	14	7
Saltzman et al.[4]	2009	593	28	<21	<3.5
Schutte et al.[39]	2008	49	4	2	4.1
Fevang et al.[12]	2007	216	21	7	3.2
Hosman et al.[11]	2007	45	3	2	4.4
Total		1726	202	98	5.7

Table 2: Agility clinical aseptic loosening rates

Author	Year	N	Failures/ Revisions	Loosening Failures	Loosening Failure Rate
Claridge et al.[40]	2009	26	5	2	7.7
Knecht et al.[41]	2004	132	14	5	3.8
Hosman et al.[11]	2007	117	8	6	5.1
Spirt et al.[42]	2004	306	33	28	9.1
Total		581	60	41	7.1

This data sample suggests that the Agility TAR has a higher percentage of procedures failing because of aseptic loosening than the STAR. While the difference may not be that large, another difference found in clinical follow-ups was that a much larger percentage of the Agilitys (78%) [41,43] had radiolucencies at the bone-implant interface than the STARs (19%) [44]. This indicates that there was only fibrous ingrowth due to excessive relative motion and is probably predictive of aseptic loosening failure in the future.

Of the second generation TAR designs (those originating in the late 80's to early 90's); the STAR, Agility, and Buechel-Pappas (BP) have had the most commercial success. The others falling into this category include the Ramses, EKSA, and TNK, but the outcome studies for these implants are very limited if they exist at all. The mid-term failure rates reported for the BP device (11.6%) [8,26] fall in the same range as the STAR and Agility. The design improvements applied in third generation TAR implants, such as improved implant geometries and ingrowth surfaces, seem to be causing slight increases in success rates [8,26], but the number of cases and duration to follow-up period is still quite limited for these implants.

1.7 ANKLE BIOMECHANICS

The range of motion of a normal ankle is approximately 70° in the sagittal plane, 50° of PF and 20° of DF, which has been shown to decrease with age [45,46]. However, this doesn't represent its absolute maximum ROM because stretching and certain activities can cause it to exceed these passive values by over 200% [47]. During daily activities, different subsets of the overall ankle ROM are utilized. Level walking normally requires only about 15° of PF and 15° of DF [48], while running uses 20° of DF and stepping down from a step requires slightly more ROM particularly in DF (around 25° DF and 15° PF) [47]. The range of motion can get up to as high as 39.7° of DF, 24.7° of INV, 17.7° of EV, 11.7° of ER, and 27.5° of IR in specific daily activities that require a high range of motion like squatting, kneeling, and sitting cross-legged [49]. By applying a fixed joint torque in cadaveric tests, the actual ROM may not necessarily be determined because the output values depend on the magnitude and method of applied loads, but it provides a great way to systematically compare different ankle joints and replacements. A cadaveric ROM test found PF-DF, INV-EV, and IR-ER ROM limits of 28.2°-14.7°, 13.8°-5.0, and 15.2°-8.2° respectively in the intact ankle [50], however, this seems to be a quite conservative ROM limit when compared to previously mentioned data.

One reason that kinematic replication of the ankle joint is so difficult is that the instantaneous axis of rotation is constantly changing depending on its relative orientation within the joint due to the combination of sliding and rolling that occurs on the talar surface, which has a varying radius of curvature. Changes in the ankle's instantaneous axis of rotation occur in all three planes, and the axis affected by ankle motion in any of these planes. In the transverse plane, the axis generally remains parallel to the line intersecting the two malleoli throughout a range of flexion angles [20]. In the sagittal plane, the instantaneous center of rotation moves from an antero-superior to a postero-inferior position as the foot rotates from DF to PF [21]. In the frontal plane, the axis of

rotation is oriented downward laterally in DF and either downward medially or horizontal in PF [20].

The rotations of the ankle joint complex along its three axes are naturally coupled together. For this reason, ankle motion is sometimes described in terms of supination and pronation. Pronation involves the concurrent rotations of dorsiflexion, eversion, and external rotation, and supination is the opposite, which involves plantarflexion, inversion, and internal rotation. During gait, the foot pronates during midstance and supinates from heel rise to toe-off [51]. Motion coupling between axes has been classified in cadaveric experiments as rotation along a secondary axis due to applied rotation about a given axis. Although differences in motion coupling patterns are seen between studies due to differences in loading apparatuses, the same patterns of coupling in the supination/pronation relationship were observed [52,53].

Very few direct measurements of kinetic parameters are available, but we can be quite confident with indirect measurement techniques based on the strong agreement between studies analyzing the same activities with different methods [54]. Indirect measurements require the use of *in* vivo measurements to apply inverse dynamics calculations to a model of the ankle in order to predict joint loads or tissue stresses and strains depending on the complexity of the model. Considerable differences in load magnitudes occur within ankles of different specimens, even those of similar size, due largely to anatomic variation – especially of structures affecting the musculotendinous moment arms.

The ankle experiences the highest loads out of any joint in the entire body. Even during a relatively common and repetitive activity such as running, the ankle has been reported to transmit compressive forces up to 11.1-13.3 BW (approximately 7-8 kN for the average person) [14,55]. The ankle is the most distal of the large joints, which requires it to support almost the entire body weight. Compared to the hip and knee, the loads in the ankle are proportionally larger than one

would expect due solely to supporting a larger BW percentage. During walking, the tibiotalar joint experiences a maximum compressive load of approximately 5-7BW during push-off (approx. 70% of stance phase) whereas 3-4BW and 2-3BW are seen in the knee and hip respectively [15]. The architecture of the foot is such that the moment arm of the forefoot about the ankle is considerably longer than that of the Achilles tendon. This increases the magnitude of plantar flexing moment required for forward propulsion, which requires a larger force in the Achilles tendon and increases the compressive load in the joint.

The moments generated about the ankle have been measured for different contraction velocities and forms and have also been calculated with models for several activities. The maximum plantar-flexing moment in voluntary isometric contraction was found to be 232 Nm on average with a corresponding Achilles tendon tension of just over 4.5 kN (approximately 7 BW) [56]. Similar measurements have been taken with muscle contraction being applied with maximum tolerated electrical stimulation in an attempt to better isolate and control the contraction, but the maximum applied moment was much lower than the previously mentioned values (less than 75 Nm) [57]. The plantarflexion moments calculated for activities such as running, walking, and jumping agreed reasonably well with these results with maximum moments of 240 Nm (1.2 BW·fl – 50th percentile male), 120 Nm (0.6 BW·fl – 50th percentile male), and 250 Nm respectively [55,58].

In addition to the forces and moments experienced during gait, the contact pressures have also been examined with finite element models and pressure films in cadaveric experiments. While joint loads calculated for the ankle had quite reasonable agreement across a range of studies, there are more discrepancies in the calculation of contact stresses. One FEA study found maximum stresses in the talus of 3.55 MPa during push-off with a 3 kN compressive ankle load [59] whereas another found peak stresses ranging from 9-14 MPa with a 2.8 kN compressive load [60]. A scaled down cadaveric gait simulation using a pressure sensing film, found a mean peak pressure of 4.8 MPa

using a ground reaction force of 350 N [61]. This result favours the latter FEA experiment's values, but further validation is still necessary.

Possible explanations for differences in stress calculations are likely due to difficulties in modeling the behaviour of the contact surface. Inaccurate material properties, especially of the cartilage, can lead to drastically different joint contact areas. Contact area will increase with a more compliant surface, and it has also been observed to increase significantly with increased compressive force [62]. Because of the shape of the trochlea tali, an increase in contact area also occurs when the foot is in dorsiflexion compared to plantar flexion [63,64]. A number of studies have looked at effective contact areas for different foot positions, and it is generally agreed upon that the average contact area of the ankle is in the range of 300 to 500 mm^2 [62-66].

1.8 BIOMECHANICS OF THE REPLACED ANKLE

A successful total ankle replacement must fulfill three key requirements. It must reproduce the kinematic behaviour of the natural joint, be strong enough to endure the dynamic loading of the ankle over many years of use, and be accepted by and fully integrated into the body.

It has been determined that the tibiocalcaneal and calcaneofibular ligaments are essential in guiding the ankles motion in the sagittal plane during passive flexion, while the superficial tibiotalar and anterior talofibular ligaments play a role in determining range of motion limits [67]. Because the articulating surfaces are removed in a joint replacement, the ligaments are the major constraining structures that remain constant, which makes it very important to understand their role and function in ankle motion. Modelling the motion of the ankle using a 4-bar linkage with

isometric ligaments reproduced observed motion with considerable accuracy [21]. Using this model, an ankle replacement articulation geometry was designed that would be compatible with the ligament structure and throughout the flexion range of motion [68]. Expansion of this concept to create more accurate three dimensional simulations, respecting all ligaments and structures has proven to reproduce accurate kinematic behaviour essential to finite element analyses [69]. Being respectful of the ankle's remaining structural components and designing a replacement that replicates normal kinematics within these constraints is crucial in creating an effective prosthesis. While the usefulness of computer models has been demonstrated in this specific context of designing ligament compatible geometries, their biggest use is in determining stresses and strains in implant components with FEA, and more useful kinematic data can be found in cadaveric tests.

Table 3: ROM values for the Agility and STAR as determined by Valderrabano et al. (2003)

Implant	Range of Motion (degrees)					
	PF	DF	INV	EV	IR	ER
Agility	30.0	10.0	17.4	11.9	16.3	10.0
STAR	22.7	10.6	7.8	7.5	4.9	15.6

The range of motion of replaced ankles has been examined with cadaveric tests in two different studies: one by Valderrabano et al. that examined the ROM about all three axes including analysis of the Agility and STAR among others [50], and the other by Tochigi et al. that looked at the PF-DF ROM of the STAR [70]. Valderrabano's results pertaining to these two implants are summarized in Table 3. In Tochigi's experiment, the

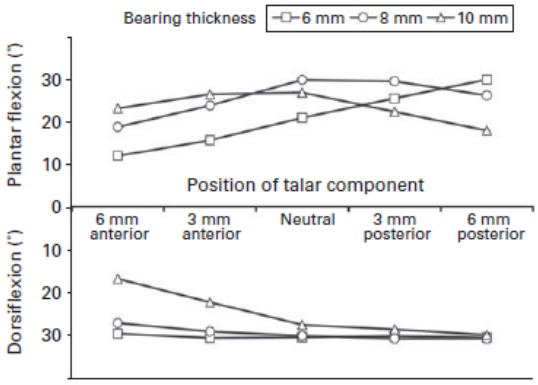

Figure 14: PF-DF range of motion of the STAR as affected by different amounts of A/P misalignment and bearing thickness. Reproduced and adapted with permission and copyright © of the British Editorial Society of Bone and Joint Surgery [66].

STAR was found to have a ROM of 29.6° PF and 30.3° DF with proper installation, although it that was found to be significantly affected by bearing thickness and A/P positioning of the talar component (fig. 14). Comparing the STAR PF-DF ROM of these two studies, we find that the Tochigi's values were considerably higher. There were differences in the loading apparatus and definition of ROM limits that are likely the cause of this discrepancy. Valderrabano's test used a 200 N axial load and a 100 Nm static moment, whereas Tochigi's test used a 300 N axial load and determined ROM limits by ligament strains or bearing lift-off. The ROM values determined by Valderrabano et al. for these implants are likely an underestimate since those of the intact ankle were quite conservative, as previously noted.

The amount of coupled rotation comparing implanted and intact ankles has been looked at also by Valderrabano et al. [52] as well as by Michelson et al. [53]. Regardless of the TAA design in question, the motion transferred from one axis to the next was consistently reduced from the intact ankle. The supination/pronation coupling relationship was still evident, but to a considerably lower degree, which varied between implant designs.

Along with coupled rotations about the other two axes, there is also mediolateral translation of the talus that accompanies PF-DF rotation. The amount of M/L translation in mobile bearing prostheses (around 5mm) is similar to that found in the intact ankle while a semi-constrained device allows much less of this motion [18].

Another important kinematic parameter related to joint translation is joint laxity, which has been examined in the intact ankle and one implanted with the STAR (fig 15). This study measured the amount of A/P and M/L translation of the talus when the ankle in the neutral position was subjected to a load limit of 150N with and without a compressive load. The joint laxity was significantly higher in the STAR ankle, which was even more pronounced in the case where

compression of the joint was included, because the 700N compressive load drastically decreased the laxity in the intact ankle while only moderately reducing the laxity in the replaced ankle. [71]

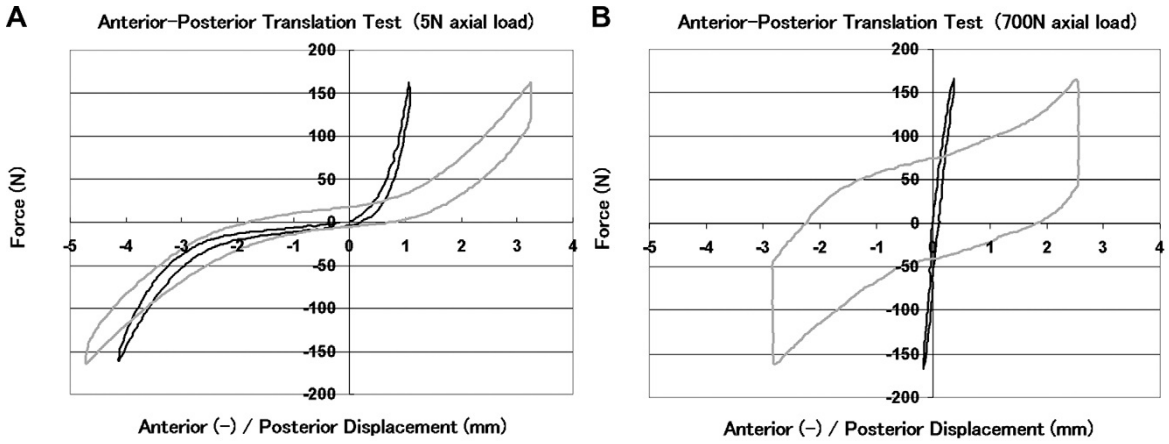

Figure 15: A/P laxity of the intact ankle (black) and STAR (gray) with 5N (left) and 700N (right) axial compression. Reproduced with permission from Elsevier via Copyright Clearance Center, Inc. (Source: Watanabe et al. 2009 [71])

The joint reaction forces and moments within a replaced ankle are nearly the same as those of a normal ankle. However, slight differences are present in people suffering from ankle arthritis [72] due to altered motion patterns of as a means of mitigating pain, which in turn reduces joint loads. After receiving an ankle replacement, the joint reaction forces within the ankle during gait were increased compared to the pre-operative condition but still lower than the normal loads (fig. 16). Other gait studies have also confirmed the improvement of several other kinetic and kinematic parameters following total ankle replacement in short to intermediate follow-up periods [25,73]. While the performance of TARs might not reach that of normal ankles, they should still be designed to withstand the loads of a normal ankle to provide a reasonable safety factor. Therefore, there is little need to explore the kinetic behaviour of the ankle much further, except with the intent of looking closer at the stresses and strains specific to the prosthesis.

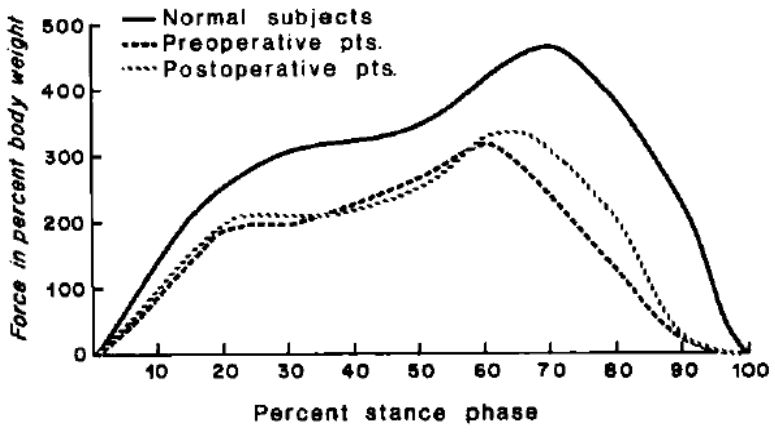

Figure 16: Ankle joint reaction force in percent body weight as a function of percent stance phase during walking gait for normal subjects, preoperative patients, and patients who have received TAA. Reproduced with permission from Lippincott Williams & Wilkins via Copyright Clearance Center (Source: Stauffer et al. 1977 [72])

In comparison to the tibial and talar components, which are built from metals much stronger than bone, the UHMWPE meniscal or bearing component is quite fragile. A number of TAA failures have been attributed to the fracture or abnormal wear of this component, giving cause for investigation into its stresses and wear rates. Finite element models are an excellent way to provide detailed information on the stresses and strains experienced by all the components of an ankle replacement. While cadaveric testing with pressure films is tedious and costly, they are necessary for validation of these models to ensure the proper parameters are used to get accurate results. Computer simulations can be used to test any number of potential loading scenarios very quickly and inexpensively once the model has been validated. In practice, this has been used to examine the effects of design modifications and improper implant alignment in existing devices, and the projected performance of a device under development.

Experimentally validated FEA models have been conducted in order to determine the stress distribution throughout the polyethylene components during gait of the Agility and Mobility total ankle replacements (DePuy). It was found that wider talar components in the Agility decreased stresses in the PE liners, but the decrease in pressure were not as much as would be expected if it

were proportional to the increase in contact area [74]. The Mobility was found to have much lower average contact pressures than the Agility for proper alignment, with the Agility (22 MPa) exceeding the yield stress of PE (18 MPa) (fig. 17). The effect of implant misalignments were looked at and marked increases in the articular contact pressures occurred when malaligned for both implants, but the increase was more dramatic in the Mobility with severe edge loading in the PE component, showing a two- to four-fold increase in maximum von Mises stresses on the inferior surface of the mobile bearing [75].

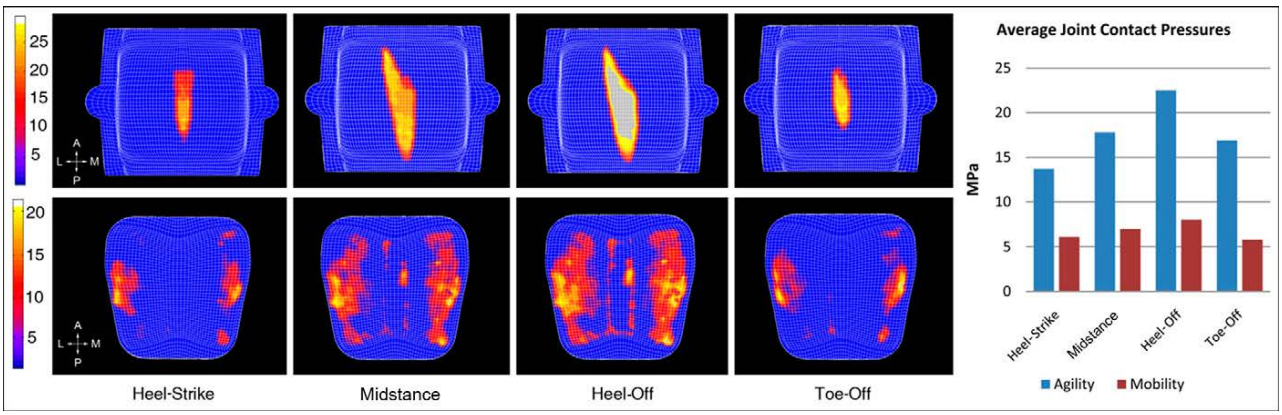

Figure 17: FEA results of contact pressures for the Agility (top/blue) and Mobility (bottom/red) in proper alignment. Image reprinted with permission from *JBJS Am*(Source: Espinosa et al. 2010 [75])

Additionally, the use of modelling as a preclinical design tool has also been implemented. The Box ankle prosthesis developed by Leardini et al. was subjected to an even more complex gait simulation, including the effects of ligaments. The design was determined to be capable of allowing the necessary range of motion without overstraining any ligaments. The contact pressures also remained below the yield stress of the polyethylene bearing throughout the simulation, reaching a maximum on the inferior surface of 16.1 MPa at 79% of the stance phase. [69]

Contact pressures are certainly linked to the wear behaviour of the PE, but these simulations cannot give us concrete evidence about the long term wear patterns or rates. In order to determine this, in vitro tests must be performed on the prosthesis. Knee joint wear simulators were modified

to fit total ankle replacements and to apply loading conditions specific to ankle during the stance phase of gait. A similar experimental procedure was performed simultaneously by two groups to determine the wear behaviour of the aforementioned novel ankle replacement design [76], and to compare the wear rates of the Buechel-Pappas with the Mobility [77]. The latter experiment found lower wear rates in the Mobility, albeit insignificant due to low sample size. This wear simulation procedure was verified to be effective by comparing the wear patterns from the simulator after 2 million cycles to those found in retrieved prostheses of the same design [78].

Despite the fact that aseptic loosening is the leading cause of total ankle replacement failure, and several studies have elucidated the role of micromotion in bone ingrowth, no studies have examined micromotion between the implant and bone to date.

1.9 *IN VITRO* ANKLE LOADING APPARATUSES

Cadaveric biomechanical tests on ankle replacements are lacking, but there are a good number of experiments on the intact ankle joint complex that can aid in developing suitable testing methodologies and understanding ankle function. Due to the foot's large number of bones and joints, it is difficult to control and replicate *in vivo* mechanics and kinematics of the simplest activities. However, efforts put toward the reproduction of these forces and motions have yielded meaningful results that provide baseline data for the intact ankle that developers of TARs can aim to reproduce.

Recent advances in robotics and control have given us the ability to simulate muscle activation by applying forces to the tendons involved in foot and ankle locomotion (fig. 18). EMG and muscle force data collected from *in vivo* gait experiments have exposed the state of muscle activity for a normal person. This technology combined with the knowledge of our natural ankle biomechanics has been synthesized to mimic gait within stance phase quite accurately [54].

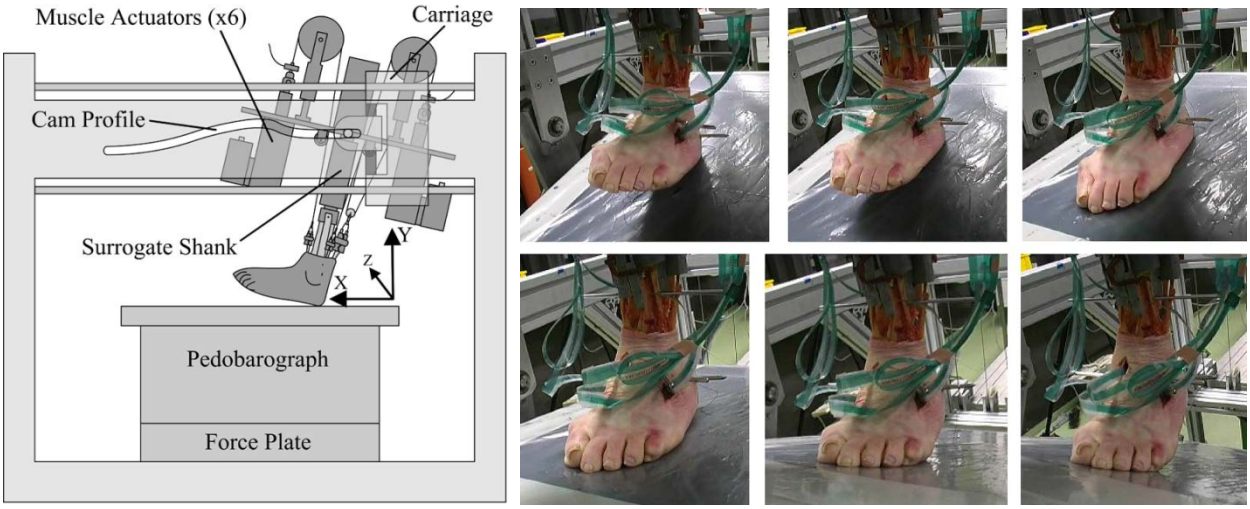

Figure 18: Schematic of a robotic stance phase gait simulator from Pennsylvania State University (left) and sequences of images from a different cadaveric gait simulator from the University of Tubingen (right). Both figures reproduced with permission from Elsevier via Copyright Clearance Center (Source: left – Hamel et al. 2004 [79]; right – Suckel et al. 2008 [80])

Experiments with these types of simulators have been an invaluable tool with which we have been able to study and better understand how the bones in the foot move and interact with each other with invasive measurement techniques [79,81,82] that provide much more accurate data than can be gathered from *in vivo* tests. This methodology has also been extrapolated to examine kinematics in ankles with various injury models [83] as well as determining joint loads in healthy [61,80] and fused ankles [84].

Less complex models which employ a variety of configurations with differing levels of constraint in both static and dynamic loading have also given us a better understanding of the ankle joint complex. The most obvious simplification from the above mentioned method is to break down the motion into static postures of the movement of interest. This still allows us to evaluate the relative positions of bones [85] and even solving for certain muscle forces required for equilibrium [86]. Basic methods using manual manipulation while taking bone position measurements have shown us which method of fracture fixation is more effective [87] and where different axes of the foot and ankle are located [88]. Manual displacement control of an axially loaded, rotationally unconstrained ankle has been used to show how ankle motion patterns change with varying fracture severities or TAA [53,89].

A few different methods of applying external loads by actuators or motors have been utilized to dynamically test the ankle. An ankle tester developed at the University of Iowa (shown in fig. 19-1) uses an MTS system to apply axial compression and IR-ER torque and a pneumatic actuator to apply A/P force to the proximal tibia, and the foot orientation is controlled by a linear servohydraulic cylinder on the PF-DF axis and pulley/weight system for the INV-EV axis. It is a 6 DOF system with automated control of 4 motions and capability for constant torque to one axis, leaving only the M/L translation axis with no loading capability [70,90-92]. A multi-axial testing device was used to test the ankle at the Mayo Clinic that is capable of applying an axial load to the proximal tibia with a linear actuator, A/P and M/L forces to the foot with a powered translation table, and an axial moment to the foot via a rotary stage (fig. 19-2) [71]. Aside from these two devices and muscle actuated gait simulators, the only other dynamic ankle tester is one developed in our lab by Chad Larson (fig. 19-3) which is capable of applying a pure moment to the foot with very minimal forces and off-axis moments.

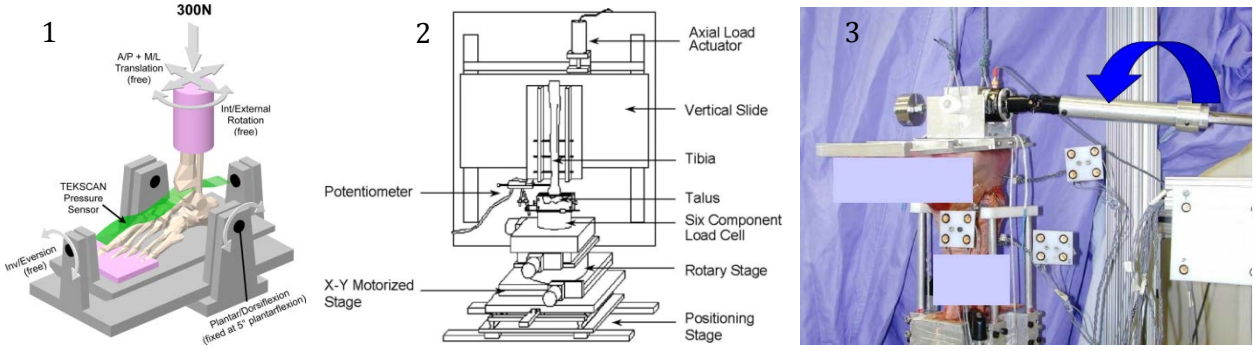

Figure 19: Ankle loading devices designed to be able to 1) apply axial load, A/P force, PF-DF/INV-EV/IR-ER moments or leaving all axes unconstrained (Univ. of Iowa) 2) apply axial load, A/P and M/L force, and axial moments (Mayo Clinic) 3) apply pure moments to the unconstrained foot (C Larson – UBC). Fig. 19-1 (Source: Anderson et al. 2010 [90] & fig. 19-2 (Source: Watanabe et al. 2009 [71]) reprinted with permission from reprinted with permission from Elsevier via Copyright Clearance Center. Fig. 19-3 reprinted with permission from Younger AS (Source: Larson et al. 2005 [93])

As with all *in vitro* biomechanical tests, there is an inherent trade-off between the degree of biofidelity and simplicity of the experiment. While more complex experiments allow for better replication of finer details, they typically also require more costly and elaborate equipment along with being technically more difficult to perform and collect data from. On the converse, simpler experiments will usually be less expensive, and can be less complicated to allow for a more robust and clear conclusion. They can still reveal important information concerning trends or comparisons in which the precise values are not of paramount importance.

1.10 MICROMOTION

1.10.1 *THEORY*

It has been observed that all skeletal tissues, ranging from ligaments to bone, can form from the same mesenchymal precursor cells. The environment in which the mesenchyme is cultivated, including mechanical stimulus, plays a large role in determining what tissue it will differentiate into. Within the field of mechanobiology, a few different theories exist on the driving mechanism(s) behind the growth and differentiation of skeletal tissue. They typically involve different combinations of stress/strain tensors or invariants. The most prominent models include those by Pauwels [94], Carter & Beaupré [95], Claes & Heigele [96], and Prendergast & Huiskes [97] illustrated in the following figures.

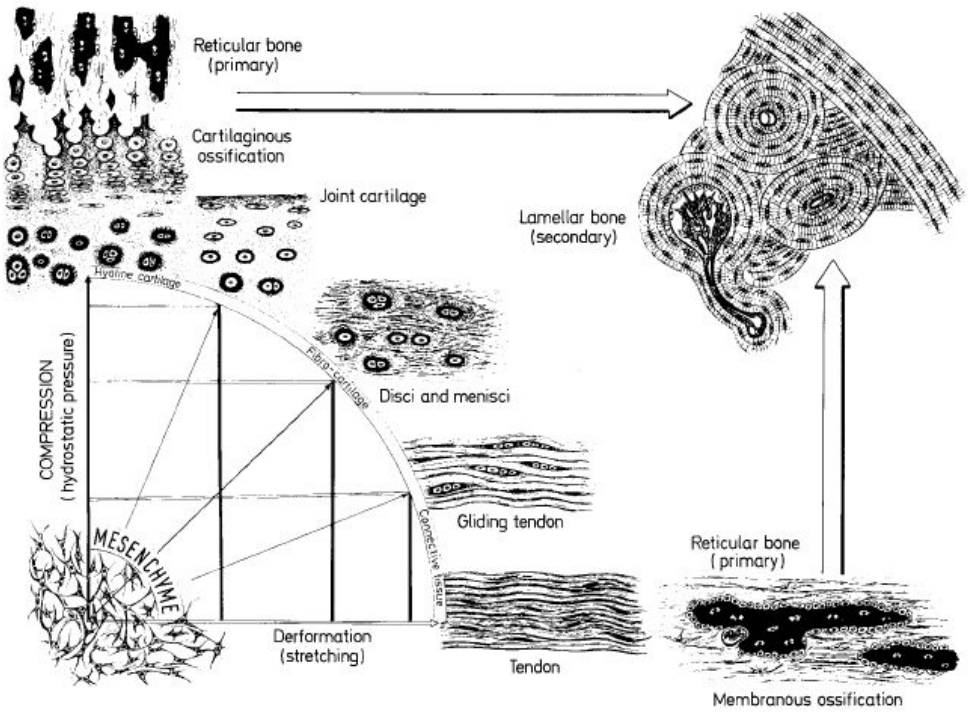

Figure 20: Mechanoregulation concept schematic of musculoskeletal connective tissue differentiation as proposed by Pauwels. Reproduced with permission from Elsevier via Copyright Clearance Center (Source: Weinans et al. 1996 [98])

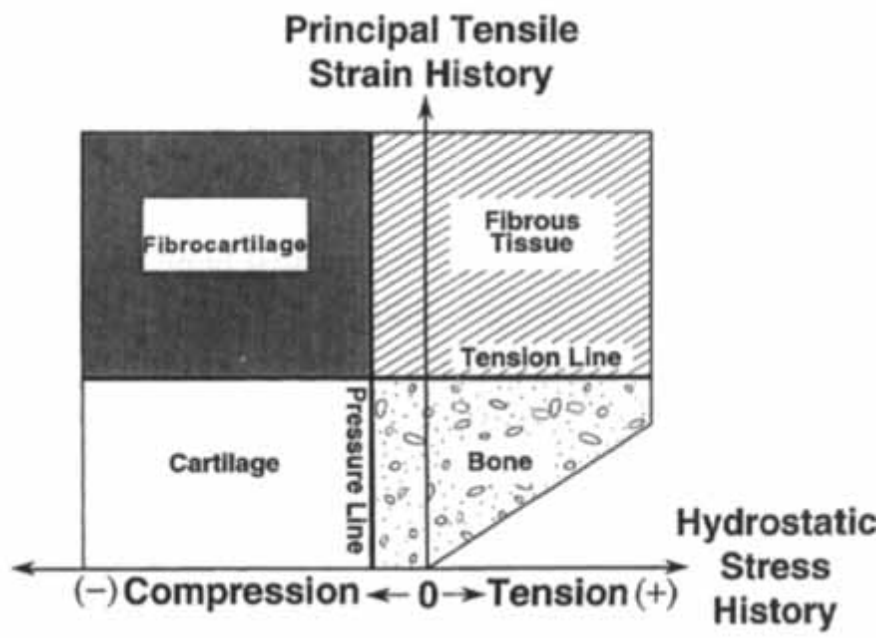

Figure 21: Mechanoregulation concept controlled by hydrostatic stress and tensile strain history as proposed by D.R. Carter. Reproduced with permission from Lippincott Williams & Wilkins via Copyright Clearance Center (Source: Carter et al. 1998 [95])

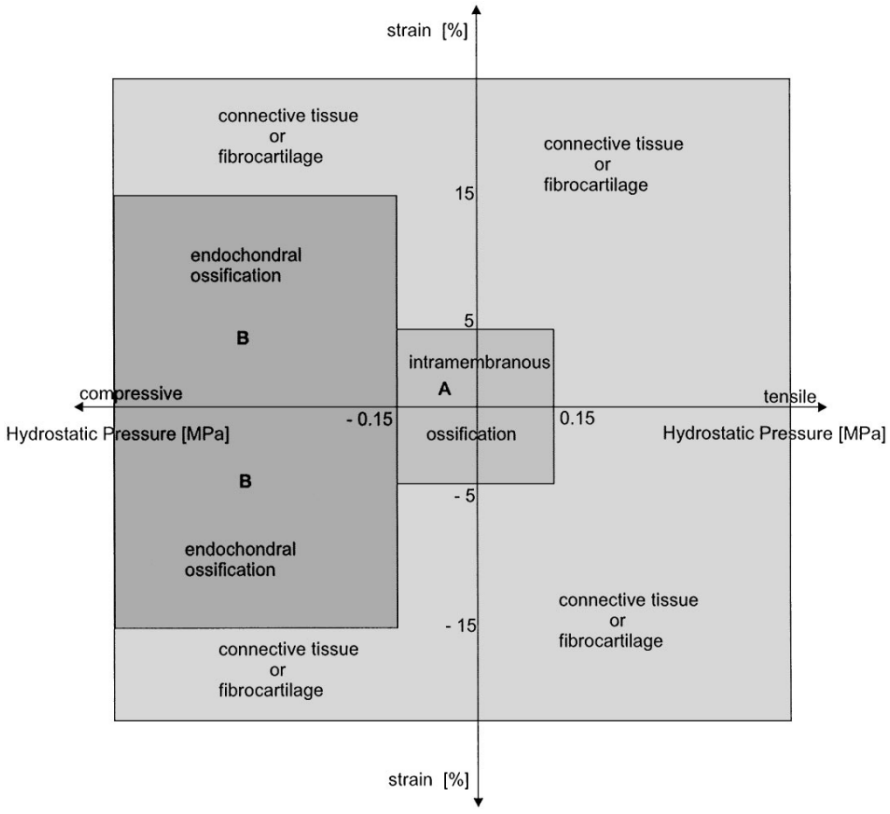

Figure 22: Mechanoregulation concept controlled by hydrostatic pressure and strain as proposed by Claes and Heigele. Reprinted with permission from Elsevier via Copyright Clearance Center (Source: Claes et al. 1999 [96])

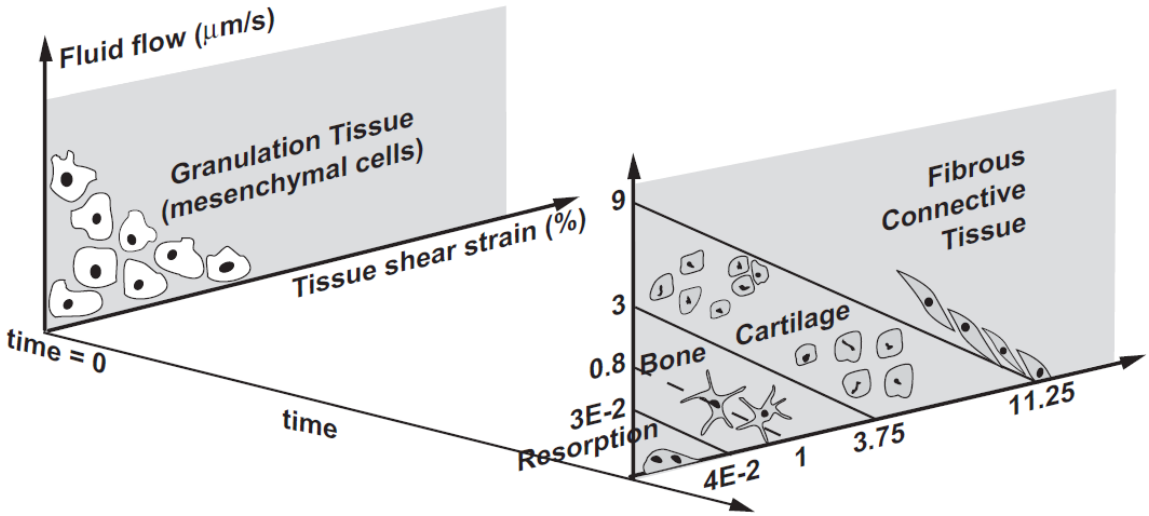

Figure 23: Biphasic mechanoregulation concept controlled by interstitial fluid velocity and solid shear deviatoric strain as proposed by Prendergast and Huiskes. Reprinted with permission from Elsevier via Copyright Clearance Center (Source: Lacroix et al. 2002 [99])

All of these theories, while differing in perspective on what the exact stimulus is behind the differentiation, agree on the fact that large shear strains promote fibrous tissue and inhibit osseous formation.

These theories have been effectively used to model and predict phenomenon such as fracture healing and fetal bone development. However, they not only apply to purely biological systems, but also to those interfacing with other materials such as orthopaedic implants. Uncemented joint replacements have a porous surface to interface with the bone and rely on bone growth into that surface for long term stabilization. The mechanical stimuli at the interface of uncemented joint replacements and the host bone are in theory directly related to the type of tissue that will form in and around the surface of the implant. Large relative motions between the implant and bone will create shear stresses in the tissue and lead to fibrous tissue differentiation, whose characteristics are undesirable for implant fixation longevity. Smaller motions will reduce shear strains and allow for continuous bone ingrowth, providing a strong and durable interface between the implant and bone.

1.10.2 *IMPLANT MICROMOTION*

Studying the micromotion in total joint replacements in order to determine which designs are less likely to fail is not a new concept, even though it has not been attempted in ankles. It has been proposed that such testing should be a requirement of new designs to ensure their quality [100]. There are several different methods that have been employed to examine the motion behaviour of different hip and knee replacements.

1.10.2.1 In vivo animal tests

Performing *in vivo* measurements is essentially the only way to observe the actual bone remodelling response around implants. However, ethical considerations make performing this type of experiment on humans undesirable. The next best approximation would be *in vivo* animal tests, of which there have been a few dog experiments of note. For a series of beagles with hip replacements, it was found that the ones that had osseointegration produced maximum recoverable deflections of 28 μm, whereas those with fibrous tissue ingrowth had maximum recoverable deflections of 150 μm in the least compliant specimen [101]. In another study all the foxhounds with hip replacements were found to have osseointegration with initial fixation micromotion measurements of up to 56 μm. After periods of either .5, 1, or 2 years to allow for bone ingrowth, the micromotion magnitudes observed dropped significantly [102]. In an effort to quantify the amount of micromotion permitting bone ingrowth, another foxhound study was performed in which constant cyclical motions of different magnitudes (0, 20, 40, and 150 μm) were applied to implants in their femurs. Those with zero and twenty microns had continuous bone ingrowth, those with forty showed partial bone ingrowth, and those with 150 μm only had fibrous ingrowth (fig. 24) [103].

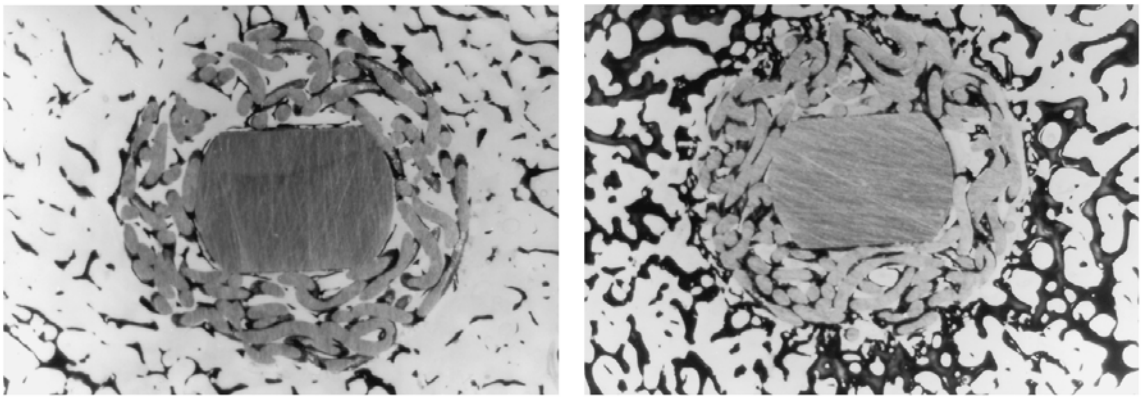

Figure 24: Photomicrographs of porous coated implants subjected to 0 and 150 µm of cyclic micromotion showing complete osseointegration (left) and disconnected bone ingrowth and fibrous tissue (right). Reprinted with permission from *JBJS Am* (Source: Jasty et al. 1997[103]).

While we can't draw a direct conclusion from these experiments on the threshold amount of initial micromotion separating human patients with bone vs. fibrous ingrowth, this does show us:

a) That a stabilization of micromotion over the healing process occurs – even though exceeding 40µm where only partial ingrowth was observed, at 56µm of initial motion there was still full osseointegration
b) A rough estimation for the order of magnitude of micromotion permitting continuous bone ingrowth. It is generally accepted now that the ingrowth threshold is between 100 - 200µm.

1.10.2.2 Ex vivo cadaveric tests

The micromotion patterns of joint replacements have been studied to analyze a number of different design characteristics of joint replacements. Examples of these characteristics include stem geometry (shape, length, diameter) [104,105], material [104], surface roughness [106], cementing techniques [107,108]. By isolating the design features that improve and hamper the initial fixation of the prostheses, superior designs were able to be implemented that minimize the risk of aseptic loosening.

Experiments have been performed to improve the testing methodology for micromotion measurements as well. To improve the accuracy of the measurement, novel measurement techniques were developed [109,110] and protocols for the standardization of how and where the measurements should be taken have been proposed [111]. A protocol for taking initial fixation measurements as a means to pre-clinically predict the loosening of hip replacements has also been put forward [100].

1.10.2.3 FEA modeling

The use of finite element modeling has proved useful in micromotion measurement. Models have been validated with the use of *in vitro* experiments and have shown good agreement. However, caution should be taken when evaluating models, and they should be validated with experimental data when possible because small changes in parameters that have no physical bearing can easily throw off measurements by an order of magnitude [112]. The usefulness of accurate models is quite broad, enabling subject specific tests [113], implant design tests with a large range of loading conditions [114], large numbers of tests with statistical population variations (weight, height, bone quality, and interface gap presence) [115], and a host of other possible applications with very detailed outcomes.

1.10.2.4 In vivo RSA

The use of models can also be applied to measurement techniques outside of the typical FEA applications to be used in conjunction with RSA. By merging these two techniques, it is possible to achieve similar accuracy and precision to standard marker-based RSA without the requirement of tantalum beads [116,117]. This expands the usefulness of RSA measurements to a much wider application base.

1.10.3 *ASEPTIC LOOSENING*

Aseptic loosening refers to the failure of orthopaedic implants by mechanical loosening in the absence of sepsis. There are two distinct methods by which this happens over different time frames. One is caused by the production of polyethylene wear particles, which triggers an immune system response that activates macrophages and sends them to the site to remove the foreign particles. Peri-prosthetic osteolysis, or bone resorption, is an unfortunate byproduct of this process that can weaken the bone-implant bond and result in mechanical loosening failure. Since this process is a result of bearing wear, it usually only initiates after 5-7 years of use [118]. The other cause of aseptic loosening, relative motion between the bone and implant, is present right from the outset and can lead to failure and revision much earlier. It has already been established that in an environment where excessive micromotion is present, osseointegration of the implant is impossible and fibrous tissue forms around the implant instead. The formation of fibrous tissue immediately following implantation does not necessarily imply aseptic loosening will occur. Three typical outcomes can arise from this scenario: the micromotion decreases over time to enable osseointegration, the micromotion stabilizes at a level that neither allows bone ingrowth nor causes circumstances requiring revision, or the micromotion increases over time and gives rise to complications requiring revision surgery [4,41]. Implant migration patterns within the first couple of years have been shown to predict aseptic loosening behaviour whose symptoms would require revision surgery quite soon or even after many years (up to ten years later) [119,120]. Although not always resulting in revision, it is commonly accepted that weak initial fixation (fibrous ingrowth) is a strong predictor of future aseptic loosening failures, similar to migration.

1.11 MOTIVATION

There is a general lack of research in the area of total ankle replacements in comparison to its hip and knee counterparts. In order to reduce their failure rate, it is important to produce similar biomechanical analyses of the joint to better understand the ankle's performance before and after replacement. Aside from the obvious outcomes of kinematic variables, the motion between the implants and their anchoring bone is of particular interest because of the large proportion of total ankle arthroplasty failures that are attributable to aseptic loosening. Aseptic loosening can occur as a result of excessive interfacial motion, which prevents continuous bone ingrowth right from the outset and fibrous tissue is formed at the interface instead. In order to prevent this from happening, it is imperative to reduce the amount of motion between the implant and bone by determining which designs are best suited to accomplish this.

1.12 OBJECTIVES

The primary objective of this study was to perform a biomechanical analysis of the cadaveric ankle to compare two commercially available total ankle replacement designs, the STAR and Agility. This analysis contained specific aims to:

1. Determine the difference in micromotion at the bone-implant interface between the Agility and STAR for both tibial and talar components
2. Determine the effect of applying a compressive load on the relative micromotion magnitudes
3. Quantify the kinematic changes imposed on the ankle by the joint replacement prostheses in comparison to each other and intact ankles

2 METHODS

2.1 EXPERIMENTAL DESIGN

This experiment was designed to simulate a range of loading scenarios in the ankle in order to observe the performance of both the STAR and Agility total ankle replacements in comparison to each other and intact ankles. The ankle testing apparatus was designed to apply a compressive load and a pure moment to the otherwise unconstrained foot. Six bilateral pairs of human cadaver ankle joints were tested in this simulator, which were initially analyzed intact and again after having received total ankle arthroplasty. Each ankle received one TAR, such that one ankle of each pair had the Agility and one had the STAR. Each test consisted of a sequence of 3 independent load applications about orthogonal axes. These axes coincided with those on the ankle defined as plantarflexion-dorsiflexion (PF-DF), inversion-eversion (INV-EV), and internal rotation-external rotation (IR-ER). Each limb was subjected to a compressed and an uncompressed test for both intact and implanted conditions.

An optoelectronic motion capture system was used to determine the 3-dimensional positions and orientations of the bones and joint replacement components during these tests. These measurements were used for determining bone-implant micromotion as well as kinematic variables such as range of motion (ROM), motion coupling (MC), and joint translation (JT).

2.2 ANKLE LOADING APPARATUS

The ankle loading apparatus used in this study of total ankle replacements had five distinct components: moment applicator, foot-plate, counterbalances, mounting rig, and follower load (fig. 25). The moment applicator was used to apply a pure moment to the foot-plate while leaving the other 5 DOF unconstrained. The foot-plate's function was to attach rigidly to the bottom of the foot, provide attachment points for the moment applicator's fixture block and counterweight cables, and facilitate the application of a compressive load. The counterbalances' purpose was to counteract the weight of the footplate and moment applicator arm so that there were no external forces or moments acting on the ankle other than the applied loads. The mounting rig was needed to fix the proximal end of the foot to the test platform and supply a means to guide the compressive load cables through the centre of the ankle. The follower load used a linear hydraulic actuator and cable system to apply a constant compressive load to the foot-plate.

This apparatus was adapted from one originally designed for loading the spine [121]. It applies a pure moment about a single axis to one end of the spinal segment while the other end was fixed to the test platform. The moment was applied in such a way that allowed the superior end to be completely unconstrained except for the axis about which the moment was being applied. This apparatus was previously modified for testing with the ankle by Chad Larson, a former M.A.Sc. student [93]. His study compared the relative strengths of different ligament grafting techniques by applying moments to the ankle about 3 orthogonal axes. The test apparatus he used was similar to the one used in the present experiment, except that no compressive loads were applied in his ligament study.

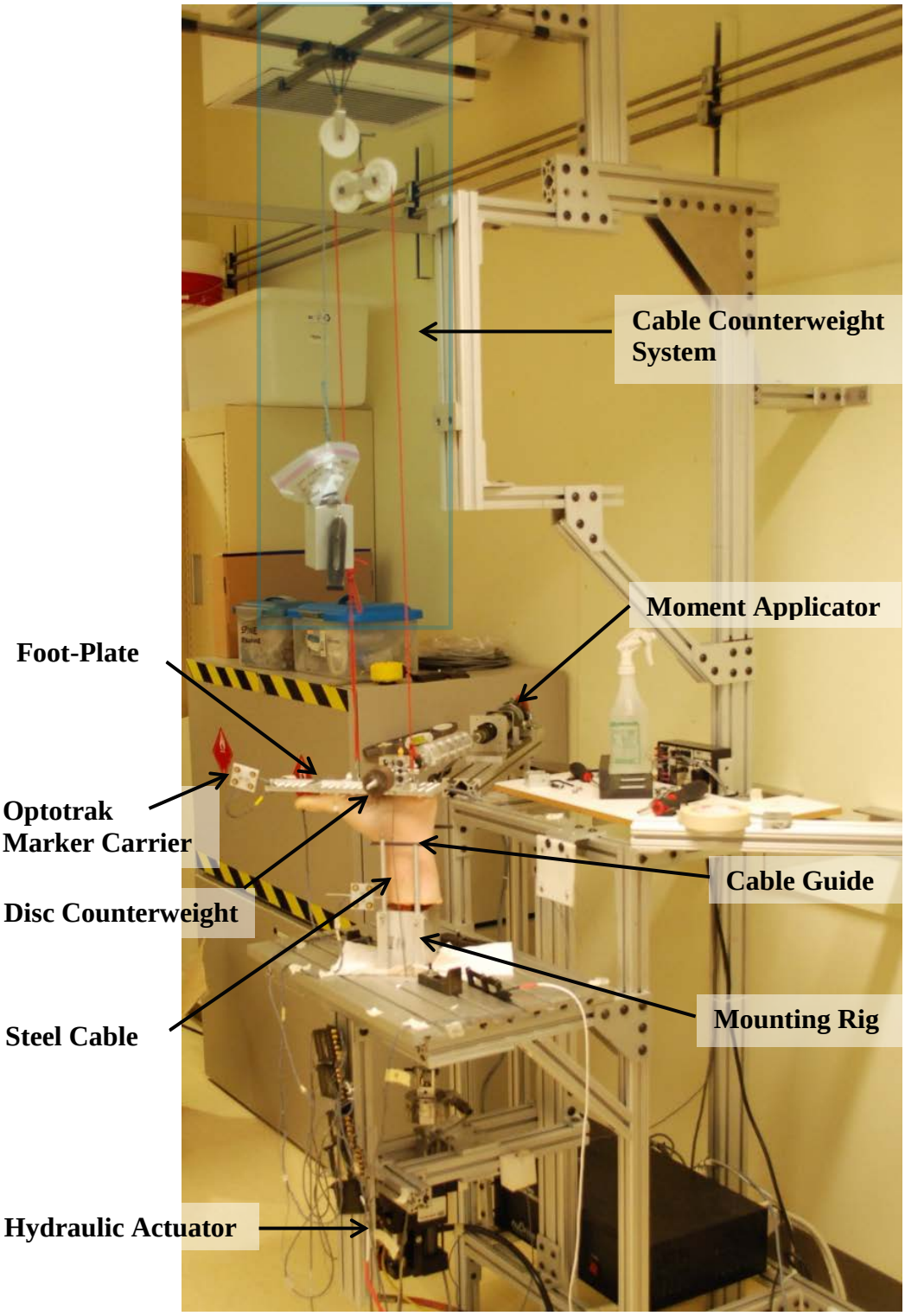

Figure 25: Ankle loading apparatus set up for PF-DF loading on the intact left foot of specimen 3

2.2.1 *FOOT-PLATE*

The foot-plate (fig. 26) was designed with an array of holes to provide locations to screw into the foot and pass ties through to secure it to the plate for all sizes and shapes of feet. A slight square recess and 10-24 threaded holes to each side were machined onto the plate bottom near the posterior end to accept the existing fixture block. A medial-lateral groove was milled out of the plate to allow the steel cable to pass underneath the block once attached. The groove was roughly underneath the ankle center when the foot was in the neutral position. Within the groove, two slots were made to hold polyethylene inserts for the cable to rest on to decrease the coefficient of sliding friction.

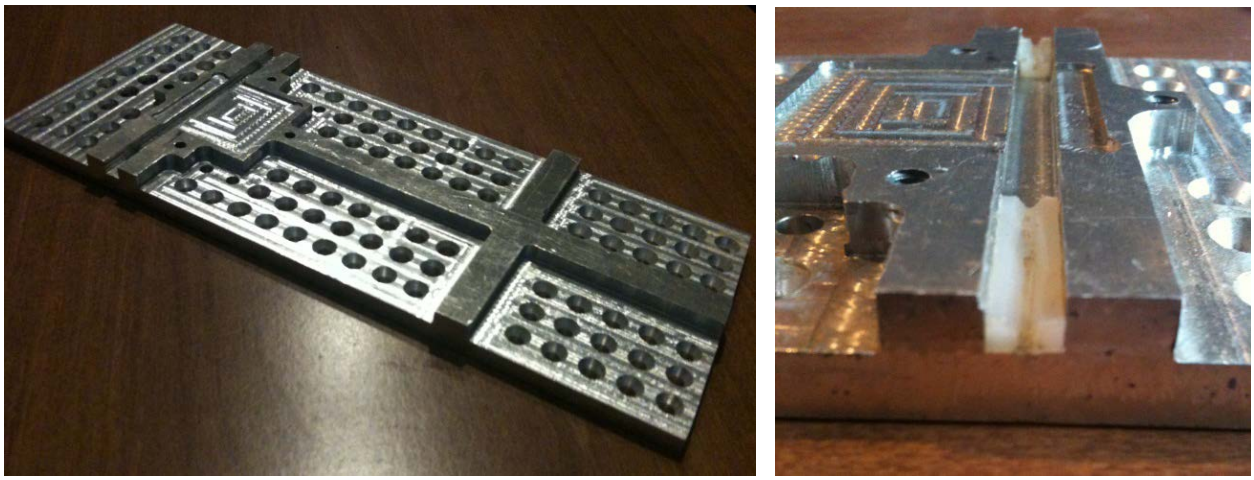

Figure 26: Foot-plate shown from the inferior aspect (left) and close up of the cable slot with polyethylene inserts (right)

2.2.2 *MOUNTING RIG*

The mounting rig built for this experiment was designed with three functions: to secure the proximal end of the limb, to fix the limb to the test platform, and to provide an adjustable cable guide system for directing the compressive load (fig. 27).

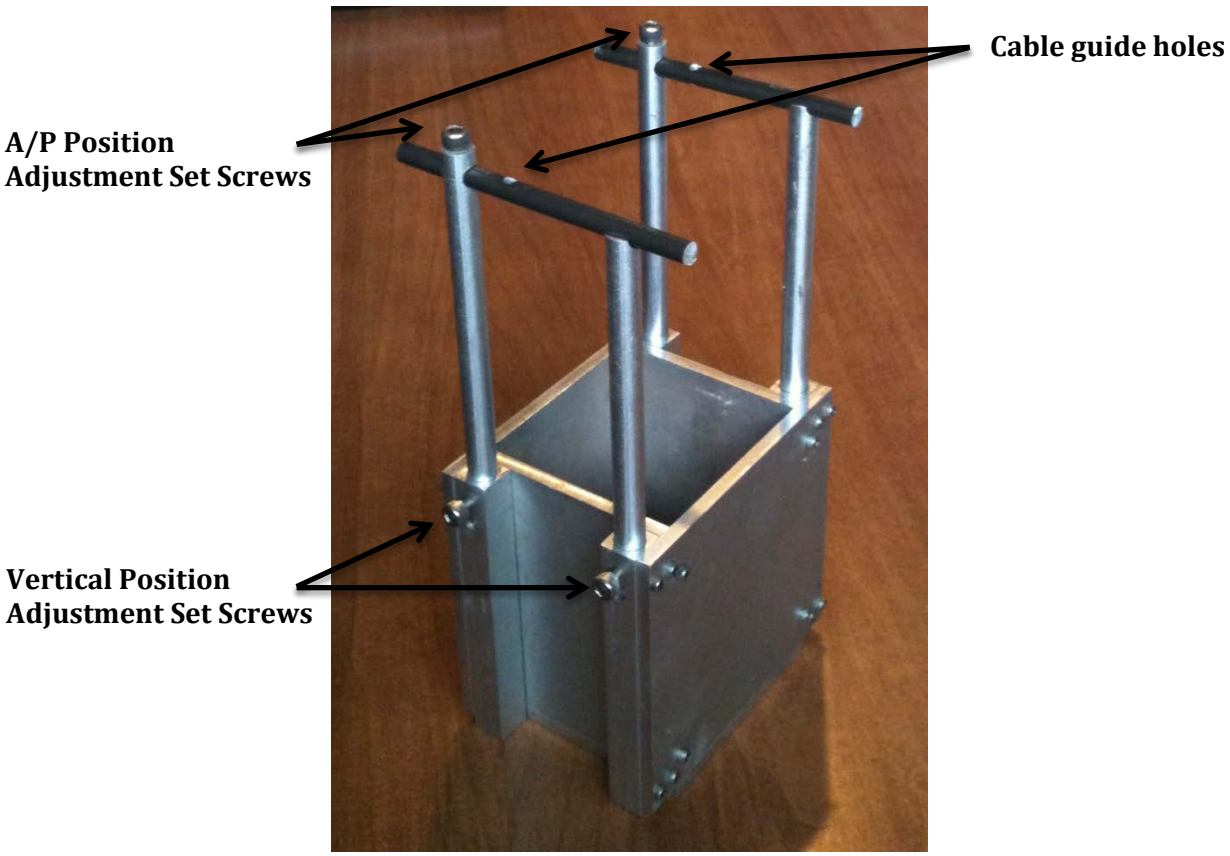

Figure 27: Mounting rig used for potting the limb, mounting it to the test platform, and guiding the compression cables

The main body of the rig consisted of a hollow rectangular box with an open top. It was precisely machined so that all joints were water-tight in order to prevent leakage while the liquid potting mixture was solidifying. The bottom plate of the rig had four holes which machine screws could pass through for attachment to the test platform. The rig was also designed with four posts in each

corner that had holes drilled through the center down its entire length. The holes in these posts were used to hold cylindrical rods, whose vertical position was adjusted and secured by means of set screws. There were holes drilled through the tops of these rods to hold two smaller rods perpendicular to them on the medial and lateral sides of the ankle. The smaller rods' anterior/posterior position could also be adjusted and held in place by set screws. Cable guide holes were drilled through the small rods in order to accommodate a steel cable. The adjustment of previously mentioned rods enabled the vertical and A/P translation of the guide holes. Details of the construction of the rig are given in Appendix C.

2.2.3 *COUNTERBALANCES*

The counterbalance system was calibrated once prior to biomechanical testing to ensure the elimination of all external loads/moments on the ankle caused by the weight of the system. This was accomplished by connecting the foot-plate to the moment application apparatus and arranging the counterbalances such that the system was suspended motionless in the air.

The first such counterbalance supported the weight of the entire configuration with a cable and pulley system. It used an aluminum box/receptacle filled with lead beads (loaded to approximately 1.8 kg), connected to a system of pulleys, which in turn were attached to anchor points on the footplate. The pulley system was free to translate along all three planes and follow the translations of the footplate during the tests. The placement of cable anchor points on the footplate were also calculated so that it did not create any additional moments and allowed it to operate optimally under a large range of angular rotations. It was determined that the optimal locations for the anchor points were as shown in figure 28.

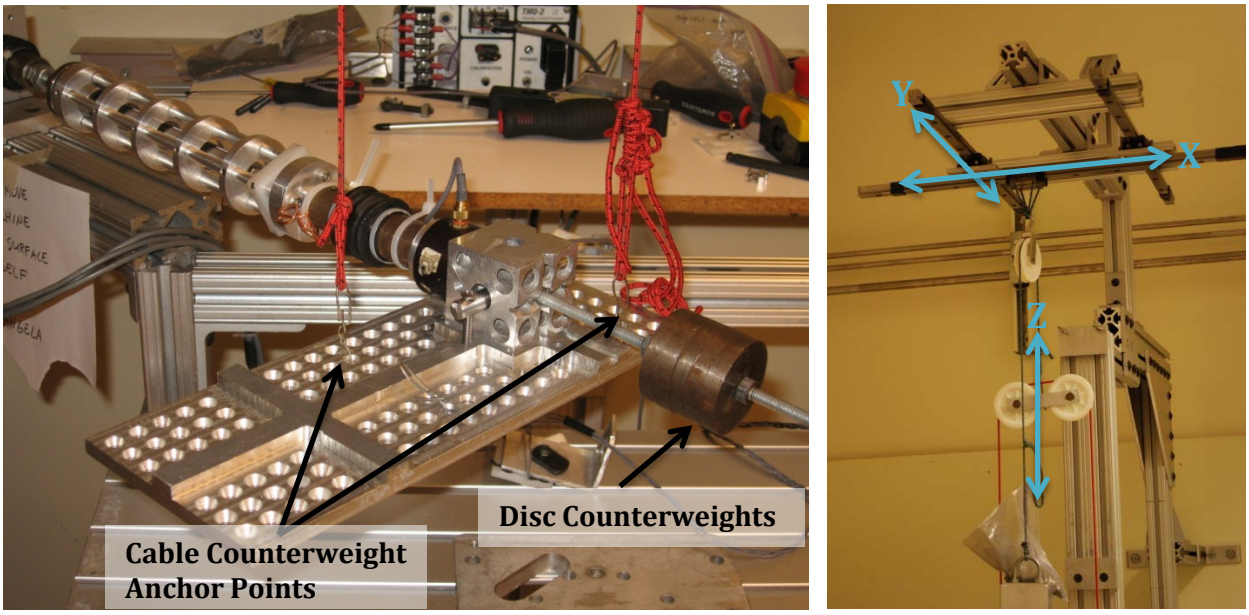

Figure 28: Foot-plate mounted to moment apparatus suspended by cable counterweight and balanced by disc counterweights (left), and counterweight pulley system attached to the test platform frame free to translate along the X, Y, and Z axes in accordance with footplate movements (right)

The second counterbalance component counteracts the moment caused by the arm of the moment apparatus. It is a threaded rod with five disc-shaped steel weights (weighing approximately 96 g each) that extends out from the fixture block of the moment applicator. Nuts on either side of the weights secure them in place and can be shifted along the length of the rod to fine tune the counter-moment without changing the overall weight of the system. Gross adjustments can also be made by adding or removing discs, but the change in total weight must then be reflected in the cable counterweight (refer to fig. 28).

2.2.4 *LOADING*

2.2.4.1 Compression

As mentioned previously, the compressive loads were applied using a 1/16" steel cable looped around the bottom of the foot-plate and a small pulley attached to a linear hydraulic actuator. The actuator used was an Instron A591-4 (Instron, Norwood, MA) with a force capacity of ±1kN and an actuator stroke of ±25mm connected to the Labtronic 8800 control unit. The actuator was fixed to the test bed, directly underneath the platform to which the limb was mounted as shown in figure 29.

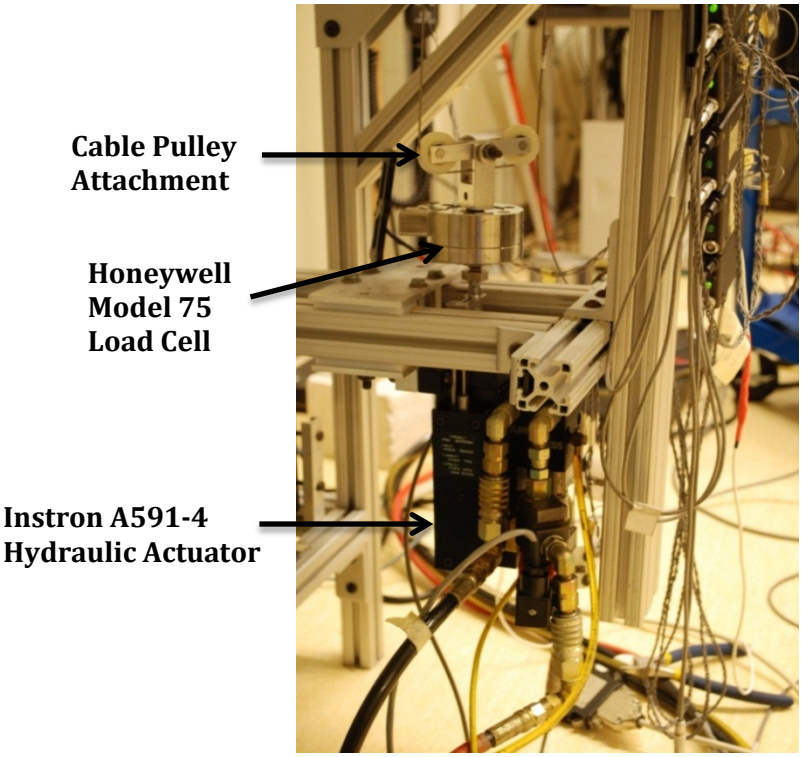

Figure 29: Instron A591-4 linear hydraulic actuator mounted below the test platform with the cable pulley attachment connected to the load cell.

There was a Honeywell Model 75 load cell (Honeywell Internaltional Inc., Columbus, OH) attached to the actuator's end effector, which measured tension and compression to a capacity of 1kN with

an accuracy of ±1.4N. An aluminum bar was attached to the load cell with pulleys on either end free to rotate about its transverse axis. The steel cable was looped around this pulley system to apply tension to the system.

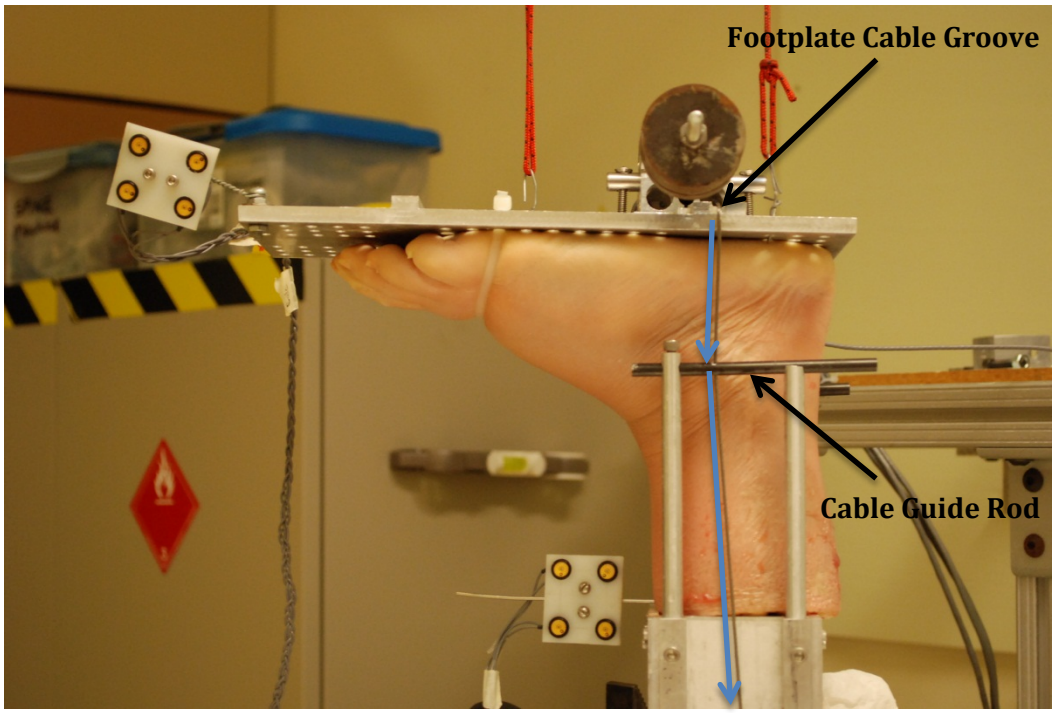

Figure 30: Foot in PF-DF loading with compressive load line of force applied directed downward from footplate cable groove through cable guide rod and down toward the hydraulic actuator

As described previously, the mounting rig was designed with a configuration of rods that enabled the vertical and A/P position of a guide hole for the cable to be easily adjusted. This allowed the cable and hence the line of action for the compressive force to be directed from the groove on the bottom of the foot plate, through the cable guide hole on the mounting rig, and downward to the hydraulic actuator (fig. 30). The main function of the cable guide was to direct the force through the axis of rotation of the ankle in the sagittal plane. This was necessary to minimize the artefact moment caused by the offset of the compressive force from the ankle axis. It was not possible to eliminate the artefact moment altogether because the ankle axis changes as the talus moves with respect to the tibia. During the experiment, constant compressive loads up to 300N were applied to

the foot. Because the location of the cable groove on the foot-plate moved along with the foot as it traveled through its range of motion, the line of force was changing throughout the test. As a result, the force wasn't a pure axial load but had a shear component as the foot rotated away from the neutral position.

2.2.4.2 Moment

The device used to apply moments in this experiment (fig. 31) was essentially the same as the one originally designed by Goertzen et al. [121] with the exception that the hollow tube around the ball spline has since been upgraded to increase its axial travel (480mm vs. 300 mm) and improve its torsional stiffness (6.5° vs. 14° angular deformation at 10 Nm applied torque). It utilized a servo motor (D50R10-0243, Designatronics, New Hyde Park, NY) with a 55:1 low-backlash planetary reduction gearbox (G23PI-0055-LB, Industrial Devices, Petaluma, CA) to apply torque to the articulating arm. The arm consisted of two universal joints (UJ-SS1000, Belden, Broadview, IL) connected by a ball spline (LBF15UU+300LE, THK, Mississauga, ONT). One U-joint was attached to the output shaft of the gearbox and the other to the torque load cell (TRT-200, Transducer Techniques, Temecula, CA), which in turn was connected to the fixture block.

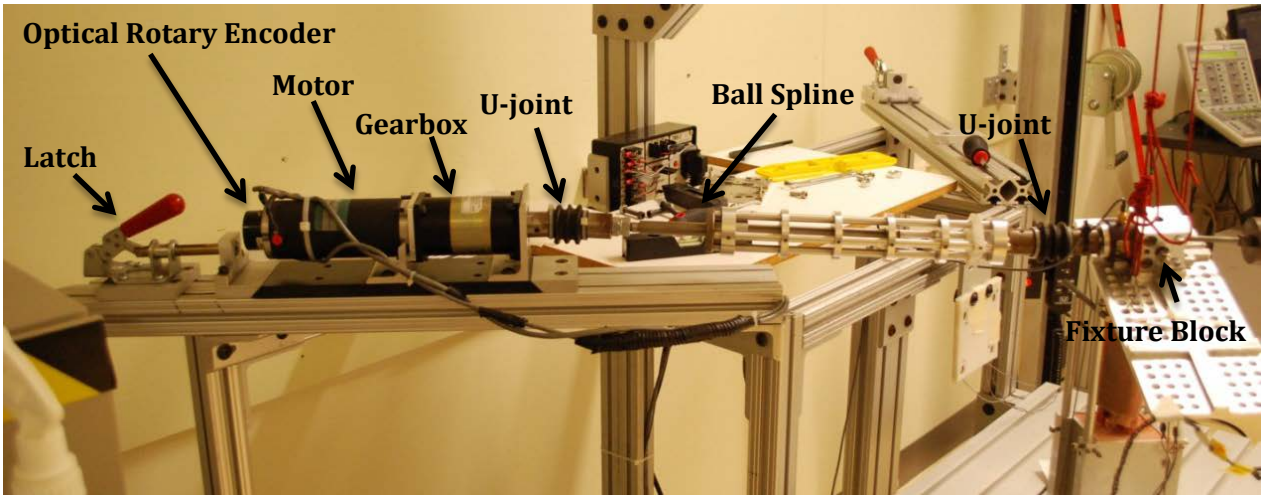

Figure 31: Moment application apparatus

This configuration allowed the motor to apply moments about a designated axis determined by the orientation of the fixture block for a range of specimen translations and rotations. It was initially determined to apply pure moments about each of 3 orthogonal axes to within 0.15 Nm with a force component of 1.49 N [121], and was again verified after implementation of the new arm.

A LabVIEW (National Instruments, Austin, TX) program was used to input the test parameters such as angular velocity, torque limits, and number of cycles. The servo motor control was facilitated by this program in conjunction with a motion control card (Flexmotion 6C) and amplifier (nuDrive 4CF-001), with feedback inputs from the optical encoder (H32R85–L0306, SDP/SI, New Hyde Park, NY) and conditioned torque cell signal (TMO-2, Transducer Techniques, Temecula, CA). A real time graphical output of the actuator angle and applied moment were displayed on the LabVIEW VI during tests.

2.3 Specimen Selection

The specimens used in this study were fresh frozen human cadaveric foot and ankle joint complexes cut off at mid-shank. They were obtained from the UBC Department of Cellular and Physiological Sciences through the Body Donation Program. Both male and female specimens of all ages were accepted. Specimens excluded from this study were only those which had severe ligament damage, deformities, or other conditions that would render a subject ineligible for a TAR surgery in clinical practice. There were 3 male and 3 female donors, which composed the demographic displayed in table 4.

Table 4: Specimen data

Specimen #	Sex	Age (yrs)	Weight (kg)	Height (cm)
H1347	M	67	60	175
H1349	M	90	80	168
H1350	F	68	81	168
H1351	M	93	73	168
H1352	F	59	73	165
H1353	F	68	45	173
Average		74.2 ± 13.9	68.7 ± 13.8	169.5 ± 3.7

2.4 SPECIMEN PREPARATION

All specimens were kept frozen at -20°C when not in use. Prior to use, the limbs were transferred to a refrigerator kept at 4°C until fully thawed, which in most cases was approximately 48 hours.

2.4.1 *POTTING*

In order to mount the limbs in the test rig, the proximal end of the tibia and fibula were potted in dental stone. To ensure that the dental stone bonded rigidly to the specimen, bone was exposed on the proximal 3-4 inches of the tibia and fibula. All tissues including the periosteum were removed using a #22 scalpel and tissue forceps.

A large retort stand and two clamps were used to align and immobilize the limb in an upside down position. The alignment of the limb was determined visually by setting the long axis of the tibia as normal to the ground (vertical in the X-Z and Y-Z planes) and setting the long axis of the foot (the line passing through the posterior most point of the calcaneus and the second metatarsal) as

parallel to the cable guides while the foot rested in the neutral position. The foot was suspended in the air with all of the exposed bone within the potting jig except for the distal half inch to provide clearance for the soft tissues.

Four ¼-20 machine screws were placed in the holes at the bottom of the potting jig with a nut on the bottom (outside of the jig) to hold the bolts in place while the potting set. The screws were firmly fixed within the dental stone once it had hardened, after which they were used to fasten the specimen to test platform.

The dental stone powder (Tru-Stone® Pink, Heraeus Kulzer, South Bend, Indiana) used has a compressive strength of 103.5 MPa and requires a liquid/powder ratio of 24 mL/100 g. It was mixed with water to a consistency that was thick yet still able to be easily poured from the mixing dish into the potting jig. The potting rig was filled to the top and the jig was disturbed to ensure it had a homogenous distribution and that no air bubbles were present.

The specimen was kept suspended upside down while the potting set. The set time according to the specifications is 9-11 minutes, but it was left to sit for approximately an hour before moving it to ensure the dental stone was fully hardened. Because the potting was still hot at this point, the specimen was placed in the refrigerator to cool before the specimen was loaded.

2.4.2 *Fastening Foot-Plate*

A foot-plate was attached to the bottom of the limbs to enable attachment to the loading apparatus. The center-line of the foot-plate was held in alignment with the long axis of the foot while two screws were put into the calcaneus through counter-bored holes in the plate (fig. 32-L). Pilot holes were drilled into the calcaneus prior to inserting the 6.5 mm cancellous bone screws (45 mm long, 32 mm thread length). The forefoot was secured using two cable ties fed through holes in the foot-

plate strapped around the distal end of the metatarsals (fig. 32-R). The cable ties were cinched down tight enough that no motion was observed between the forefoot and footplate during testing.

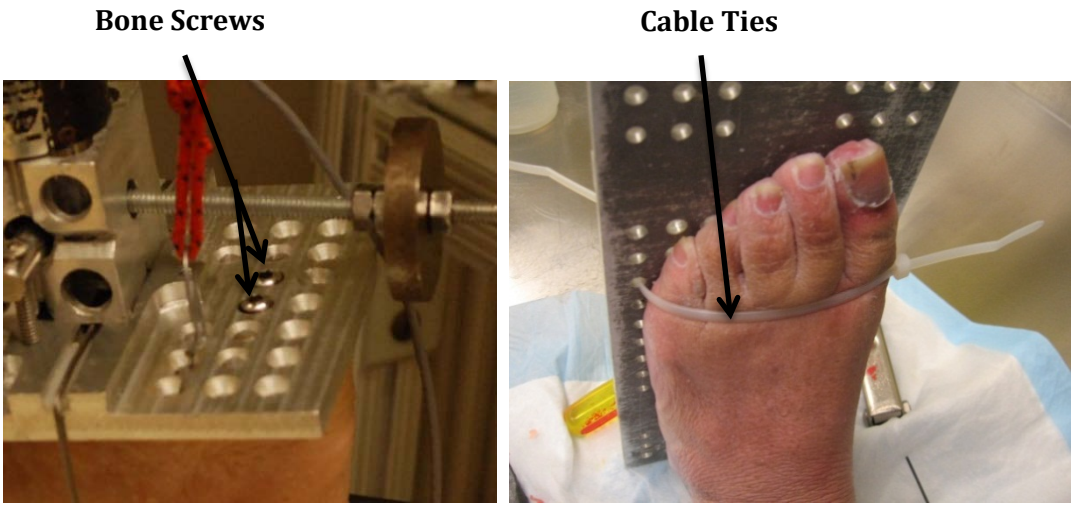

Figure 32: Bone screws passing through the foot-plate into the calcaneus (left) and cable ties wrapping around forefoot and through footplate (right).

2.4.3 *JOINT REPLACEMENT SURGERY*

After each specimen was tested intact, one of two joint replacement surgeries was performed on it. The surgeries were performed by foot and ankle surgeon, Dr. Alastair Younger, who has clinical experience with both of these procedures.

The surgical instrumentation included specialized cutting jigs, pins, guides, drill bits, measurement devices, and various other tools to ensure accurate alignment and installation of the implant donated by the manufacturer. Other generic tools used were oscillating and reciprocating saws, a drill, osteotomes, rongeurs, surgical tweezers and forceps, and scalpels.

The Agility total ankle replacement surgery was performed on the left limb and details of the surgical technique can be found in Appendix D. The STAR implant was installed in the right limb of the pair, and the details of this first generation STAR procedure can be found in Appendix E.

2.5 MEASUREMENT METHOD

The Optotrak Certus® (Northern Digital Inc., Waterloo, ON) was used for taking bone and implant position measurements. It is an optoelectronic motion capture system that tracks the 3D position of infrared LED diodes. These markers were grouped into arrays of 4 and attached to polyethylene marker carriers. They were arranged in rectangular groupings to enable the calculation of rigid body translations and rotations. The Optotrak is specified to have a single marker 3D accuracy of 0.1 mm and a resolution of 0.01 mm. Further validation was performed to determine the accuracy of measurements taken with the four marker arrangement and transformation algorithm used in this experiment (see Appendix F). The Optotrak measurements were found accurate to within 0.012 mm for translations and 0.09° for rotations, with a precision of 0.005 mm and a repeatability of 0.002 mm.

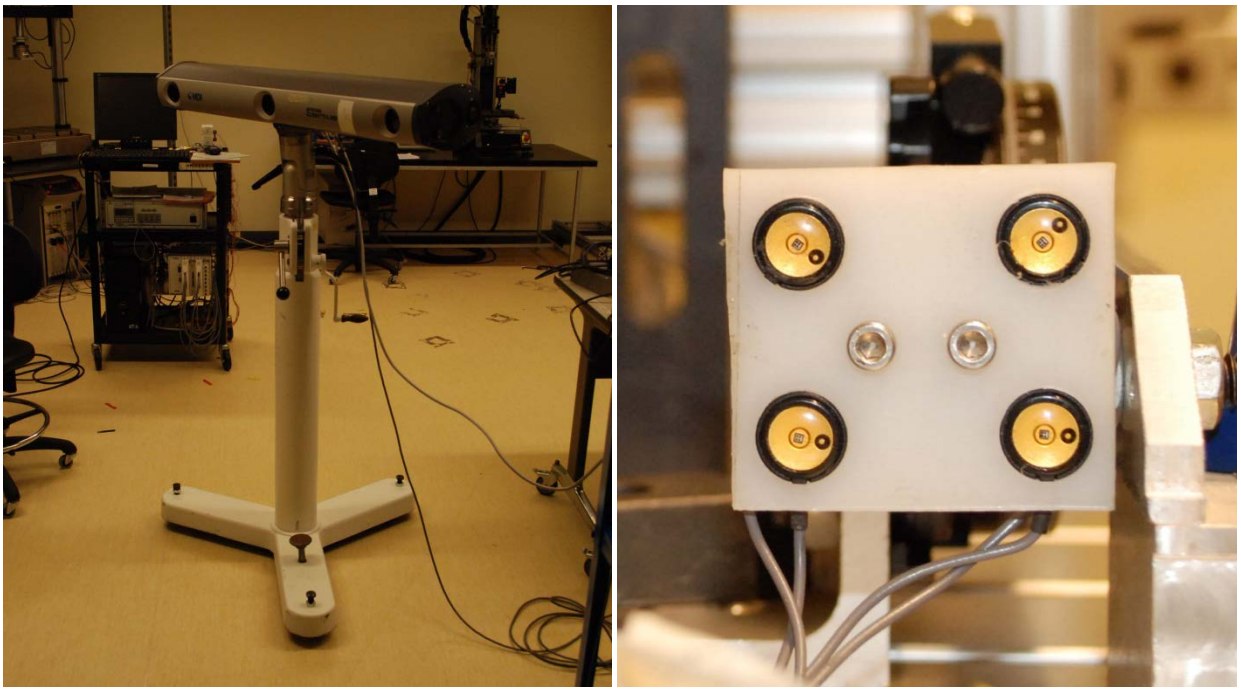

Figure 33: Optotrak Certus motion capture system. Optotrak camera (left) and PE marker carrier with 4 LED diodes (right)

2.6 TEST PROTOCOL

2.6.1 *TEST CONDITIONS*

A total of six pairs of limbs were tested in this experiment. One limb out of the pair was used to test the Agility implant, while the other was used for the STAR implant in this bilateral comparison procedure. Each limb was subjected to four tests – two performed on the intact ankle and the same two repeated after total ankle replacement (see table 5 for details). One test was with a constant compressive preload representing ½ BW (or 1/8 BW for INV-EV) and the other one was with a minimal preload (15N). Each test comprised a sequence of three orthogonal load applications, during which the ankle was cycled through its ROM about the given axis three times. The behaviour of ankles was found to be consistent from the third cycle onward; therefore, the test was stopped after completion of the third cycle to minimize damage caused to soft tissues. The three orthogonal axes were chosen to be aligned as close as possible to those of PF-DF, INV-EV, and IR-ER (fig. 34).

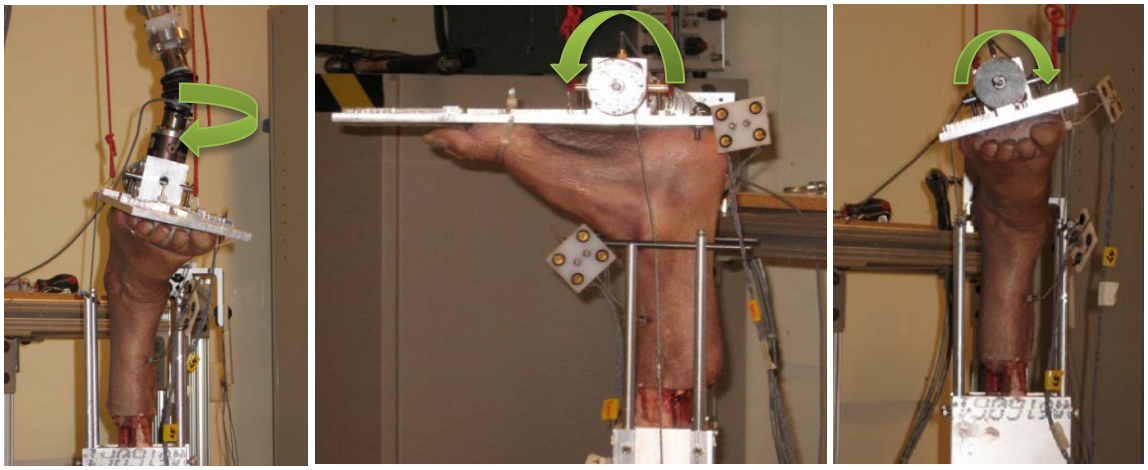

Figure 34: Ankle test apparatus setup for the 3 loading directions: IR-ER (left), PF-DF (middle), and INV-EV (right)

For the uncompressed conditions, a 15 N compressive load was applied to stabilize the joint. For the compressed conditions in PF-DF and IR-ER, 300 N was chosen as it represented roughly ½ BW. Angular displacement limits for the implanted PF-DF tests were determined on a specimen by specimen basis. They were defined based on either a percentage of the intact ROM, component/bone interference, or bearing lift-off.

Table 5: Loading conditions

	Intact: uncompressed	Intact: compressed	Implanted: uncompressed	Implanted: compressed
PF-DF	15 N compression 5 N·m torque limit	300 N compression 5 N·m torque limit	15 N compression Angular displacement limit	300 N compression Angular displacement limit
INV-EV	15 N compression 3 N·m torque limit	75 N compression 3 N·m torque limit	15 N compression 3 N·m torque limit	75 N compression 3 N·m torque limit
IR-ER	15 N compression 3 N·m torque limit	300 N compression 3 N·m torque limit	15 N compression 3 N·m torque limit	300 N compression 3 N·m torque limit

2.6.2 *TEST PROCEDURE*

2.6.2.1 Initial Test Prep

Each specimen received from the UBC body donation program varied slightly in the shank length. The depth of bone within the potting could be adjusted slightly to compensate for limb length; however, ensuring that the limb was securely fastened was of utmost importance and a minimum of 3 inches of bone depth would be required of the total 4 inch jig depth. This resulted in differences in the overall height of the mounted limbs between specimens. This difference was accounted for by adjusting the height of the test platform such that the arm of the moment applicator was parallel to the ground. This was required to maintain the alignment used to set the counterbalances and to prevent interference between the moment applicator and the test platform.

At this point, the Instron and Optotrak were also set up. The Instron was powered on, warmed up, and calibrated. The Optotrak was plugged in and initialized with the LabVIEW program, and all the Optotrak markers were verified for connectivity and proper arrangement.

2.6.2.2 Markers

There were a few methods employed to attach the Optotrak marker carriers to the rigid bodies of interest. In order to get accurate rigid body transforms, it is important that all four markers on a given marker carrier are visible throughout the entire test. Since all the bodies that had to be tracked were in such close proximity, the marker carriers had to be placed strategically to prevent any markers from getting blocked.

K-wire pins were used for attaching the marker carriers to bone. The K-wire was bent prior to insertion to avoid accidentally widening the hole and causing it to loosen. As a result, it was impossible to insert the pins with a drill in the conventional manner. A pilot hole considerably smaller than the K-wire was drilled into the bone, and the pin was inserted into the hole with a snug friction fit. There was a steel block, which was connected to the K-wire and a small nail by set screws. This K-wire/nail block prevented rotation of the pin within the bone.

Each Agility implant component had a 10-32 threaded hole that was designed to aid in the installation of the implant during surgery. Machine screws, which had a flexible galvanized steel wire (ø = .0475 in) fixed to them with a nut, were threaded into these holes (fig. 35). The wire was twisted about itself to increase its rigidity. The marker carriers were attached at the ends of these wires.

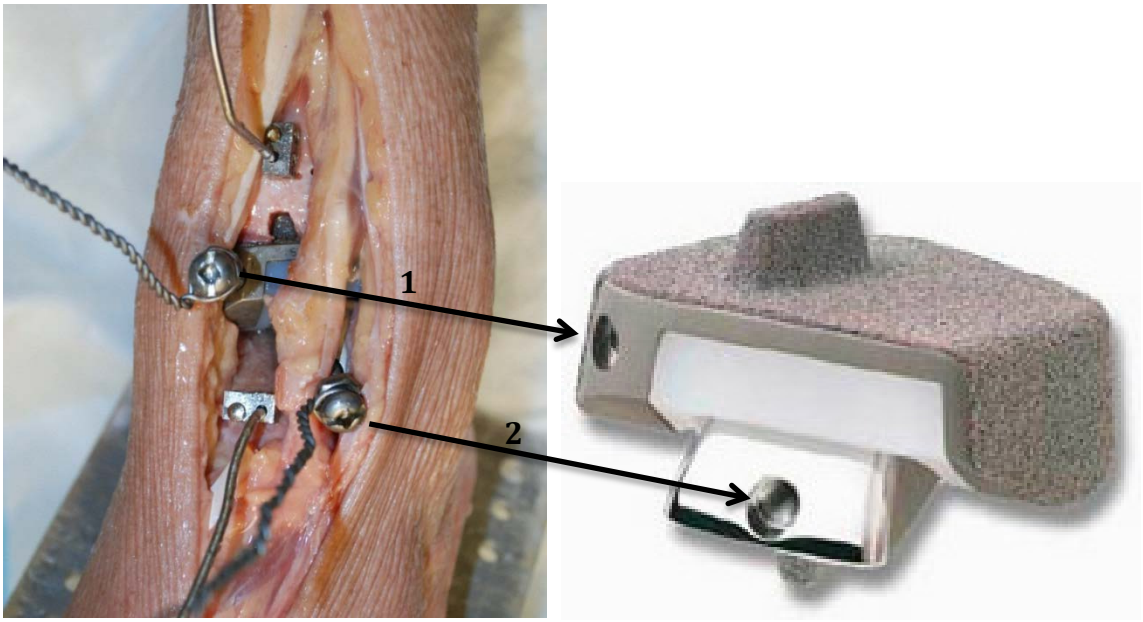

Figure 35: Marker mounting locations for the Agility TAR. Screws with mounting wires threaded into the tibial (1) and talar (2) installation holes are shown

The STAR components only had flat and curved surfaces that were accessible after the implant was installed; hence, glue (Instant Krazy Glue®, One Easton Oval, Columbus, OH) was used to attach marker mounts. The tibial component had a space on the proximal aspect just anterior to the fixation barrels where a wire was able to sit without touching any bone. The wire was looped to create a larger surface contact area where it attached to the implant, and the portion that extended outward was twisted to increase rigidity. On the talar component, the only available area was the convex articulating surface. A small steel block with a hole for a K-wire pin and a set screw was glued onto the front corner of the talar implant where it had clearance from the mobile polyethylene bearing and bony elements throughout the entire range of motion (fig. 37).

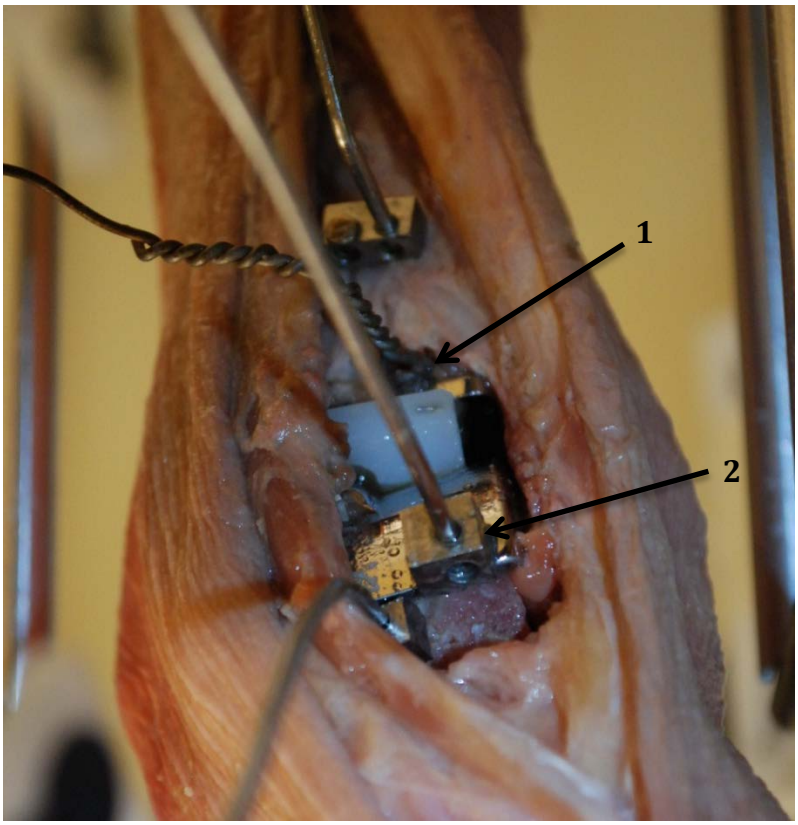

Figure 36: Marker mounting locations for the STAR: twisted wire glued to the proximal side of tibial component (1) and mounting block glued to bottom corner of talar component (2)

The polyethylene marker carriers were built with a steel block fastened to the back. These blocks have small holes parallel to the carrier surface to allow it to slide onto the K-wire pins or other wires protruding from the specimen and are held in place by a set screw. The pins were strategically fixed to the specimen to reduce marker overlap. The fine adjustment of the marker carriers' orientation with respect to the wire in conjunction with the wire positioning enabled us to ensure that none of the LEDs were blocked. The final adjustments were made while the Optotrak was running with the LabVIEW program giving feedback of the whether or not the camera was picking up the LED's signal. At this point, adjustment of the K-wires themselves were kept to a minimum in order to reduce the chance of loosening their connection to the bone, and adjustments in the camera orientation and the marker positions were used liberally instead. When a potential

setup had been configured, the foot was moved to its most extreme poses in its range of motion and the marker signals were checked and further adjustments were made if there were any obstructions.

2.6.2.3 Ankle Axis of Rotation

It is difficult to approximate the axis of rotation for the ankle joint in the sagittal plane because its position and orientation changes as the ankle moves, but an optimal position was found for each specimen that best approximated it for all loading applications. As a starting point, the vertical position of the cable guides was estimated based on the implant geometry or anatomical landmarks, which was roughly around the distal tips of the malleoli. Subsequently, a 200 Newton compressive load was applied to the ankle and an optimal configuration of the cable guides' A/P positions was determined empirically. The configuration was evaluated by setting the cable guide positions, rotating the foot about its flexion axis by hand, and feeling the magnitude of induced moment caused by the compressive force. The guide positions were then adjusted slightly and the process was repeated until the position was found that minimized the induced moment caused by the compressive load. After the optimal cable guide positions were found, the set screws were tightened down so that the guide positions wouldn't shift when the ankle was loaded.

2.6.2.4 Reference Position

A reference position was required for the calculation of all the joint angular and translational displacements. The foot was put into the neutral position and Optotrak data was collected for a few seconds without any motion. The neutral position was defined as the orientation when the footplate was parallel to the ground along the PF-DF axis, while the foot was allowed to take on its natural alignment about the INV-EV and IR-ER axes.

2.6.2.5 Digitize points

It is necessary to know where certain points on the limb are in reference to the Optotrak coordinate system. These are required to locate points of interest or define other coordinate systems for use in post-processing. While the foot was still in the exact same position as in the static shot, a digitizing probe was used to identify the location of specific landmarks and record their position. The Optotrak probe consists of a rigid plastic body housing six LED markers with a steel tip protruding from the body. While the tip touched the desired point and at least three of the markers were visible to the Optotrak camera, the position could be captured with the press of a button in the Labview VI. Details of the digitized points will be shown in the following analysis sections.

2.6.2.6 Apply Loads

Depending on which test was being run, the designated compressive load was applied. The position of the foot was then moved as close to neutral as possible before initiating the test. A custom Labview program designed and validated previously for similar studies was used to coordinate the Optotrak data recording and the moment application. This program implemented a PID controller to cause the servo motor to supply a torque that maintained a constant angular velocity until it reached either the torque or angular displacement limit designated for the specific test. Following this, it reversed the angular velocity until it reached the limit in the opposite direction and repeated this process until it completed 3 cycles. The following figures show a typical example of the loading applied to the foot displayed as time traces of the applied moment (fig. 37) and resulting angular displacement (fig. 38).

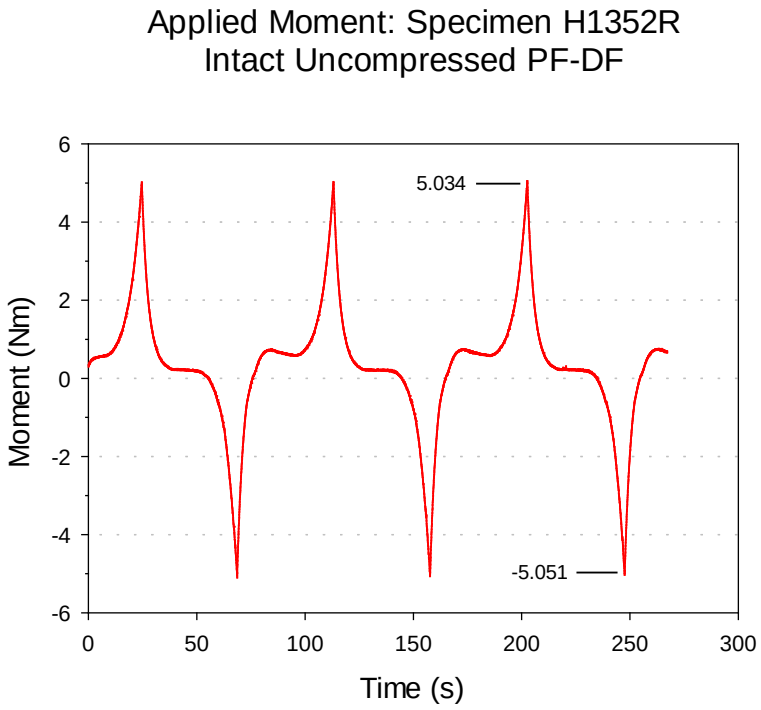

Figure 37: Sample of applied moment measured by the torque load cell for uncompressed PF-DF loading set to limits of 5Nm

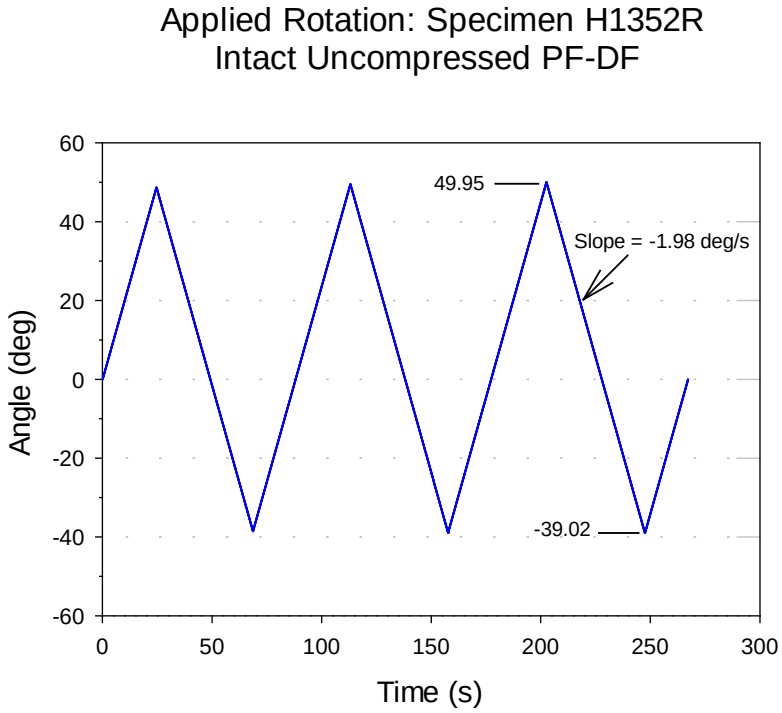

Figure 38: Sample of angular displacement of the servo motor as measured by the optical encoder for uncompressed PF-DF loading set to an angular velocity of 2 deg/s.

2.7 DATA ACQUISITION

The 3D position data of the bones and implant components was recorded with the Optotrak Certus system. The Optotrak camera was connected to its system control unit, which was connected to the computer with a specialized PCI card. The data from the Optotrak was collected and managed with the LabVIEW (National Instruments, Austin, TX) virtual interface that was custom designed to coordinate motion capture and control load application through the moment application apparatus.

The data from the moment application apparatus was not used for any of the outcomes of the study, but it was used for feedback required to control the loading. The applied moment was measured by the torque sensor (TRT-200, Transducer Techniques, Temecula, CA) connected to the fixture block. The signal from the torque cell was first passed to the torque sensor signal conditioner (TMO-2, Transducer Techniques, Temecula, CA) before it was sent to the DAQ unit (nuDrive 4CF-001, National Instruments, Austin, TX). The angular displacement of the foot was approximated by the optical rotary encoder (H32R85-L0306, SDP, Designatronics, New Hyde Park, NY) connected to the servo motor. The signal from the optical encoder was also sent to the DAQ unit. Both the angular displacement and torque signals were sent through the motion control card (Flexmotion-6C, National Instruments, Austin, TX) from this unit to the computer. The LabVIEW VI used the feedback signals from the motion control card to adjust the signal sent through the power amplifier (also the DAQ unit – nuDrive 4CF-001) to the servo motor.

2.8 DATA ANALYSIS/PROCESSING

The Optotrak .dat files were first converted to .csv files using NDI file conversion wizard. Matlab programs were written to manipulate and perform preliminary analysis on the .csv data (AppendixG). The 3D position data was analyzed by comparing each successive frame to the initial static shot in order to determine the kinematic variables and relative bone-implant displacements. By assuming rigid bodies (including the markers with respect to their targets), it was possible to determine the transformation matrix required to take the marker set (and by association the bone/implant of interest) from the initial position to the final position. The method used in this study for this computation was the least-squares algorithm described by Veldpaus et al.[122]. This computation gives an estimate of the translation vector and rotation matrix of a moving body from the spatial coordinates of at least three non-collinear markers. Joint rotations, joint translations, and bone/implant motions were then determined by applying the rotation matrices and translation vectors of the rigid bodies to their local coordinate frames.

2.9 KINEMATIC ANALYSIS

All kinematic data was represented here in the joint coordinate system (JCS)[123], which eliminated the angles' dependence on the order of rotations about the joint axes. Although the JCS is a non-orthogonal basis, it provides a more anatomically relevant definition of the rotations while allowing for better comparison between different studies. Specifically, the definition of the ankle joint coordinate system used landmarks and axes as proposed by Wu et al.[124] as shown in figure 39.

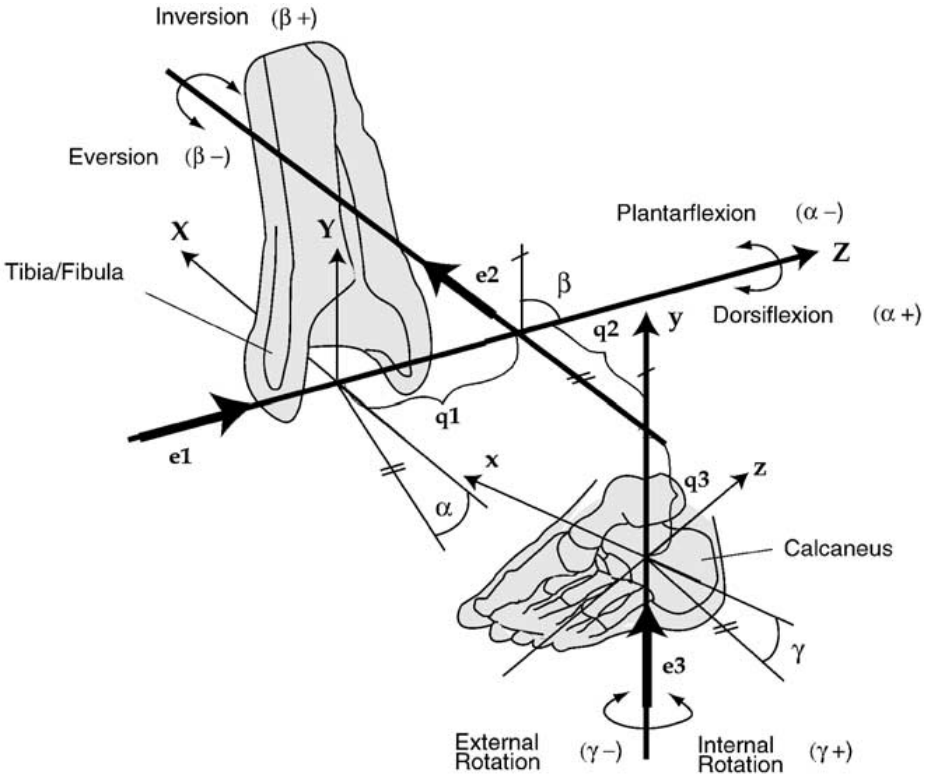

Figure 39: Joint coordinate system definition for the ankle. Reprinted with permission from Elsevier via Copyright Clearance Center (Source: Wu et al. 2002[124])

e_1: Flexion axis: fixed to the tibia/fibula, pointing laterally and passing through the tips of the medial and lateral malleoli.
Rotation (α): dorsiflexion (positive) or plantar-flexion (negative)
Displacement (q_1): lateral (positive) or medial (negative) shift

e_3: Long axis: fixed to the calcaneus, pointing cranially and along the long axis of the tibia while in neutral position.
Rotation (γ): internal rotation (positive) or external rotation (negative)
Displacement (q_3): compression (positive) or distraction (negative)

e_2: Floating axis: normal to e_1 and e_3.
Rotation (β): inversion (positive) or eversion (negative)
Displacement (q_2): anterior (positive) or posterior (negative) drawer

The only deviation from Wu's coordinate system was in defining the long axis of the tibia. This axis is pointing cranially along the line intersecting the midpoint of the medial and lateral condyles of the tibial plateau and the midpoint of the medial and lateral malleoli. However, it was not possible to locate the condyles because the limb was cut off mid-shank. Instead, it was approximated by the line intersecting the midpoint of the malleoli and centroid of the most proximal segment of the tibia available[125].

The points that required digitizing for the JCS and all kinematic analysis were as follows:

1. Medial malleolus
2. Lateral malleolus
3. Medial edge of tibia
4. Lateral edge of tibia
5. Posterior edge of tibia

2.9.1 *JOINT ROTATIONS*

The joint rotations were calculated according to the joint coordinate system definition. Because the reference axes rotate along with the joint, it allows for a more relevant description of the angular displacements observed. In this specific experiment the tibia was essentially fixed (aside from slight bone deformations due to loading), thus the flexion axis fixed to the tibia was the only axis that remained relatively stationary. For the 'long' and the 'third' axes, the effects of this coordinate system were much more pronounced. The rotations calculated for a given axis were those of the rotations in the plane that contained this axis as its normal vector in the current frame's orientation.

2.9.2 *Range of Motion*

The range of motion as defined in this experiment was the largest angle observed in both positive and negative directions of rotation about the primary axis. That is to say, the primary axis was the axis about which the testing apparatus was applying the moment. The range of motion is a good way to compare different specimens because it is a very simple computation outputting a scalar value. As such, it is commonly reported and inter-study calculation differences are minimal.

2.9.3 *Motion Coupling*

In this study, coupled motion was defined as the rotation along axes that were not the primary axis. While the primary axis was being cycled through its range of motion by the moment application apparatus, the other two axes were unconstrained and free to rotate naturally. Because the joints of the foot and ankle are interrelated in a complex manner and are not orthogonal unidirectional hinges, motion along the other axes occurred as the primary motion was induced. The motion coupling ratio used to describe this motion was the maximum induced ROM about a secondary axis divided by the maximum ROM of the primary axis during the third cycle of loading. The motion coupling plots show the mean value of the secondary axis angles as a function of the primary axis angle for the uncompressed conditions when loaded in the forward and reverse directions separately. Because not all of the specimens had the same primary ROM as the others, the graphs displayed the ROM over which the majority of specimens had data.

2.9.4 *JOINT TRANSLATIONS*

The joint centre in neutral position was taken as the midpoint between the distal tips of the lateral and medial malleoli. The joint translations were defined as the movement of the joint centre fixed to the calcaneus reference frame with respect to its initial position in the tibial reference frame. These were calculated by determining the transformation matrix between the calcaneus marker array in a given frame and that of its initial static shot, and applying it to the joint center. After the displacement vector was determined in the Optotrak reference frame, it was decomposed into components along the JCS axes. The JT magnitudes were taken as the difference between the maximum and minimum values of the final cycle.

2.10 BONE-IMPLANT RELATIVE MOTION

Along with the digitization of all the anatomical landmarks for defining the coordinate system in kinematic analysis, separate coordinate systems and reference points were created from digitized points on the implants for the analysis of the motion between the bone and implant. Separate coordinate systems were necessary for both components of each implant, and were defined as shown in figure 40.

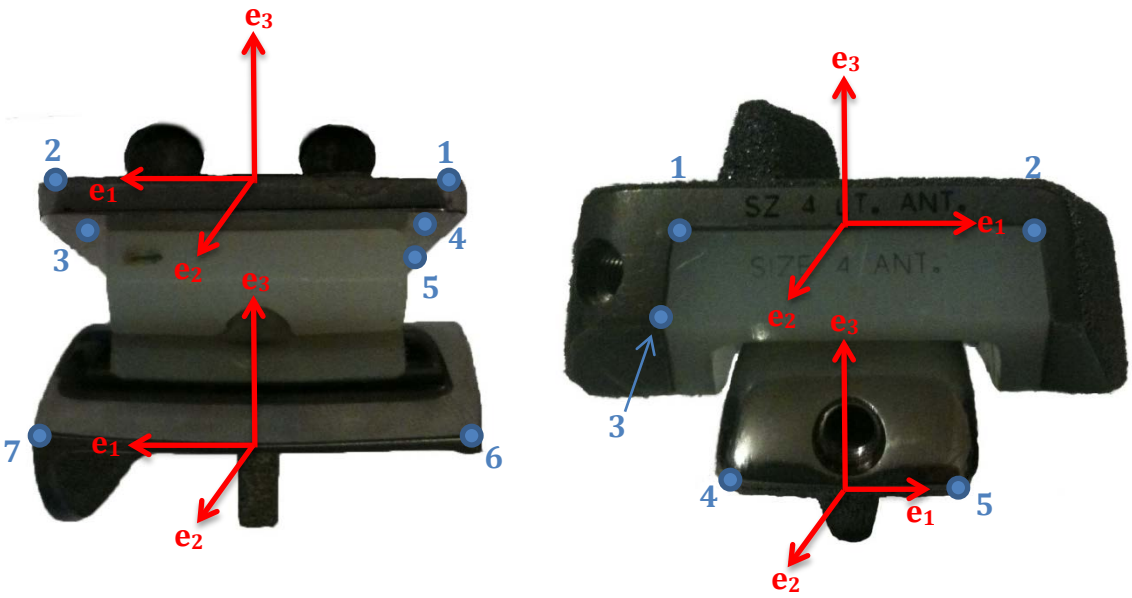

Figure 40: Implant-specific coordinate frames and the corresponding digitized points required to define them with the STAR on the left and Agility on the right.

STAR:

Tibia:
O: midpoint of *1* and *2*
e_1: *2-1*
e_3: (*4-3*) cross (*5-4*)
e_2: e_3 cross e_1

Talus:
O: midpoint of *6* and *7*
e_1: *7-6*
e_3: $e_{3\text{tibia}}$
e_2: e_3 cross e_1

Agility:

Tibia:
O: midpoint of *1* and *2*
e_1: *2-1*
e_2: (*2-1*) cross (*1-3*)
e_3: e_1 cross e_2

Talus:
O: midpoint of *4* and *5*
e_1: *5-4*
e_3: $e_{3\text{tibia}}$
e_2: e_3 cross e_1

The dimensions of the implants were measured, and the locations of the implant corners were determined within the implant coordinate system. This allowed us to calculate the 3D translations of the four corners and determine their relative displacements. Calculating the motion of the corners was required to ensure that the reported micromotion magnitudes were the maximum values across the entire surface of the implant interface. Rotation of the implant with respect to the bone could cause certain corners to experience larger micromotion magnitudes than others depending upon the axis of rotation.

Comparing the motion between the implant and bone for the STAR and Agility was the main objective of this project. There are a number of different ways in this behaviour can be quantified. We chose to use the magnitude of displacement because it is a scalar quantity that easily translates to the ingrowth tissue's tensile strain. The primary outcome measure used was the maximum relative displacement magnitude of the third cycle.

2.11 Statistical Analysis

2.11.1 *Micromotion*

All statistical results were considered significant with $p < 0.05$. Errors are reported as one standard deviation.

Six two-way repeated measures ANOVA's were performed on the micromotion data to determine the effects of implant type and compression on the amount of motion between the implant and bone. One of these ANOVAs was performed for each of the two implant components (tibial and talar) by three loading directions (PF/DF, INV/EV, and IR/ER).

The effect of compression was analyzed as a repeated measure, but the effect of implant type was not because the differences between the left and right ankle are not necessarily negligible despite the fact that they are from the same person. Student-Newman-Keuls tests were used for post-hoc comparisons.

2.11.2 *KINEMATICS*

All kinematic variables were analyzed with three-way ANOVAs, which had 2 repeated measures and one factorial comparison. Analysis was performed on the range of motion, motion coupling ratios, and joint translation magnitude measurements to assess the effect of implant type (Agility vs. STAR), ankle condition (intact vs. implanted), and compression (uncompressed vs. compressed). In the analysis, the three variables used were 'Implant', 'Condition', and 'Compression'. As a main effect, the implant variable represented the difference between the left and right ankles, including the intact and implanted (Agility and STAR respectively) conditions. The condition variable referred to the difference between intact and implanted ankles (both implant types). The compression variable referred to the difference between the uncompressed and compressed tests. The interaction between condition and implant was the most intriguing because it showed the effect that each of the two implant types had on the intact ankles. The interaction between compression and implant showed how compression affected the left and right ankles. The interaction between condition and compression showed the difference in how the implanted and intact ankles were affected by compression. The interaction between condition, compression, and implant showed the differences in how the two implant types were affected by compression. Since the differences between the left and right ankles were mainly due to specimen variation or caused by an interaction with implant type, the effect of implant and the interaction between implant and compression were not a focus of this analysis.

The two repeated measures within a specimen were compressive load and ankle condition. As previously mentioned, the type of ankle replacement was not a repeated measure because they were not performed on the same ankle and inter-specimen variability was not negligible. One ANOVA was performed on the total ROM magnitude for each direction analyzed (two in total: INV-EV and IR-ER). Two ANOVAs were performed for each loading direction since there were two axes of coupled motion, which resulted in a total of six. Nine ANOVAs were performed on the JT data – three for each loading direction, which corresponded to the three JCS translations (q_1, q_2, and q_3).

3 RESULTS

3.1 BONE-IMPLANT RELATIVE MOTION

The data from specimen H1351 in figure 41 shows a representative example of the relative motion magnitude seen at the corner of greatest motion for the talar implant. Each motion trace was normalized in the x axis for cycle duration. Both compressed and uncompressed data are plotted in order to compare how compression and implant type affect the amount of motion observed.

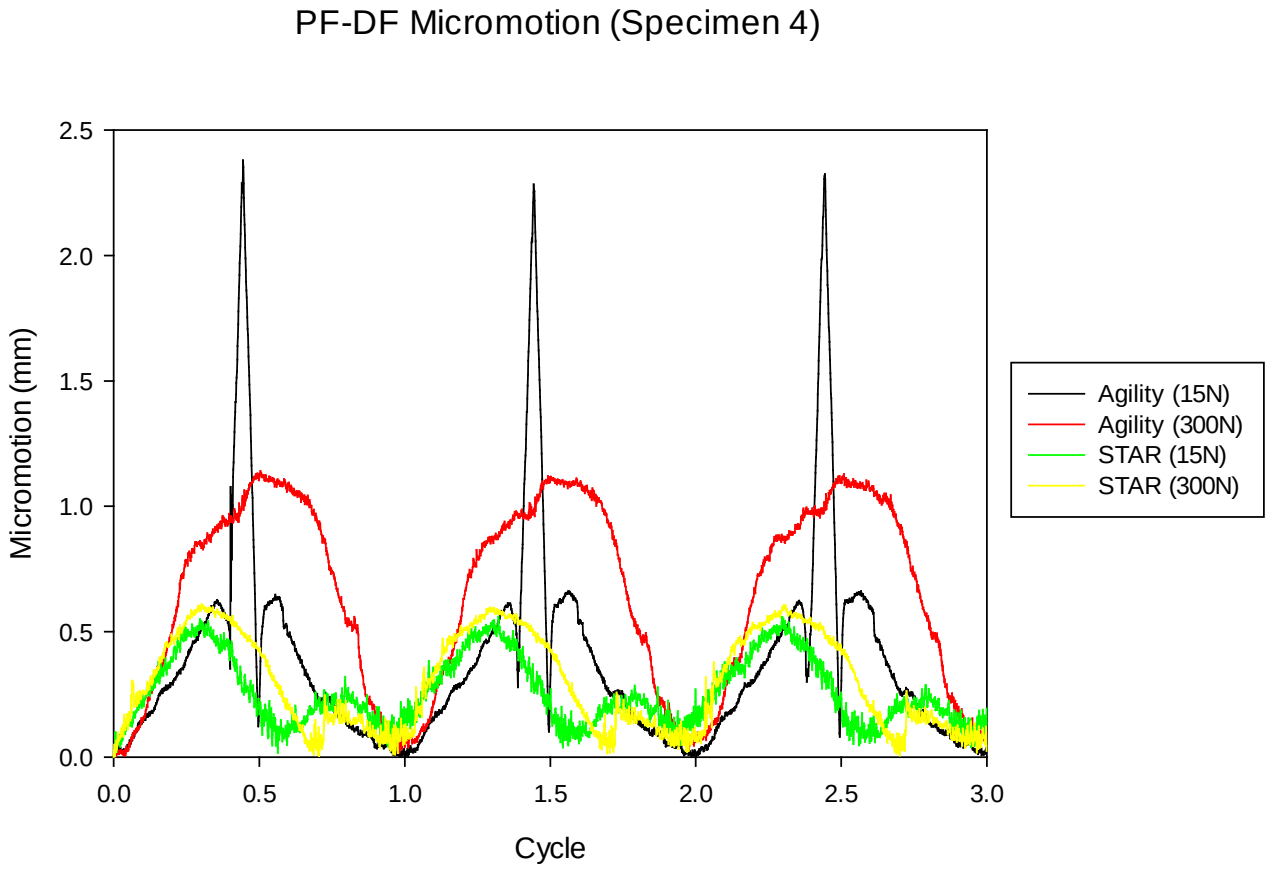

Figure 41: Specimen 4 micromotion magnitudes over 3 cycles of PF-DF for the talar component of both implants with and without compression. Ankles start in the neutral position and are plantarflexed initially, reaching their maximum PF angle just prior to 50% corresponding to their peak micromotion magnitudes. In the STAR another micromotion peak occurs at approximately 80% of the cycle, which corresponds to the maximum DF angle.

In this example, one can see that the uncompressed Agility component had a spike in which the relative motion increased substantially, corresponding to its peak plantar-flexion range of motion. Visual inspection showed that this spike was the result of the anterior two corners of the implant lifting off the bone (see figure 42). This lifting off phenomenon occurred in 4 out of the 6 unloaded PF-DF tests for the talar component of the Agility. However, this same phenomenon did not occur during the same test when a compressive force was added.

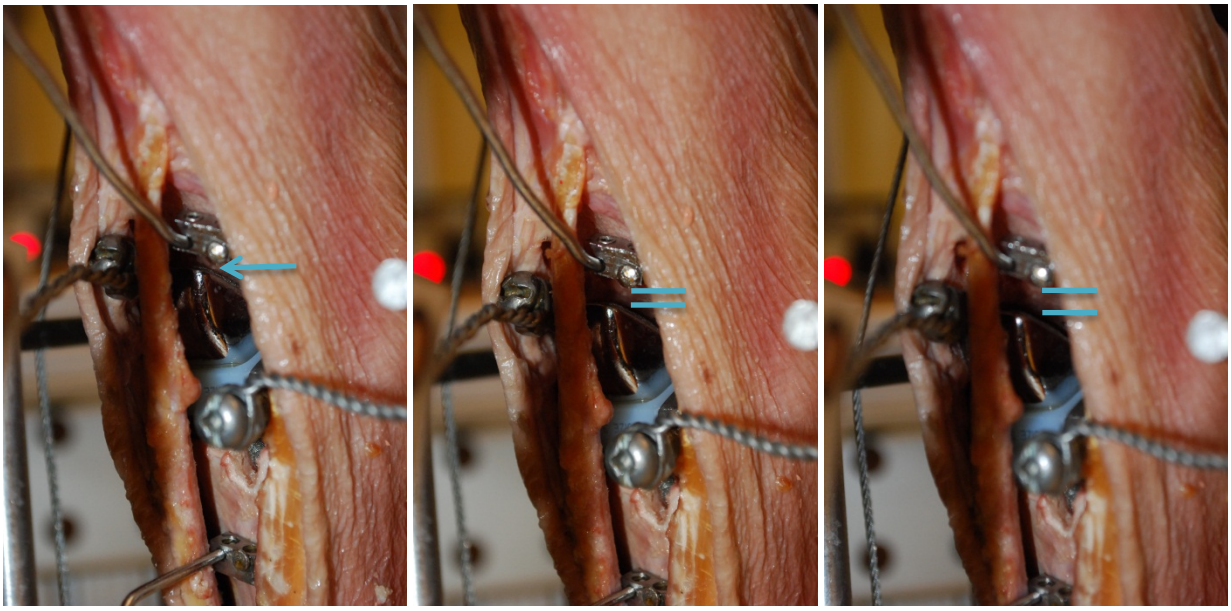

Figure 42: Consecutive photos of the uncompressed PF-DF test for the Agility illustrating talar component lift-off from left to right.

Generally, the STAR implant components had lower mean micromotion magnitudes than the Agility, and the tibial components of the implants typically had lower magnitudes of relative motion than found in the talar components.

3.1.1 *TIBIAL COMPONENT MICROMOTION*

For the tibial component, the mean micromotion magnitudes the Agility displayed were larger than the STAR in all loading configurations except for PF-DF with compression (fig. 43).

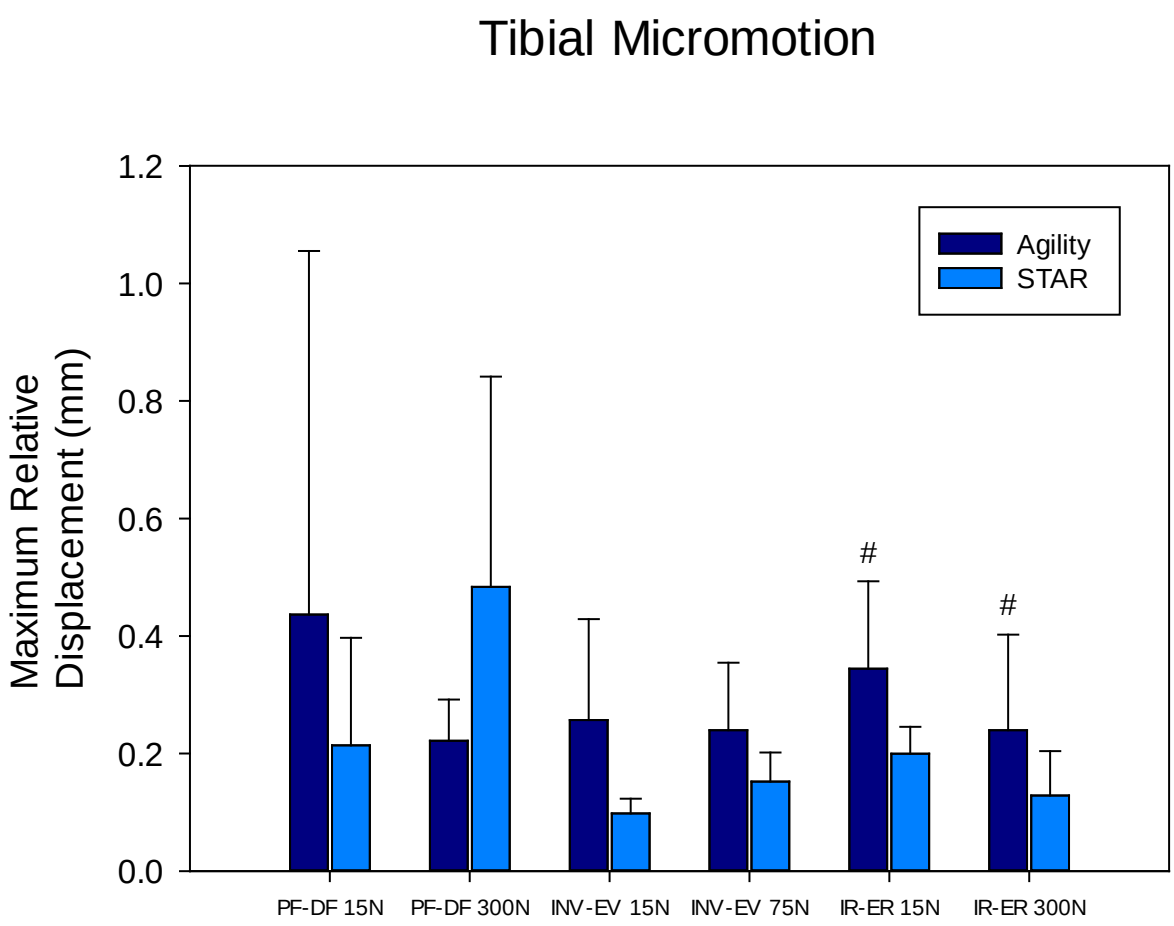

Figure 43: Peak micromotion magnitudes for the tibial component for all loading scenarios. Micromotion values are plotted as mean with error bars as one standard deviation. # p=0.040

In PF-DF, there were no significant differences in tibial component micromotion (main effects: 'Implant Type' p = 0.503, 'Compression' p = 0.151; interaction: 'Implant Type' x 'Compression' p = 0.520). In INV-EV loading, the difference between the mean micromotion magnitudes of the Agility and STAR, 0.248 and 0.125 mm respectively, was determined to be the only significant difference (main effects: 'Implant Type' p = 0.037, 'Compression' p = 0.599; interaction: 'Implant Type' x

'Compression' p = 0.321). In the IR-ER direction, the decrease in micromotion caused by applying a compressive load was found be significant while the effect of implant type was not quite significant (main effects: 'Implant Type' p = 0.062, 'Compression' p = 0.019; interaction: 'Implant Type' x 'Compression' p = 0.602).

3.1.2 *TALAR COMPONENT MICROMOTION*

The mean micromotion magnitudes associated with the STAR were consistently lower than the Agility in the talar component (see fig. 44). In all three loading directions, applying a compressive load decreased the mean micromotion in the Agility implants, but had varying effects on the STAR. In PF-DF, both effects and the interaction between them was found to be significant (main effects: 'Implant Type' p = 0.002, 'Compression' p = 0.037; interaction: 'Implant Type' x 'Compression' p = 0.027). The mean micromotion in the Agility was 1.235 mm higher than in the STAR. The inclusion of a compressive load in the test decreased the amount of micromotion for the talus in PF-DF, but there was also a significant interaction between compression and implant type. In this test we saw compression decreased the micromotion in the Agility (p = 0.006) but had no significant effects on the STAR (p = 0.892). In INV-EV, the amount of micromotion observed in the Agility was almost significantly higher than the STAR, but no significant differences were found due to either implant type, compression, or their interaction (main effects: 'Implant Type' p = 0.085, 'Compression' p = 0.242; interaction: 'Implant Type' x 'Compression' p = 0.263). Similarly to PF-DF, significant differences were found due to both effects and their interaction in IR-ER (main effects: 'Implant Type' p = 0.040, 'Compression' p < 0.001; interaction: 'Implant Type' x 'Compression' p = 0.003). Compression decreased the combined motion of the implants, but there was a significant difference between how compression affected each implant such that the Agility motion was significantly decreased (p < 0.001) but STAR motion was not (p = 0.138).

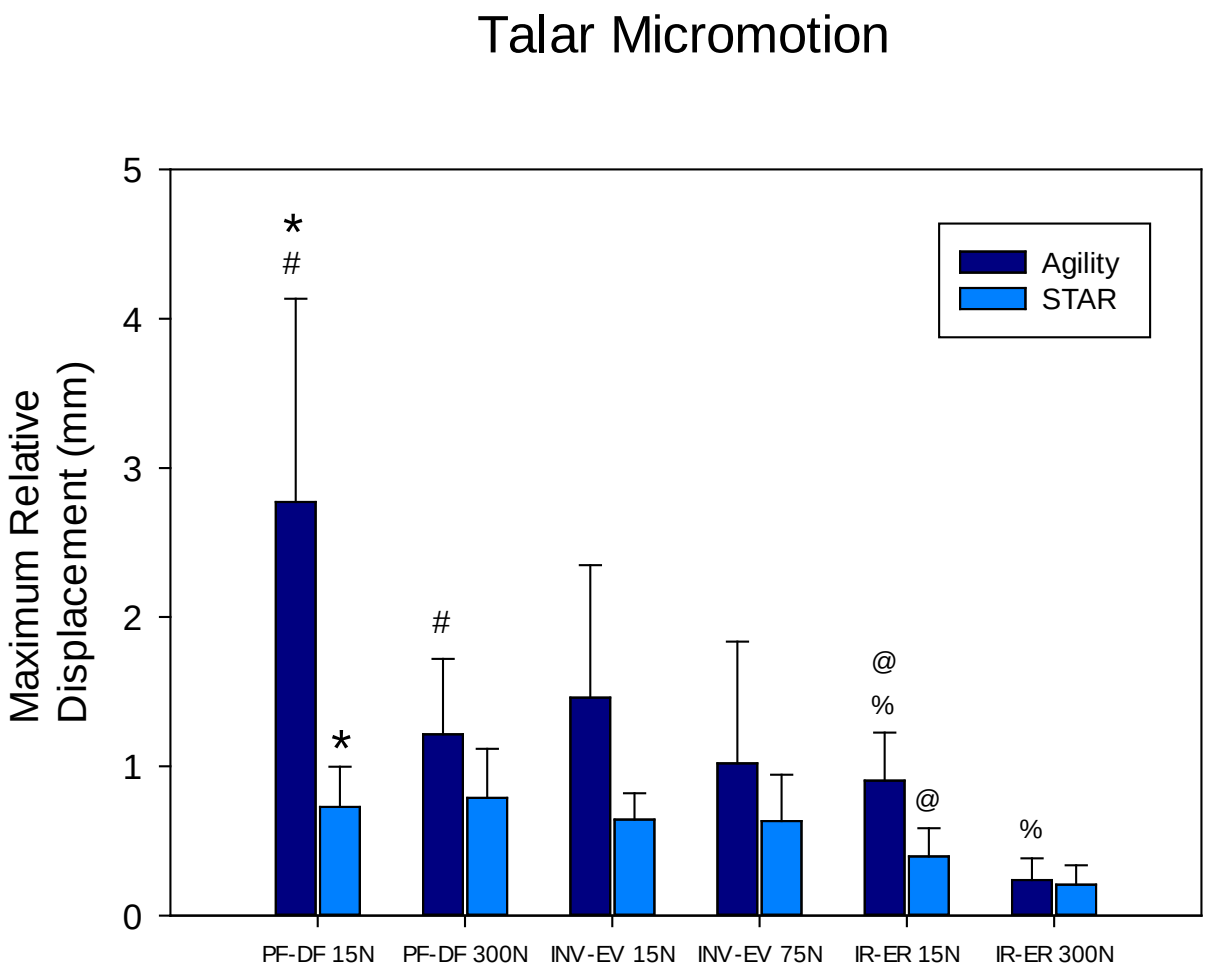

Figure 44: Peak micromotion magnitudes for the talar component for all loading scenarios. Values given as mean with error bars as one standard deviation. * p<0.001; # p=0.006; @ p=0.001; % p<0.001

3.2 KINEMATIC BEHAVIOUR

3.2.1 *JOINT ROTATIONS*

The following sets of plots (fig. 45-47) are time traces of the joint angles according to the JCS convention for the 3 rotational axes. Examples from the experimental set were selected that appeared to be the most representative of the typical behaviour of most specimens. These plots give a good general idea of what is going on from the kinematics perspective. One can start to see some of the quantities (ROM and MC) that will be looked at in further detail in the following sections. Qualitatively, there were some similarities and some differences between the two implants and the intact ankles. Even though there were exceptions and even contradictions due to large inter-specimen variability (even between the left and right intact feet from the same donor), some general trends in the kinematic patterns were evident.

These plots showed that the primary axis in each of the loading directions had relatively constant angular velocity, in accordance with the applied load. There were times when the slope of this curve deviated from the norm, which usually coincided with rapid changes in the other axes or an increase in joint stiffness (required torque). Meanwhile, the other two axes were free to rotate to their natural tendency. Each ankle had its own repeatable signature motions about these secondary axes, but there was agreement in their general patterns. They followed a pronation/supination coupling behaviour as expected, but the degree of this coupling varied between the different groups.

Plantarflexion-Dorsiflexion

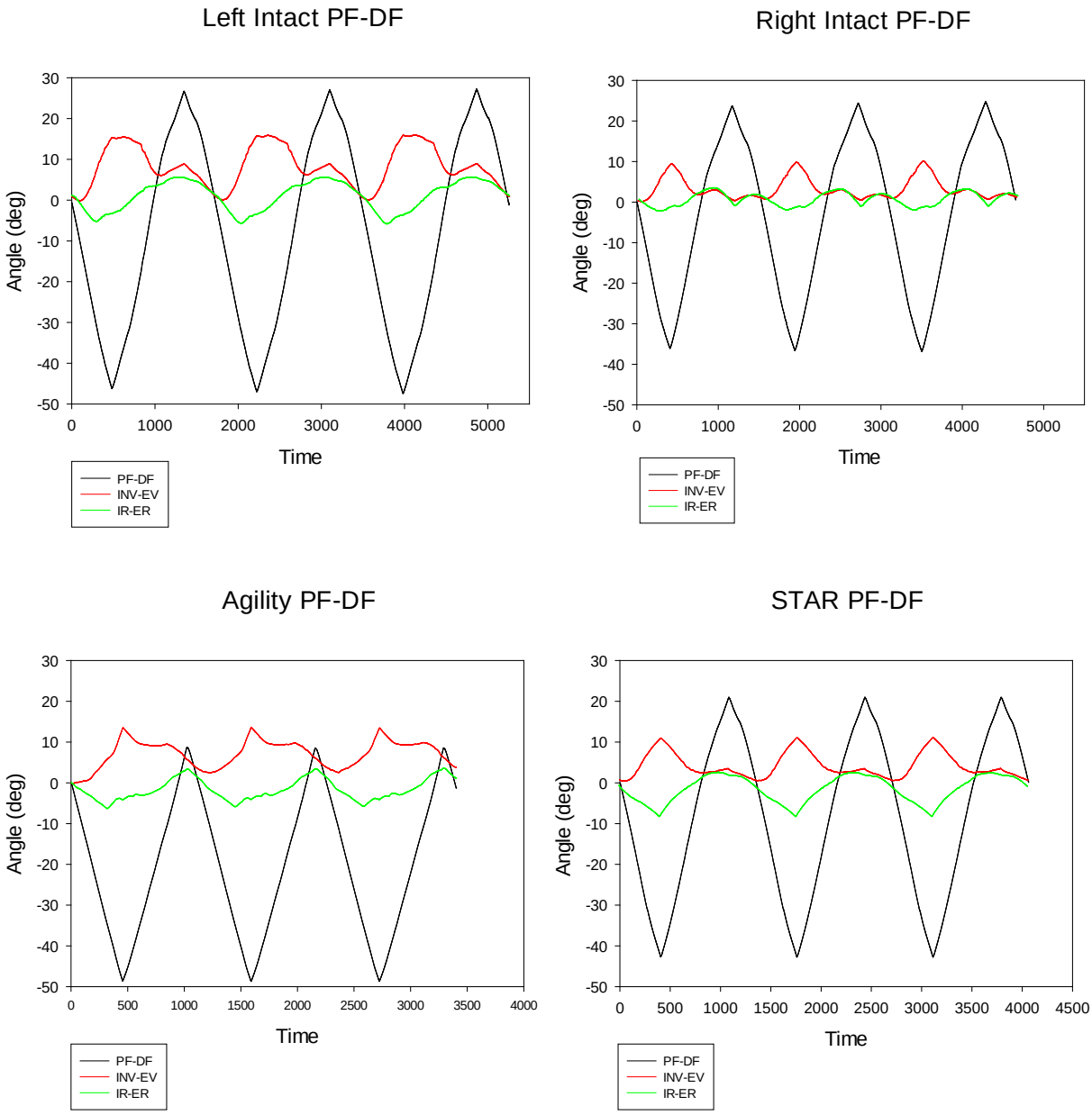

Figure 45: Representative sample of joint angles in uncompressed PF-DF loading for left and right intact, Agility, and STAR ankles. Black lines denote the primary/driven axis of rotation, where DF is positive and PF is negative. Red lines denote INV-EV rotations, where INV angles are positive. Green lines denote IR-ER rotations, where IR angles are positive.

Inversion-Eversion

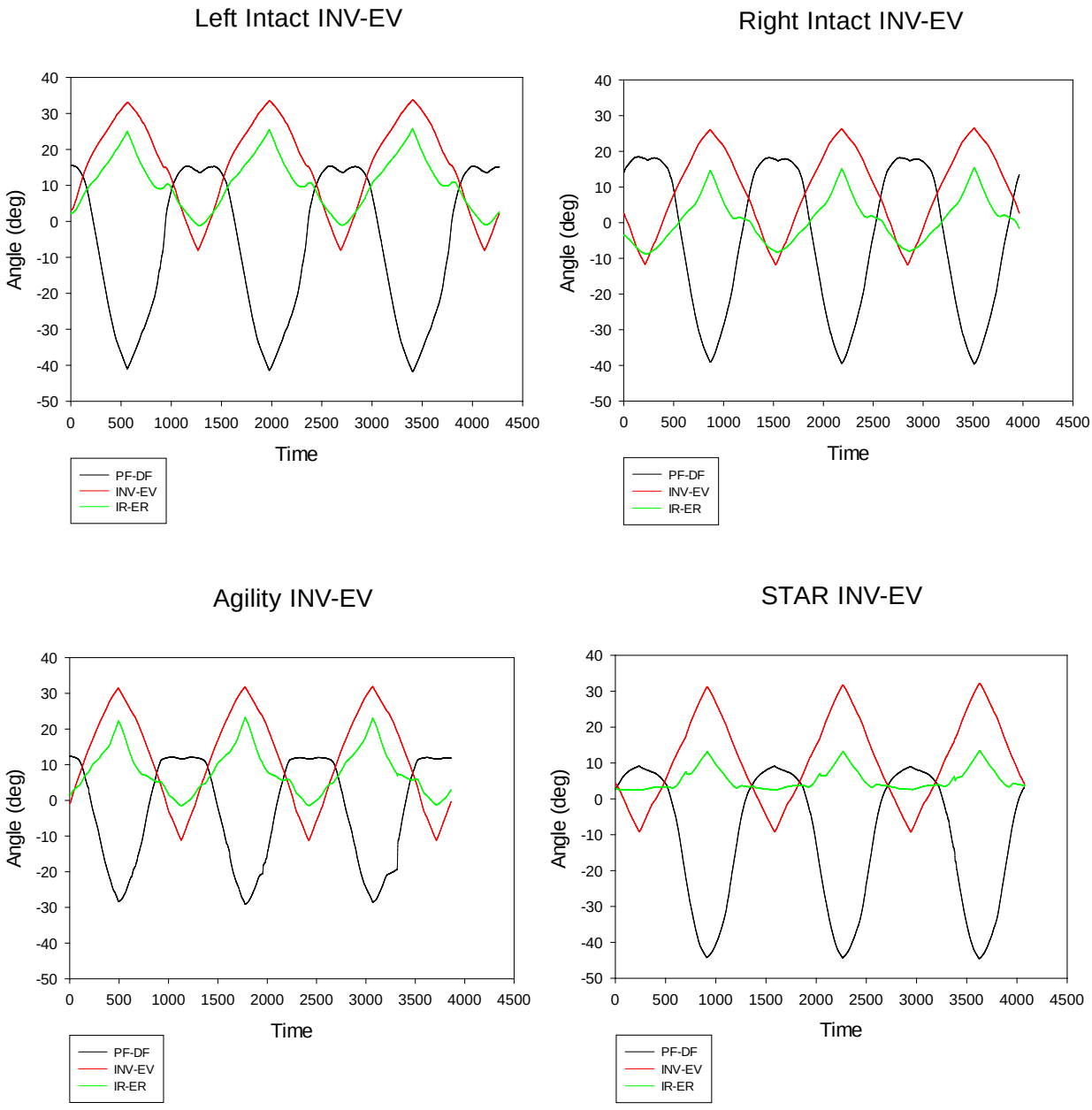

Figure 46: Representative sample of joint angles in uncompressed INV-EV loading for left and right intact, Agility, and STAR ankles. Red lines denote the primary/driven axis of rotation, where INV is positive and EV is negative. Black lines denote PF-DF rotations, where DF angles are positive. Green lines denote IR-ER rotations, where IR angles are positive.

Internal-External Rotation

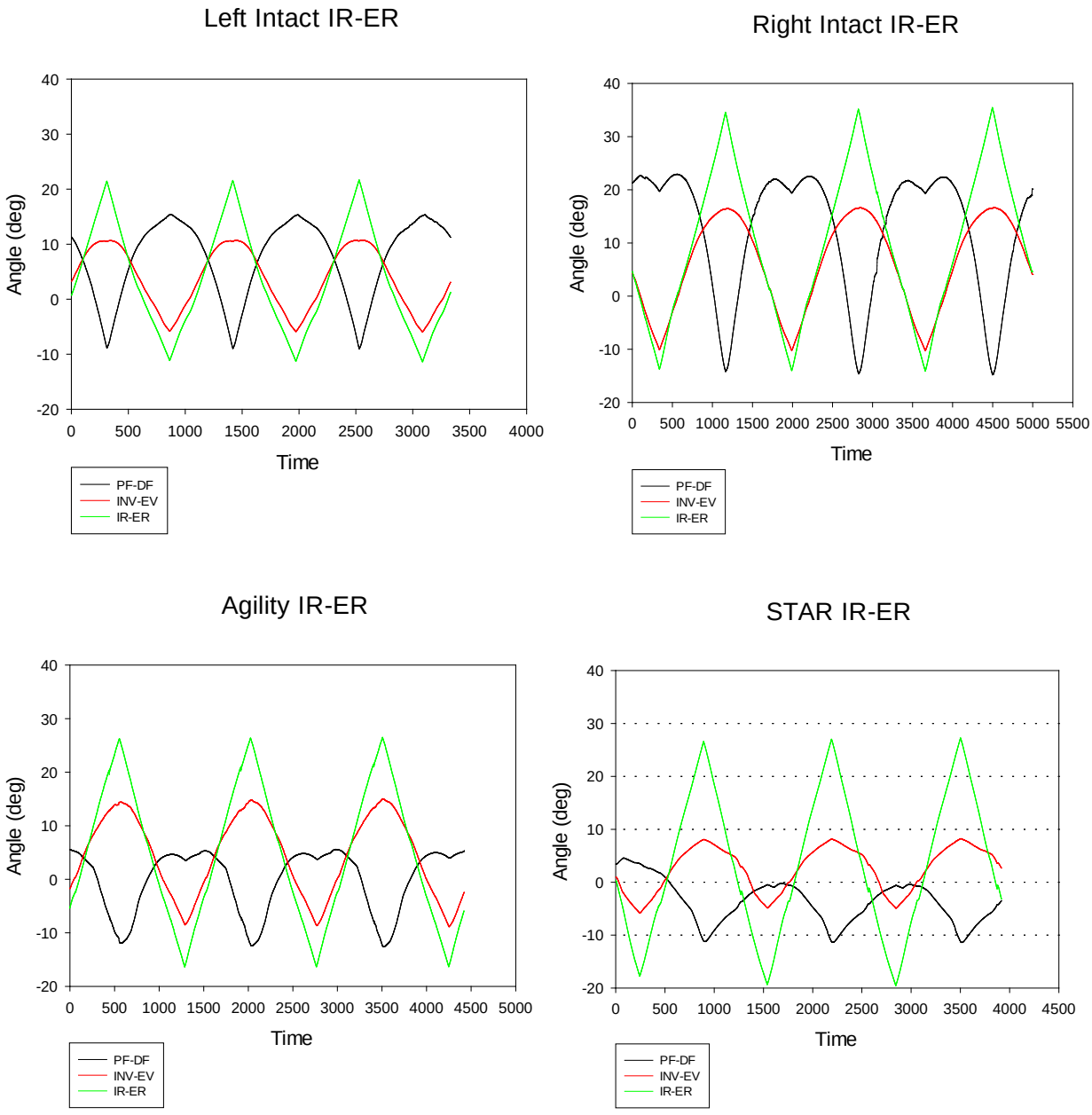

Figure 47: Representative sample of joint angles in uncompressed IR-ER loading for left and right intact, Agility, and STAR ankles. Green lines denote the primary/driven axis of rotation, where IR is positive and ER is negative. Black lines denote PF-DF rotations, where DF angles are positive. Red lines denote INV-EV rotations, where INV angles are positive.

In PF-DF (fig. 45), the foot went into inversion and external rotation as it was plantar-flexed, and it became internally rotated and decreased its amount of inversion and in some cases increase again to another inversion peak as it was dorsiflexed. In INV-EV (fig. 46), the foot plantar flexed as it became inverted. The IR-ER angle followed the INV-EV angle quite closely and became internally rotated while inverted and externally rotated while everted. When the foot went into eversion, it naturally fell back to a neutral or slightly dorsiflexed orientation. In IR-ER (fig. 47), we found that it plantar-flexed as it became internally rotated and dorsiflexed when externally rotated. The INV-EV angle followed the IR-ER angle, becoming inverted with IR and everted with ER, similar to the way the IR-ER angle followed the INV-EV angle in the INV-EV test. The magnitude of plantar-flexion occurring in this test was much smaller than that seen in the INV-EV test.

3.2.2 *RANGE OF MOTION*

The range of motion was determined for both INV-EV and IR-ER; however, measurements for the PF-DF ROM in the implanted ankles could not be attained due to the limitations of the testing setup (table 6).

Table 6: Range of motion in degrees along the three primary axes at applied moment limits (5 Nm for PF-DF and 3 Nm for INV-EV and IR-ER)

	Compression	**Intact**		**Agility**		**STAR**	
PF-DF	15 N	-50.4 ± 7.2	26.5 ± 4.1	-	-	-	-
	300 N	-40.4 ± 5.4	27.8 ± 5.0	-	-	-	-
INV-EV	15 N	-8.1 ± 5.8	23.7 ± 6.3	-10.5 ± 3.0	27.4 ± 6.3	-5.7 ± 2.1	24.5 ± 4.4
	75 N	-6.8 ± 3.8	22.8 ± 6.2	-9.2 ± 3.9	29.5 ± 2.7	-6.9 ± 2.3	23.2 ± 4.1
IR-ER	15 N	-12.2 ± 4.0	28.4 ± 6.5	-16.6 ± 6.2	28.5 ± 8.2	-12.3 ± 6.2	25.3 ± 4.7
	300 N	-5.3 ± 3.1	7.8 ± 4.4	-8.1 ± 2.1	4.8 ± 3.3	-2.9 ± 2.0	9.5 ± 3.0

Inversion-Eversion

The INV-EV ROM was significantly decreased by compression, but none of the other factors had a significant effect (main effects: 'Implant' $p = 0.176$, 'Condition' $p = 0.197$, 'Compression' $p = 0.019$; interactions: 'Implant' x 'Condition' $p = 0.630$, 'Compression' x 'Implant' $p = 0.058$, 'Condition' x 'Compression' $p = 0.904$, 'Condition' x 'Compression' x 'Implant' $p = 0.769$).

The mean ROM of the STAR was lower than the Agility in both inversion and eversion in uncompressed and compressed loading (fig. 48-49); however, this observation could have been misleading if the intact baseline was overlooked because the STAR prosthesis actually showed a similar trend of increasing the total INV-EV ROM, which was quite evident in figure 50. The mean intact range of motion for the right ankles (red) was lower than that of the left ankles (blue) by approximately 10 and 7 degrees in the 15 N and 75 N compression scenarios respectively. Despite being a relatively large difference (31.9% and 24.8% of the average ROM respectively), it was determined to be not significant (15N: $p = 0.909$; 75N: $p = 0.948$).

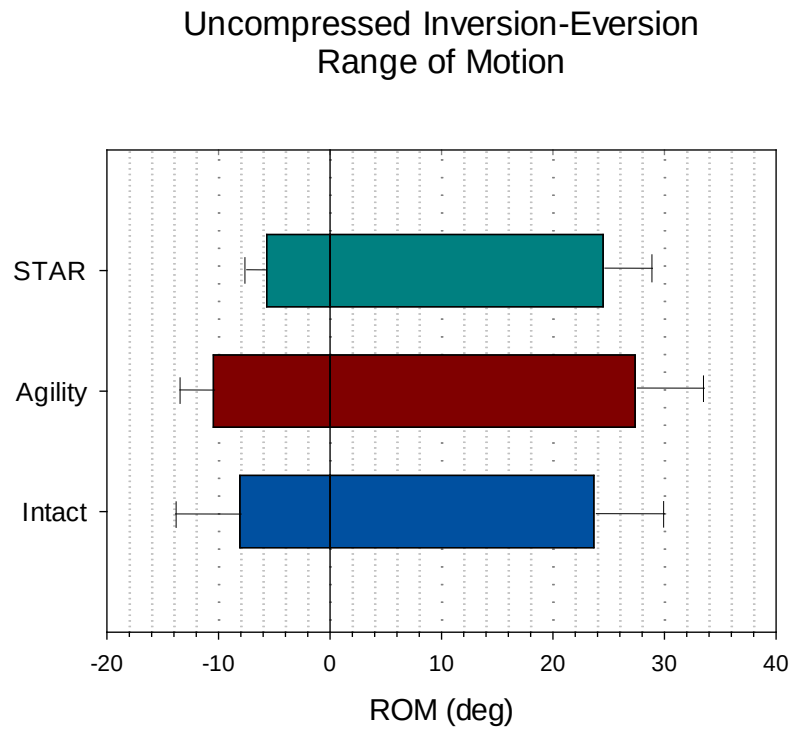

Figure 48: Range of motion for INV-EV at 3 Nm torque limits with a 15 N preload, showing mean peak inversion (positive) and eversion (negative) angles. Error bars denote one standard deviation.

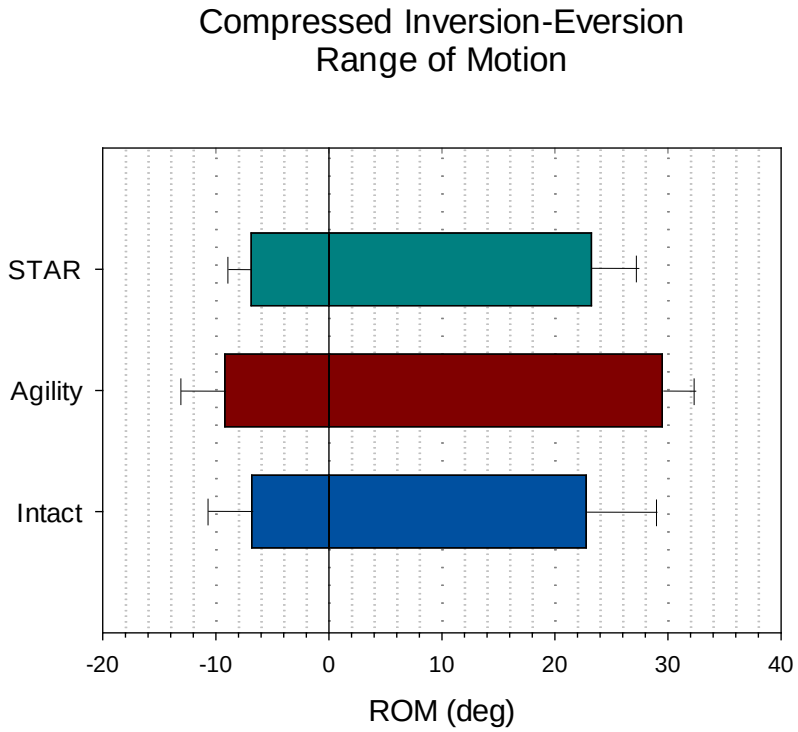

Figure 49: Range of motion for INV-EV at 3 Nm torque limits with a 75 N preload, showing mean peak inversion (positive) and eversion (negative) angles. Error bars denote one standard deviation.

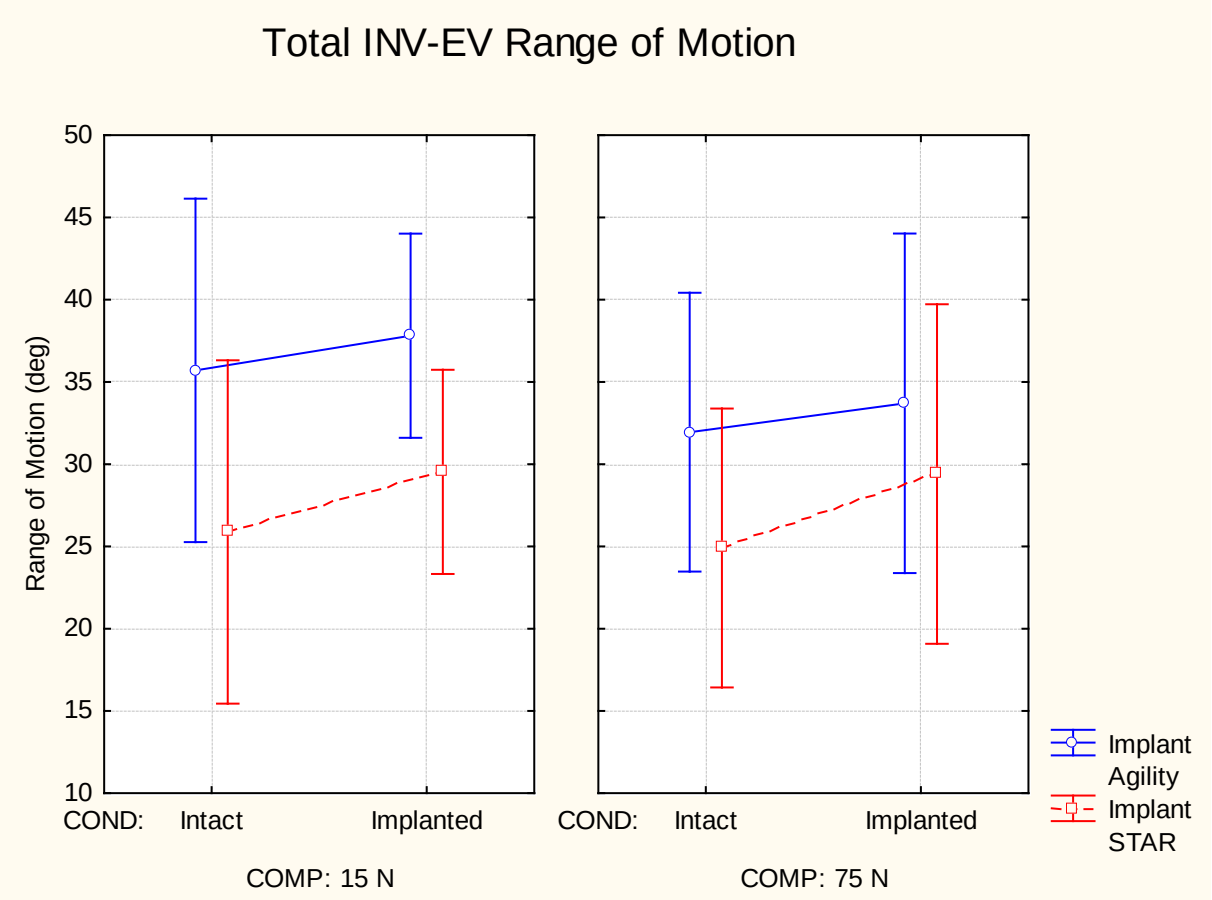

Figure 50: Total INV-EV ROM showing the interaction between compression, condition, and implant type. Values shown are mean ROM in degrees, and vertical bars denote 0.95 confidence interval.

Internal-External Rotation

The IR-ER ROM was only significantly affected by compression (main effects: 'Implant' $p = 0.418$, 'Condition' $p = 0.923$, 'Compression' $p < 0.001$; interactions: 'Implant' x 'Condition' $p = 0.495$, 'Compression' x 'Implant' $p = 0.104$, 'Condition' x 'Compression' $p = 0.611$, 'Condition' x 'Compression' x 'Implant' $p = 0.919$).

In the IR-ER loading direction, the inclusion of compression had a huge effect on the kinematics of the ankle, which was quite evident even to the naked eye. The compression inhibited supination of the foot, decreasing the range of motion about the IR-ER axis for all test conditions, which can be clearly seen from comparing figure 51 to figure 52. This resulted in a decrease in mean combined ROM from approximately 41° to 13° when compression was applied. The effect that the two ankle replacements had on their intact counterparts was not the same. Although insignificant, the Agility increased the mean ROM by 2.3° ($p = 0.300$) and 1.0° ($p = 0.890$) whereas the STAR decreased the ROM by 0.8° ($p = 0.715$) and 1.7° ($p = 0.713$) in the uncompressed and compressed cases respectively (see fig. 53).

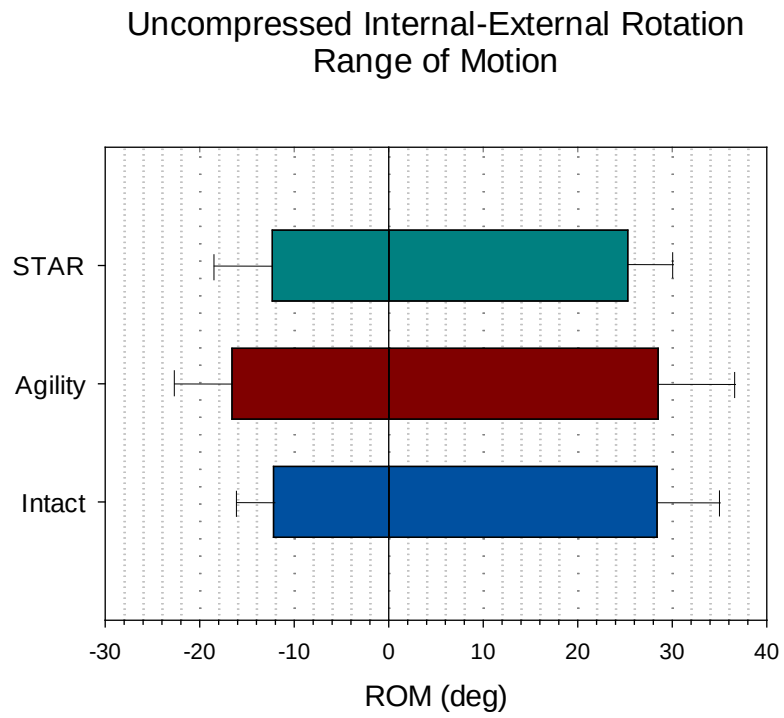

Figure 51: Range of motion for IR-ER at 3 Nm torque limits with a 15 N preload, showing mean peak internal (positive) and external (negative) rotation angles of the foot. Error bars denote one standard deviation.

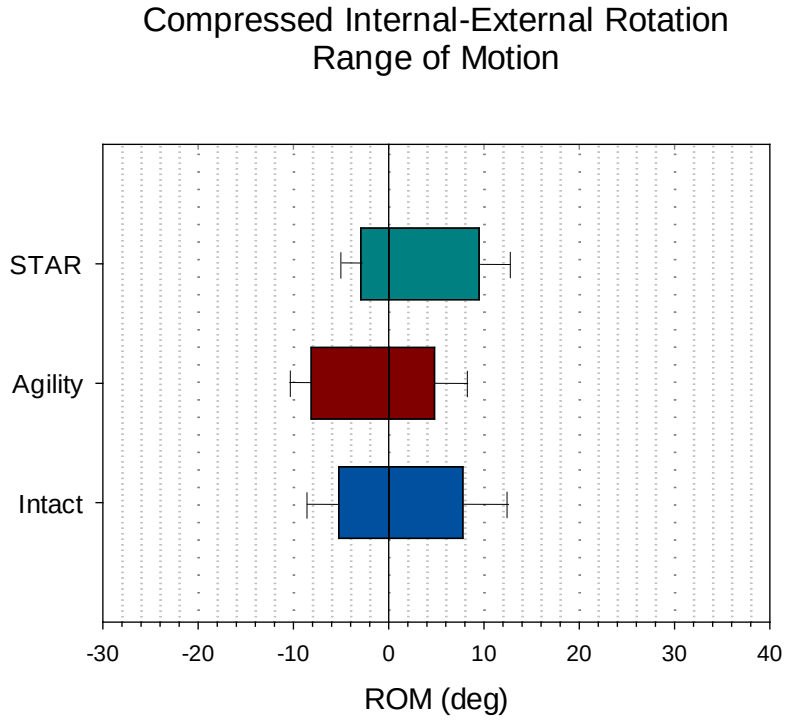

Figure 52: Range of motion for IR-ER at 3 Nm torque limits with a 300 N preload, showing mean peak internal (positive) and external (negative) rotation angles of the foot. Error bars denote one standard deviation.

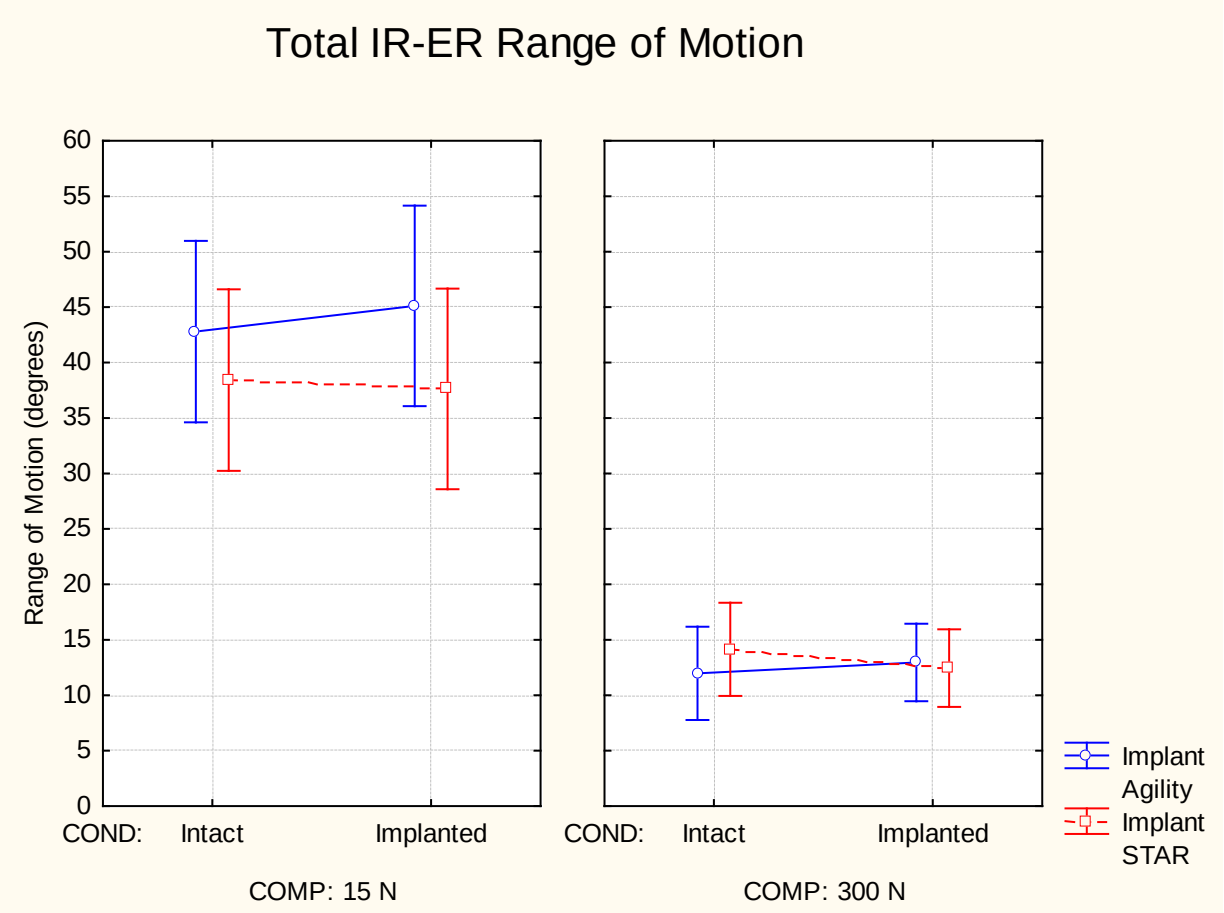

Figure 53: Total IR-ER ROM showing the interaction between compression, condition, and implant type. Values shown are mean ROM in degrees, and vertical bars denote 0.95 confidence interval.

3.2.3 *MOTION COUPLING*

The motion coupling ratios for PF-DF were the smallest of the 3 loading directions. Both of the secondary rotation magnitudes in this loading direction were lower than 20% of the PF-DF ROM. Also, the magnitudes of motion coupling in each direction were nearly equal (details in table 8). The magnitude of total coupled motion was also the least in this loading direction, and values rarely exceeded 10 degrees about either axis.

Plantarflexion-Dorsiflexion Loading

No significant differences were found in the INV-EV:PF-DF motion coupling ratios (main effects: 'Implant' $p = 0.777$, 'Condition' $p = 0.468$, 'Compression' $p = 0.060$; interactions: 'Implant' x 'Condition' $p = 0.167$, 'Compression' x 'Implant' $p = 0.253$, 'Condition' x 'Compression' $p = 0.937$, 'Condition' x 'Compression' x 'Implant' $p = 0.342$).

Compression tended to decrease the amount of motion coupling and was nearly significant in its effect ($p = 0.0597$) and it brought the mean combined MC ratio from 0.167 to 0.131 (fig. 54). The Agility and STAR seemed to have a different effect on the MC ratio, which was a decrease caused by the Agility and an increase caused by the STAR (fig. 56). Although there were no significant differences between the coupling ratios, there are subtler differences that can be seen in the pattern of their coupling (fig. 55). The minimum INV-EV angle is occurs part way into the PF cycle, and it was found to occur around different angles of PF for each implant. Compared to the normal ankle, it occurred sooner for the Agility and later for the STAR. During DF, both implants followed the normal pattern relatively well, but the Agility's pattern was slightly closer.

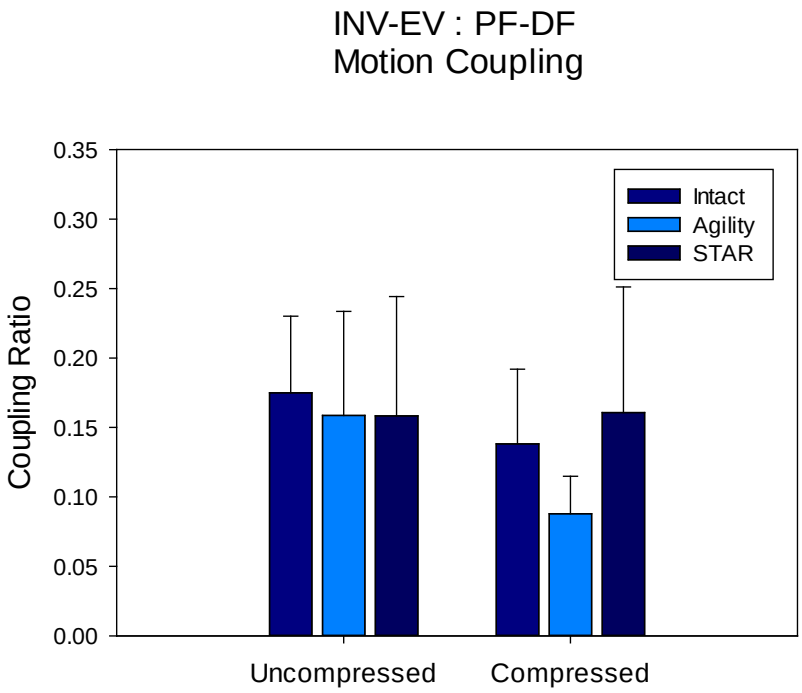

Figure 54: Mean INV-EV motion coupling ratios in the PF-DF loading direction with error bars as one standard deviation.

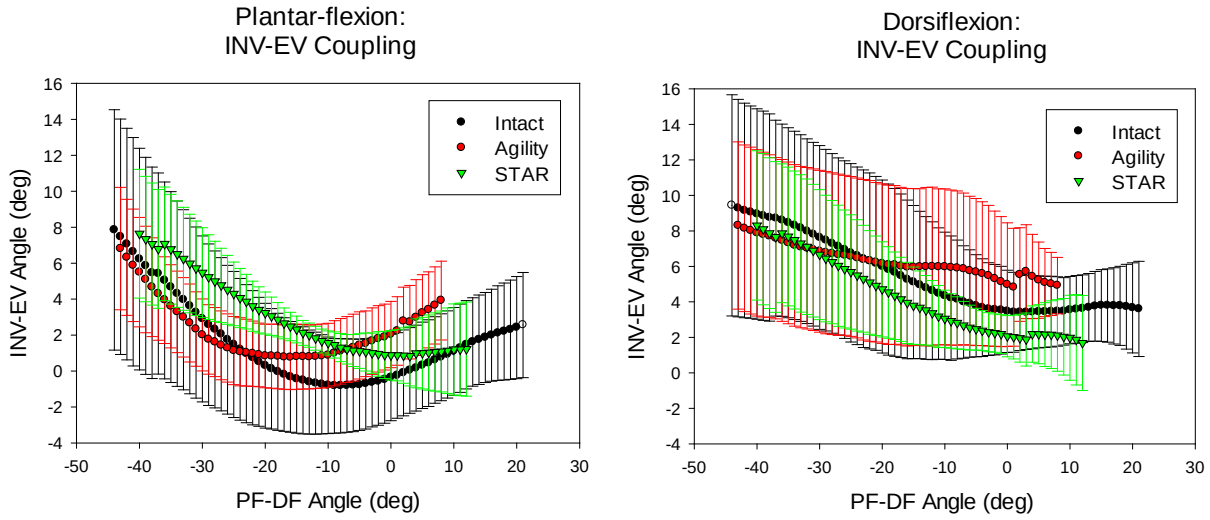

Figure 55: INV-EV motion coupling mean values (±SD) plotted as a function of PF-DF angle in forward (PF, on left) and reverse (DF, on right) direction. Positive angles denote INV and DF.

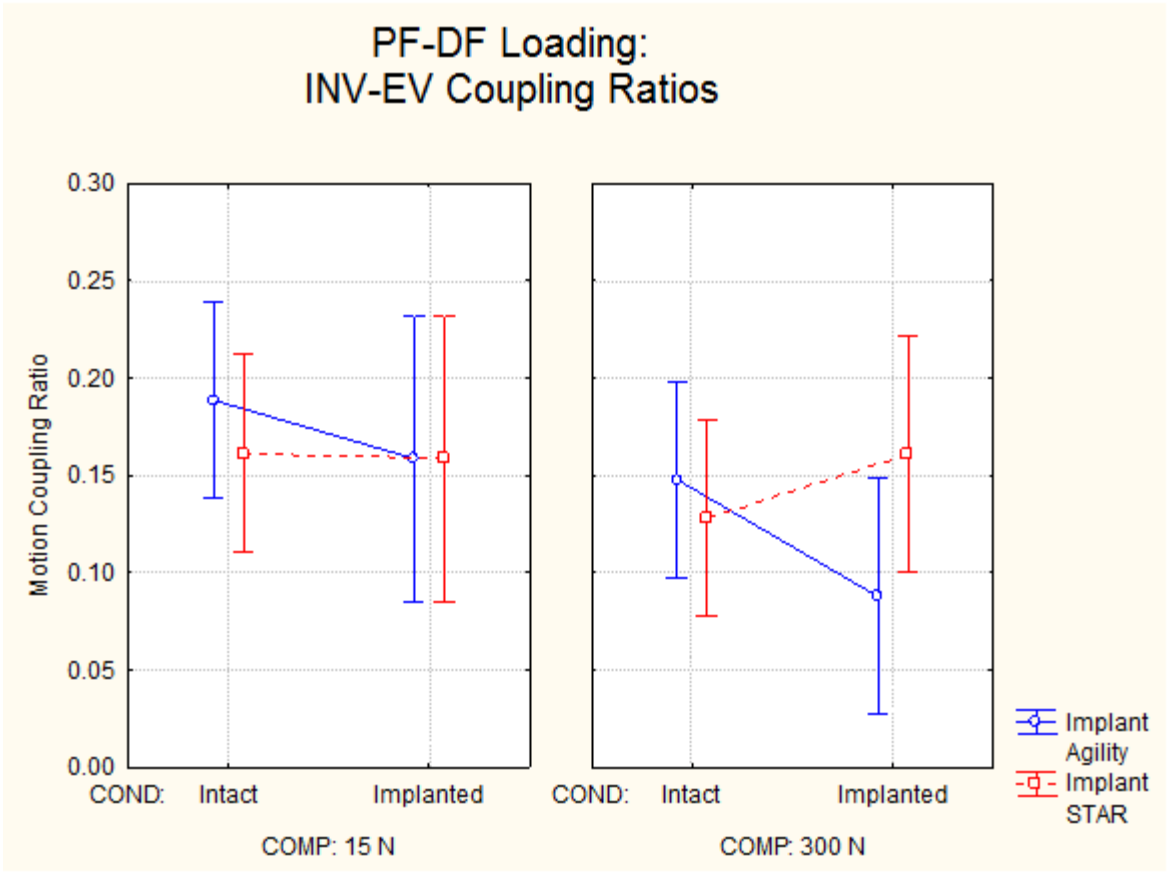

Figure 56: INV-EV:PF-DF motion coupling ratios showing the interaction between implant type, compression, and ankle condition. Vertical bars denote 0.95 confidence intervals

Similarly to INV-EV:PF-DF, there were no significant differences in the IR-ER:PF-DF coupling ratios caused by compression or implant type (fig. 57) (main effects: 'Implant' p = 0.396, 'Condition' p = 0.633, 'Compression' p = 0.697; interactions: 'Implant' x 'Condition' p = 0.194, 'Compression' x 'Implant' p = 0.405, 'Condition' x 'Compression' p = 0.995, 'Condition' x 'Compression' x 'Implant' p = 0.703).

In contrast with the previous MC direction, the Agility increased the IR-ER coupling and the STAR decreased it (fig. 59), which was the most pronounced difference in this test, albeit insignificant (p = 0.194). Looking at the IR-ER angle as a function of PF-DF angle (fig. 58), the Agility curve seemed to resemble the intact curve more closely.

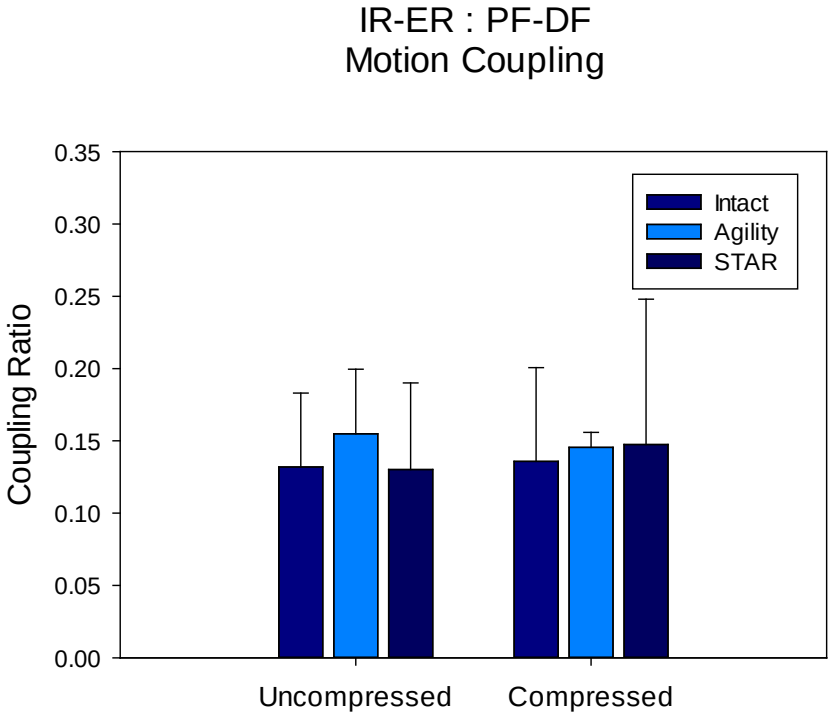

Figure 57: Mean IR-ER motion coupling ratios for the PF-DF loading direction with error bars as one standard deviation.

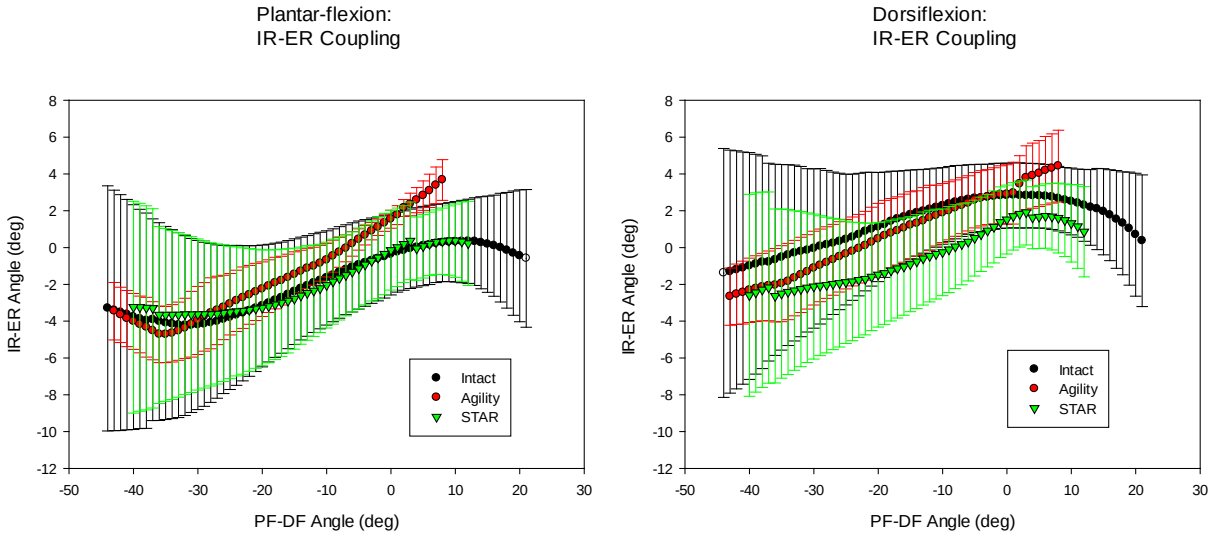

Figure 58: IR-ER motion coupling mean values (±SD) plotted as a function of PF-DF angle in forward (PF, on left) and reverse (DF, on right) direction. Positive angles denote IR and DF.

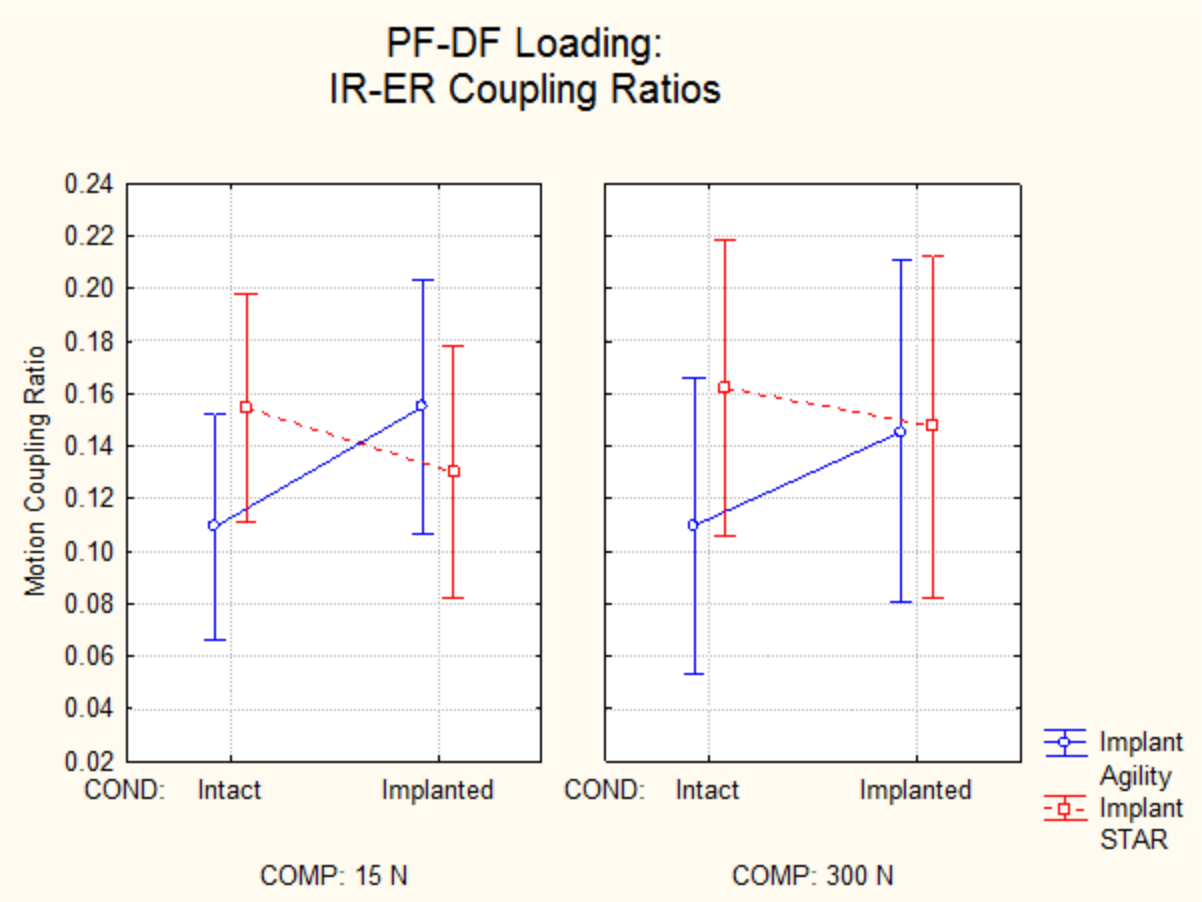

Figure 59: IR-ER:PF-DF motion coupling ratios showing the interaction between implant type, compression, and ankle condition. Vertical bars denote 0.95 confidence intervals

Inversion-Eversion Loading

The MC ratios observed in INV-EV were the largest of the three loading directions. This is especially evident in PF-DF coupling, with the mean ratio of the intact limbs nearing 2. The PF-DF MC ratio decreased from 1.866 to 1.120 when comparing intact and implanted ankles ($p = 0.004$). The IR-ER ratio was also significantly reduced by the replacement of the ankle joint with these prostheses, bringing the mean ratio from 0.786 to 0.540 ($p = 0.002$). Additionally for IR-ER coupling, there was a significant interaction between compression and ankle condition ($p = 0.010$), which indicates that

the intact ankles' ratio was increased by the compressive load whereas the implanted ankles' ratio experienced a decrease due to compression.

In INV-EV loading, the PF-DF coupling ratios were significantly reduced by replacing the joint, but no significant differences were found between the implants or due to compression. There were no significant interactions between the effects either (main effects: 'Implant' $p = 0.540$, 'Condition' $p = 0.004$, 'Compression' $p = 0.131$; interactions: 'Implant' x 'Condition' $p = 0.743$, 'Compression' x 'Implant' $p = 0.797$, 'Condition' x 'Compression' $p = 0.074$, 'Condition' x 'Compression' x 'Implant' $p = 0.468$).

The PF-DF MC ratio in INV-EV loading was clearly lower in the implanted cases, even to the point that post-hoc tests found significant differences between intact and both implants in the uncompressed and compressed loading scenarios (fig 60). Generally speaking, plantarflexion was linearly related to inversion, except for a plateau region that occurred close to the ankle's dorsiflexion limit. During inversion, the shape of the coupling curves was quite similar between the implants and intact cases, but the slope change was more pronounced and occurred at a slightly larger angle for the intact case (8° vs. 6°) and DF plateau was at larger angle for the intact ankle (fig. 61 left). During eversion, the shapes of the implanted ankles deviated from the intact curve more and lacked the distinguishable plateau region seen in inversion (fig. 61 right). For the most part, the implants behaved similarly to each other and caused a comparable decrease in the MC ratio compared to the intact ankles in both compressed and uncompressed tests (fig. 62).

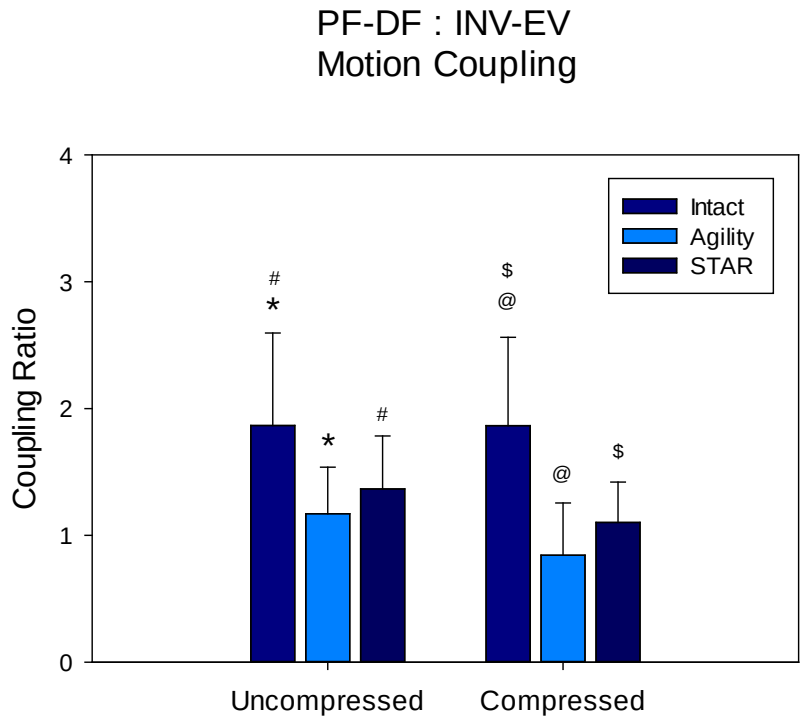

Figure 60: Mean PF-DF motion coupling ratios in the INV-EV loading direction with error bars as one standard deviation. * p=0.005; # p=0.017; @ p=0.001; $ p=0.004

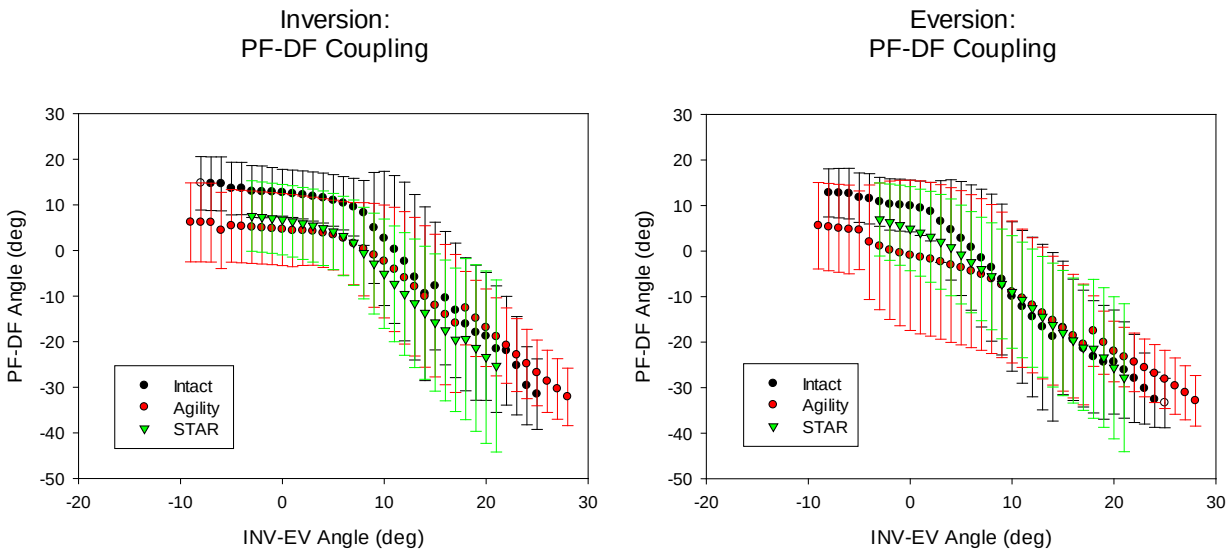

Figure 61: PF-DF motion coupling mean values (±SD) plotted as a function of INV-EV angle in forward (INV, on left) and reverse (EV, on right) direction. Positive angles denote DF and INV.

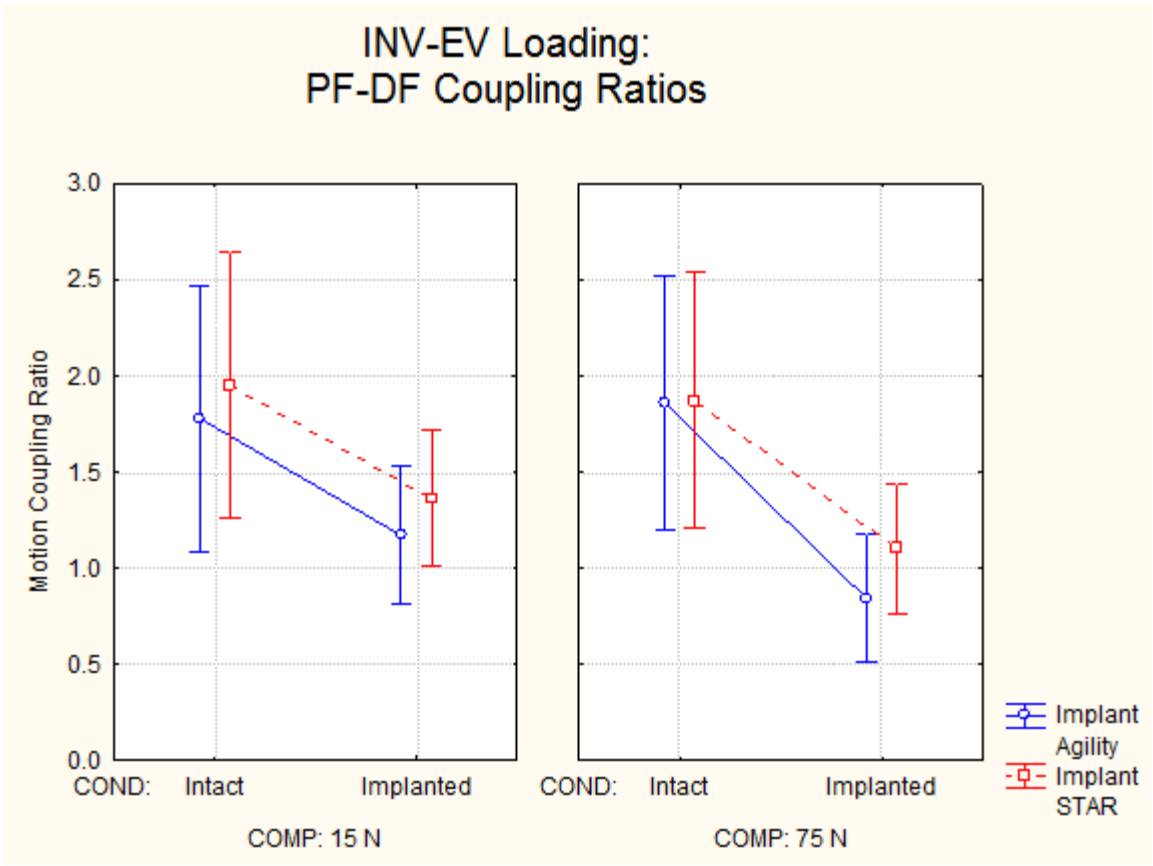

Figure 62: PF-DF:INV-EV motion coupling ratios showing the interaction between implant type, compression, and ankle condition. Vertical bars denote 0.95 confidence intervals

The coupling ratios of IR-ER to INV-EV were significantly decreased from intact to implanted ankles, and the interaction between ankle condition and compression was also found to be significant (main effects: 'Implant' p = 0.322, 'Condition' p = 0.002, 'Compression' p = 0.578; interactions: 'Implant' x 'Condition' p = 0.918, 'Compression' x 'Implant' p = 0.893, 'Condition' x 'Compression' p = 0.010, 'Condition' x 'Compression' x 'Implant' p = 0.063).

IR-ER motion was coupled quite strongly to INV-EV motion, and they had a nearly linear relationship throughout the ROM with the exception of the STAR. The MC curve of the Agility followed very closely to the intact pattern, but the STAR differed quite a bit, which had slope change at around 17° of inversion not present in the other ankle conditions (fig. 64). There was a

significant difference in MC ratios between the STAR and intact conditions during the uncompressed test, but both implants caused a decrease in MC during the compressed test (fig. 63). The interaction between compression, ankle condition, and implant type was almost significant since compression increased the mean MC ratio in the intact ankles, decreased it in ankles with the Agility, and had little effect on it in ankles with the STAR (fig. 65).

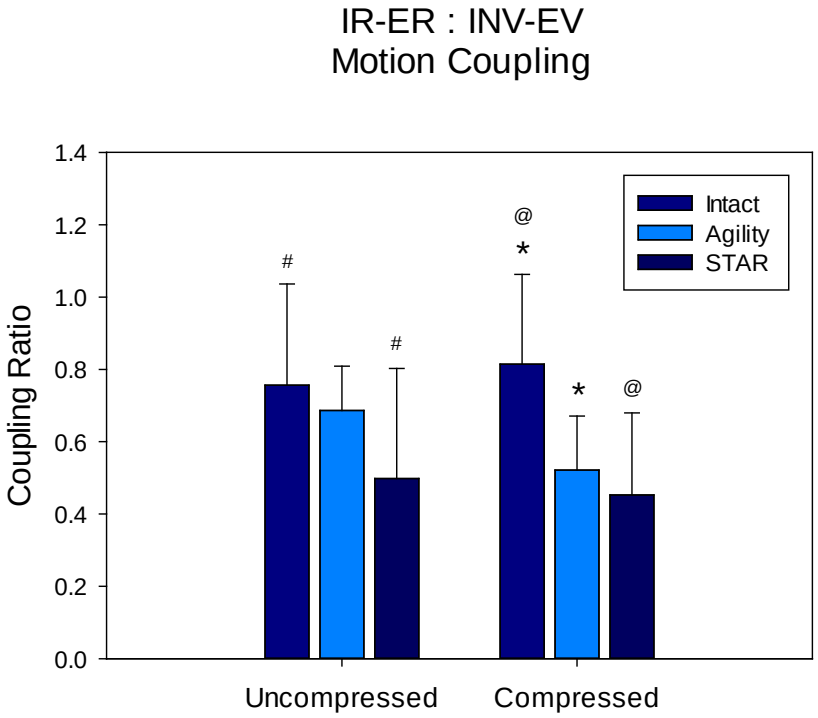

Figure 63: Mean IR-ER motion coupling ratios in the INV-EV loading direction with error bars as one standard deviation. * p<0.001; # p=0.007; @ p=0.003

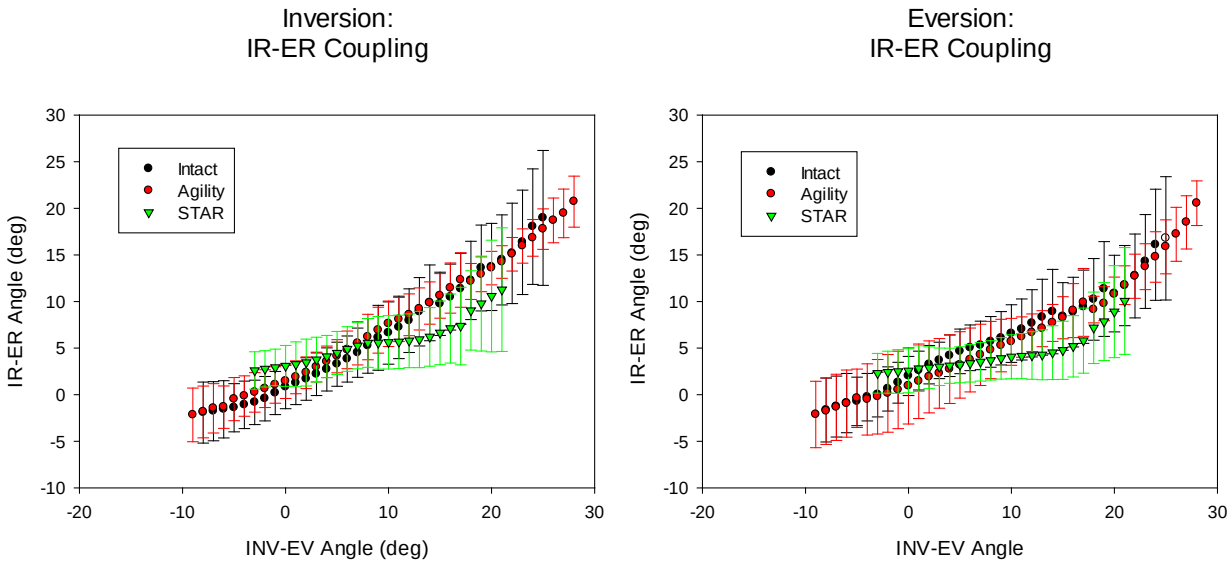

Figure 64: IR-ER motion coupling mean values (±SD) plotted as a function of INV-EV angle in forward (INV, on left) and reverse (EV, on right) direction. Positive angles denote IR and INV.

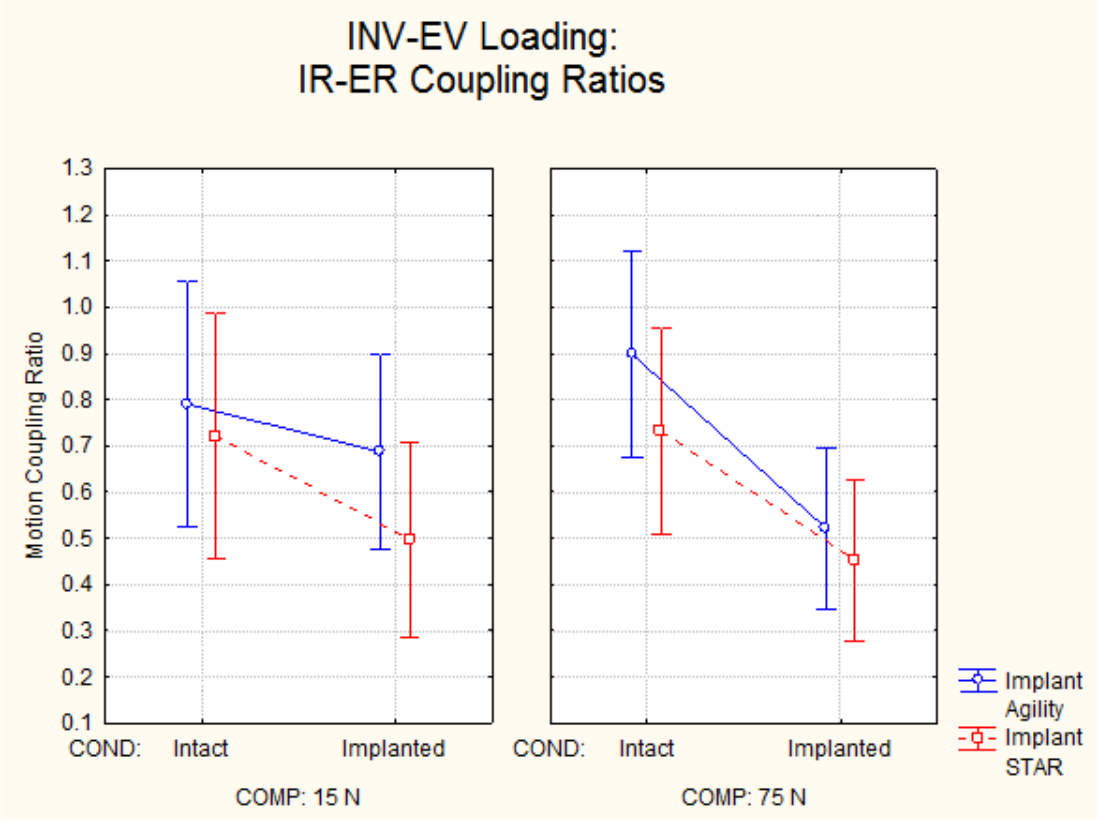

Figure 65: IR-ER:INV-EV motion coupling ratios showing the interaction between implant type, compression, and ankle condition. Vertical bars denote 0.95 confidence intervals

Internal-External Rotation Loading

The motion coupling patterns induced by IR-ER loading were similar to those of INV-EV, although smaller ratios were observed in this type of loading, especially in PF-DF MC. The application of compression during these tests reduced the overall motion in all axes by a large amount, which produced some interesting results. In both PF-DF and INV-EV coupling, the effects of compression and ankle condition had significant effects.

The PF-DF motion coupled to IR-ER was significantly decreased from intact to implanted ankles, and there was a significant decrease caused by compression. The mean motion coupling ratio was reduced by the compressive load from 0.589 to 0.453 and by implementing TAAs from 0.667 to 0.375. The Agility and STAR implants had nearly identical effects on the PF-DF motion coupling. Surprisingly, we also found a that the MC ratio in the left ankles was decreased by compression more than the right ankles leading to significant interaction between compression and implant (main effects: 'Implant' $p = 0.359$, 'Condition' $p < 0.001$, 'Compression' $p = 0.008$; interactions: 'Implant' x 'Condition' $p = 0.912$, 'Compression' x 'Implant' $p = 0.029$, 'Condition' x 'Compression' $p = 0.258$, 'Condition' x 'Compression' x 'Implant' $p = 0.998$).

The mean PF-DF:IR-ER MC ratios were decreased by compression in all ankles, but those replaced with the Agility prosthesis were the affected the most (fig. 66); however, the post-hoc analysis didn't find this to be significant ($p = 0.059$). As expected, the ankle plantar flexed during IR and dorsiflexed during ER in accordance with the supination-pronation relationship. The motion coupling curves of all conditions took on a similar shape, with a curve of downward concavity during IR and one with a less pronounced curvature and a slight inflection near the beginning of the cycle in ER (fig. 67). Although slight differences are visible between the implants in their MC curves, their effects on the MC ratios are almost identical (fig. 68).

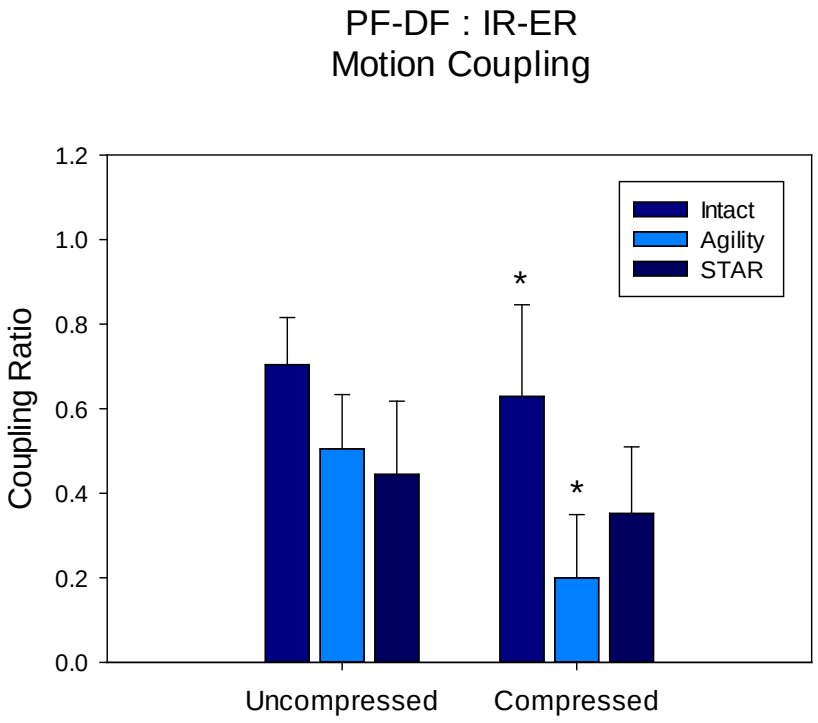

Figure 66: Mean PF-DF motion coupling ratios in the IR-ER loading direction with error bars as one standard deviation. *p=0.044

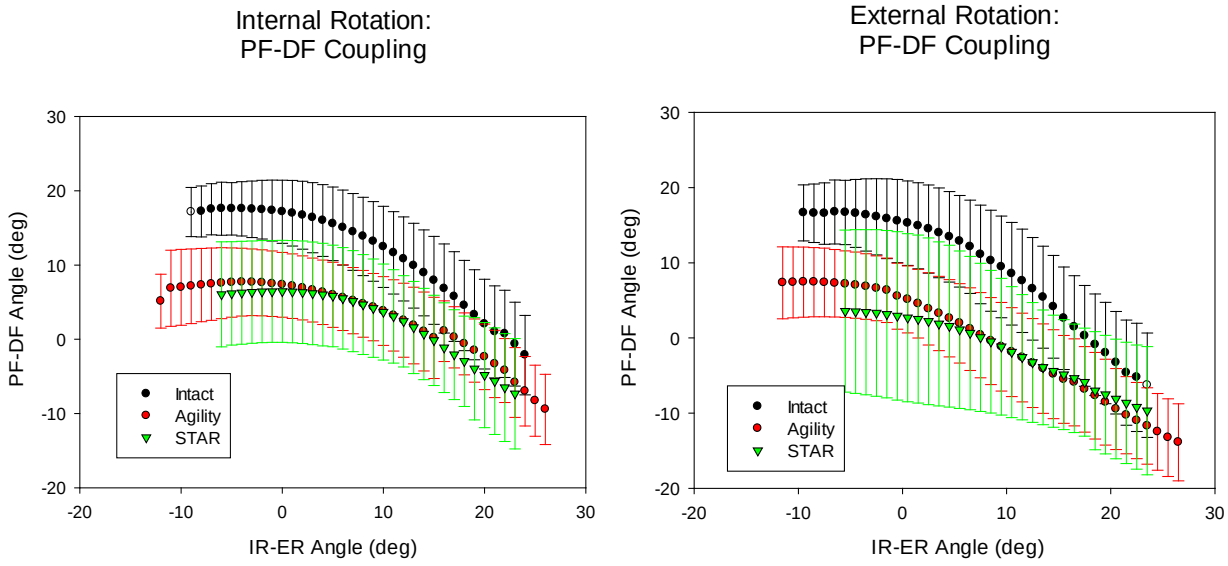

Figure 67: PF-DF motion coupling mean values (±SD) plotted as a function of IR-ER angle in forward (IR, on left) and reverse (ER, on right) direction. Positive angles denote DF and IR.

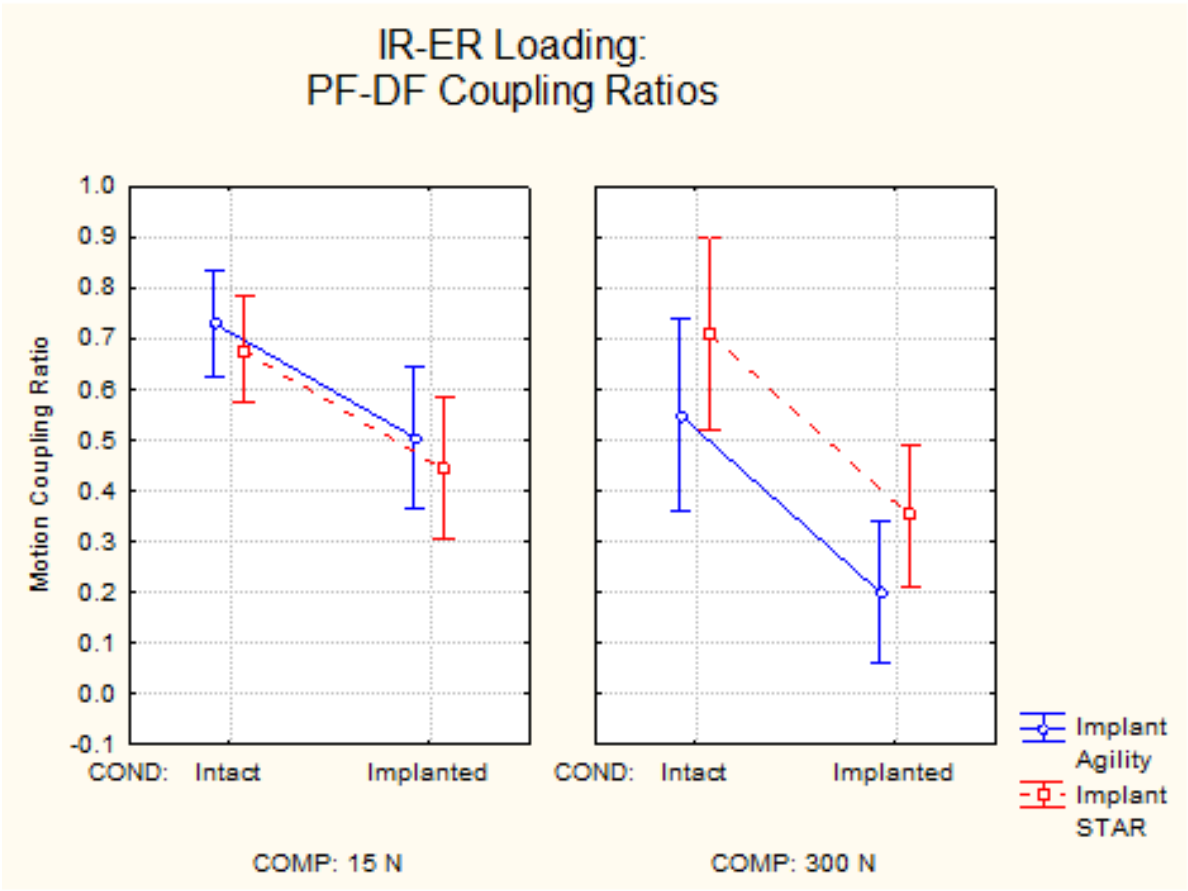

Figure 68: PF-DF:IR-ER motion coupling ratios showing the interaction between implant type, compression, and ankle condition. Vertical bars denote 0.95 confidence interval.

The MC ratio of INV-EV motion to IR-ER loading was found to be significantly decreased by joint replacement and significantly increased by compression (main effects: 'Implant' p = 0.786, 'Condition' p = 0.025, 'Compression' p = 0.024; interactions: 'Implant' x 'Condition' p = 0.588, 'Compression' x 'Implant' p = 0.722, 'Condition' x 'Compression' p = 0.104, 'Condition' x 'Compression' x 'Implant' p = 0.347)

The application of compression increased the ratio of coupled INV-EV motion of all ankle conditions and a significant difference was found for ankles with the STAR (fig. 69). Neither implant replicated the intact MC pattern very well (fig. 70). Despite reaching a similar maximum INV angle, the

Agility's curve had a shallower curve and lower EV angle as a result. The STAR's curve deviated more from the intact case than the Agility, and it exhibited an even shallower slope and a lower INV angle. In uncompressed loading, replacing the ankle joint with either implant resulted in comparable decreases in INV-EV coupling. Under compression, however, the Agility caused a minor decrease in mean coupling ratio while the STAR caused a minor increase (fig. 71).

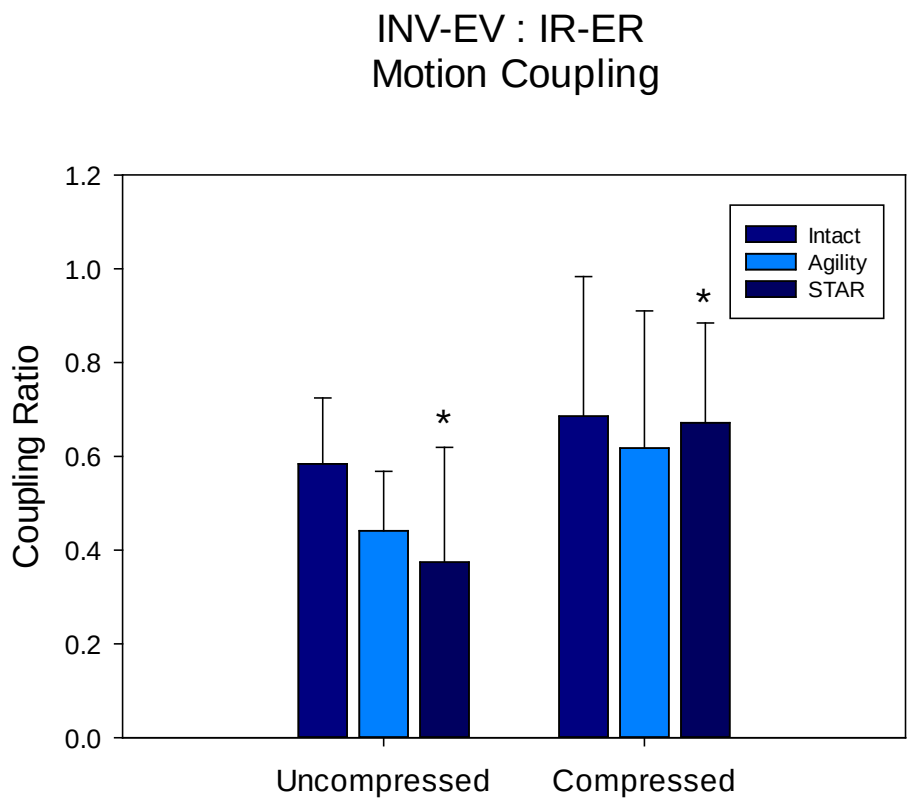

Figure 69: Mean INV-EV motion coupling ratios in the IR-ER loading direction with error bars as one standard deviation. *p=0.032

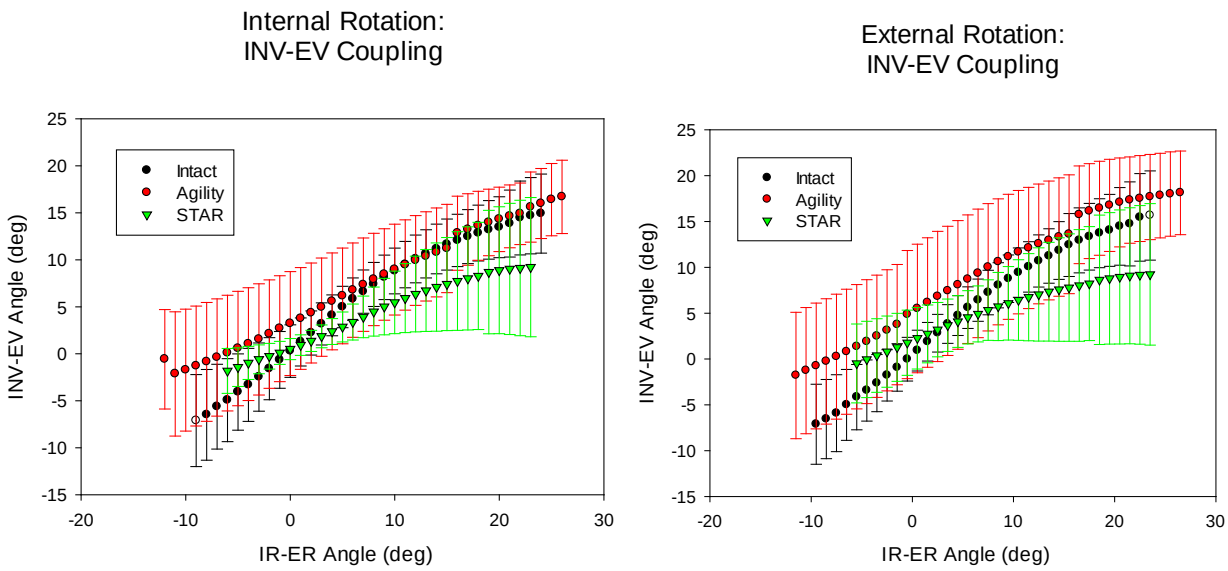

Figure 70: INV-EV motion coupling mean values (±SD) plotted as a function of INV-EV angle in forward (IR, on left) and reverse (ER, on right) direction. Positive angles denote INV and IR.

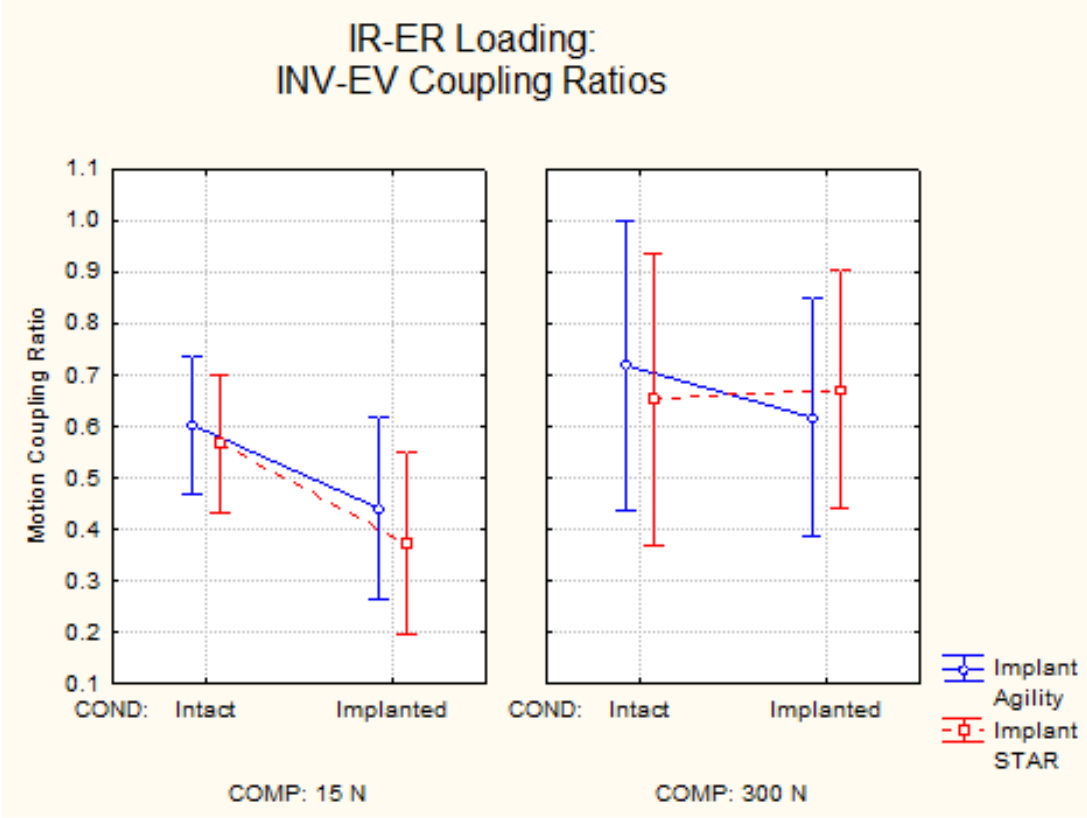

Figure 71: INV-EV:IR-ER motion coupling ratios showing the interaction between implant type, compression, and ankle condition. Vertical bars denote 0.95 confidence intervals

3.2.4 *JOINT TRANSLATION*

Medial/Lateral Joint Translation

The mediolateral translation of the foot was calculated as the joint centre's displacement along the flexion axis, denoted q_1 in the JCS. It was the largest when the ankle was loaded in INV-EV by approximately a factor of 2 (fig. 72).

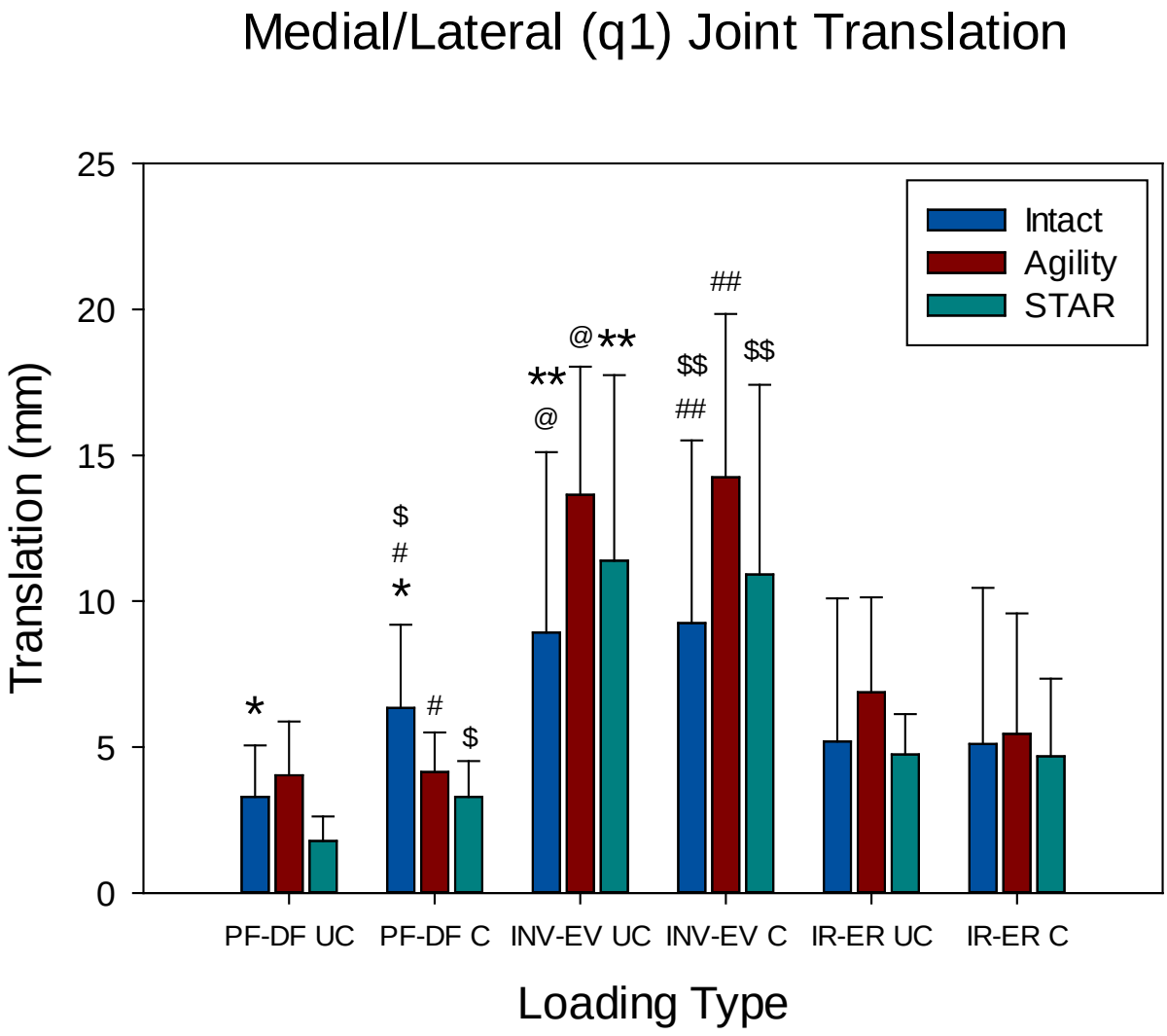

Figure 72: Mean translation of the JCS origin along the medial/lateral axis with error bars as one standard deviation. UC denotes uncompressed loading and C denotes compressed loading. *p=0.005(L), 0.002 (R); #p=0.003; $p=0.007; @p=0.002; **p<0.001; ##p=0.001; $$p<0.001

In the PF-DF loading direction, compression was found to increase the amount of translation more in intact ankles than in the replaced ankles. The effects of compression and ankle condition were found to cause significant increases and decreases in this motion respectively, but the previously mentioned effect played a large role in this result (fig. 73) (main effects: 'Implant' p = 0.158, 'Condition' p = 0.019, 'Compression' p = 0.001; interactions: 'Implant' x 'Condition' p = 0.681, 'Compression' x 'Implant' p = 0.242, 'Condition' x 'Compression' p = 0.003, 'Condition' x 'Compression' x 'Implant' p = 0.484). Post hoc analysis revealed that the only significant comparisons were those with the compressed intact ankles.

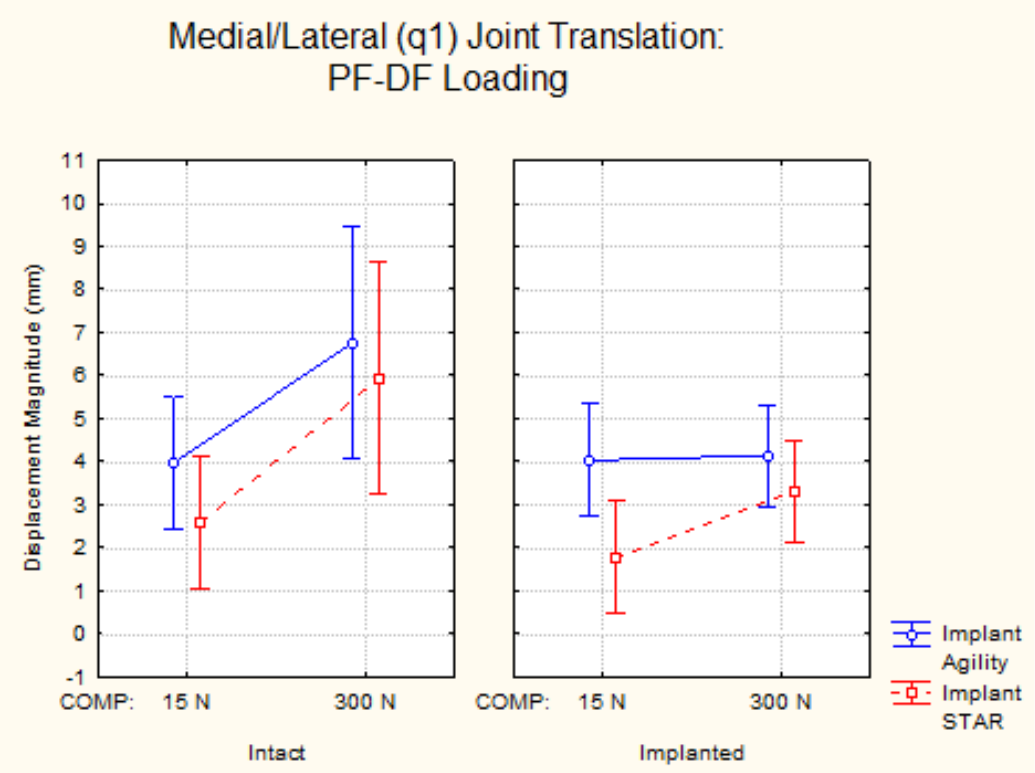

Figure 73: Translation of the JCS origin along the medial/lateral axis due to PF-DF loading showing the interaction of compression, condition, and implant type. Values shown are mean peak displacements in millimeters, and vertical bars denote 0.95 confidence intervals.

Under INV-EV loading, replacing the joint resulted in a larger amount of M/L translation, and the effect was slightly more pronounced in the STAR than the Agility but not significant (fig. 74). This also resulted in significant post-hoc tests between intact and Agility, and between intact and STAR for both the compressed and uncompressed tests (fig. 72) (main effects: 'Implant' p = 0.194, 'Condition' p = 0.015, 'Compression' p = 0.653; interactions: 'Implant' x 'Condition' p = 0.246, 'Compression' x 'Implant' p = 0.497, 'Condition' x 'Compression' p = 0.518, 'Condition' x 'Compression' x 'Implant' p = 0.242).

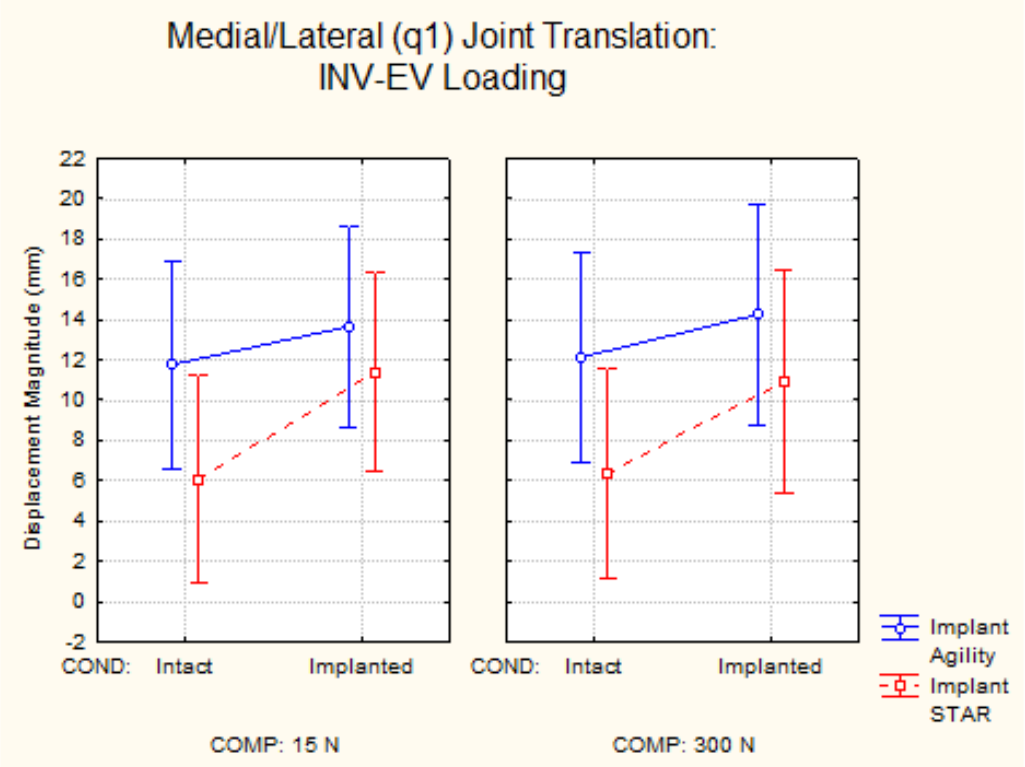

Figure 74: Translation of the JCS origin along the medial/lateral axis due to INV-EV loading, showing the interaction of compression, condition, and implant type. Values shown are mean peak displacements in millimeters, and vertical bars denote 0.95 confidence intervals.

There were no significant effects found in this direction of joint translation when loaded in IR-ER (main effects: 'Implant' p = 0.304, 'Condition' p = 0.791, 'Compression' p = 0.623; interactions: 'Implant' x 'Condition' p = 0.537, 'Compression' x 'Implant' p = 0.216, 'Condition' x 'Compression' p = 0.419, 'Condition' x 'Compression' x 'Implant' p = 0.325).

Anterior/Posterior Joint Translation

The anteroposterior translation of the foot was calculated as the joint centre's displacement along the A/P axis of the foot, denoted q_2 in the JCS. The largest difference in the A/P joint translation was found in the STAR under PF-DF loading (fig. 75).

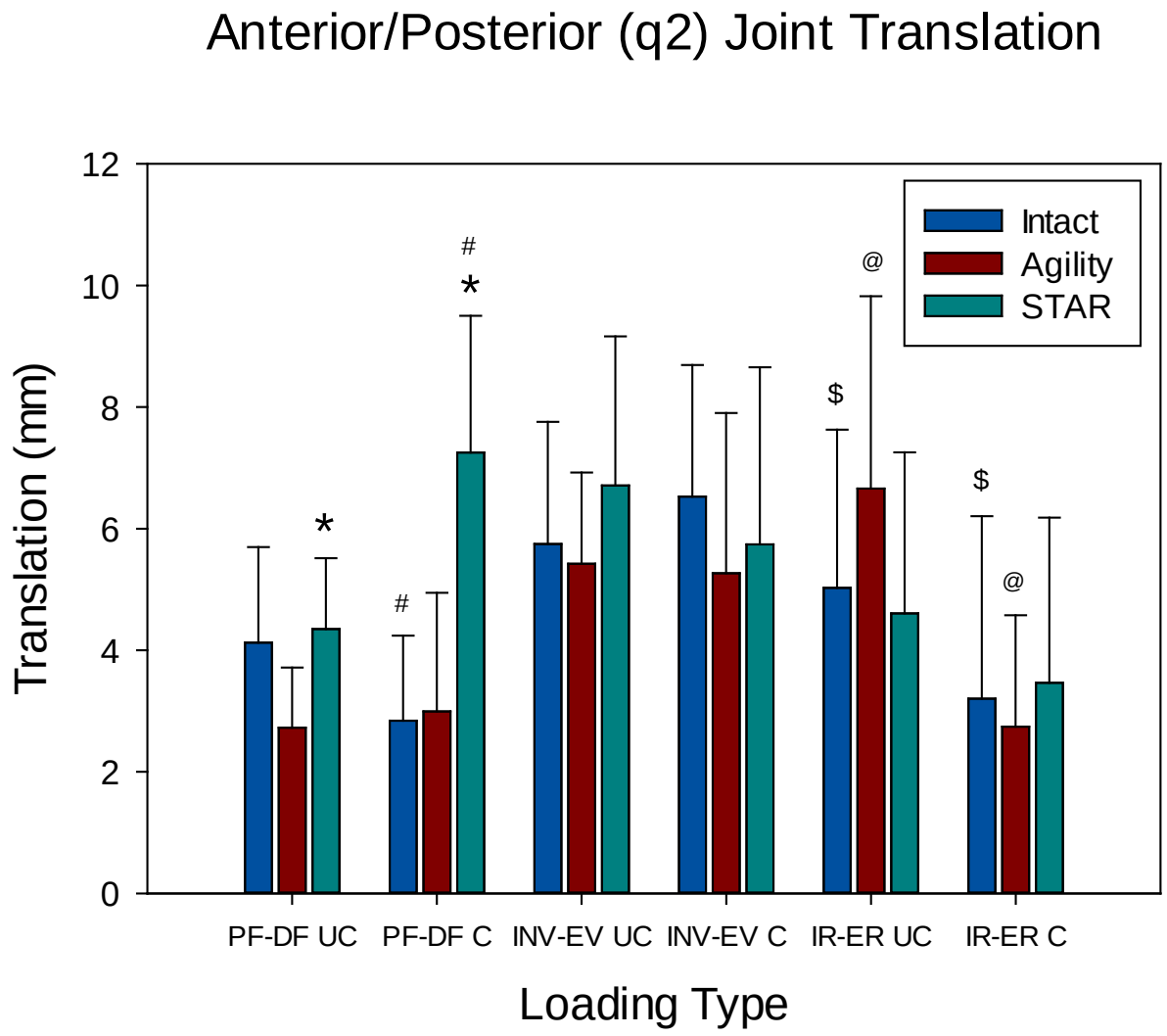

Figure 75: Mean translation of the JCS origin along the anterior/posterior axis with error bars as one standard deviation. *p=0.002; #p<0.001; $p=0.038 (L); @p=0.018

In PF-DF loading, there were significant differences in the A/P translation of the foot due to the effects of implant and condition, and the compression-condition and compression-condition-implant interactions (main effects: 'Implant' p = 0.044, 'Condition' p = 0.017, 'Compression' p = 0.712; interactions: 'Implant' x 'Condition' p = 0.002, 'Compression' x 'Implant' p = 0.164, 'Condition' x 'Compression' p = 0.001, 'Condition' x 'Compression' x 'Implant' p = 0.032). When compression was introduced, the amount of translation in the STAR ankles was significantly increased (fig. 76). There was also a significant difference found in the compressed case between the intact ankles and those with the STAR (fig. 75).

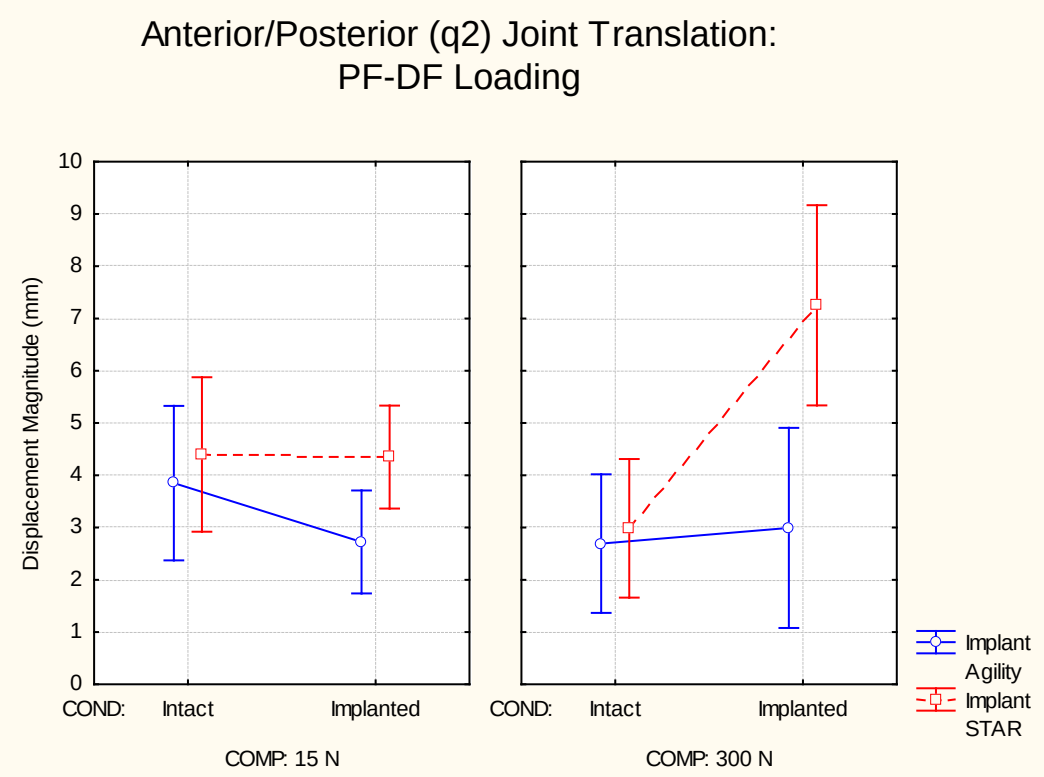

Figure 76: Translation of the JCS origin along the anterior/posterior axis due to PF-DF loading, showing the interaction of compression, condition, and implant type. Values shown are mean peak displacements in millimeters, and vertical bars denote 0.95 confidence intervals.

No significant differences were found in INV-EV loading (main effects: 'Implant' p = 0.637, 'Condition' p = 0.613, 'Compression' p = 0.768; interactions: 'Implant' x 'Condition' p = 0.075, 'Compression' x 'Implant' p = 0.712, 'Condition' x 'Compression' p = 0.108, 'Condition' x 'Compression' x 'Implant' p = 0.492).

In IR-ER loading, compression was found to significantly decrease the amount of A/P translation (fig. 77) (main effects: 'Implant' p = 0.420, 'Condition' p = 0.720, 'Compression' p = 0.032; interactions: 'Implant' x 'Condition' p = 0.799, 'Compression' x 'Implant' p = 0.143, 'Condition' x 'Compression' p = 0.439, 'Condition' x 'Compression' x 'Implant' p = 0.999). There were also significant post-hoc tests between the compressed and uncompressed tests for the left intact ankle and for the Agility.

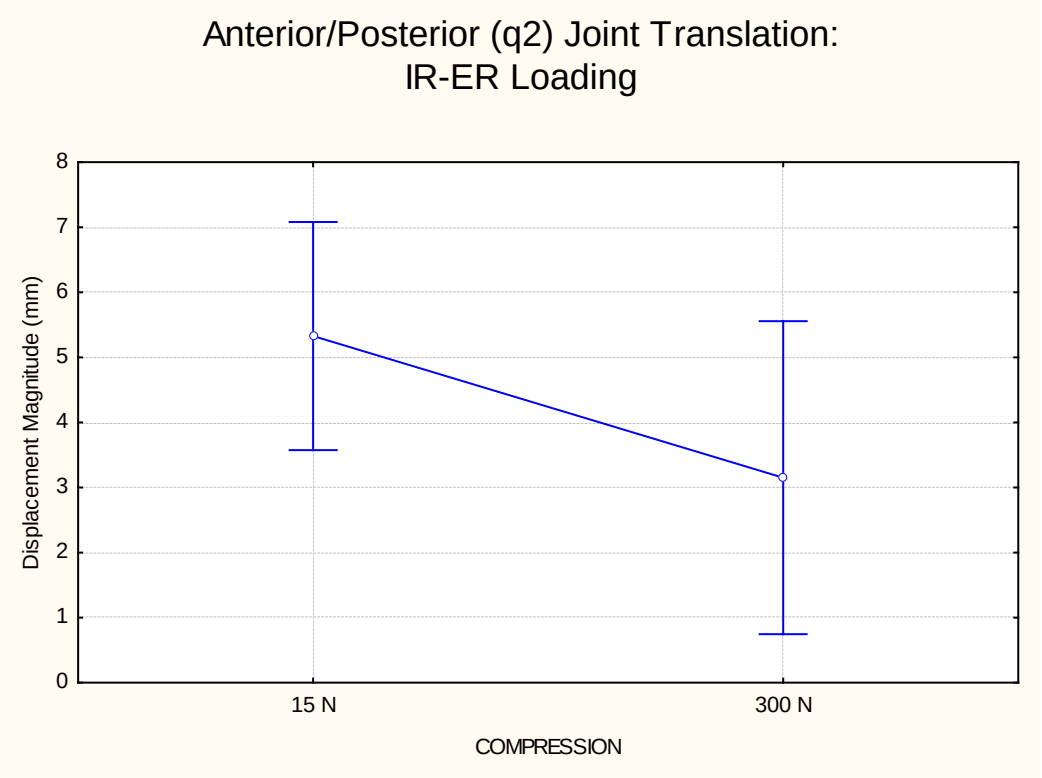

Figure 77: Translation of the JCS origin along the anterior/posterior axis due to IR-ER loading, showing the effect of compression. Values shown are mean peak displacements in millimeters, and vertical bars denote 0.95 confidence intervals.

Compression/Distraction Joint Translation

The compression/distraction translation of the foot was calculated as the joint centre's displacement along the C/D axis of the foot, denoted q_3 in the JCS. The most C/D translation occurred in PF-DF loading, and the least occurred in IR-ER loading (fig. 78).

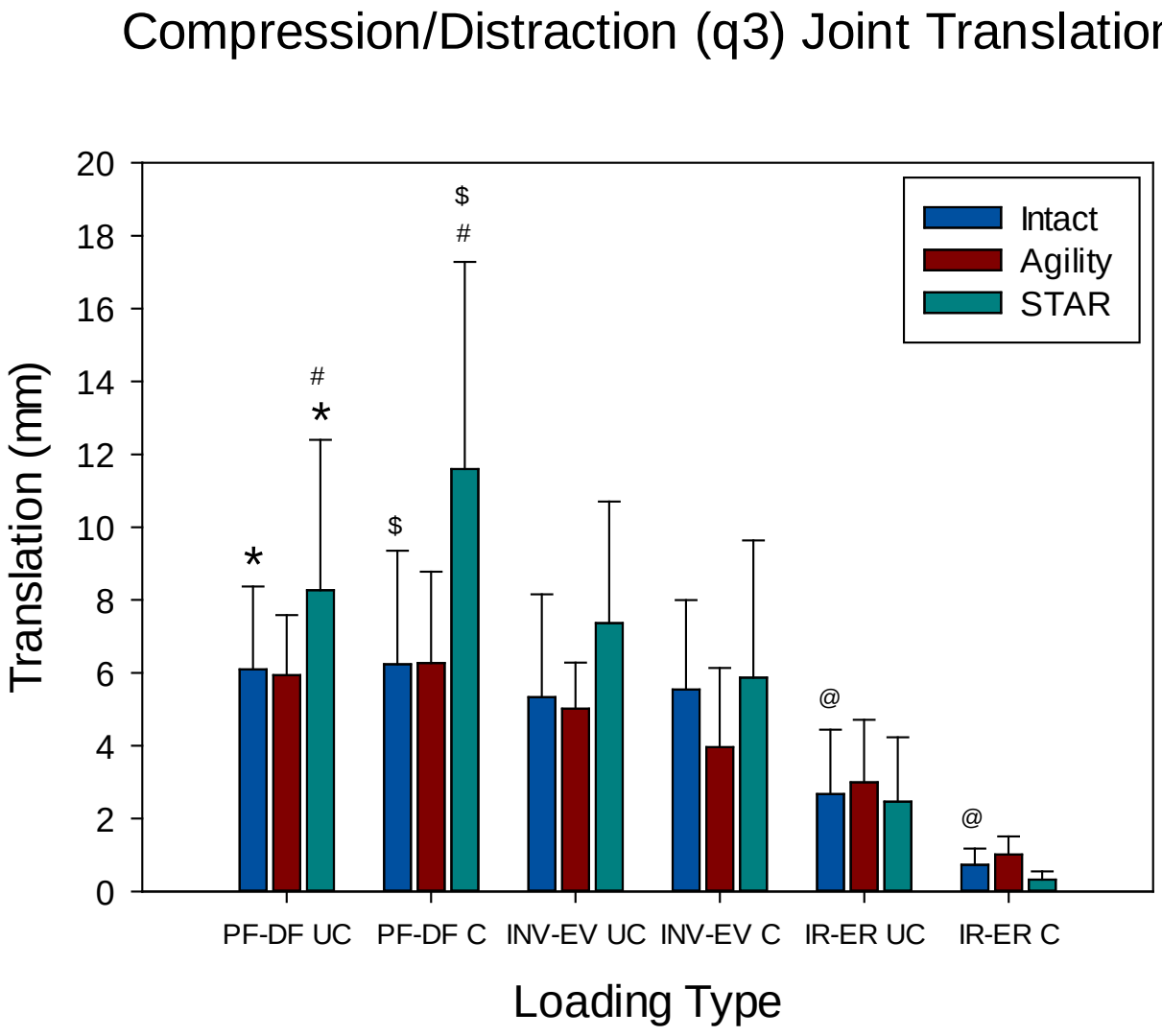

Figure 78: Mean translation of the JCS origin along the compression/distraction axis with error bars as one standard deviation. *p<0.001; #p<0.001; $p<0.001; @p=0.031 (L)

In PF-DF, the main effects of compression and implant type were significant, but there were also significant interactions found between condition and compression and between implant type, condition, and compression (fig. 79) (main effects: 'Implant' p = 0.459, 'Condition' p = 0.062, 'Compression' p = 0.023; interactions: 'Implant' x 'Condition' p = 0.016, 'Compression' x 'Implant' p = 0.096, 'Condition' x 'Compression' p = 0.001, 'Condition' x 'Compression' x 'Implant' p = 0.001). This is because compression was only significant in the ankles with the STAR. Post-hoc analysis revealed significant differences between the intact ankles and those implanted with the STAR for both uncompressed and compressed cases, as well as between the compressed and uncompressed tests of the STAR (fig. 78).

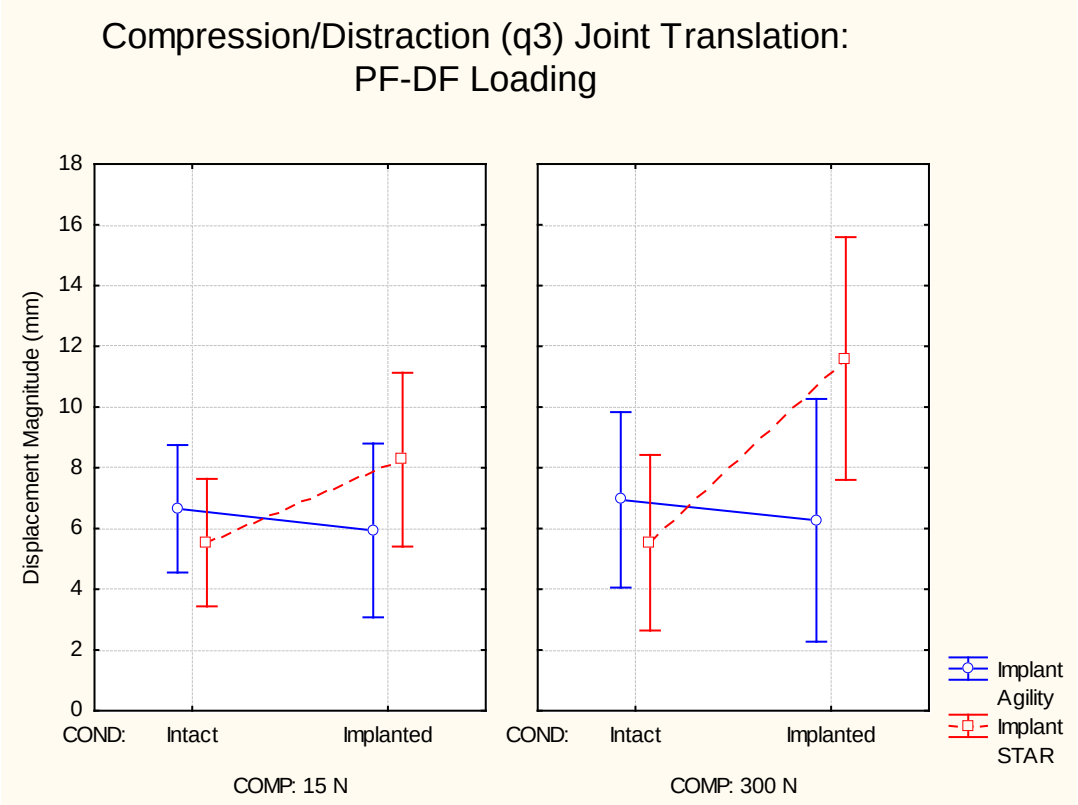

Figure 79: Translation of the JCS origin along the compression/distraction axis due to PF-DF loading, showing the interaction of compression, condition, and implant type. Values shown are mean peak displacements in millimeters, and vertical bars denote 0.95 confidence intervals.

In INV-EV, there was a significant effect of implant type (main effects: 'Implant' p = 0.644, 'Condition' p = 0.842, 'Compression' p = 0.477; interactions: 'Implant' x 'Condition' p = 0.020, 'Compression' x 'Implant' p = 0.987, 'Condition' x 'Compression' p = 0.282, 'Condition' x 'Compression' x 'Implant' p = 0.759). Implanting ankles with the Agility caused a decrease in C/D joint translation, whereas the STAR caused an increase (fig. 80).

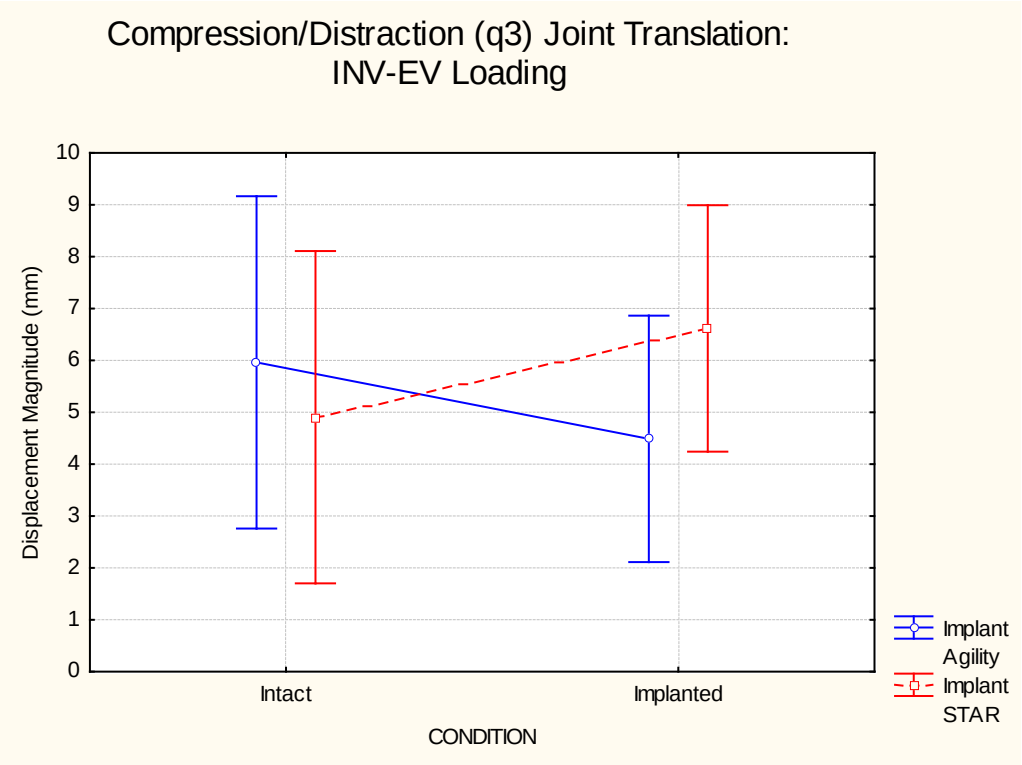

Figure 80: Translation of the JCS origin along the compression/distraction axis due to PF-DF loading, showing the interaction between condition and implant type. Values shown are mean peak displacements in millimeters, and vertical bars denote 0.95 confidence intervals.

During IR-ER loading, compression was found to decrease the joint translation in this direction (fig. 81) (main effects: 'Implant' p = 0.145, 'Condition' p = 0.990, 'Compression' p = 0.0001; interactions: 'Implant' x 'Condition' p = 0.815, 'Compression' x 'Implant' p = 0.453, 'Condition' x 'Compression' p = 0.863, 'Condition' x 'Compression' x 'Implant' p = 0.358).

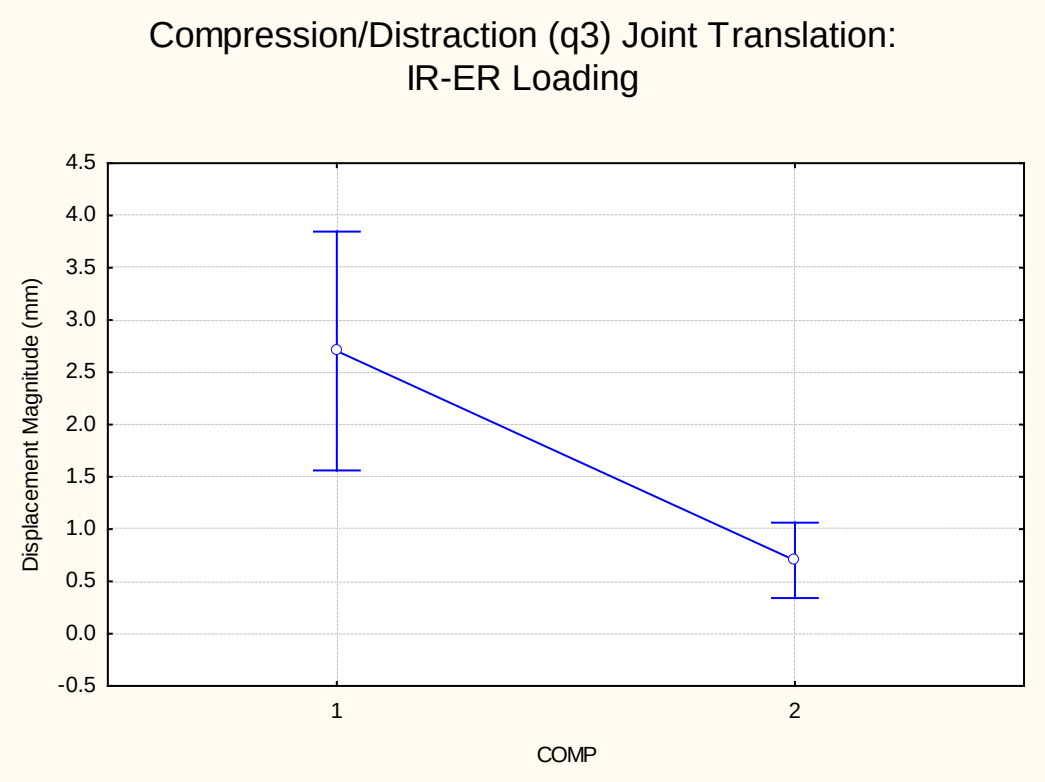

Figure 81: Translation of the JCS origin along the compression/distraction axis due to PF-DF loading, showing the compression. Values shown are mean peak displacements in millimeters, and vertical bars denote 0.95 confidence intervals.

4 DISCUSSION

Micromotion at the bone-implant interface of uncemented prostheses has been proven to be an important factor in osseointegration and overall implant fixation. To my knowledge, this is the first cadaveric experiment to analyze the micromotion patterns of total ankle replacements. It is important to know the micromotion behaviour of different TAAs in order to reduce the risk of aseptic loosening failure by enabling clinicians to make educated decisions on which designs to use along with improving the performance of new designs under development.

Along with implant osseointegration, reproduction of normal ankle kinematics is another important factor in the success of a joint replacement. Properly designed joint replacements will have articulating surface geometries that allow proper range of motion, motion coupling, and joint translation within the confines of the bony and ligamentous structure of the ankle joint.

This study found the Agility to exhibit patterns of larger micromotion than the STAR. Clinically, failure rates due to aseptic loosening are higher in the Agility (shown previously in tables 1 & 2), which corroborates this finding and supports the idea that larger motions at the bone-implant interface translate to weakened implant fixation. Several kinematic differences were found between the intact and implanted ankles indicating that there is room for improvement on the articulation geometry design for both of these models.

4.1 LOADING APPARATUS

The loading apparatus was designed with emphasis placed on maximizing the versatility of the testing rig in order to create a comprehensive loading protocol. As mentioned earlier, the device

used in this study was an adaptation of a loading apparatus previously developed in our lab by Chad Larson for studying the ankle, which was in turn an adaptation of one originally designed for applying loads to the human spine. This ankle loading apparatus proved to be a great method to apply pure moments to the foot while leaving the 5 remaining DOF unconstrained. However, it was believed to be important that micromotion patterns were studied with a compressive load applied to the ankle in this study. Consequently, modifications were made to his design to allow for compression to be applied via a steel cable tensioned by a hydraulic actuator.

It was imperative for this simulator to be able to induce a number of different types of loading scenarios for this project because there are a range of fundamentally different types of loading that an ankle will be subjected to *in vivo*. It has been shown in total hip and knee replacements that some loading types, associated with certain activities, induce greater amounts of micromotion and are more critical to determining the quality of implant fixation [114,126,127]. It is currently unknown which loading types are the most critical for ankle replacements or whether it is dependent on implant design, therefore, it was necessary to examine several different loading scenarios. Even though the ankle won't be subjected to all of these loads on a regular basis, the potential for these loading scenarios to occur is evident. Testing the micromotion magnitude at the extreme ranges of motion provides a measure of the 'worst case scenario'. Versatility of loading was gained at the expense of complexity and biofidelity of each specific test. Accuracy in reproducing the motions and loads of common specific tasks, such as gait, are important when determining long term effects because these are the loads experienced in a high frequency. Implementing these types of loading is more suitable for studying polyethylene wear, implant migration, and specific details about a certain task. Focusing on the specifics of a certain task wouldn't contribute significantly to the overall objective of determining the maximum micromotion magnitudes for each implant that could be expected clinically. The loading apparatus design we settled on was able to manipulate the ankle through its entire range of motion through a combination of rotations about 3 axes with and

without compression. At the level of the bone-implant surface, this would induce a wide spectrum of loads and give a well-rounded indication of the implant's overall initial fixation.

Another advantage to this design that complements its versatility was its simple setup. This quality enabled quick transition between the different tests being performed. Since there were 6 loading variations on a given testing day, being able to carry out the tests rapidly was important to minimize the amount of time that the cadaveric limbs remained thawed.

In this experiment, there were two preload conditions. A 15 N preload was used for the uncompressed loading scenario, while a 300 N preload was used for the compressed loading scenario. Two different preloads were used to determine if the addition of a compressive load had an effect on the micromotion and kinematic behaviour of ankles with different total ankle replacements. For the compressed case, 300 N was chosen because it represents roughly half of the body weight of an average person. Other studies that have performed biomechanical testing on cadaver ankles have also used this same preload [53,70], which makes using 300 N very desirable for the purposes of comparing results with these studies. This is much lower than the compressive forces the ankle experiences even in low intensity activity (walking is approximately 3-5 BW), but this load is justifiable because very minimal weight bearing is recommended in the first 2 weeks following surgery. Due to the nature of the loading apparatus, applying a much larger compressive load would create excessive shear stresses, artefact moments, and pose a risk of causing damage to the limb. The reason for using a 75 N compression for the INV-EV conditions instead of 300 N was that this loading puts the ankle in a compromised position which limits its ability to withstand compression and this posed a risk of damaging the limb. Additionally, the higher load wouldn't allow the ankle to follow the same kinematic pattern or experience its full range of motion because the larger load made the foot more susceptible to becoming locked in plantarflexion due to the moment artefact.

Compared to maximum plantarflexion moment of 232 Nm previously measured[56], the applied moment of 5 Nm in this direction is no comparison. This is because the 232 Nm was an active moment (applied by muscle activation), whereas the applied moments in this experiment were passive (applied externally). Since no muscle activation was simulated in this cadaveric test, the muscles and tendons were inconsequential, and the only structures resisting the applied moments were the bones, ligaments, and other soft tissues of the ankle. These structures' ability to resist moments is quite minimal in comparison, and damage to the limb would be inevitable if such large moments were applied to the joint. The benefit of applying pure moments in this manner is that it is much more repeatable and consistent across specimens. It allows us to know the exact loads that are being applied regardless of specimen anthropometry.

One drawback of modifying the spine machine for the loading apparatus was that it required the limb to be mounted upside down with the tibia fastened to the table. This means that the direction in which the force of gravity acted on the foot and implants was reversed. This could have had a minor effect on the kinematics of the foot as well as the micromotion of the implants in the uncompressed loading scenarios where there were no other vertical forces acting. For example, the Agility talar component lift-off that was observed during uncompressed PF-DF loading may not have occurred if the foot were oriented with the foot downward. If the foot was oriented right side up, the force of gravity likely would have kept the talar component in contact with the talus when compression on the anterior portion was decreased. Although less micromotion would have been observed in this loading scenario if no lift-off occurred, it is very unlikely that the decrease would be substantial enough to impact the overall outcome significantly.

The other consequence of this apparatus design was that it limited our options for how to apply the compressive load. The most feasible option for the compressive load application with this setup was using steel cable and a hydraulic actuator. If we break it down for simplicity, the cable

essentially acts on the footplate as two point loads of constant magnitude, one on either side. The line of force created by the tension in the cable is constantly changing direction as the foot rotates through its range of motion. If we examine motion in the sagittal plane, we know that the instantaneous flexion axis of a healthy ankle translates along an arc from a postero-inferior to an antero-superior position as the ankle goes from plantar-flexion to dorsiflexion (fig. 82) [21].

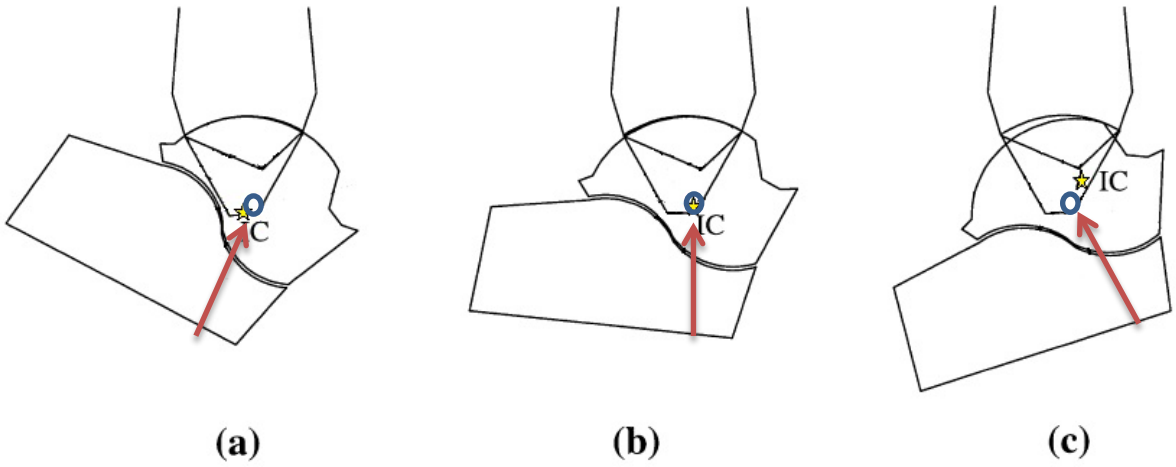

Figure 82: Locations of instantaneous center of rotation (IC denoted by yellow star) for the ankle in the sagittal plane with the location of cable guide (blue circle) and direction of compressive force (red arrow) at 23° plantarflexion (a), at 0° -neutral- (b), and at 25° dorsiflexion (c) as adapted from Leardini et al. 1999. Reprinted with permission from Elsevier via Copyright Clearance Center, Inc.

For ankles with arthroplasty, we can deduce where their axis of rotation will be based on the geometry of the implant. For the two implants under investigation, their flexion axes are coincident with the center of curvature of talar articulating surface. The Agility's flexion axis remains for the most part stationary because it is a 2-component/fixed-bearing design, whereas the STAR's flexion axis is mobile relative to the tibia, allowing it to translate in the A/P direction and rotate about the axis perpendicular to the plane of the tibial component (fig. 83).

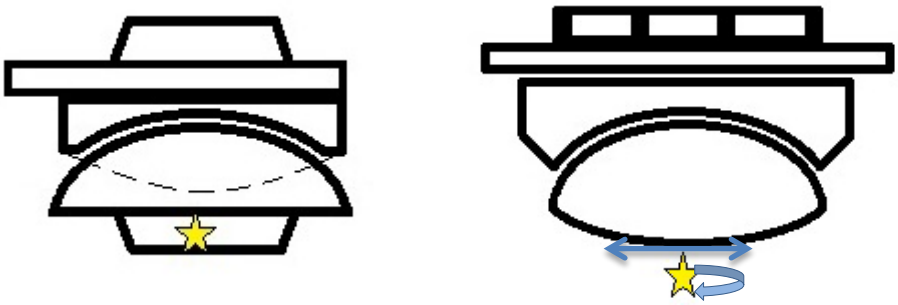

Figure 83: Sagittal plane schematic view of Agility (left) and STAR (right) with stars depicting the instantaneous center of rotation.

When the cable's line of force was not passing directly through the ankle's axis of rotation, the compression caused an undesirable additional moment about the ankle. In PF-DF loading, this artefact moment did not impede the loading apparatus from creating the desired kinematic pattern because it was directly counteracted by the applied moment, although it did affect the torque measurements obtained from the load cell governing the moment applicator. In INV-EV and IR-ER, however, this created some difficulties because there was nothing to resist the artefact moment, and the ankle could become locked in plantarflexion or dorsiflexion if the artefact moment exceeded a certain threshold. The cable guides were implemented to reduce this effect by decreasing the moment arm of the compression about the axis of rotation, which was investigated in detail by Cripton et al. for the spine [128]. As shown in figure 83, this loading setup was designed to stabilize the ankle, with the artefact moment rotating the ankle back to the neutral position.

For the range of motion (23° PF to 25° DF), the intact specimens were found to be 'stable' with minimal effects of the moment artefact. However, instances were encountered during testing where this was not the case. Because locating the flexion axis was done empirically, it was not possible to be entirely sure that the cable guides were at the ideal location. As such, at larger plantarflexion angles, such as those nearing its ROM limit, the effect of errors in the axis approximation was magnified. Additionally, the artefact moment was more problematic in the case of the STAR because the shear force, which was caused by the compressive load as the foot deviates from neutral

position, translated the foot in the A/P direction. As the foot translated, so did its flexion axis and the plantarflexing moment was increased. Because of these effects, extreme care was required to prevent it from locking in either DF or PF, and in some cases testing had to be restarted with further adjustments to the cable guide locations.

The effect that this compressive load had about the other axes was stabilizing instead, such that the further the foot rotated, the larger the moment caused by the compression was to return the foot back to neutral position. In INV-EV, the geometry of the loading device caused the moment arm of the steel cable to be slightly longer on the side opposite to the direction that it was rotating. This created a moment in the frontal plane that rotated the foot back to neutral position (fig. 84). In IR-ER, a stabilizing artefact moment was also created but by a different mechanism. As the foot rotated, the cable slots on either edge of the foot-plate translated away from the cable guide holes such that the tension in the cables had a component in the transverse plane perpendicular to the foot's IR-ER axis in the opposite direction to its rotation (fig. 85).

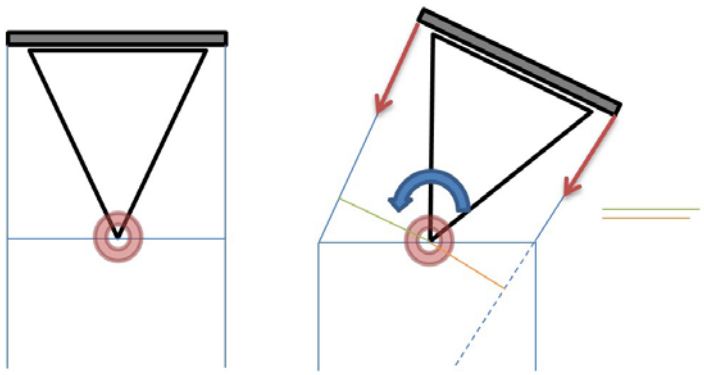

Figure 84: A schematic diagram of the loading apparatus in the frontal plane showing the lines of force for the steel cables (red arrows) and their moment arm lengths (orange/green lines) that illustrate the stabilizing artefact moment (blue arrow) about the ankle's INV-EV center of rotation.

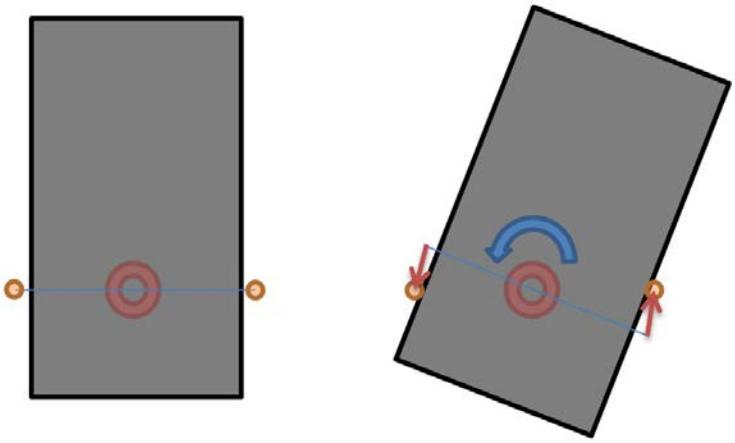

Figure 85: A schematic diagram of the loading apparatus in the transverse plane showing the projections of the cable tension (red arrows) directed from the cable slots toward the cable guide holes (orange circles) that illustrate the stabilizing artefact moment (blue arrow) about the ankle's IR-ER center of rotation.

The approach used in this experiment was an approximation of the loading and resulting motion seen in live patients. Applying compression and a pure moment to the foot is not equivalent to the compression and moment created by tendon tension; however, it was not the intention to simulate this but instead to subject the bone-implant interface to a range of stresses that it may experience *in vivo.* The fact that it was a cadaveric test reduced the inter-subject variations on loading patterns, and as in this particular study, reduced anatomical differences by comparing two implants on the left and right ankles of the same subject. Despite its limitations, it is valuable as a pre-clinical testing tool that offers a means of applying repeatable loading patterns in cadaveric ankles.

4.2 MICROMOTION-LOOSENING RELATION

The topic of micromotion between bones and implants has been studied extensively in regards to analyzing the bone-prosthesis interface and its initial fixation for both hip and knee replacements. Since the link between the amount of motion at this interface and the strength of the bone-implant

bond in uncemented implants had been established, numerous studies have been performed in order to reduce the relative motion and improve the bond in total hip and knee arthroplasty. As aseptic loosening continues to persist as the leading cause of revision surgery in total ankle arthroplasty, it is undeniable that the field would benefit from similar research.

The micromotion threshold for osseointegration originates from several studies concerning bone ingrowth in canines. As mentioned earlier, Pilliar et al. measured the amount of relative motion after the initial healing phase, and those without bone ingrowth allowed 150 μm or more [101]. Jasty et al. found that complete, partial, and no osseointegration occurred when implants were subjected to 20, 40, and 150 μm of constant oscillatory motion following implantation [103], and that full osseointegration occurred for implants exhibiting 56 μm of micromotion initially post-implantation [102]. A direct link cannot be drawn between these experimental outcomes and this study because they were performed on canines and they used slightly different measurement techniques. Due to the complex processes occurring within a live subject, we cannot suggest that initial post-op human cadaveric micromotion is equivalent either to a constant magnitude cyclic relative displacement or to the amount of recoverable displacement after complete integration. However, the measurement in the latter of Jasty's experiments is very similar to the measurement performed in the current study and others that look at the initial fixation of joint replacements. All of the dogs in his experiment had full osseointegration and the largest micromotion observed was 56 μm, which shows that this level of micromotion is tolerable but does not give an absolute cut-off value. With these findings and the results of initial fixation tests performed on hip/knee replacements, the threshold currently adopted by those in the field of total joint replacements is around 150 microns. Regardless of what is accepted, it remains that there is no maximum micromotion value that we can ascribe to an osseointegration threshold, but it can be stated for certain that lower micromotion magnitudes are favourable.

The amount of micromotion observed in this study was much larger than expected. There are currently no studies of micromotion in TAA prostheses in the literature to compare to, therefore, our only basis for comparison was contemporary hip and knee micromotion measurements. Hip and knee replacements typically exhibit micromotion magnitudes in the range of 100-200 μm when subjected to *in vivo* loading patterns [114,115,127]. Even the STAR, which had the lesser relative motion of the two implants, had a mean maximum micromotion magnitude of 789 μm. These results exceed the 150 μm threshold by a factor of greater than 5.

The micromotion values from these tests were expected to be larger than the 150 μm characteristic of hip and knee replacements for three reasons:

1) The aseptic loosening rates of these ankle replacements are higher than most hip/knee replacements;
2) The loading apparatus was designed to stress the bone-implant interface by pushing it to the limits of its ROM;
3) Relatively low compressive forces were applied.

However, the amount by which they exceeded this threshold was still surprising. It was found that even a modest 300 N compressive load had a significant effect on the micromotion magnitudes. *In vivo* loading applies much larger compressive loads to the ankle joint than this value, by a factor of 6 to 10 during level walking. At this point we are unsure of what effect such a large compressive load would have. Typically, larger loads are associated with larger bone-implant interface stresses, but it is possible that because the prostheses are designed with flat surfaces on both the tibia and talus, which are normal to compressive axial loads for the majority of activities, that increased compression would reduce motion due to increased friction.

Clinically, the failure rate due to aseptic loosening is 5.7% for the STAR and 7.1% for the Agility, which indicates more than 90% of them are not failing by this mechanism. Therefore, it is safe to

assume that clinically these implants are either experiencing more than 150 μm and still achieving osseointegration or not experiencing such large micromotions because the patient is careful and these tests are an overestimate of the actual *in vivo* micromotions. While this may seem to contradict the findings of Jasty et al., it is important to remember that the process of implant integration is time dependent and involves many complex biological factors that are not completely understood at this point. This implies that during the healing process, there are factors at work to reduce the amount of motion from what was observed during this experiment to a magnitude of relative motion below the threshold for continuous bone ingrowth. These factors could include inflammation to restrict range of motion, pain to discourage excessive use/weight-bearing, or intermediate ingrowth medium (such as fibrous tissue) or partial bone ingrowth to secure the implant.

Since the micromotion values found in this study were higher than the 150 μm threshold, it is impossible to draw a direct relationship between these two values. However, it was determined that the implant with greater relative bone-implant motion, the Agility, was also the implant with greater aseptic loosening rates. While it is possible that this correlation was coincidental, it is very unlikely that the two are not related due to the links previously confirmed between micromotion and bone ingrowth. Therefore, it is believed that higher aseptic loosening rates were attributable to a less secure initial fixation resulting in a larger magnitude of micromotion patterns. Consequently, the type of measurement obtained here was effective as a relative gauge to determining the implant's ability to accept bone ingrowth and produce a strong bond between the bone and implant.

4.3 SURGEON SKILL

There is a substantial learning curve for foot and ankle surgeons in performing total ankle replacements. It has been shown that surgeon experience with a given ankle replacement plays a large role in the perioperative complication rate [129]. Success rates reported by the inventors of these devices exceed those of other foot/ankle surgeons as we can see by comparing independent TAA survivorship studies with those of national joint registers. We can infer from these two facts, that surgeon skill would in all likelihood play a large role in affecting aseptic loosening rates. With this in mind, it is important for the surgeon(s) performing these to have similar skill/experience with each implant to provide a meaningful comparison. Fortunately, the foot and ankle surgeon collaborator on this project was quite familiar with and proficient in the techniques of both procedures, and he performed all surgeries himself to eliminate surgeon variance.

Surgeon skill was important in this study since the success of these procedures relies heavily on both the alignment of the implants and the precision of the cuts. The position of each component has 6 degrees of freedom, 3 rotational and 3 translational, and all 6 of both implant components must be properly aligned with respect to each other and the ankle in order for the joint replacement to function as designed [70]. Among many other things, misalignment will create abnormal ankle dynamics which can induce large stresses on the implant components or bone as well as at the bone-prosthesis interface leading to micromotion. Although these jigs eliminate a great deal of the variability in the alignment of the cuts, the surgeon's expertise is required to attach and align the jig with respect to the ankle and usually also the talar component with respect to the tibia. Surgeon skill is also important in making the cuts straight and flat. It may seem trivial because the jigs guide the saw blades, but in order to get a flat cut the surgeon often has to go in free hand afterwards because the blades are flexible and skive upwards toward the back. Because the

implants are manufactured with flat edges on their interfacial surfaces, the flatness of the cut is crucial to maximize surface contact area and ensure a tight and proper fit.

4.4 IMPLANT DESIGN CONSIDERATIONS

Stresses and strains at the bone-prosthesis interface will be largely determined by four separate factors. These include external loads, load transfer between the implants at the articulation surfaces, load transfer between the implants and bones, and the quality of the fit and finish of the implant's peripheral surfaces.

The first factor is the loading applied to the ankle joint. This is caused by the external loads on the foot and is affected by the activity being performed. While restrictions on activity levels and types of movements can be given to patients, the external loading conditions are for the most part uncontrollable and should be seen as a constraint rather than a variable.

The second factor is how the external load is transferred across the ankle joint between the implant components. This is governed by the implant articulation geometries, and the main differences between two- and three-component implants are evident in this area. In a two-component semi-constrained device such as the Agility, the two implant components are fixed in the A/P direction with respect to each and there are significantly more shear forces transferred between them as a result. In a mobile bearing prosthesis such as the STAR, the talar and tibial components can translate with respect to each other and the shear forces are instead resisted by the ligaments and other soft tissues of the ankle. Along with these differences, there are also less dramatic differences in load transfer that are affected by the component shapes. One issue of crucial importance is stress

concentration in the PE bearing because it has a relatively low yield stress. In order to reduce the stresses, avoiding delamination and excessive wear, the articulation surfaces must be designed to maximize contact area and minimize edge loading.

The third factor is the implant geometry at the bone interface, which plays a more direct role in the micromotion behaviour. The geometry of the implant surface in contact with the bone is a critical factor in determining its effectiveness at resisting interfacial motion. Ideally, the majority of the implant will experience compression over the range of activities. Compression is desirable because it will cause the implant to remain in close contact with the bone and increase the frictional force. Shear loading, on the other hand, is detrimental because it creates tensile strains that inhibit bone ingrowth into the implant. Different geometries can produce varying combinations of interfacial stresses depending on the external load being applied and how they are transferred across the joint. Given that the ankle will experience a range of external loading scenarios, the design must be effective at resisting forces and moments about each axis to varying degrees. This is quite evident when we compare the micromotion patterns of the different loading directions.

The fourth factor is the fit and finish of the implant into the bone. Greater friction between the prosthesis and bone will help prevent slipping between the two surfaces and resist the forces imposed by the implant loading. This can be affected by the implant surfaces, the surgical jig design, and surgeon experience/skill. There have been a number of different types of coatings used on implants to improve the bone ingrowth potential of an implant, including hydroxyapatite (and other calcium phosphates), cobalt chromium alloys, and titanium to name a few. Along with different coating materials, there are also a number of coating application techniques that result in varying pore sizes and shapes [130]. The Agility uses a sintered bead coating, and the STAR has a titanium plasma spray coating. The uncemented version of the STAR implant was originally designed with a single coating plasma spray, but clinical evidence suggests higher osseointegration

rates after the transition to a dual coating of titanium and calcium phosphate [8,37]. Both coatings have shown success in the past and since cadaveric studies cannot evaluate bone-ingrowth, they could not be compared in this study. However, the plasma spray approach seemed to have a greater surface roughness, which would be beneficial in increasing the friction factor. The jigging systems for each implant were of similar quality, being from the same generation, and each had their own shortcomings. Where the jigs left room for error, surgeon skill and experience with the procedure came into play to ensure proper implant fit and alignment.

The results of the tests performed in this study showed that the Agility had larger micromotion magnitudes than the STAR in both tibial and talar components. This suggests that one or more of the design differences between these two prostheses helps to reduce the tensile stresses and strains at the bone-implant interface. These implant designs differed in all three of the implant related factors previously mentioned, which makes it hard to determine the precise effects of each variable. I believe that differences in all three areas made partial contributions to this result. Because the STAR is an unconstrained 3-component prosthesis, the shear stresses transferred between the implants were reduced. The geometry of the interface favours the STAR implant's talar component because it has a larger surface contact area that is concave rather than flat, which increases the friction between the surfaces and provides greater resistance to motion in a wider range of loading scenarios. As for the tibial component geometry, the Agility's had a larger surface contact area and was better suited to resist A/P forces but required a large amount of bone resection, while the STAR's barrels provided good stability in all directions except A/P but were highly dependent on bone quality for fixation strength. Judging the overall fit by the amount of force required to remove the implants after testing, the STAR's talar component had a better fit, while the tibial components were fairly similar.

4.5 DIFFERENCES IN KINEMATIC BEHAVIOUR

Attempting to reproduce the kinematic behaviour of normal ankles in a prosthetic device is important in order to restore the patient's normal motion and reduce the cascading effect that small changes can have on the body. It is also important because the ankle and all of the structures around it (especially ligaments) have been optimized for its function from many decades of remodelling. By replicating its normal patterns, the stresses in these structures, and consequently the prosthesis, are able to be minimized. The kinematic parameters examined in this study were range of motion (ROM), motion coupling (MC), and joint translation (JT). Despite the challenges posed by a large variance between specimens and a low sample size (N = 6), it was possible to tease out some significant differences between the intact ankles and ones that were replaced with the Agility and STAR prostheses.

4.5.1 *RANGE OF MOTION*

At the talocrural joint, the primary motion occurring is ankle flexion (PF-DF) or rotation in the sagittal plane. Because of this, it would be expected that the main differences in ROM between implants would be found about this axis. Despite being able to determine the PF-DF ROM limits with reasonable accuracy through other means, the test setup did not allow for the application of applied moment limits to implanted specimens. Therefore, this aspect of the kinematic analysis could not be included in this study. However, complete analysis of the INV-EV and IR-ER ROM was able to be performed.

Slight changes were observed between the mean INV-EV and IR-ER ROM values of the intact and replaced joints, but they were found to be well within the range of values expected from random variation within the sample population. Although testing a larger sample size might reveal data that

proves otherwise, the absence of detectable differences implies that these joint replacements don't hinder the function of the ankle substantially by either restricting its motion or making it unstable.

It cannot be concluded for certain that there was no difference between the STAR and intact ROM, but it can still point toward some interesting implications. Considering the architecture of the STAR in the frontal and transverse planes, it is apparent that this prosthesis does not allow any INV-EV motion, and it does not provide any resistance to IR-ER motion. This reinforces the fact that the majority of INV-EV motion occurs in the subtalar and transverse tarsal joints and not in the talocrural joint. Concerning IR-ER rotation, it tells us the bony geometry of the talocrural joint plays only a small role in restricting this motion and instead this responsibility lies with the soft tissues of the ankle.

Compared to the ranges of motion determined by Valderrabano et al. (fig. 86), the range of values found in this study (see table 6) were not surprising. The ROM in INV-EV found in this study was slightly higher, but this is to be expected because compression was found to significantly decrease total ROM and the applied axial compressions (15 N and 75 N) were lower than the 200 N used in their study. The amount of ROM in the IR-ER direction was also in agreement since the ROM for the uncompressed and compressed tests in this study encompassed the values found by Valderrabano in accordance with the applied compression (15

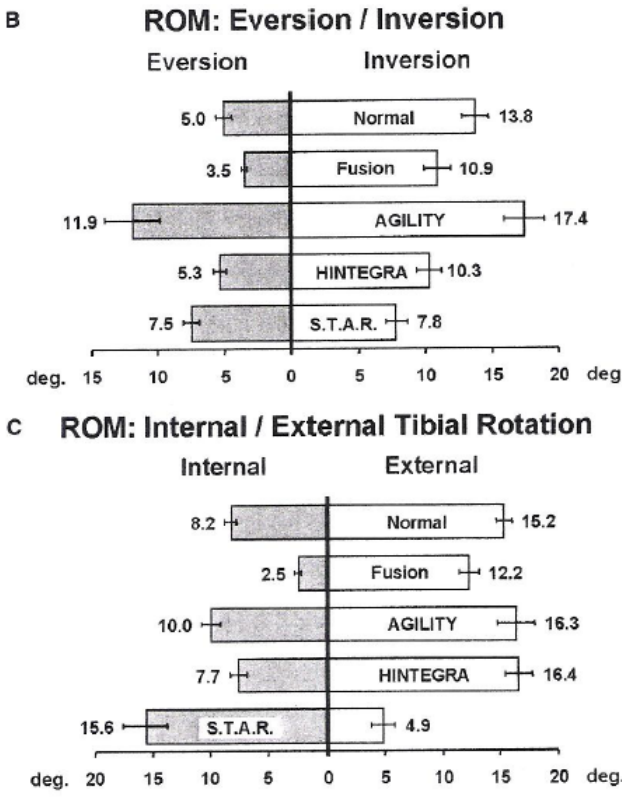

Figure 86: ROM in INV-EV (top) and tibial IR-ER (bottom) due to 100 Nm static applied torque with 200 N of axial compression from Valderrabano et al. 2003 pt. 1. Copyright © 2012 by the American Orthopaedic Foot and Ankle Society, Inc., originally published in Foot & Ankle International, 24(12):881-886 and reproduced here with permission.

< 200 < 300 N). The effects that the Agility and STAR had in comparison to the intact ankle, despite being insignificant, were in agreement with these previous observations in all but one case. Replacement of the ankle with an Agility prosthesis caused increases in ROM for both INV-EV and IR-ER, and replacement with the STAR caused a decrease in ROM for IR-ER. The disagreement occurred in INV-EV for the STAR, and it was found to cause an increase in ROM for this study in contradiction to the observation of a decrease by them. Some differences here can be accounted for with the different coordinate frame definitions, since we used a JCS based off anatomical landmarks but they used orthogonal axes coincident with the applied moments.

Valderrabano et al. also found that use of the STAR was accompanied by a shift toward ER (or internal tibial rotation), which was the opposite of what was observed in the compressed IR-ER test of this study (fig. 52). However, this effect can be convoluted by differences in the definition of neutral position. Because only the PF-DF axis was constrained during the initial static shot, the INV-EV and IR-ER axes were left to align to the most stable position rather than aligning to the same neutral position as the intact case.

4.5.2 *COUPLED MOTION*

The motion coupling ratios were smallest when the ankle was loaded in PF-DF. This result makes sense because the PF-DF has the largest ROM, which created a large denominator in the coupling ratio. Despite this, the magnitude of coupled motion was also the least in PF-DF, which tells us that motion coupling to the flexion axis is generally the weakest. The coupling of INV-EV to IR-ER and vice versa was considerably stronger. The results of the study by Valderrabano et al. agree with these findings [52]. Although, they didn't look at PF-DF coupling to other directions, the results presented here show that PF-DF had a stronger coupling relationship to INV-EV and IR-ER loading than in the reverse direction. This can be explained by the fact that maximum inversion and

internal rotation occur in supination, and maximum eversion and external rotation occur in pronation, whereas maximum PF/DF occurs independently of these motions.

Only two studies have been performed that have examined the phenomenon of motion coupling in total ankle replacements that provide a basis for comparison. The one by Michelson et al. only reported IR-ER motion coupled to PF-DF loading, which applied manual angular rotation to the PF-DF axis with the other axes unconstrained while under a 300 N axial load with the foot upside-down [53]. The one by Valderrabano et al. looked at the INV-EV and IR-ER coupled to PF-DF and INV-EV coupled to IR-ER and vice versa, which manually applied rotation about each of the three axes with the others unconstrained under a 200 N axial compression with the foot right side up [52].

The coupling patterns differed slightly, with the Agility matching the intact motion better in some instances and the STAR matching it better in others. The consequence of the exact motion patterns is unknown, but it is assumed that the closer a TAA design matches the intact ankle the better. In this respect, neither implant proved to be convincingly superior over the other.

In PF-DF, the amount of IR-ER motion coupling for the intact ankle in the current study (MC ratio = 0.136 ± 0.065) agreed quite well with the findings of Michelson et al. (MC ratio ≈ 0.13), but Valderrabano et al. found a smaller amount of coupling (MC ratio ≈ 0.08). This makes sense because the testing methodologies of this study and that of Michelson et al. were quite similar. However, when looking at unconstrained TARs (STAR in this and Valderrabano's study and the Irvine Ankle Arthroplasty in Michelson's study), the results of these two studies were closer to each other (MC ratio ≈ 0.04) than they were to the results of the current study (MC ratio = 0.147 ± 0.101). The explanation for the disagreement between the coupling found here and in Michelson's study could be due to the different TAR design examined.

Comparing the other three coupling patterns (PF-DF→INV-EV, INV-EV→IR-ER, and IR-ER→INV-EV) to those found by Valderrabano, a consistent trend of larger coupling ratios in the current study emerges across all ankle conditions. This difference is likely due to differences between the loading apparatuses. The presence of friction within Valderrabano's loading device could prevent some motion in the secondary axes. The orientation of the foot may also have a small effect on the ankle motion because the forces of gravity would interact with the foot in different ways.

If we look at the relative differences between the intact and implanted ankles, there is some agreement and some disagreement. The motion coupling ratio for INV-EV due to PF-DF was lowest in the Agility for both studies, but the STAR had a higher mean ratio than the intact ankle in this study. The IR-ER motion caused by INV-EV was highest in the intact ankles and lowest in the ankles with the STAR, which agreed with the prior results. There was little difference in INV-EV caused by IR-ER between implants in compressed loading, but the uncompressed loading found the intact to be highest, followed by the Agility and the STAR in agreement with Valderrabano.

4.5.3 *Joint Origin Translation*

Joint translation in the M/L direction was the largest when the applied moment was about the INV-EV axis. This makes sense because mediolateral direction is approximately parallel to the plane of induced rotation. The STAR caused a slightly larger increase in M/L motion than the Agility, but the difference was not significant. This result also makes sense because the talus is free to slide in the M/L direction with respect to the tibia in both implants, but it is slightly less constrained in the STAR. When loaded about the PF-DF axis, compression was found to increase the amount of M/L translation in the intact ankles but not the implanted ones, and it increased from a magnitude which wasn't significantly different from the implanted ankles to one that was larger.

The main effects in A/P translation were those of compression in PF-DF and IR-ER loading, both of which are easily explained. When the ankle dorsiflexes and plantarflexes, a proportion of the applied compressive load acts as a shear force in the A/P direction instead of in axial compression because of the design of the loading apparatus. Because the talar component is free to translate in the A/P direction with respect to the tibia in the STAR, it is expected that increased joint laxity in this direction would be present, and this was confirmed by Watanabe et al. [71]. The decrease in translation due to compression in IR-ER loading was likely due to the significant decrease in ROM (decrease of approximately 69% averaged across all ankle conditions).

Similarly to A/P translation, the STAR produced an increase in C/D translation in PF-DF and compression caused a decrease for all conditions in IR-ER. One might intuitively think that there should be very little C/D translation occurring in TARs because the materials are not very compliant compared to cartilage, and the compressive load applied is relatively low. However, the C/D axis is fixed to the calcaneus and as such is not always oriented parallel to the long axis of the tibia. This provides a logical explanation for the correlation with the A/P translation in PF-DF, since the A/P translation with respect to the tibia can be decomposed to components in both C/D and A/P directions in the calcaneus reference frame. The compression effect in IR-ER loading is also likely due to the large decrease in IR-ER ROM from compression.

No other studies have examined this exact quantity, so there is no ideal reference material to compare to. The third part of Valderrabano's study reported mediolateral talar translation during PF-DF [18], which isn't directly comparable to the M/L translation reported in this study, but it is worth discussing. They found that the intact ankles and the ones with the STAR had similar magnitudes at around 5 mm, but the ankles replaced with the Agility had much less translation at closer to 1.5 mm. The translation magnitudes were close to the average values found in the present investigation, but a large decrease in M/L translation was not observed in the Agility. Reasons for

the disparity are not likely due to the different M/L translation definition, but could be due to differences in the loading mechanism.

4.6 Motion Dependence on Loading Direction

The motion patterns of the implants with respect to the bone were quite dependent on the loading direction. This was expected because applying moments about different axes will in turn transfer different loads to the implants. This illustrates the need to apply a number of different loading conditions to the ankle joint in order to obtain a representative sample of micromotion. This idea is also backed up by results from the FEA simulations by Chong et al. [114] where a number of different activities were approximated by the applied loading conditions and found considerably different relative displacements along the surface of the implant. Depending on how the implant interface geometry is designed, one type of loading or another may create more micromotion.

The tibial component would be expected to show less micromotion than the talar component because it has a larger contact area and is supported on the medial and lateral sides in addition to the flat, finned surface. It would be expected to show the most motion when loaded in PF-DF based on increased A/P shear force because it is semi-constrained and the loading device induces shear loading in PF-DF. Because of the orientation of the fin, one would expect the Agility's talar component to be more prone to motion when loaded about the PF-DF and INV-EV axes than the IR-ER axis. In PF-DF, it would be susceptible to A/P sliding along the talar fin groove. When loaded in INV-EV, the implant would be expected to rocker about the fin's long axis.

The tibial component of the STAR would be expected to show very low levels of micromotion because the bearing is not constrained to it and therefore the only forces transferred to the implant are compressive forces normal to the implant and shear forces from due to friction. The A/P direction would be most susceptible to motion since it is parallel to the barrel orientation, hence PF-DF loading would be expected to show the highest micromotion. One might expect even lower levels of micromotion for IR-ER loading because there are no rotational constraints on the bearing in that direction, resulting in minimal force transfer. For the talar component, we would expect much higher interfacial strains in PF-DF and INV-EV. PF-DF would have larger micromotion because the majority of force is being directed parallel to its stability fin. Larger motions would be expected in INV-EV because rotation in frontal plane is constrained by the device geometry. The loading would induce a large stresses in the edge of the PE causing the implant to rocker about this axis.

These predictions based on geometry were quite accurate for the most part. The differences found in the micromotion between loading directions for the Agility's tibial component was quite minimal, but it did have less motion than the talar component as expected. The micromotion at its talar component agreed with the theoretical predictions as well, showing the smallest micromotion magnitudes in the IR-ER loading direction. The PF-DF direction had more micromotion than the INV-EV direction, which was not necessarily expected, and this was attributable to the large motions observed during component lift-off during the uncompressed loading. During compressed loading where no lift-off occurred, the talar component had comparable micromotion magnitudes in both PF-DF and INV-EV, which were still higher than IR-ER. For the STAR's tibial component, the most amount of micromotion occurred during PF-DF loading in accordance with expectation, especially when loaded with compression since it increases the friction force between the bearing and tibial component and hence the A/P shear force. The talar component's micromotion also lived up to the expectation, since it exhibited larger magnitudes in PF-DF and INV-EV than IR-ER.

4.7 LARGE INTER-SPECIMEN VARIANCE

It is normally expected that there will be noticeable differences between the kinematic behaviour of different specimens, especially when they are from people of varying body types and sizes. It is also expected that there would be quite significant changes to the kinematics of an ankle that has had any operation performed on it, especially a total joint replacement. It was surprising to find that the variation in the kinematic parameters measured (ROM, MC, and JT) was sometimes larger between specimens (even different limbs from the same donor) than the changes caused by replacing the joint. Typically, there were more similarities between an intact limb and the same limb with a joint replacement than there were between two intact ankles or two ankles with the same implant.

Large inter-specimen variance made it difficult to find significant differences in the kinematic parameters between the STAR and Agility. However, taking advantage of the paired analysis between the intact and implanted conditions of the same ankle enabled us to find some significant changes. In order to extract differences between the implants, a larger sample size would be required or implanting the same ankle with two different implants sequentially to allow for a paired analysis between the implants as well.

4.8 OPTOTRAK MEASUREMENTS

To my knowledge, no other studies have been performed that measure implant micromotion for total ankle replacements. As such, a discussion of measurement device options in light of the unique challenges of this joint is necessary to understand the trade-offs being made. Doing this type of analysis on a cadaveric ankle joint has some unique challenges that aren't present in the hip or

knee; hence, techniques utilized in these studies were not necessarily transferrable. The measurement methods that were considered included: linear variable differential transformer (LVDT) arrays, extensometers, radiostereometric analysis (RSA), and optoelectronic.

LVDT arrays have great accuracy (2 μm – mean error 1.6μm [108]) but can only measure relative movement and would not be useful to analyze the kinematics of the ankle. Even if we weren't concerned about the kinematics, these arrays are very heavy, bulky, and would not fit in the small confines of the ankle joint without restricting its motion. Similarly to LVDTs, extensometers have very high accuracy but are only capable of measuring linear relative displacements. Systems of extensometers have not been created that can measure 3-dimensional motions to my knowledge. Additionally, they require a relatively large amount of space.

The accuracy of RSA is lower than the previously mentioned measurement option (under optimal conditions can be as low as 6μm [131], but typically on the order of 20μm), but it comes with considerable advantages in other areas. It doesn't require any massive devices to be physically attached to what is being measured. At most it would require tantalum beads or some other type of small fiducial to be inserted into the bones and implants. Because it uses x-rays, tissues obstructing the view would not be a concern, and reattaching the anterior capsule would be possible; however, obstruction of the x-rays by the footplate and mounting jig would be an issue when setting up the system if they weren't constructed with radiolucent materials.

RSA has been used for migration and micromotion measurements for joint replacements numerous times in the past and has proven to be effective. For this particular application RSA was the only option other than optoelectronic measurements that could reliably measure the relative motion of both tibial and talar implant components as well as the 3d tibiocalcaneal kinematics. The major drawbacks of RSA are that it is quite complex to set up including fiducial bead insertion and their arrangement, it requires a large amount of radiation which limits the ability to monitor visually

from up close, and data analysis is quite complex. Therefore, this method was the runner-up to optoelectronic measurement.

There are a number of different optoelectronic measurement methods, including both custom made and commercially available systems. A custom CCD camera measurement system has been used for micromotion measurement of radial head arthroplasty implants and was capable of just slightly lower accuracy/resolution than the LVDT at 7 μm [105]. However, this custom measurement setup is specifically useful for relative displacement measurements with respect to a relatively stationary reference, but the talus and talar component would be moving a substantial amount. Its effectiveness at measuring 3-dimensional kinematics and relative displacements between two objects moving relatively large amounts is unverified. It is also unlikely that a camera could be positioned in such a way that the target area would be optimally located and visible throughout the various motions of the ankle. On the other hand, commercially available optoelectronic systems are capable of measuring 3-dimensional motion.

The method of measurement chosen to track the motion of the individual bones and implant components was optoelectronic, and more specifically the Optotrak Certus. This method of measurement was desirable because it was minimally invasive and was feasible to implement within the confines of the ankle joint. It required only K-wire pins extending out from the bones and similar extensions from the implants. This permitted full range of motion in all directions with a few exceptions limiting the dorsiflexion of implanted ankles. It did require considerable effort in the strategic placement and adjustment of markers to ensure each was free from obstructions and optimally located throughout the entire range of motion for all three axes. Another benefit of using this method was that data collection issues would be minimized because previous work with this equipment meant that data acquisition systems and programs were already set up and debugged.

While convenient from the initial setup and data collection point of view, this approach did have its limitations.

Optoelectronic methods are typically considered to be too inaccurate for micromotion measurement and thus have not been used for this application. Since the equipment was readily available, it was worth investigating as a possible option nonetheless. The technical specifications of the Optotrak Certus state that it has a 3-D spatial accuracy of 0.1 mm with a resolution of 0.01mm, which would not be accurate enough for micromotion measurements since they are typically less than 0.2mm. However, this claim is too modest. The accuracy validation test performed on our particular Optotrak Certus system (Appendix F) showed that for the ranges of measurements performed in this experiment, the accuracy was better than 10μm with a resolution of around 5μm. Another accuracy test that mimicked the relative displacement measurements came up with an average error of around 30μm. Pilot testing confirmed this level of accuracy to be sufficient for discerning differences between the micromotion patterns of different implants.

The challenge of ensuring that all markers remained unobstructed required some of the marker sets to be projected out a significant distance away from the bone or implant to which they were attached. The increased marker attachment length had two negative consequences: increased susceptibility to vibrational noise and larger loads/moments exerted by the marker on their target.

4.9 LIMITATIONS

4.9.1 *PF-DF ANGULAR LIMITS*

It was discovered that while testing the implanted ankles in the PF-DF direction with torque limits that the range of motion in plantar-flexion became exceedingly high. The ROM was so far beyond the normal range that the polyethylene insert in the STAR was getting dislocated. Even though the anterior capsule of the ankle doesn't govern the kinematics and guide the ankle to the same degree as the ligaments, it still plays a major role in controlling its range of motion limit in plantar-flexion. The anterior capsule could not be sewn back up because Optotrak measurements were dependent on the components being exposed. Therefore, angular displacement limits were imposed on the implanted PF-DF tests instead of torque limits. These limits were determined by considering their range of motion in the intact PF-DF test as well as other limits imposed by the particular case, such as marker attachment interference, bearing liftoff, etc. This unfortunately restricted us from being able to take any range of motion measurements for the implants in PF-DF. Angular limits were also used on one specimen in INV-EV because the ankle turned out to be slightly unstable with excess ligament laxity on the lateral side.

4.9.2 *FOOT ALIGNMENT*

The main challenge accompanying potting the proximal tibia/fibula in dental stone was the alignment of the limb within the mounting rig. The goal was to have the foot plate aligned square with the mounting rig while the foot is in its neutral position (the natural pose of the foot while standing). This would entail having the long axis of the tibia normal to the plane of the ground, with the long axis of the foot (posterior most point of the calcaneus along the second metatarsal) normal to the frontal plane of the mounting jig, and the foot plate parallel to the ground. Obtaining this

ideal alignment is quite difficult because the definition of tibial long axis and frontal plane depend on landmarks on the proximal tibia (which was unavailable), but it is not technically necessary. However, it is necessary for the alignment technique to be consistent for proper inter-specimen kinematics comparisons. The most important axis to keep consistent is the flexion axis because neutral position, as defined by the static shot during test setup, was when the foot plate was level to the ground about the flexion axis. The other axes were close to level because of how the limb was potted; however, they were not constrained by the torque applicator like the flexion axis and thus would fall into the foot's natural alignment as a self-correcting mechanism. The neutral orientation of the foot about the flexion axis could not be obtained in a similar manner because the foot would naturally fall into dorsiflexion because of the weight distribution of the foot. Therefore, slight deviations in the alignment of the tibia about the flexion axis within the potting would reproduce that same deviation in PF-DF angle measurements.

The rotational alignment is the most difficult and critical component, but the translational placement also has some requirements. Axially, we need the bone to be submerged deep enough to ensure the dental stone would create a strong, rigid bond to the bone. In the transverse plane, the most important consideration is that the two malleoli were somewhat centered between the cable guide posts in the A/P direction to allow for proper configuration of the cable guides to coincide with the flexion axis. Also, the ankle had to be positioned within the confines of the posts in the M/L direction to ensure clearance for the foot.

4.9.3 *Pure Moment Assumption*

The torque applicator was verified to produce an isolated moment about the specified axis with negligible forces and moments about the other axes for a range of motion of the spine when set up with proper counter-balances. The magnitude of the off-axis moments increased with the amount of

angular displacement deviating from the initial position. For small angles such as those seen in a single functional spinal unit, which is what it was designed for, this is a great approximation. However, the ankle has a much larger range of motion (over 80° of total motion in one specific case of PF-DF), and while the off-axis moments are still very small with respect to the applied moment, their precise magnitude was not measured.

4.9.4 *SAMPLE SIZE*

The number of limb pairs tested and compared was only 6, which is quite low but typical in cadaveric testing. In many cases the low sample size does not hinder the effectiveness of these tests because the differences observed for a given treatment are very large in comparison to the standard deviation within a group. However, the low sample size does limit the power of the study and the ability to detect small differences. In the present study, several comparisons were found to have low p values that were not below 0.05. This shows that there could possibly be a relation between these, but that it is still within possibility that the difference could just be due to random variation. If a larger number of specimens were tested, we would probably find that these relations with a low p value are indeed significant.

4.10 FUTURE WORK

4.10.1 *MICROMOTION*

Since this is the first micromotion study for total ankle replacements, there is a lot of room to build on and expand this body of research. For this specific comparison of implants, it would be useful to test a larger sample size in order to support these findings and tease out some of the relations that were nearly found to be significant. It would also be of benefit to the TAA community to know where other implants on the market stand in this area. With a more comprehensive catalogue of the micromotion characteristics of each implant, it would be possible to determine which implants will provide the highest probability of complete osseointegration and to infer which design components and geometries contribute to creating strong initial fixation.

The testing methodology has room for improvements to be made as implied previously. While the accuracy of the Optotrak was sufficient to compare the micromotion of these two implants, it may not be capable of discerning differences in other implants with lower micromotion magnitudes. The objective of this research is to reduce the micromotion and achieve higher long-term success rates, comparable to hip/knee arthroplasty. Consequently, we expect that eventually the micromotion magnitudes will be reduced to comparable levels as well (lower than 200μm), and the differences to be found between implants will be too small for the Optotrak to accurately detect. As mentioned earlier, RSA is a very promising alternative measurement method because it offers better accuracy with proven efficacy in micromotion measurement [117] and is even less intrusive, and it has been used in dynamic applications [132] but not yet verified in total joint replacements.

The loading profiles chosen for this experiment were intentionally very general and not necessarily representative of any specific tasks. Loading versatility was desirable in this specific application, but it can also be of interest to determine more detailed information about the micromotion

patterns for specific activities. The applied loads could be refined to closer replicate precise loading patterns and include fluctuations in compression and varying angular velocities over the course of the loading. One might be interested in the gait because it is a very repetitive motion that all patients will be performing, or one might be interested in determining which activities the patient should not take part in during this initial healing phase. A more complex loading simulator must be used to carry out experiments for this purpose, such as gait simulators with muscle actuation [54,61].

In vivo analysis can also be useful for analyzing specific tasks with a greater degree of biofidelity. Doing in vivo tests would limit the measurement method to RSA and require the prosthesis in question to be approved to clinical testing at a minimum. In vivo testing wouldn't be as effective for comparing between implant types because patient variability would come in to play and it would be very difficult to control for applied loading. However, it would be quite effective at comparing within patient activities.

Another possible avenue of work in this area would be to refine the testing protocol to a format that is practical for standardized testing. All new implant designs must satisfy certain requirements before they can be approved for clinical testing, and ideally this would include a micromotion analysis to ensure adequate initial fixation. It would likely be much further into the future, but if we can establish the importance of a test like this in reducing the risk of aseptic loosening failure, it would be required to create a testing protocol that would be appropriate for all implant testing at a national level.

4.10.2 *KINEMATICS*

In this particular study where we were analyzing micromotion and kinematics with the same measurement system, our investigation of kinematics was incomplete because of the limitations imposed by having to measure the implant motion. Switching the motion measurement system to RSA would eliminate these limitations and allow a complete kinematic analysis. However, this is only an improvement if both need to be measured simultaneously.

In order to properly compare kinematic differences between implants and specimens for the compressed configurations, modifications need to be made to the compressive load application. Either a more accurate and repeatable way of setting the cable guides to the joint axis of rotation needs to be established, or a different method of applying the compressive load that doesn't influence the kinematic behaviour as strongly needs to be used. Otherwise, analyzing the compressed kinematic patterns will be pointless because one would not be able to distinguish between differences caused by variables of interest and those cause by loading variations.

Another interesting and possibly more relevant kinematic analysis would be one comparing different joint replacements in gait simulation. An experiment along these lines would give us an idea of how different ankle replacements affect the ankle kinematics in a more practical setting with better transference into real world application.

4.11 CONTRIBUTIONS

This is the first study to date that has analyzed the relative bone-implant motion for TAA. An effective testing methodology has been developed for this end, providing future researchers with detailed information on this procedure and several considerations for future work and improvements to this technique.

The micromotion data from this experiment provides evidence supporting the hypothesis that higher initial post-operative micromotion magnitudes correlate with higher aseptic loosening rates. The implications of this are:

1. We need to know the initial fixation micromotion magnitudes for all implants on the market. Use ones with lower values to reduce probability of aseptic loosening failure.
2. Shows the importance of micromotion metric in predicting aseptic loosening. We should be testing for micromotion magnitudes post implantation in pre-clinical analysis to determine relative loosening risks and design/modify devices with features to minimize this value.

This also shows that the initial fixation of these two devices is insufficient to facilitate proper osseointegration even when subjected loads much lower than experienced *in vivo*. This emphasizes the need to eliminate all unnecessary weight bearing and loading within the first few weeks to enable continuous bone ingrowth to occur and fortify the bone-implant bond before using it.

While kinematic analysis of the STAR and Agility is not novel, the data produced by this experiment supplements the data already published with look at several different kinematic variables from a new ankle loading simulator.

5 CONCLUSION

The Agility was determined to exhibit a greater amount of micromotion between the bone and prosthesis than the STAR for the tibial component in INV-EV, and for the talar component in PF-DF and IR-ER. Aside from the previously noted tests, the differences found between the two implants were insignificant, despite the Agility having higher mean micromotion magnitudes than the STAR in all but one test. This agrees with the hypothesis of this study that higher clinically observed aseptic loosening rates are correlated with larger micromotion values immediately post-operatively.

Micromotion magnitudes were found to be affected by loading direction and compression, which confirms the need to apply a variety of loading conditions to obtain a comprehensive micromotion analysis.

Kinematic changes were observed after replacement of the ankle joint in a few comparisons, but due to large interspecimen variability the majority of differences were found insignificant. Consequently, no meaningful conclusions were able to be drawn from these analyses.

This is the first time micromotion has been studied in total ankle replacements, and a novel method for this analysis was developed for this experiment. Results from this study suggest the importance of this line of testing. Improving this methodology and adapting it for the analysis of other implants in use, and for the pre-clinical analysis of new implant designs would be beneficial in addressing the aseptic loosening issues in TAA.

REFERENCES

1. . *Arthroscope*: The Arthritis Society, 2004.
2. Cushnaghan J, Dieppe P. Study of 500 patients with limb joint osteoarthritis. I. Analysis by age, sex, and distribution of symptomatic joint sites. *Ann Rheum Dis* 1991;50(1):8-13.
3. Extremity Reconstruction: Procedural Volumes: © 2010 PearlDiver Technologies, Inc:Source: PearlDiver Patient Records Database and Center for Medicare & Medicaid Services Databases.
4. Saltzman CL, Mann RA, Ahrens JE, Amendola A, Anderson RB, Berlet GC, et al. Prospective controlled trial of STAR total ankle replacement versus ankle fusion: initial results. *Foot Ankle Int* 2009;30(7):579-96.
5. Piriou P, Culpan P, Mullins M, Cardon JN, Pozzi D, Judet T. Ankle replacement versus arthrodesis: a comparative gait analysis study. *Foot Ankle Int* 2008;29(1):3-9.
6. Hintermann B. *Total Ankle Arthroplasty: Historical Overview, Current Concepts and Future Perspectives*. St. Stefan, Austria: Springer-Verlag/Wien, 2005.
7. Cluett J. Ankle Arthritis: What is ankle arthritis? *About.com Guide*, 2010.
8. Henricson A, Nilsson JA, Carlsson A. 10-year survival of total ankle arthroplasties: a report on 780 cases from the Swedish Ankle Register. *Acta Orthop* 2011;82(6):655-9.
9. Skytta ET, Koivu H, Eskelinen A, Ikavalko M, Paavolainen P, Remes V. Total ankle replacement: a population-based study of 515 cases from the Finnish Arthroplasty Register. *Acta Orthop* 2010;81(1):114-8.
10. Henricson A, Skoog A, Carlsson A. The Swedish Ankle Arthroplasty Register: An analysis of 531 arthroplasties between 1993 and 2005. *Acta Orthop* 2007;78(5):569-74.
11. Hosman AH, Mason RB, Hobbs T, Rothwell AG. A New Zealand national joint registry review of 202 total ankle replacements followed for up to 6 years. *Acta Orthop* 2007;78(5):584-91.
12. Fevang BT, Lie SA, Havelin LI, Brun JG, Skredderstuen A, Furnes O. 257 ankle arthroplasties performed in Norway between 1994 and 2005. *Acta Orthop* 2007;78(5):575-83.
13. Labek G, Thaler M, Janda W, Agreiter M, Stockl B. Revision rates after total joint replacement: cumulative results from worldwide joint register datasets. *J Bone Joint Surg Br* 2011;93(3):293-7.
14. Burdett RG. Forces predicted at the ankle during running. *Med Sci Sports Exerc* 1982;14(4):308-16.
15. Michael JM, Golshani A, Gargac S, Goswami T. Biomechanics of the ankle joint and clinical outcomes of total ankle replacement. *J Mech Behav Biomed Mater* 2008;1(4):276-94.
16. Saltzman CL, Salamon ML, Blanchard GM, Huff T, Hayes A, Buckwalter JA, et al. Epidemiology of ankle arthritis: report of a consecutive series of 639 patients from a tertiary orthopaedic center. *Iowa Orthop J* 2005;25:44-6.
17. Barnett CH, Napier JR. The axis of rotation at the ankle joint in man; its influence upon the form of the talus and the mobility of the fibula. *J Anat* 1952;86(1):1-9.
18. Valderrabano V, Hintermann B, Nigg BM, Stefanyshyn D, Stergiou P. Kinematic changes after fusion and total replacement of the ankle: part 3: Talar movement. *Foot Ankle Int* 2003;24(12):897-900.
19. Murray MP, Drought AB, Kory RC. Walking Patterns of Normal Men. *J Bone Joint Surg Am* 1964;46:335-60.
20. Lundberg A, Svensson OK, Nemeth G, Selvik G. The axis of rotation of the ankle joint. *J Bone Joint Surg Br* 1989;71(1):94-9.
21. Leardini A, O'Connor JJ, Catani F, Giannini S. A geometric model of the human ankle joint. *J Biomech* 1999;32(6):585-91.

22. Mow VC, Ratcliffe A, Poole AR. Cartilage and diarthrodial joints as paradigms for hierarchical materials and structures. *Biomaterials* 1992;13(2):67-97.
23. Shepherd DE, Seedhom BB. Thickness of human articular cartilage in joints of the lower limb. *Ann Rheum Dis* 1999;58(1):27-34.
24. Hip and Knee Replacements in Canada—2011 Annual Statistics (Clinical Data). *CJRR Reports*: Canadian Institute for Health Information, 2011.
25. Brodsky JW, Polo FE, Coleman SC, Bruck N. Changes in gait following the Scandinavian Total Ankle Replacement. *J Bone Joint Surg Am* 2011;93(20):1890-6.
26. Gougoulias N, Khanna A, Maffulli N. How successful are current ankle replacements?: a systematic review of the literature. *Clin Orthop Relat Res* 2010;468(1):199-208.
27. Rippstein PF, Huber M, Coetzee JC, Naal FD. Total ankle replacement with use of a new three-component implant. *J Bone Joint Surg Am* 2011;93(15):1426-35.
28. Stengel D, Bauwens K, Ekkernkamp A, Cramer J. Efficacy of total ankle replacement with meniscal-bearing devices: a systematic review and meta-analysis. *Arch Orthop Trauma Surg* 2005;125(2):109-19.
29. Haddad SL, Coetzee JC, Estok R, Fahrbach K, Banel D, Nalysnyk L. Intermediate and long-term outcomes of total ankle arthroplasty and ankle arthrodesis. A systematic review of the literature. *J Bone Joint Surg Am* 2007;89(9):1899-905.
30. Kitaoka HB, Patzer GL. Clinical results of the Mayo total ankle arthroplasty. *J Bone Joint Surg Am* 1996;78(11):1658-64.
31. Wynn AH, Wilde AH. Long-term follow-up of the Conaxial (Beck-Steffee) total ankle arthroplasty. *Foot Ankle* 1992;13(6):303-6.
32. Kaya M, Nagoya S, Sasaki M, Kukita Y, Yamashita T. Primary total hip arthroplasty with Asian-type AML total hip prosthesis: follow-up for more than 10 years. *J Orthop Sci* 2008;13(4):324-7.
33. Kim YH, Kim JS, Cho SH. Primary total hip arthroplasty with the AML total hip prosthesis. *Clin Orthop Relat Res* 1999(360):147-58.
34. Nercessian OA, Wu WH, Sarkissian H. Clinical and radiographic results of cementless AML total hip arthroplasty in young patients. *J Arthroplasty* 2001;16(3):312-6.
35. Gougoulias NE, Khanna A, Maffulli N. History and evolution in total ankle arthroplasty. *Br Med Bull* 2009;89:111-51.
36. Anderson T, Montgomery F, Carlsson A. Uncemented STAR total ankle prostheses. Three to eight-year follow-up of fifty-one consecutive ankles. *J Bone Joint Surg Am* 2003;85-A(7):1321-9.
37. Karantana A, Hobson S, Dhar S. The scandinavian total ankle replacement: survivorship at 5 and 8 years comparable to other series. *Clin Orthop Relat Res* 2010;468(4):951-7.
38. Wood PL, Prem H, Sutton C. Total ankle replacement: medium-term results in 200 Scandinavian total ankle replacements. *J Bone Joint Surg Br* 2008;90(5):605-9.
39. Schutte BG, Louwerens JW. Short-term results of our first 49 Scandanavian total ankle replacements (STAR). *Foot Ankle Int* 2008;29(2):124-7.
40. Claridge RJ, Sagherian BH. Intermediate term outcome of the agility total ankle arthroplasty. *Foot Ankle Int* 2009;30(9):824-35.
41. Knecht SI, Estin M, Callaghan JJ, Zimmerman MB, Alliman KJ, Alvine FG, et al. The Agility total ankle arthroplasty. Seven to sixteen-year follow-up. *J Bone Joint Surg Am* 2004;86-A(6):1161-71.
42. Spirt AA, Assal M, Hansen ST, Jr. Complications and failure after total ankle arthroplasty. *J Bone Joint Surg Am* 2004;86-A(6):1172-8.
43. Kopp FJ, Patel MM, Deland JT, O'Malley MJ. Total ankle arthroplasty with the Agility prosthesis: clinical and radiographic evaluation. *Foot Ankle Int* 2006;27(2):97-103.
44. Valderrabano V, Hintermann B, Dick W. Scandinavian total ankle replacement: a 3.7-year average followup of 65 patients. *Clin Orthop Relat Res* 2004(424):47-56.

45. Boone DC, Azen SP. Normal range of motion of joints in male subjects. *J Bone Joint Surg Am* 1979;61(5):756-9.
46. Soucie JM, Wang C, Forsyth A, Funk S, Denny M, Roach KE, et al. Range of motion measurements: reference values and a database for comparison studies. *Haemophilia* 2011;17(3):500-7.
47. Lark SD, Buckley JG, Jones DA, Sargeant AJ. Knee and ankle range of motion during stepping down in elderly compared to young men. *Eur J Appl Physiol* 2004;91(2-3):287-95.
48. Nordin M, Frankel VH. *Basic biomechanics of the musculoskeletal system*. 3rd ed. Philadelphia: Lippincott Williams & Wilkins, 2001.
49. Hemmerich A, Brown H, Smith S, Marthandam SS, Wyss UP. Hip, knee, and ankle kinematics of high range of motion activities of daily living. *J Orthop Res* 2006;24(4):770-81.
50. Valderrabano V, Hintermann B, Nigg BM, Stefanyshyn D, Stergiou P. Kinematic changes after fusion and total replacement of the ankle: part 1: Range of motion. *Foot Ankle Int* 2003;24(12):881-7.
51. Adelaar RS. The practical biomechanics of running. *Am J Sports Med* 1986;14(6):497-500.
52. Valderrabano V, Hintermann B, Nigg BM, Stefanyshyn D, Stergiou P. Kinematic changes after fusion and total replacement of the ankle: part 2: Movement transfer. *Foot Ankle Int* 2003;24(12):888-96.
53. Michelson JD, Schmidt GR, Mizel MS. Kinematics of a total arthroplasty of the ankle: comparison to normal ankle motion. *Foot Ankle Int* 2000;21(4):278-84.
54. Sharkey NA, Hamel AJ. A dynamic cadaver model of the stance phase of gait: performance characteristics and kinetic validation. *Clin Biomech (Bristol, Avon)* 1998;13(6):420-33.
55. Giddings VL, Beaupre GS, Whalen RT, Carter DR. Calcaneal loading during walking and running. *Med Sci Sports Exerc* 2000;32(3):627-34.
56. Bobbert MF, van Ingen Schenau GJ. Isokinetic plantar flexion: experimental results and model calculations. *J Biomech* 1990;23(2):105-19.
57. Arampatzis A, De Monte G, Morey-Klapsing G. Effect of contraction form and contraction velocity on the differences between resultant and measured ankle joint moments. *J Biomech* 2007;40(7):1622-8.
58. Bobbert MF, Huijing PA, van Ingen Schenau GJ. A model of the human triceps surae muscle-tendon complex applied to jumping. *J Biomech* 1986;19(11):887-98.
59. Gefen A, Megido-Ravid M, Itzchak Y, Arcan M. Biomechanical analysis of the three-dimensional foot structure during gait: a basic tool for clinical applications. *J Biomech Eng* 2000;122(6):630-9.
60. Anderson DD, Goldsworthy JK, Shivanna K, Grosland NM, Pedersen DR, Thomas TP, et al. Intra-articular contact stress distributions at the ankle throughout stance phase-patient-specific finite element analysis as a metric of degeneration propensity. *Biomech Model Mechanobiol* 2006;5(2-3):82-9.
61. Suckel A, Muller O, Wachter N, Kluba T. In vitro measurement of intraarticular pressure in the ankle joint. *Knee Surg Sports Traumatol Arthrosc* 2010;18(5):664-8.
62. Kimizuka M, Kurosawa H, Fukubayashi T. Load-bearing pattern of the ankle joint. Contact area and pressure distribution. *Arch Orthop Trauma Surg* 1980;96(1):45-9.
63. Macko VW, Matthews LS, Zwirkoski P, Goldstein SA. The joint-contact area of the ankle. The contribution of the posterior malleolus. *J Bone Joint Surg Am* 1991;73(3):347-51.
64. Wan L, de Asla RJ, Rubash HE, Li G. Determination of in-vivo articular cartilage contact areas of human talocrural joint under weightbearing conditions. *Osteoarthritis Cartilage* 2006;14(12):1294-301.
65. Driscoll HL, Christensen JC, Tencer AF. Contact characteristics of the ankle joint. Part 1. The normal joint. *J Am Podiatr Med Assoc* 1994;84(10):491-8.
66. Ramsey PL, Hamilton W. Changes in tibiotalar area of contact caused by lateral talar shift. *J Bone Joint Surg Am* 1976;58(3):356-7.

67. Leardini A, O'Connor JJ, Catani F, Giannini S. Kinematics of the human ankle complex in passive flexion; a single degree of freedom system. *J Biomech* 1999;32(2):111-8.
68. Leardini A, Moschella D. Dynamic simulation of the natural and replaced human ankle joint. *Med Biol Eng Comput* 2002;40(2):193-9.
69. Reggiani B, Leardini A, Corazza F, Taylor M. Finite element analysis of a total ankle replacement during the stance phase of gait. *J Biomech* 2006;39(8):1435-43.
70. Tochigi Y, Rudert MJ, Brown TD, McIff TE, Saltzman CL. The effect of accuracy of implantation on range of movement of the Scandinavian Total Ankle Replacement. *J Bone Joint Surg Br* 2005;87(5):736-40.
71. Watanabe K, Crevoisier XM, Kitaoka HB, Zhao KD, Berglund LJ, Kaufman KR, et al. Analysis of joint laxity after total ankle arthroplasty: cadaver study. *Clin Biomech (Bristol, Avon)* 2009;24(8):655-60.
72. Stauffer RN, Chao EY, Brewster RC. Force and motion analysis of the normal, diseased, and prosthetic ankle joint. *Clin Orthop Relat Res* 1977(127):189-96.
73. Detrembleur C, Leemrijse T. The effects of total ankle replacement on gait disability: analysis of energetic and mechanical variables. *Gait Posture* 2009;29(2):270-4.
74. Miller MC, Smolinski P, Conti S, Galik K. Stresses in polyethylene liners in a semiconstrained ankle prosthesis. *J Biomech Eng* 2004;126(5):636-40.
75. Espinosa N, Walti M, Favre P, Snedeker JG. Misalignment of total ankle components can induce high joint contact pressures. *J Bone Joint Surg Am* 2010;92(5):1179-87.
76. Affatato S, Leardini A, Leardini W, Giannini S, Viceconti M. Meniscal wear at a three-component total ankle prosthesis by a knee joint simulator. *J Biomech* 2007;40(8):1871-6.
77. Bell CJ, Fisher J. Simulation of polyethylene wear in ankle joint prostheses. *J Biomed Mater Res B Appl Biomater* 2007;81(1):162-7.
78. Affatato S, Taddei P, Leardini A, Giannini S, Spinelli M, Viceconti M. Wear behaviour in total ankle replacement: a comparison between an in vitro simulation and retrieved prostheses. *Clin Biomech (Bristol, Avon)* 2009;24(8):661-9.
79. Hamel AJ, Sharkey NA, Buczek FL, Michelson J. Relative motions of the tibia, talus, and calcaneus during the stance phase of gait: a cadaver study. *Gait Posture* 2004;20(2):147-53.
80. Suckel A, Muller O, Langenstein P, Herberts T, Reize P, Wulker N. Chopart's joint load during gait. In vitro study of 10 cadaver specimen in a dynamic model. *Gait Posture* 2008;27(2):216-22.
81. Nester CJ, Liu AM, Ward E, Howard D, Cocheba J, Derrick T, et al. In vitro study of foot kinematics using a dynamic walking cadaver model. *J Biomech* 2007;40(9):1927-37.
82. Whittaker EC, Aubin PM, Ledoux WR. Foot bone kinematics as measured in a cadaveric robotic gait simulator. *Gait Posture* 2011;33(4):645-50.
83. Michelson JD, Hamel AJ, Buczek FL, Sharkey NA. Kinematic behavior of the ankle following malleolar fracture repair in a high-fidelity cadaver model. *J Bone Joint Surg Am* 2002;84-A(11):2029-38.
84. Suckel A, Muller O, Herberts T, Wulker N. Changes in Chopart joint load following tibiotalar arthrodesis: in vitro analysis of 8 cadaver specimens in a dynamic model. *BMC Musculoskelet Disord* 2007;8:80.
85. Stahelin T, Nigg BM, Stefanyshyn DJ, van den Bogert AJ, Kim SJ. A method to determine bone movement in the ankle joint complex in vitro. *J Biomech* 1997;30(5):513-6.
86. Hansen ML, Otis JC, Kenneally SM, Deland JT. A closed-loop cadaveric foot and ankle loading model. *J Biomech* 2001;34(4):551-5.
87. Shimamura Y, Kaneko K, Kume K, Maeda M, Iwase H. The initial safe range of motion of the ankle joint after three methods of internal fixation of simulated fractures of the medial malleolus. *Clin Biomech (Bristol, Avon)* 2006;21(6):617-22.

88. Lewis GS, Sommer HJ, 3rd, Piazza SJ. In vitro assessment of a motion-based optimization method for locating the talocrural and subtalar joint axes. *J Biomech Eng* 2006;128(4):596-603.
89. Michelson JD, Waldman B. An axially loaded model of the ankle after pronation external rotation injury. *Clin Orthop Relat Res* 1996(328):285-93.
90. Anderson DD, Tochigi Y, Rudert MJ, Vaseenon T, Brown TD, Amendola A. Effect of implantation accuracy on ankle contact mechanics with a metallic focal resurfacing implant. *J Bone Joint Surg Am* 2010;92(6):1490-500.
91. Tochigi Y, Rudert MJ, Saltzman CL, Amendola A, Brown TD. Contribution of articular surface geometry to ankle stabilization. *J Bone Joint Surg Am* 2006;88(12):2704-13.
92. McKinley TO, Tochigi Y, Rudert MJ, Brown TD. The effect of incongruity and instability on contact stress directional gradients in human cadaveric ankles. *Osteoarthritis Cartilage* 2008;16(11):1363-9.
93. Larson CR, Oxland TR, Sjovold SG, Devries G, Veri JP, Awwad M, et al. Biomechanical Comparison of Ankle Ligament Reconstructive Techniques. *Focus on Tomorrow*. Richmond, BC: Workers' Compensation Board of BC, 2005:20.
94. Pauwels F. *Biomechanics of the locomotor apparatus : contributions on the functional anatomy of the locomotor apparatus*. Berlin ; New York: Springer-Verlag, 1980.
95. Carter DR, Beaupre GS, Giori NJ, Helms JA. Mechanobiology of skeletal regeneration. *Clin Orthop Relat Res* 1998(355 Suppl):S41-55.
96. Claes LE, Heigele CA. Magnitudes of local stress and strain along bony surfaces predict the course and type of fracture healing. *J Biomech* 1999;32(3):255-66.
97. Prendergast PJ, Huiskes R, Soballe K. ESB Research Award 1996. Biophysical stimuli on cells during tissue differentiation at implant interfaces. *J Biomech* 1997;30(6):539-48.
98. Weinans H, Prendergast PJ. Tissue adaptation as a dynamical process far from equilibrium. *Bone* 1996;19(2):143-9.
99. Lacroix D, Prendergast PJ. A mechano-regulation model for tissue differentiation during fracture healing: analysis of gap size and loading. *J Biomech* 2002;35(9):1163-71.
100. Maher SA, Prendergast PJ. Discriminating the loosening behaviour of cemented hip prostheses using measurements of migration and inducible displacement. *J Biomech* 2002;35(2):257-65.
101. Pilliar RM, Lee JM, Maniatopoulos C. Observations on the effect of movement on bone ingrowth into porous-surfaced implants. *Clin Orthop Relat Res* 1986(208):108-13.
102. Jasty M, Bragdon CR, Zalenski E, O'Connor D, Page A, Harris WH. Enhanced stability of uncemented canine femoral components by bone ingrowth into the porous coatings. *J Arthroplasty* 1997;12(1):106-13.
103. Jasty M, Bragdon C, Burke D, O'Connor D, Lowenstein J, Harris WH. In vivo skeletal responses to porous-surfaced implants subjected to small induced motions. *J Bone Joint Surg Am* 1997;79(5):707-14.
104. Harman MK, Toni A, Cristofolini L, Viceconti M. Initial stability of uncemented hip stems: an in-vitro protocol to measure torsional interface motion. *Med Eng Phys* 1995;17(3):163-71.
105. Ferreira LM, Stacpoole RA, Johnson JA, King GJ. Cementless fixation of radial head implants is affected by implant stem geometry: an in vitro study. *Clin Biomech (Bristol, Avon)* 2010;25(5):422-6.
106. Choi D, Park Y, Yoon YS, Masri BA. In vitro measurement of interface micromotion and crack in cemented total hip arthroplasty systems with different surface roughness. *Clin Biomech (Bristol, Avon)* 2010;25(1):50-5.
107. Skwara A, Figiel J, Knott T, Paletta JR, Fuchs-Winkelmann S, Tibesku CO. Primary stability of tibial components in TKA: in vitro comparison of two cementing techniques. *Knee Surg Sports Traumatol Arthrosc* 2009;17(10):1199-205.

108. Albert C, Patil S, Frei H, Masri B, Duncan C, Oxland T, et al. Cement penetration and primary stability of the femoral component after impaction allografting. A biomechanical study in the cadaveric femur. *J Bone Joint Surg Br* 2007;89(7):962-70.
109. Buhler DW, Oxland TR, Nolte LP. Design and evaluation of a device for measuring three-dimensional micromotions of press-fit femoral stem prostheses. *Med Eng Phys* 1997;19(2):187-99.
110. Maher SA, Prendergast PJ, Lyons CG. Measurement of the migration of a cemented hip prosthesis in an in vitro test. *Clin Biomech (Bristol, Avon)* 2001;16(4):307-14.
111. Monti L, Cristofolini L, Viceconti M. Methods for quantitative analysis of the primary stability in uncemented hip prostheses. *Artif Organs* 1999;23(9):851-9.
112. Viceconti M, Muccini R, Bernakiewicz M, Baleani M, Cristofolini L. Large-sliding contact elements accurately predict levels of bone-implant micromotion relevant to osseointegration. *J Biomech* 2000;33(12):1611-8.
113. Pettersen SH, Wik TS, Skallerud B. Subject specific finite element analysis of implant stability for a cementless femoral stem. *Clin Biomech (Bristol, Avon)* 2009;24(6):480-7.
114. Chong DY, Hansen UN, Amis AA. Analysis of bone-prosthesis interface micromotion for cementless tibial prosthesis fixation and the influence of loading conditions. *J Biomech* 2010;43(6):1074-80.
115. Viceconti M, Brusi G, Pancanti A, Cristofolini L. Primary stability of an anatomical cementless hip stem: a statistical analysis. *J Biomech* 2006;39(7):1169-79.
116. Hurschler C, Seehaus F, Emmerich J, Kaptein BL, Windhagen H. Comparison of the model-based and marker-based roentgen stereophotogrammetry methods in a typical clinical setting. *J Arthroplasty* 2009;24(4):594-606.
117. Trozzi C, Kaptein BL, Garling EH, Shelyakova T, Russo A, Bragonzoni L, et al. Precision assessment of model-based RSA for a total knee prosthesis in a biplanar set-up. *Knee* 2008;15(5):396-402.
118. Atkins GJ, Haynes DR, Howie DW, Findlay DM. Role of polyethylene particles in peri-prosthetic osteolysis: A review. *World J Orthop* 2011;2(10):93-101.
119. Grewal R, Rimmer MG, Freeman MA. Early migration of prostheses related to long-term survivorship. Comparison of tibial components in knee replacement. *J Bone Joint Surg Br* 1992;74(2):239-42.
120. Ryd L, Albrektsson BE, Carlsson L, Dansgard F, Herberts P, Lindstrand A, et al. Roentgen stereophotogrammetric analysis as a predictor of mechanical loosening of knee prostheses. *J Bone Joint Surg Br* 1995;77(3):377-83.
121. Goertzen DJ, Lane C, Oxland TR. Neutral zone and range of motion in the spine are greater with stepwise loading than with a continuous loading protocol. An in vitro porcine investigation. *J Biomech* 2004;37(2):257-61.
122. Veldpaus FE, Woltring HJ, Dortmans LJ. A least-squares algorithm for the equiform transformation from spatial marker co-ordinates. *J Biomech* 1988;21(1):45-54.
123. Grood ES, Suntay WJ. A joint coordinate system for the clinical description of three-dimensional motions: application to the knee. *J Biomech Eng* 1983;105(2):136-44.
124. Wu G, Siegler S, Allard P, Kirtley C, Leardini A, Rosenbaum D, et al. ISB recommendation on definitions of joint coordinate system of various joints for the reporting of human joint motion--part I: ankle, hip, and spine. International Society of Biomechanics. *J Biomech* 2002;35(4):543-8.
125. Siegler S, Udupa JK, Ringleb SI, Imhauser CW, Hirsch BE, Odhner D, et al. Mechanics of the ankle and subtalar joints revealed through a 3D quasi-static stress MRI technique. *J Biomech* 2005;38(3):567-78.
126. Kassi JP, Heller MO, Stoeckle U, Perka C, Duda GN. Stair climbing is more critical than walking in pre-clinical assessment of primary stability in cementless THA in vitro. *J Biomech* 2005;38(5):1143-54.

127. Pancanti A, Bernakiewicz M, Viceconti M. The primary stability of a cementless stem varies between subjects as much as between activities. *J Biomech* 2003;36(6):777-85.
128. Cripton PA, Bruehlmann SB, Orr TE, Oxland TR, Nolte LP. In vitro axial preload application during spine flexibility testing: towards reduced apparatus-related artefacts. *J Biomech* 2000;33(12):1559-68.
129. Haskell A, Mann RA. Perioperative complication rate of total ankle replacement is reduced by surgeon experience. *Foot Ankle Int* 2004;25(5):283-9.
130. Kienapfel H, Sprey C, Wilke A, Griss P. Implant fixation by bone ingrowth. *J Arthroplasty* 1999;14(3):355-68.
131. Madanat R, Makinen TJ, Moritz N, Mattila KT, Aro HT. Accuracy and precision of radiostereometric analysis in the measurement of three-dimensional micromotion in a fracture model of the distal radius. *J Orthop Res* 2005;23(2):481-8.
132. Koning OH, Kaptein BL, van der Vijver R, Dias NV, Malina M, Schalij MJ, et al. Fluoroscopic Roentgen stereophotogrammetric analysis (FRSA) to study three-dimensional stent graft dynamics. *J Vasc Surg* 2009;50(2):407-12.

APPENDIX A: TAA FAILURES AND THEIR CAUSES

Author	Year	Implant	Total	Failures/ Revisions	Aseptic Loosening/ Subsidence	Instability	Malalignment	Infection	PE Failure	Bone Fracture	Pain	Other
Anderson	2003	STAR	51	12	7		2		2		1	
Claridge	2009	Agility	26	5	2	1		2				
Karantana	2009	STAR	52	8	2				2	2	2	
Wood	2008	STAR	200	24	14			1	6	3		
Fevang	2007	STAR	216	21	7	3	7	2	2	1	5	
		TPR	32	6	6							
Henricson	2007	STAR	303	71	27	3	15	10	5	2	9	
		BP	92	16	1	8	1	1	1		4	
		AES	69	8		4		2	1		1	
Hosman	2007	Agility	117	8	6		1	1				
		STAR	45	3	2						1	
		Mobility	29	0								
		Ramses	11	2	1			1				
Skytta	2010	STAR	217	31	16	6	4	3	2			
		AES	298	28	7	17	1	1	1	1		
Knecht	2004	Agility	132	14	5		1	1	3	3		1
Schutte	2008	STAR	49	4	2			2				
Spirt	2004	Agility	306	33	28			1				4
Vaupel	2009	Agility		10	7	1					2	
Criswell	2012	Agility	41	16	unknown							
Total				304	140	43	32	28	25	12	25	5
Percentage					46.1	14.1	10.5	9.2	8.2	3.9	8.2	1.6

APPENDIX B: INDICATIONS FOR TAA

Author	Year	Implant	Total	PTOA	POA	RA	Other
Anderson	2003	star	51	10	13	28	0
Claridge	2009	agility	28	14	10	4	0
Karantana	2009	star	50	12	24	14	0
Wood	2008	star	200	25	56	119	0
Fevang	2007	star tpr	216 32	57	53	129	9
Henricson	2007	star bp aes other	303 92 69 67	175	119	216	21
Hosman	2007	agility star mobility ramses	117 45 29 11	34	144	24	0
Knecht	2004	agility	132	61	38	31	2
Spirt	2004	agility	306	199	77	13	17
Criswell	2012	agility	41	25	2	5	9
Hurowitz		agility	62	37	12	10	3
Kopp		agility	40	24	8	8	0
Valderrabano		star	68	48	9	11	0
Buechel		bp	75	55	8	9	3
San Giovanni		bp	31	0	0	31	0
Naal		bp & mobility	101	47	35	19	0
Valderrabano		hintegra	152	115	21	16	0
Bonnin		salto	98	43	22	29	4
Total			2416	981	651	716	68
Percentage				40.60	26.95	29.64	2.81

APPENDIX C: MOUNTING RIG

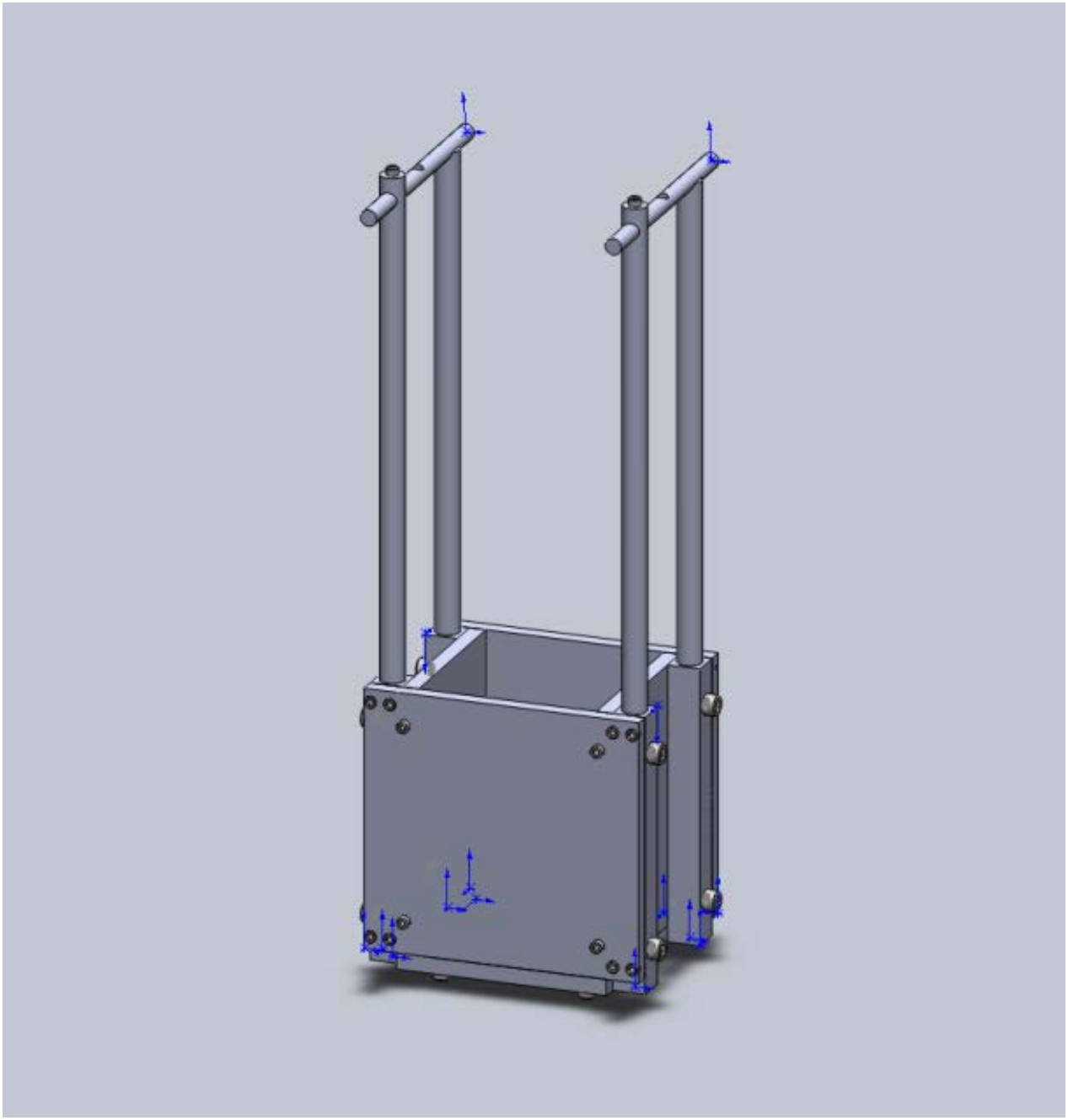

ITEM NO.	PART NUMBER	DESCRIPTION	QTY.
1	Side1		2
2	Side2		2
3	Bottom		1
4	block1		2
5	block2		2
6	post1		2
7	post2		2
8	guide		2
9	HX-SHCS 0.25-20x0.5x0.5-N		44

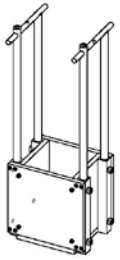

UNLESS OTHERWISE SPECIFIED: DIMENSIONS ARE IN MILLIMETERS SURFACE FINISH: TOLERANCES: LINEAR: ANGULAR:

FINISH:

DEBUR AND BREAK SHARP EDGES

DO NOT SCALE DRAWING

REVISION

	NAME	SIGNATURE	DATE
DRAWN			
CHK'D			
APPV'D			
MFG			
Q.A.			

TITLE:

potting and cable guides

MATERIAL:

DWG. NO.

A3

WEIGHT:

SCALE:1:5

SHEET 1 OF 1

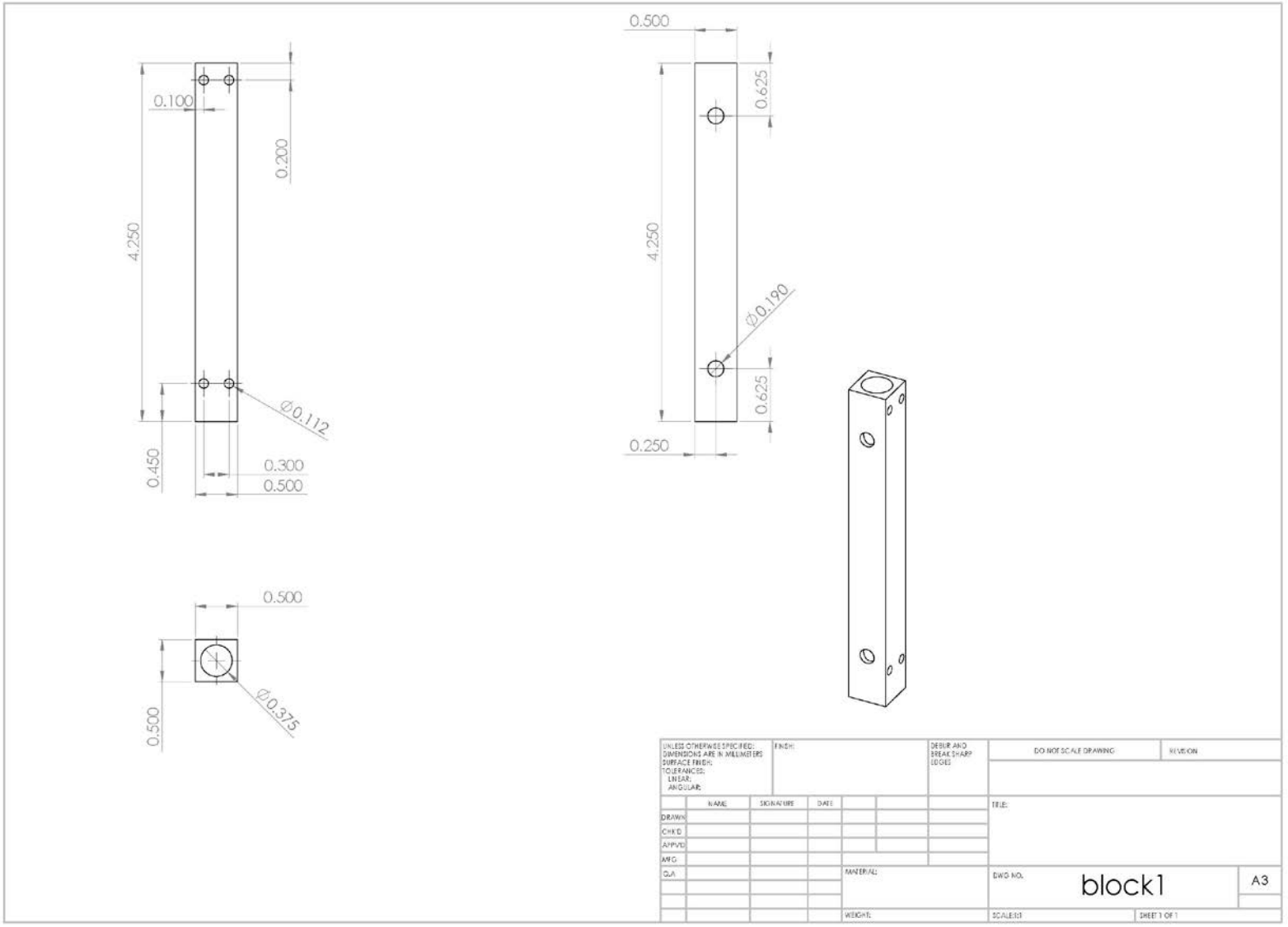
0.100
0.200
4.250
Ø0.112
0.450
0.300
0.500
0.500
0.500
Ø0.375
0.500
0.625
4.250
Ø0.190
0.625
0.250
UNLESS OTHERWISE SPECIFIED:
DIMENSIONS ARE IN MILLIMETERS
SURFACE FINISH:
TOLERANCES:
LINEAR:
ANGULAR:
FINISH:
DEBUR AND BREAK SHARP EDGES
DO NOT SCALE DRAWING
REVISION
NAME
SIGNATURE
DATE
DRAWN
CHKD
APPVD
MFG
QA
TITLE:
MATERIAL:
DWG NO.
block1
A3
WEIGHT:
SCALE:1:1
SHEET 1 OF 1

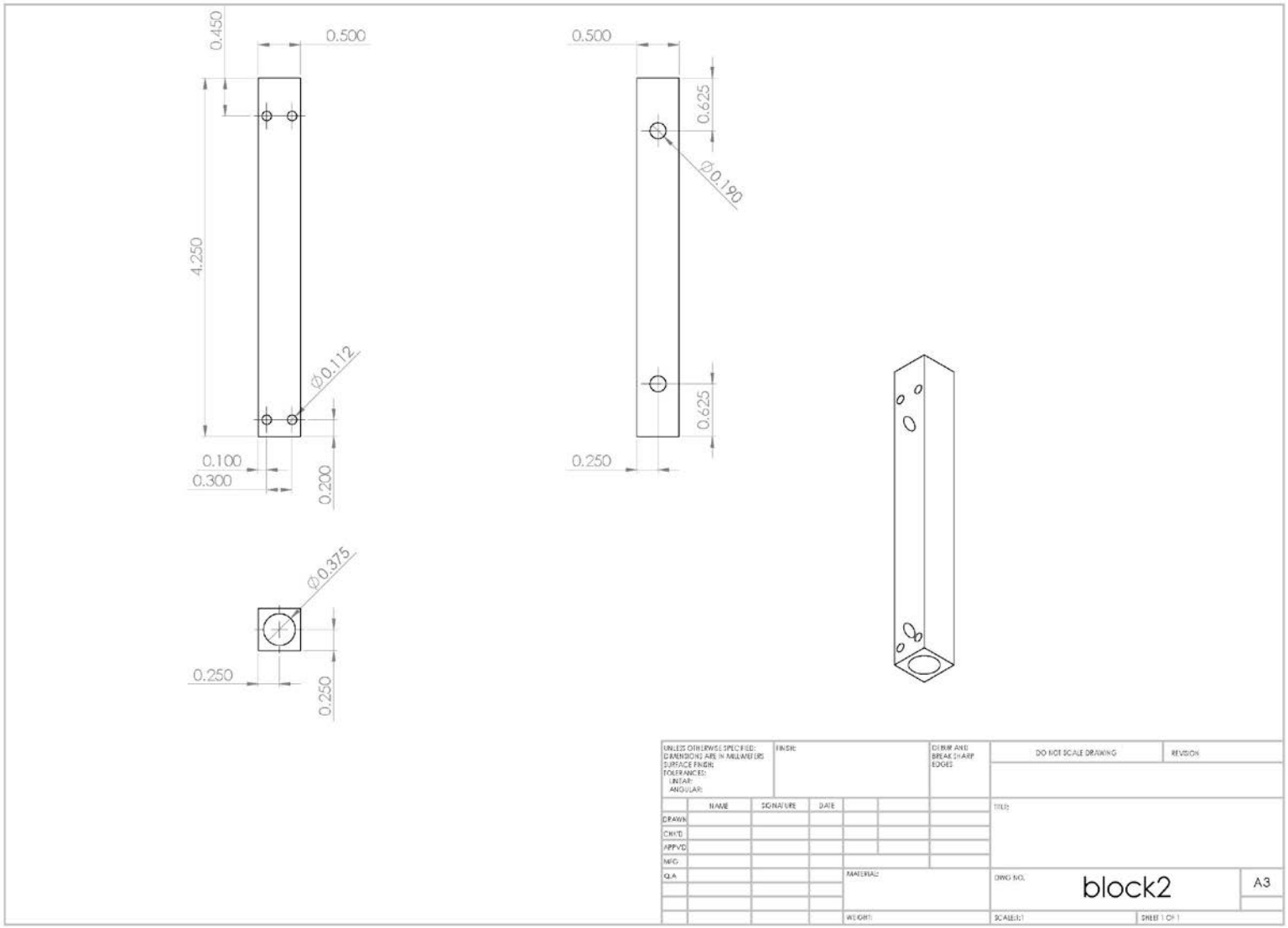
0.450
0.500
4.250
Ø0.112
0.100
0.300
0.200
Ø0.375
0.250
0.250
0.500
0.625
Ø0.190
0.625
0.250
UNLESS OTHERWISE SPECIFIED:
DIMENSIONS ARE IN MILLIMETERS
SURFACE FINISH:
TOLERANCES:
LINEAR:
ANGULAR:
FINISH:
DEBUR AND BREAK SHARP EDGES
DO NOT SCALE DRAWING
REVISION
NAME
SIGNATURE
DATE
DRAWN
CHK'D
APPV'D
MFG
Q.A
MATERIAL:
WEIGHT:
TITLE:
DWG NO.
block2
A3
SCALE:1:1
SHEET 1 OF 1

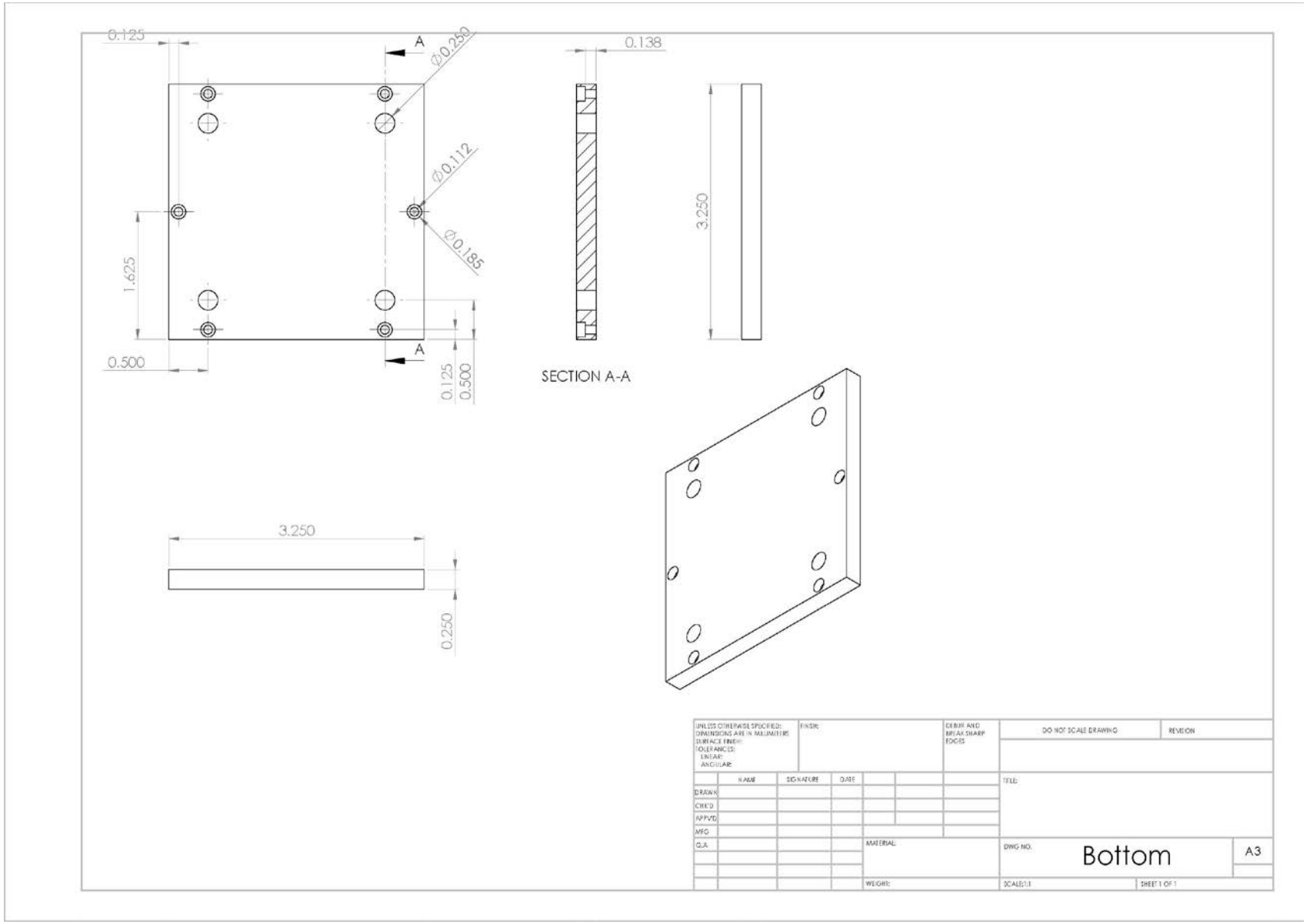
0.125
A
Ø0.250
Ø0.112
Ø0.185
1.625
0.500
A
0.125
0.500
0.138
3.250
SECTION A-A
3.250
0.250
UNLESS OTHERWISE SPECIFIED:
DIMENSIONS ARE IN MILLIMETERS
SURFACE FINISH:
TOLERANCES:
LINEAR:
ANGULAR:
FINISH:
DEBUR AND BREAK SHARP EDGES
DO NOT SCALE DRAWING
REVISION
NAME
SIGNATURE
DATE
DRAWN
CHK'D
APP'VD
MFG
Q.A
MATERIAL:
WEIGHT:
TITLE:
DWG NO.
Bottom
A3
SCALE:1:1
SHEET 1 OF 1

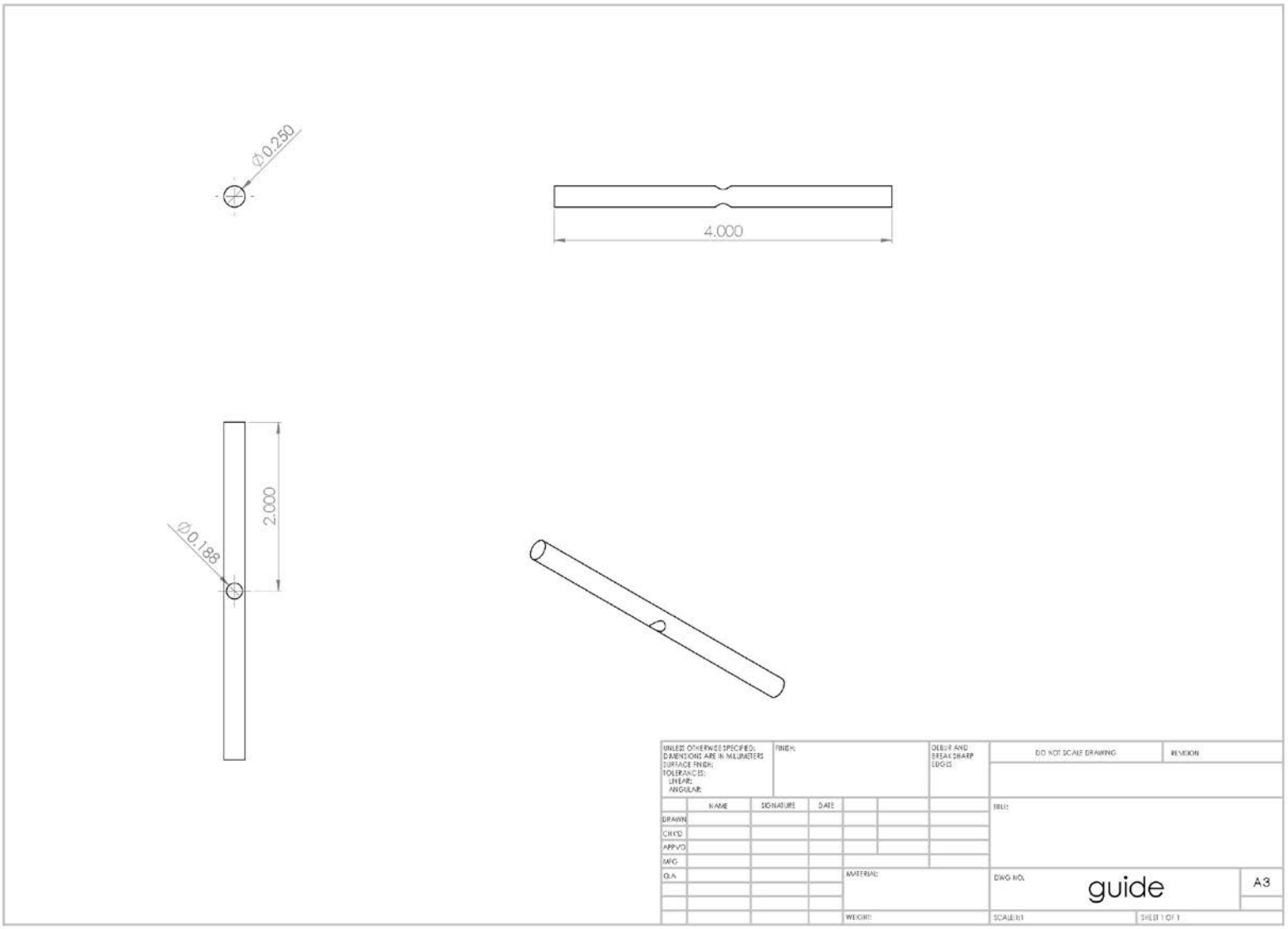
Ø0.250
4.000
2.000
Ø0.188
UNLESS OTHERWISE SPECIFIED:
DIMENSIONS ARE IN MILLIMETERS
SURFACE FINISH:
TOLERANCES:
LINEAR:
ANGULAR:
FINISH:
DEBUR AND BREAK SHARP EDGES
DO NOT SCALE DRAWING
REVISION
NAME
SIGNATURE
DATE
DRAWN
CHK'D
APP'D
MFG
Q.A
MATERIAL:
WEIGHT:
TITLE:
DWG NO.
guide
A3
SCALE:1:1
SHEET 1 OF 1

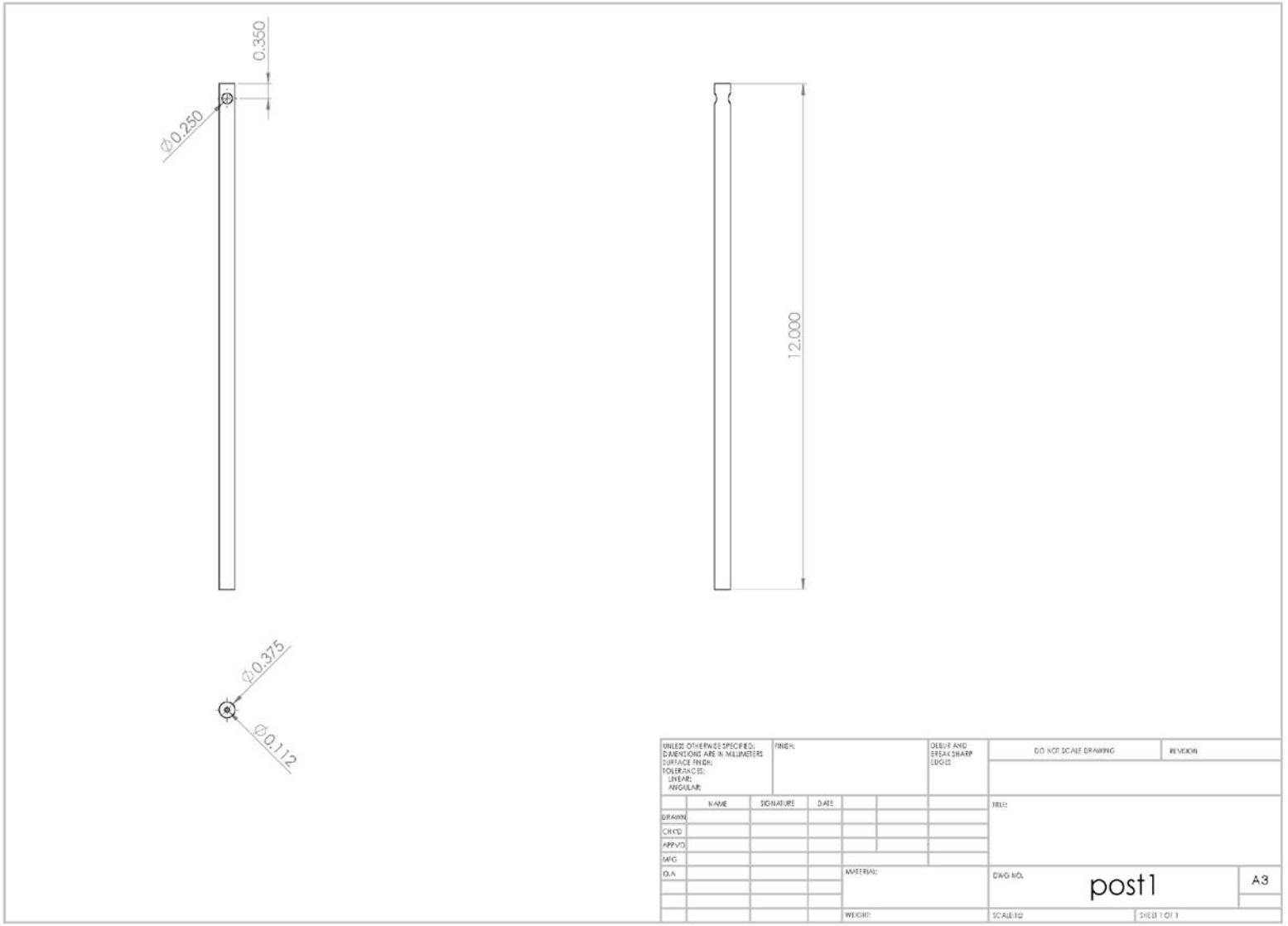
0.350
Ø0.250
12.000
Ø0.375
Ø0.112
UNLESS OTHERWISE SPECIFIED:
DIMENSIONS ARE IN MILLIMETERS
SURFACE FINISH:
TOLERANCES:
LINEAR:
ANGULAR:
FINISH:
DEBUR AND BREAK SHARP EDGES
DO NOT SCALE DRAWING
REVISION
NAME
SIGNATURE
DATE
DRAWN
CHKD
APPVD
MFG
QA
TITLE:
MATERIAL:
DWG NO.
post1
A3
WEIGHT:
SCALE:1:2
SHEET 1 OF 1

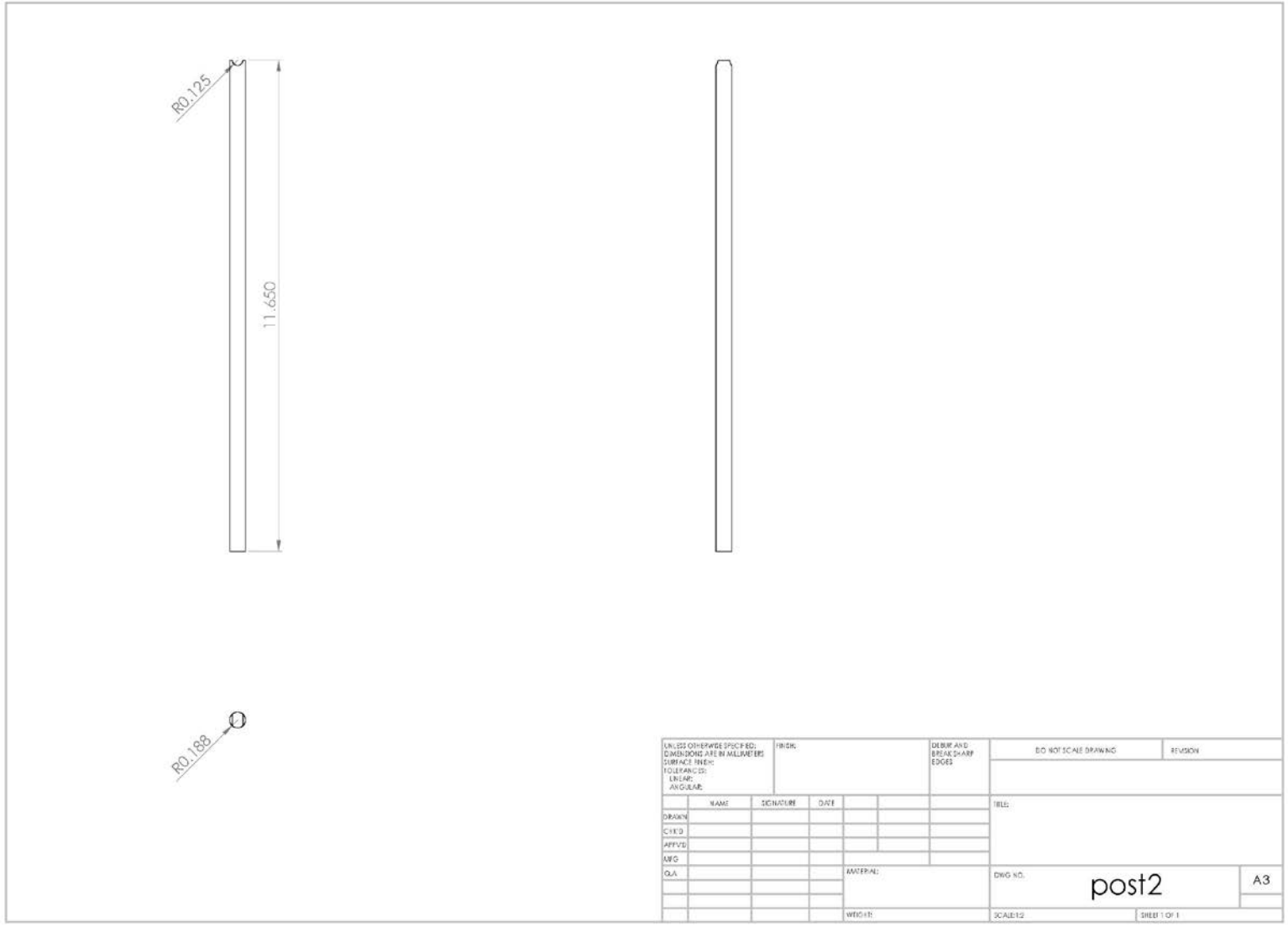
R0.125
11.650
R0.188
UNLESS OTHERWISE SPECIFIED:
DIMENSIONS ARE IN MILLIMETERS
SURFACE FINISH:
TOLERANCES:
LINEAR:
ANGULAR:
FINISH:
DEBUR AND BREAK SHARP EDGES
DO NOT SCALE DRAWING
REVISION
NAME
SIGNATURE
DATE
DRAWN
CHKD
APPVD
MFG
QA
TITLE:
MATERIAL:
DWG NO.
post2
A3
WEIGHT:
SCALE:1:2
SHEET 1 OF 1

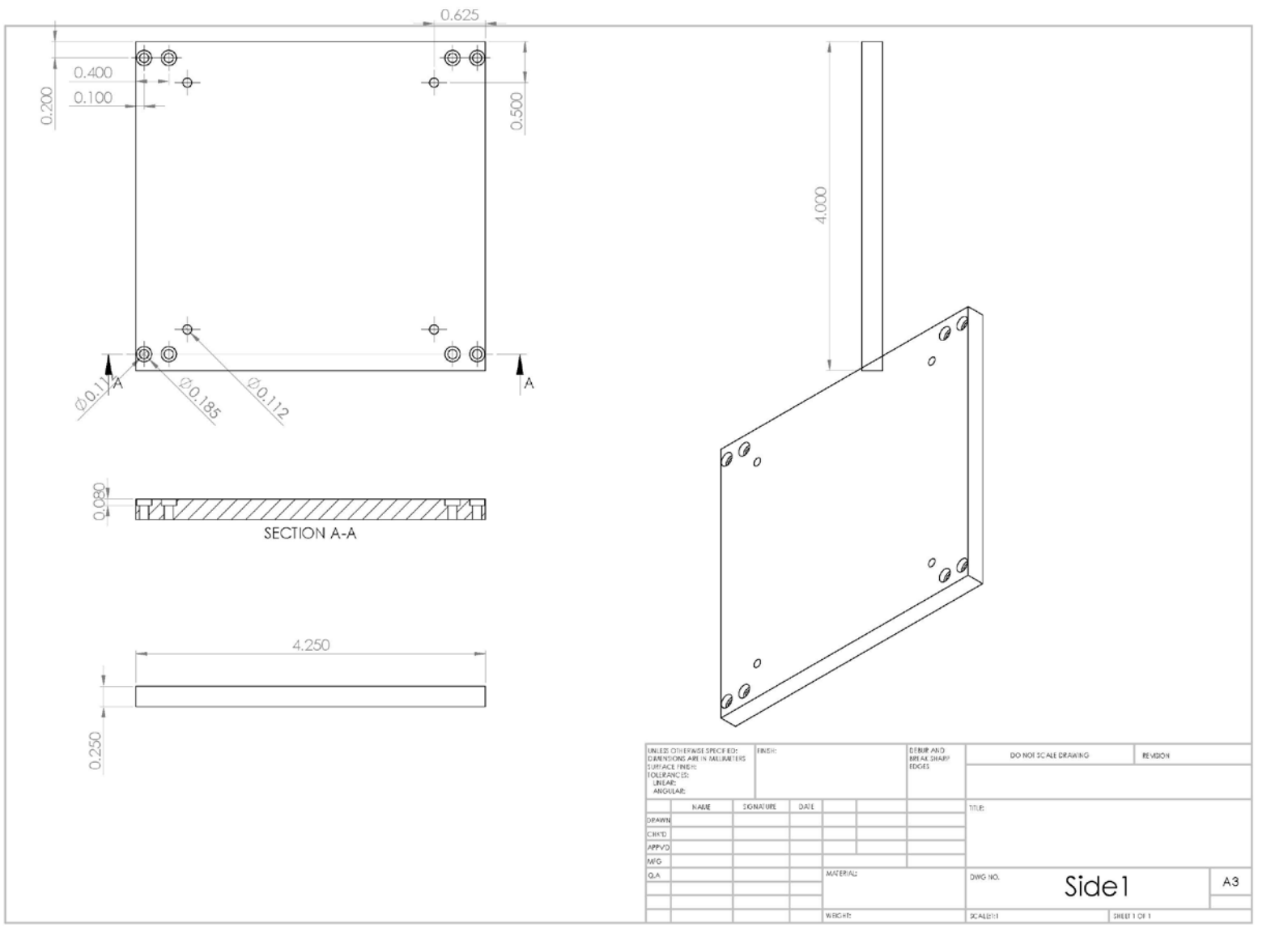
0.625
0.400
0.100
0.200
0.500
Ø0.112
Ø0.185
Ø0.112
A
A
0.080
SECTION A-A
4.250
0.250
4.000
UNLESS OTHERWISE SPECIFIED:
DIMENSIONS ARE IN MILLIMETERS
SURFACE FINISH:
TOLERANCES:
LINEAR:
ANGULAR:
FINISH:
DEBUR AND BREAK SHARP EDGES
DO NOT SCALE DRAWING
REVISION
NAME
SIGNATURE
DATE
DRAWN
CHK'D
APPV'D
MFG
Q.A
TITLE:
MATERIAL:
DWG NO.
Side1
A3
WEIGHT:
SCALE:1:1
SHEET 1 OF 1

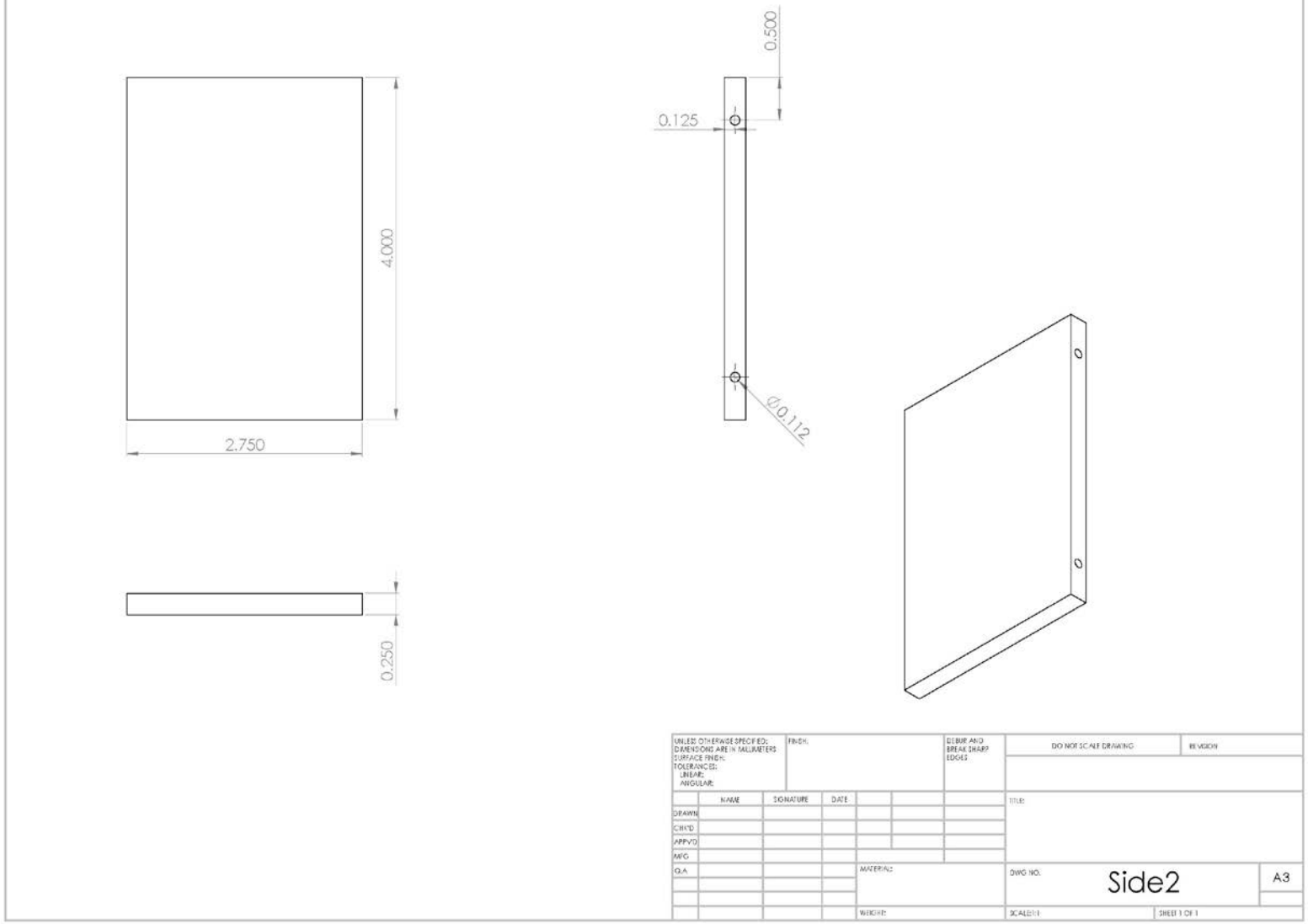
0.500
0.125
4.000
2.750
Ø0.112
0.250
UNLESS OTHERWISE SPECIFIED:
DIMENSIONS ARE IN MILLIMETERS
SURFACE FINISH:
TOLERANCES:
LINEAR:
ANGULAR:
FINISH:
DEBUR AND BREAK SHARP EDGES
DO NOT SCALE DRAWING
REVISION
NAME
SIGNATURE
DATE
DRAWN
CHK'D
APPV'D
MFG
Q.A
MATERIAL:
WEIGHT:
TITLE:
DWG NO.
Side2
A3
SCALE:1:1
SHEET 1 OF 1

APPENDIX D: AGILITY SURGICAL PROCEDURE

1. Open joint and separate the syndesmosis

2. Align and secure jig to the tibia

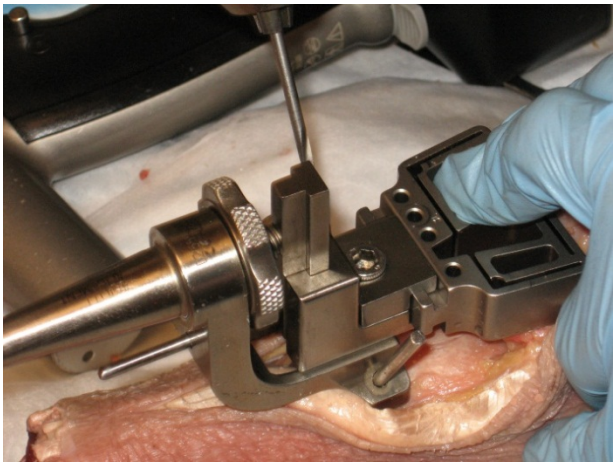

3. Make flat cuts to tibia and talus

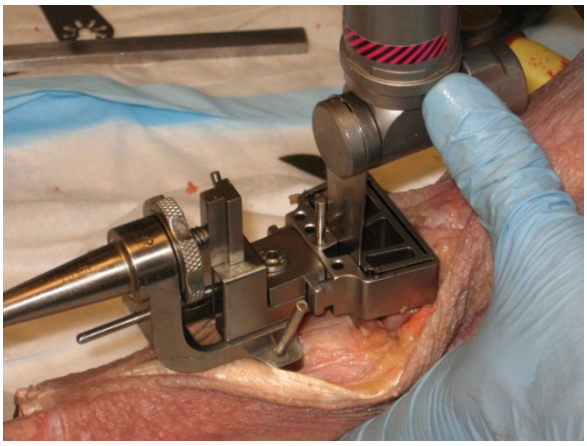

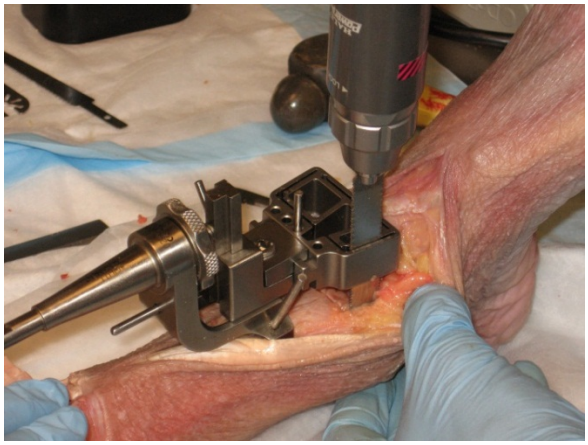

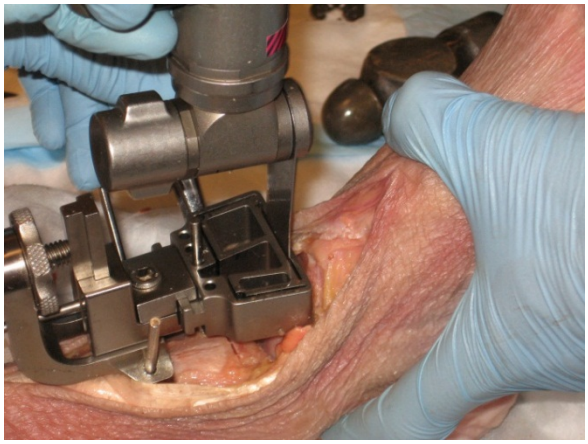

4. Make tibial fin cut

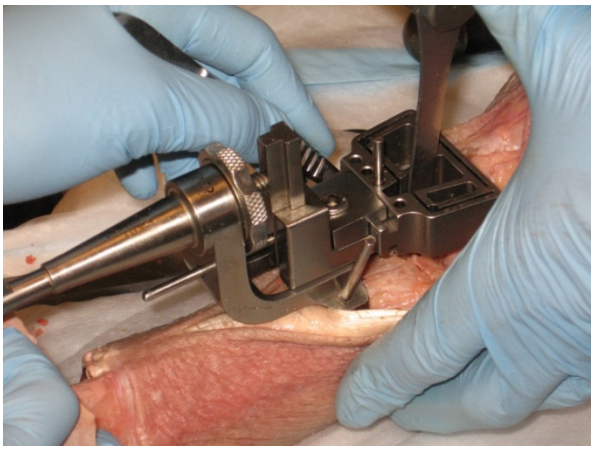

5. Clean up cuts and remove bone fragments

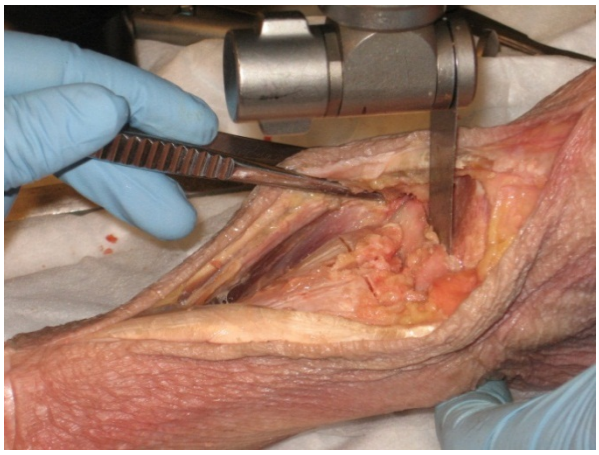

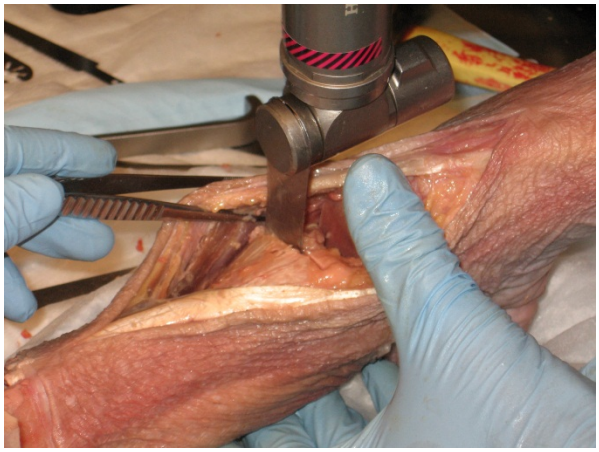

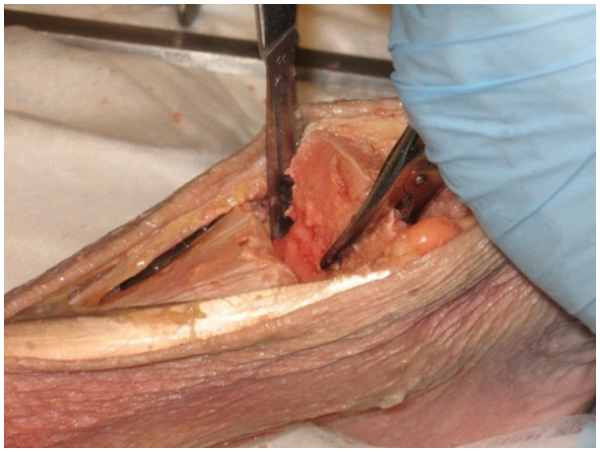

6. Insert trial tibial component to help align jig for talar fin cut

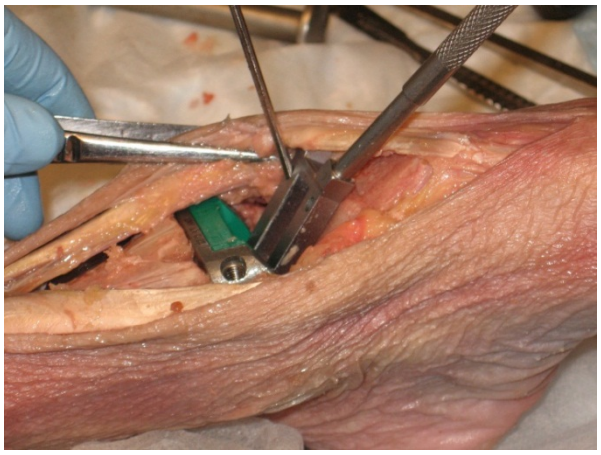

7. Drill and rasp out talar fin slot

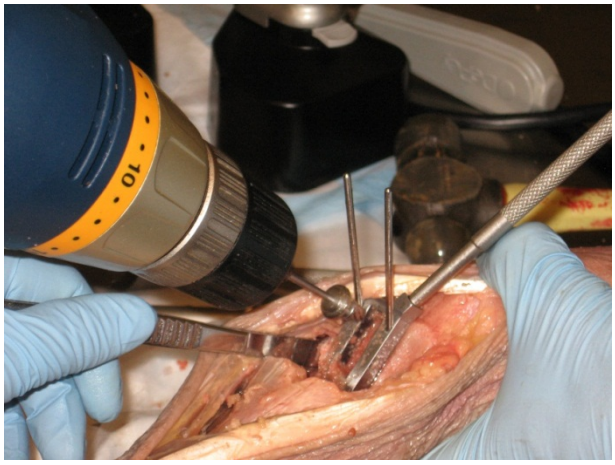

8. Install final components (no image)

9. Fuse the syndesmosis with a plate and screws

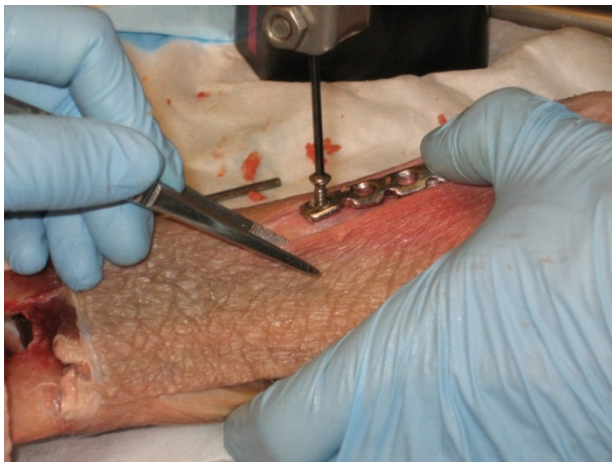

APPENDIX E: STAR SURGICAL PROCEDURE

1. Secure and align the jig on the tibia

2. Select the appropriate size guide and make the flat tibial cut

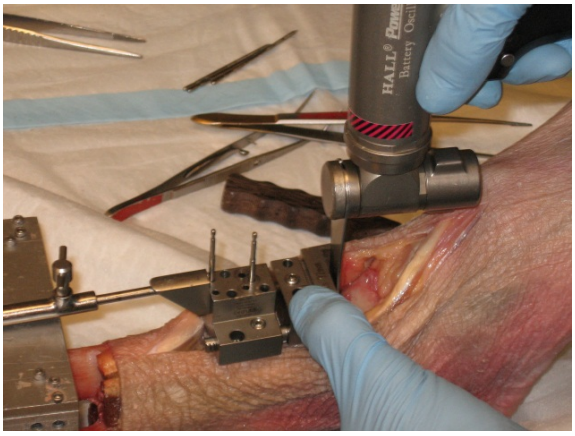

3. Remove the bone from the tibial cut

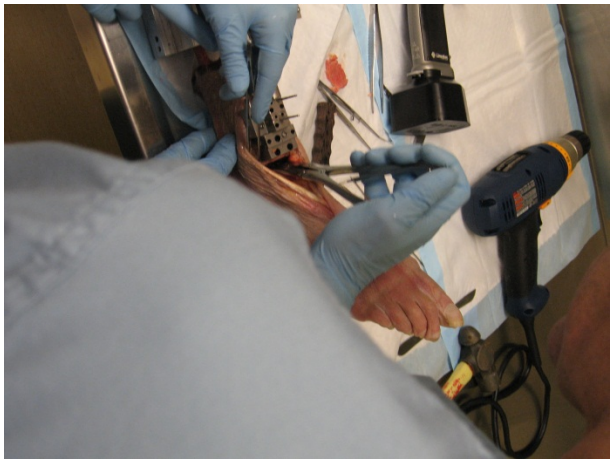

4. Make flat talar cut

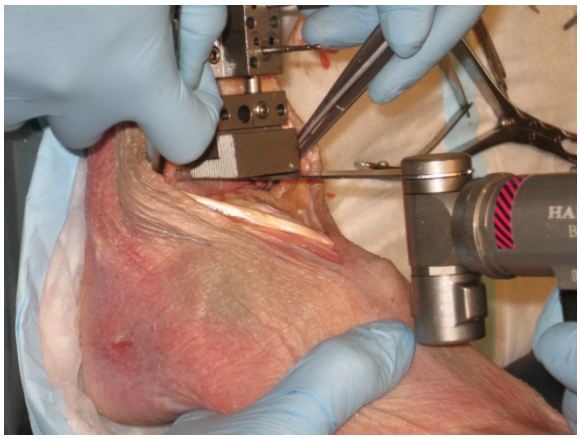

5. Select proper size talar component and align/secure jig for side cuts

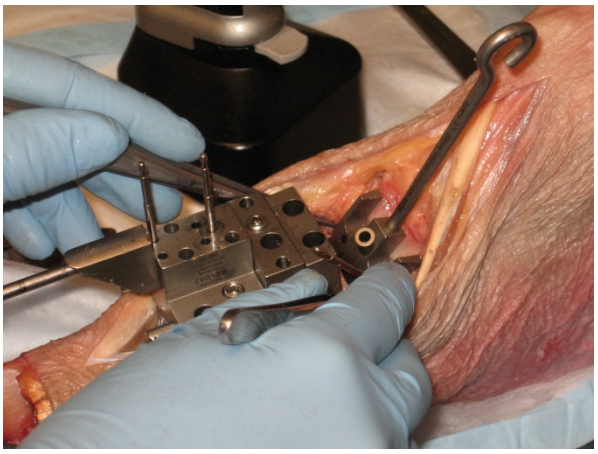

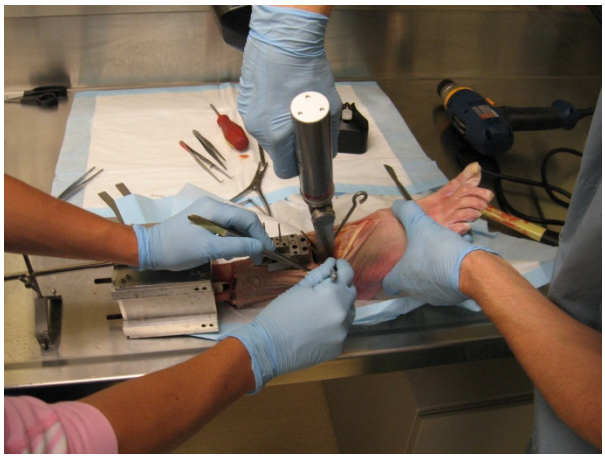

6. Remove bone fragments and clean up cuts

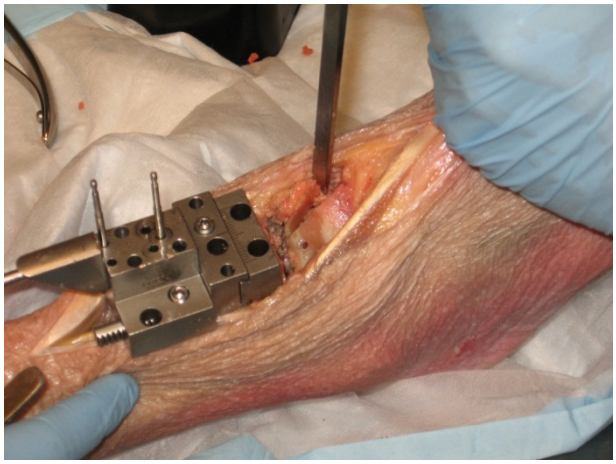

7. Fasten jig for diagonal A/P cuts

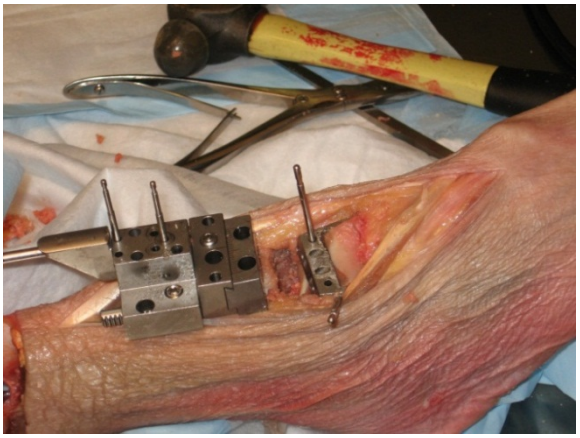

8. Make diagonal A/P cuts

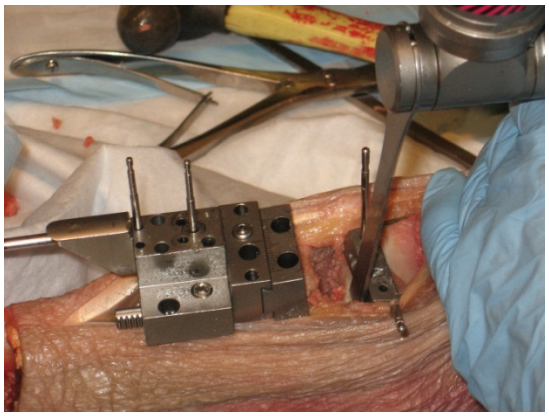

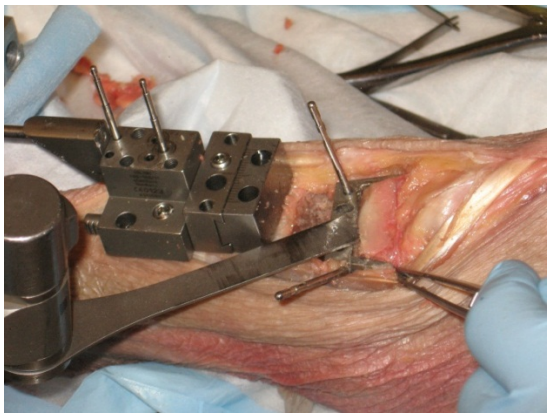

9. Attach jig and drill out fin slot

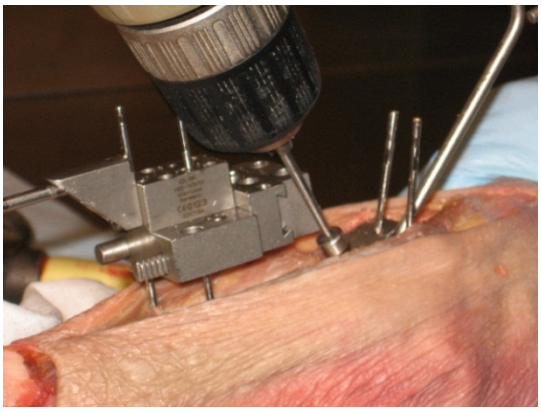

10. Clean out slot and install talar component


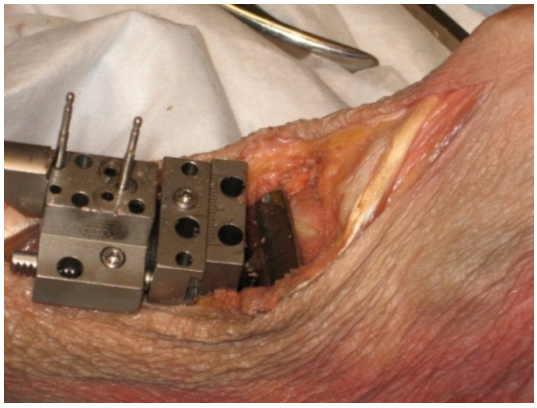

11. Drill out barrel holes and install tibial component

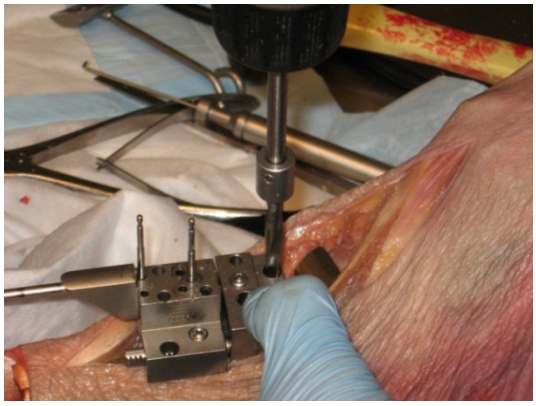
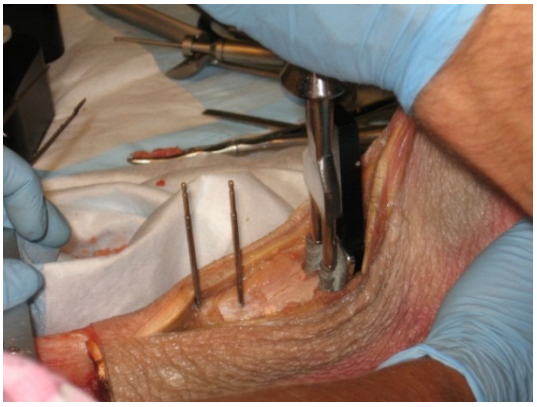

12. Select appropriate size meniscal component and insert (no image)

APPENDIX F: OPTOTRAK ACCURACY STUDY

F.1 SETUP

The accuracy study was performed using a linear translation platform (A25 graduated knob 3.5" UniSlide®, Velmex Inc., Bloomfield, NY) and a high precision rotation mount (PR01, Thorlabs Inc., Newton, NJ). The translational accuracy, the rotational accuracy, the combined accuracy when translations and rotations are applied, and the accuracy of measuring the relative displacement when using digitized points (as was employed in my experiment) were calculated.

The A25 Unislide is a screw-drive linear translation platform with a resolution of one thousandth of an inch and a travel of 3.5 inches. Its lead screw is calibrated to have a lead error of less than .0015 in/10 in length (0.015%). For the range being operated at (0 - .394 in), the resultant measurement error was less than 8 μm.

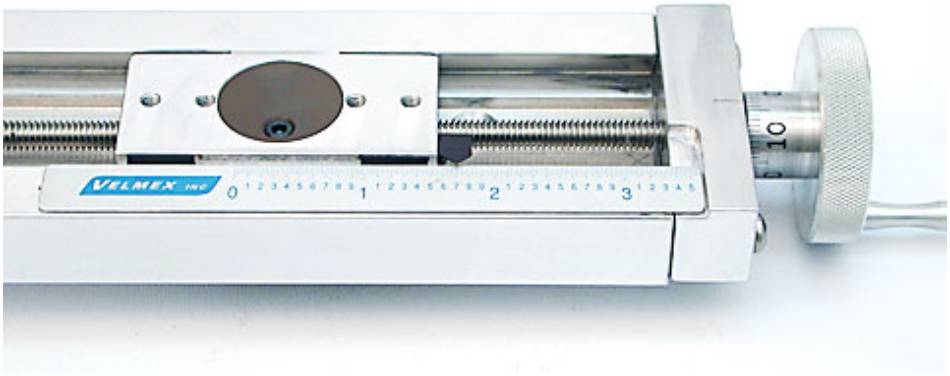

Figure 87: Velmex A25 Unislide

The PR01 is a high precision rotation mount with coarse rotation divisions of 1° and a vernier scale resolution of 5 arcmin, and fine rotation adjustment via micrometer with divisions of 2.4 arcmin, which has a resolution of 1 arcmin across a ±5° range and an accuracy of better than 1%.

Figure 88: Thorlabs PR01

The PR01 was mounted to an L-bracket, which in turn was mounted to the Unislide. A marker carrier was attached to the PR01 by a wire fixed to a ¼-20 machine screw by a nut, and the screw was threaded into one of the holes in the PR01.

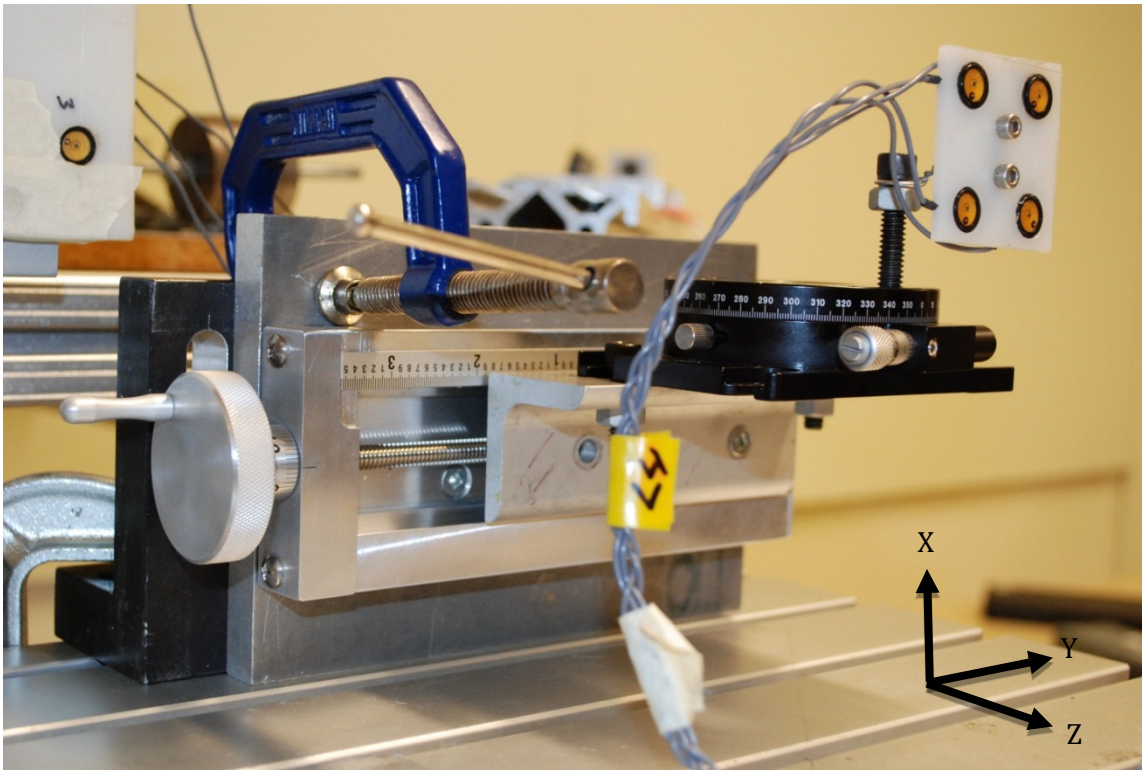

Figure 89: Optotrak accuracy test setup

F.2 PROTOCOL

The accuracy protocol was performed with the Optotrak at 3 separate distances away from the target markers: 1.5m, 2.0m, and 2.5m. Measurements were taken at several increments along/about each of the 3 axes to calculate the directional error over a range of translations and rotations (see tables 7-10).

The coordinate frame was designated to mimic that of the Optotrak: with positive X vertically up, Y horizontally to the right, and Z toward the camera.

Firstly, the whole assembly was clamped to the test bed such that the direction of the Unislide and/or PR01 was aligned with the axis of interest. As aligning it exactly with the Optotrak was impossible, specific points on the PR01 and/or Unislide were digitized in order to set up local axes for the measurements. The arrangement of digitized points varied depending on which test was being performed, and for the pure translation measurement the magnitude of the displacement was used rather than the projection onto the local reference frame.

The translational and angular displacements were determined using the transformation matrix (as previously described) between the initial and incremental target shots. Measurements were taken for 10 seconds at each increment, and the accuracy and precision were calculated.

The relative displacement test (fig. 90) was intended to mimic the micromotion measurement being done during the live tests. An aluminum bar with a tab was attached to the PR01 rotational platform, which was fixed to the table by the previously used L-bracket. An aluminum block with a tab was clamped to the table. The two tabs were aligned and set to flush in the zero degree position on the PR01. The tips of the tabs were digitized and the distance between them was determined with the Optotrak and Matlab program, as well as being mechanically measured with a micrometer for the gold standard.

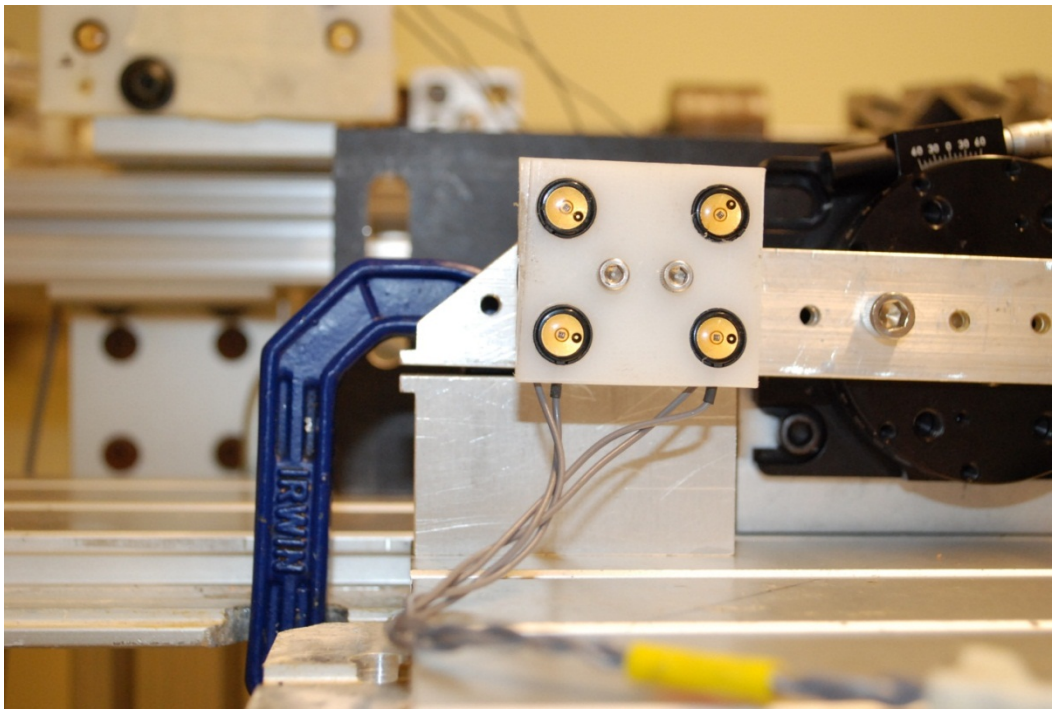

Figure 90: Relative displacement accuracy test setup

Table 7: Translation accuracy test increments

Displ.	mm	0.0254	0.1016	0.508	1.016	2.032	5.0038	10.0076
	in	0.001	0.004	0.02	0.04	0.08	0.197	0.394

Table 8: Rotation accuracy test increments

Angle	deg	0.04	0.16	0.48	1	5	10	20	40
	min	2.4	9.6	28.8					

Table 9: Combined translation and rotation accuracy test increments

Displ.	mm	0.1016	0.1016	0.1016	2.032	2.032	2.032	10.0076	10.0076	10.0076
	in	0.004	0.004	0.004	0.08	0.08	0.08	0.394	0.394	0.394
Angle	deg	0.16	1	10	0.16	1	10	0.16	1	10
	min	9.6			9.6			9.6		

Table 10: Relative displacement accuracy test increments

Angle	deg	0	0.04	0.16	0.32	0.68	1	2	4	6
	min		2.4	9.6	19.2	40.8				

Displacements and angle errors were determined for all three axes. The test combining translations and rotations were performed only once at each Optotrak distance with translation along the Y-axis and rotation about the X-axis. This was done to see whether the translational and rotational errors would be compounding or independent. The relative displacement test was performed twice, using rotations about the Y and Z axes.

F.3 RESULTS

The results from this accuracy test show that the setup used in this study were actually much better than the 0.1 mm stated in its specifications (table 11). The translational accuracy was closer to 10 μm with a resolution of 5 μm. The rotational accuracy was better than 0.1 degree. The accuracy of measuring relative displacements of digitized points was found to be approximately 30 μm, which is a manageable error considering the magnitudes of relative displacements were typically 0.1 mm or greater. However, the error estimates in this test were likely an overestimation due to the uncertainty and human error in the micrometer measurements.

Table 11: Results of the Optotrak accuracy study. Values are the average of the 1.5m and 2.0m tests. Repeatability and precision are given as one standard deviation, and accuracies are given as mean error ± 95% confidence interval.

Dir.	Repeatability (mm)	Precision (mm)	Trans Acc (mm)	Ang. Acc (deg)	Rel. Displ. (mm)
X	.0013	.0026	0.0036 ± 0.0070	0.0222 ± 0.0629	-
Y	.0016	.0025	-0.0077 ± 0.0044	0.0064 ± 0.0321	0.0306 ± 0.0181
Z	.0022	.0052	0.0035 ± 0.0029	-0.0141 ± 0.0309	-0.0078 ± 0.0081

F.4 ACCURACY STUDY DATA

Table 12: Repeatability (mm)

Direction	Optotrak Distance 1.5	2.0	2.5
X	0.000795	.001822	0.009622
Y	0.001021	.002093	0.016139
Z	0.001953	.002357	0.014485

Table 13: Precision (mm) – standard deviation of 500 frames (10 sec x 50 Hz) averaged over 5 trials randomly selected

Direction	Optotrak Distance 1.5	2.0	2.5
X	0.002198	0.002918	0.003336
Y	0.002636	0.002271	0.003178
Z	0.004698	0.005641	0.008302

Table 14: Displacement error measurements (mm)

Opto dist. (m)	Dir	0.0254	0.1016	0.508	1.016	2.032	5.0038	10.0076	Average Bias
1.5	X	0.0293	0.1016	0.4722	1.0282	2.0215	5.0157	10.0225	
		0.0039	0.0000	-0.0358	0.0122	-0.0105	0.0119	0.0149	0.0127 ± 0.0114
1.5	Y	0.0321	0.1005	0.5072	1.0139	2.0307	5.0005	10.0037	
		0.0067	-0.0011	-0.0008	-0.0021	-0.0013	-0.0033	-0.0039	0.0027 ± 0.0021
1.5	Z	0.0295	0.1008	0.5117	1.0153	2.0339	5.0043	10.0019	
		0.0041	-0.0008	0.0037	-0.0007	0.0019	0.0005	-0.0057	0.0025 ± 0.0020
2.0	X	0.0255	0.1038	0.5153	1.0240	2.0411	5.0168	10.0219	
		0.0001	0.0022	0.0073	0.0080	0.0091	0.0130	0.0143	0.0077 ± 0.0052
2.0	Y	0.0134	0.0881	0.4987	1.0049	2.0206	4.9824	9.9839	
		-0.0120	-0.0135	-0.0093	-0.0111	-0.0114	-0.0214	-0.0237	0.0146 ± 0.0056
2.0	Z	0.0284	0.1150	0.5193	1.0187	2.0354	5.0170	10.0064	
		0.0030	0.0134	0.0113	0.0027	0.0034	0.0132	-0.0012	0.0069 ± 0.0055
2.5	X	0.0307	0.1011	0.5057	1.0239	2.0417	5.0122	10.0217	
		0.0053	-0.0005	-0.0023	0.0079	0.0097	0.0084	0.0141	0.0069 ± 0.0046
2.5	Y	0.0181	0.0834	0.4859	0.9897	2.0138	4.9793	9.9762	
		-0.0073	-0.0182	-0.0221	-0.0263	-0.0182	-0.0245	-0.0314	0.0211 ± 0.0077
2.5	Z	0.0152	0.0919	0.5020	1.0110	2.0176	4.9956	9.9968	
		-0.0102	-0.0097	-0.0060	-0.0050	-0.0144	-0.0082	-0.0108	0.0092 ± 0.0032

Table 15: Rotation error measurements (deg)

Opto dist. (m)	Axis	0.04	0.16	0.48	1	5	10	20*	40*	Average Bias
1.5	X	0.0383	0.1608	0.4824	0.9944	4.9917	9.9785	20.0794	40.4069	
		-0.0017	0.0008	0.0024	-0.0056	-0.0083	-0.0215	0.0794	0.4069	0.0067 ± 0.0078
1.5	Y	0.0348	0.1553	0.4801	0.9901	4.9604	9.9315	20.0328	39.9791	
		-0.0052	-0.0047	0.0001	-0.0099	-0.0396	-0.0685	0.0328	-0.0209	0.0213 ± 0.0271
1.5	Z	0.0431	0.1628	0.4872	0.9851	4.9570	9.9943	20.0555	40.1141	
		0.0031	0.0028	0.0072	-0.0149	-0.0430	-0.0057	0.0555	0.1141	0.0128 ± 0.0154
2.0	X	0.0423	0.1757	0.4823	0.9977	5.0035	9.9732	20.0425	39.8656	
		0.0023	0.0157	0.0023	-0.0023	0.0035	-0.0268	0.0425	-0.1344	0.0088 ± 0.0103
2.0	Y	0.0181	0.1344	0.4582	0.9890	4.9650	10.1222	20.1279	40.0828	
		-0.0219	-0.0256	-0.0218	-0.0110	-0.0350	0.1222	0.1279	0.0828	0.0396 ± 0.0412
2.0	Z	0.0362	0.1557	0.4700	0.9850	4.9626	9.9380	19.9210	39.8671	
		-0.0038	-0.0043	-0.0100	-0.0150	-0.0374	-0.0620	-0.0790	-0.1329	0.0221 ± 0.0231
2.5	X	0.0391	0.1524	0.4508	0.9749	4.9751	9.9990	19.9896	39.6905	
		-0.0009	-0.0076	-0.0292	-0.0251	-0.0249	-0.0010	-0.0104	-0.3095	0.0148 ± 0.0130
2.5	Y	0.0037	0.1201	0.4344	0.9562	4.9041	9.9907	20.1364	40.1338	
		-0.0363	-0.0399	-0.0456	-0.0438	-0.0959	-0.0093	0.1364	0.1338	0.0451 ± 0.0282
2.5	Z	0.0438	0.1595	0.4801	0.9852	4.9589	9.9268	19.9537	39.9585	
		0.0038	-0.0005	0.0001	-0.0148	-0.0411	-0.0732	-0.0463	-0.0415	0.0223 ± 0.0294

* 20 and 40 degree measurements were not used in calculating the average errors because they were taken using the coarse adjustment on the PR01

Table 16: Relative displacement error measurements (mm)

Opto Dist. (m)	Rot. Axis		Rotation (deg) 0	0.04	0.16	0.32	0.68	1	2	4	6	Average Bias
1.5	Y	Meas.	6.18	6.21	6.46	6.81	7.54	8.19	10.32	14.52	18.77	
		Calc.		6.221	6.463	6.806	7.570	8.248	10.375	14.606	18.858	
		Err.		0.011	0.003	-0.004	0.030	0.058	0.055	0.086	0.088	0.0419 ± 0.0349
	Z	Meas.	6.245	6.28	6.55	6.84	7.585	8.235	10.34	14.61	18.88	
		Calc.		6.291	6.525	6.837	7.585	8.247	10.356	14.593	18.855	
		Err.		0.011	-0.025	-0.003	0.000	0.012	0.016	-0.017	-0.025	0.0136 ± 0.0091
2.0	Y	Meas.	6.19	6.24	6.45	6.81	7.51	8.16	10.31	14.57	18.81	
		Calc.		6.230	6.481	6.817	7.578	8.229	10.347	14.559	18.781	
		Err.		-0.010	0.031	0.007	0.068	0.069	0.037	-0.011	-0.029	0.0328 ± 0.0246
	Z	Meas.	6.21	6.26	6.505	6.855	7.585	8.22	10.36	14.57	18.80	
		Calc.		6.273	6.494	6.828	7.570	8.235	10.336	14.546	18.780	
		Err.		0.013	-0.011	-0.027	-0.015	0.015	-0.024	-0.024	-0.020	0.0186 ± 0.0059

Table 17: Combined translation and rotation error measurements (mm & deg)

		Displacement (mm)						
Opto dist. (m)	Angle	.1016	Error (mm;deg)	2.032		10.0076		Average Bias
1.5	.16	0.0944	-0.0072	2.0246	-0.0074	9.9968	-0.0108	
		0.1589	-0.0011	0.1609	0.0009	0.1614	0.0014	
1.5	1	0.1078	0.0062	2.0351	0.0031	9.9978	-0.0098	
		0.9961	-0.0039	1.0006	0.0006	0.9863	-0.0137	
1.5	10	0.1787	0.0771	2.1002	0.0682	10.0723	0.0647	
		9.9805	-0.0195	9.9766	-0.0234	9.9740	-0.0260	
2.0	.16	0.0867	-0.0149	2.0064	-0.0256	9.9700	-0.0376	
		0.1634	0.0034	0.1578	-0.0022	0.1601	0.0001	
2.0	1	0.0893	-0.0123	2.0060	-0.0260	9.9765	-0.0311	
		0.9832	-0.0168	0.9900	-0.0100	0.9837	-0.0163	
2.0	10	0.0258	-0.0758	1.9111	-0.1209	9.8566	-0.1510	
		9.9818	-0.0182	9.9869	-0.0131	10.0199	0.0199	
2.5	.16	0.1251	0.0235	2.0134	-0.0186	10.0045	-0.0031	
		0.1412	-0.0188	0.1762	0.0162	0.1668	0.0068	
2.5	1	0.4157	0.3141	2.0499	0.0179	10.0013	-0.0063	
		0.9764	-0.0236	1.0087	0.0087	1.0094	0.0094	
2.5	10	3.8869	3.7853	4.2973	2.2653	10.4299	0.4223	
		9.5323	-0.4677	9.9755	-0.0245	9.9744	-0.0256	

APPENDIX G: MATLAB DATA ANALYSIS PROGRAMS

G.1 OPT_ANKLE_ANGLES.M

```
% opt_ankle_angles.m
% Modified Sept 12, 2011 by Kurt McInnes

% opt_pfj_angles_Ankle_Version.m
% Modified  August 9, 2005 by Craig Davidson
% This file has been modified to analyze the optotrak ankle data

% Make sure to check that the path directory is correct and no other
ankle
% sample's directories are open as well as this can give erroneous
data.

% Make sure Matlab directory is set to desired output directory

% opt_pfj_angles.m
% June 10 2003 by Dave Wilson
% written to analyze pfj and tfj kinematics from Optotrak data

% modified from:
% all_pfj_angles.m
% modified January 10, 2000 to do patellar kinematics
% should only be used from within masterpfj
% modified from pli3.m
% June 8, 1999 by Dave Wilson
% for determining flexion angles for patellofemoral studies

%%
clear all
clf

NAME = 'C004';                % data file name - used for input (e.g.
C006)
SAMPLE = 'H1352R';             % specimen id # - used for output name
(e.g. H1347L)
NUM = '7';                    % Digitized point file # associated with
specific run.
LOAD = 'PF-DF 15N -18-40';  % loading configurations - used for output
name
side = 'r';                  % r/l changes direction conventions
imp = 2;                     % none = 1; star = 2; agility = 3
% for implants - make sure correct dimension file is referenced on
Line 225

name_of_output = [SAMPLE '_' LOAD];
opto_freq = 20; %optotrak data collection frequency[Hz]
```

```
errthresh = 1; % see below
maxthresh = 1; % see below
% errthresh: error level at which markers are rejected in trs
% maxthresh: error level at which angle results are rejected and
assigned the value "NaN"

% This path is the directory of each test you are doing -
% e.g. 'X:\Oxland\Ortho_Eng\Kurt\H1119R\MATLAB Input'
path(path,['H:\WORKING DIR\MATLAB Input\' SAMPLE])

%% Markers associated with rigid bodies

% baseframe = [1 2 3 4];
tibia_m = [5 6 7 8];
calca_m = [9 10 11 12];

if imp > 1
talus_m = [13 14 15 16];
tib_implant_m = [17 18 19 20];
tal_implant_m = [21 22 23 24];

SUFF = ['S_TIBIA'; 'S_CALCA'; 'S_TALUS'; 'S_TIBIM'; 'S_TALIM';
'DIGITIZ']; %static shot marker and digitize point files
% Use con_digi.m and con_static.m - make sure converted files are
moved into the working directory
else
SUFF = ['S_TIBIA'; 'S_CALCA'; 'DIGITIZ'];
end

%% DEFINING COORDINATE SYSTEMS
disp('WORKING OUT REFERENCE AXES')

    for q = 1:size(SUFF,1)

      filename = [SUFF(q,:),NUM,'.csv'];
      filesuff = [SUFF(q,:),NUM];
      filesave = SUFF(q,:);
      eval([ 'load -ascii ', filename,';']);
      eval([ filesave, ' = ', filesuff,';']);

    end
    % This loop loads up the files so you dont need to use the file
numbers

    % convention: this assigns axes as follows:
    % e1: Rotations ? - Dorsiflexion +ve, Plantarflexion -ve;
displacement q1 - lateral +ve, medial -ve
    % e2: Rotations ? - Inversion +ve, Eversion -ve; displacement q2 -
anterior +ve, posterior -ve
    % e3: Rotations ? - Internal +ve, External -ve; displacement q3 -
compression +ve, distraction -ve
```

```
    % as per Wu et al. J. Biomech 35 (2002)

    % ANATOMICAL REFERENCE POINTS
        %1=MM(medial maleolus);2=LM(lateral maleolus);3,4,5=prox tib;
        %PT = centroid of prox tib points
        PT = (DIGITIZ(3,:) + DIGITIZ(4,:) + DIGITIZ(5,:))/3;
        IM = (DIGITIZ(1,:) + DIGITIZ(2,:))/2;

        % AXES for kinematics analysis according to JCS convention
        ltib = unitv(PT' - IM')';
        ftib = unitv(DIGITIZ(2,:)' - DIGITIZ(1,:)')';
        ttib = ucross(ltib,ftib);

        lcal = ltib;
        fcal = ftib;
        tcal = ttib;

        % ORIGIN for kinematics analysis according to JCS convention
        tibrefpt = IM;
        calrefpt = IM;

        if imp==2          %2=STAR
            %  AXES  for  implant  coordinate  frames  derived  from
digitized pts
            ftibimp = unitv(DIGITIZ(7,:)' - DIGITIZ(6,:)')'; %e1
            ltibimp             =             ucross((DIGITIZ(10,:)'-
DIGITIZ(9,:)')',(DIGITIZ(8,:)'-DIGITIZ(9,:)')'); %e3
            ttibimp = ucross(ltibimp,ftibimp); %e2
            ftibimp   =   ucross(ttibimp,ltibimp);   %ensure   e1   is
orthogonal to e3 and e2

            ftalimp = unitv(DIGITIZ(12,:)' - DIGITIZ(11,:)')';
            ltalimp = ltibimp;
            ttalimp = ucross(ltalimp,ftalimp);
            ltalimp = ucross(ftalimp,ttalimp);

            % ORIGINS for tibial and talar implant coordinate frames
            tibimprefpt = ((DIGITIZ(6,:)'+DIGITIZ(7,:)')/2)';
            tib2refpt = tibimprefpt;
            talimprefpt = ((DIGITIZ(11,:)'+DIGITIZ(12,:)')/2)';
            tal2refpt = talimprefpt;

        elseif imp==3      %3=Agility
            ftibimp = unitv(DIGITIZ(7,:)' - DIGITIZ(6,:)')';
            ttibimp      =      ucross(ftibimp,(DIGITIZ(8,:)'      -
DIGITIZ(6,:)')');
            ltibimp = ucross(ftibimp,ttibimp);
            ttibimp = ucross(ltibimp,ftibimp);

            ftalimp = unitv(DIGITIZ(10,:)' - DIGITIZ(9,:)')';
            ltalimp = ltibimp;
            ttalimp = ucross(ltalimp,ftalimp);
```

```
            ltalimp = ucross(ftalimp,ttalimp);

            tibimprefpt = ((DIGITIZ(6,:)'+DIGITIZ(7,:)')/2)';
            tib2refpt = tibimprefpt;
            talimprefpt = ((DIGITIZ(9,:)'+DIGITIZ(10,:)')/2)';
            tal2refpt = talimprefpt;
        end

    % note that the longitudinal axes will always be oriented
proximally, flexion axes will be oriented laterally, and third axes
will be oriented anteriorly

% Making axes fit convention for the left foot
    if side == 'l'
        ttib = -ttib;
        tcal = -tcal;
        if imp==2
            ltibimp = -ltibimp;
            ttalimp = -ttalimp;
            ltib2 = ltibimp; ftib2 = ftibimp; ttib2 = ttibimp;
%duplicate tibial implant coordinate frame - to be attached to tibia
            ltal = ltalimp; ftal = ftalimp; ttal = ttalimp; %duplicate
talar implant coordinate frame - to be attached to talus
        elseif imp==3
            ttalimp = -ttalimp;
            ttibimp = -ttibimp;
            ltib2 = ltibimp;ftib2 = ftibimp;ttib2 = ttibimp;
            ltal = ltalimp;ftal = ftalimp;ttal = ttalimp;
        end
    elseif imp > 1
            ltib2 = ltibimp;ftib2 = ftibimp;ttib2 = ttibimp;
            ltal = ltalimp;ftal = ftalimp;ttal = ttalimp;
    end


    %% plot the systems and the reference markers (check to make sure
they are oriented properly)

    clf
    hold on

    plot_marks(S_TIBIA)
    plot_marks(S_CALCA)

    if imp > 1
    plot_marks(S_TALUS)
    plot_marks(S_TIBIM)
    plot_marks(S_TALIM)
    end

    plot_sys(calrefpt,fcal,lcal,tcal,80)
    plot_sys(tibrefpt,ftib,ltib,ttib,80)
```

```
    if imp > 1
    plot_sys(tal2refpt,ftal,ltal,ttal,80)
    plot_sys(tibimprefpt,ftibimp,ltibimp,ttibimp,80)
    plot_sys(talimprefpt,ftalimp,ltalimp,ttalimp,80)
    end

    axis('equal')
    view(ftib)
    hold off

    disp('Axis systems in the ankle ')
    %pause
    keyboard



%% DETERMINE JOINT ANGLES AND RELATIVE DISPLACEMENTS
    % load the continuous files

        disp('CONTINUOUS DATA')

    % load data
    % must convert C# dat file to csv first.
    filename = [NAME,'.csv'];
    filesuff = NAME;

    workstr = [ 'load -ascii ', filename];
    failstr = [filesuff, ' = NaN;'];

    filesuff

    %eval(workstr)

    eval(workstr,failstr)
    %eval([ filesave, ' = ', filesuff,';'])

    % analyze continuous data
    eval(['A  =', NAME,';']) %this sets A equal to the optotrak motion
file
    A = A(2:size(A,1),:);

    if imp > 1
    %  Define  4  corner  vectors  from  origin(static  refpt)  in
global(optotrak) frame


%%%%%%%%%%%%%%%%%%%%%%%%%%%%%%%%%%%%
    dim_STAR_MtibStal;
%%%%%%%%%%%%%%%%%%%%%%%%%%%%%%%%%%%%
```

```
    c1a = x1a*ftibimp + y1a*ttibimp + z1a*ltibimp;
    c2a = x2a*ftibimp + y2a*ttibimp + z2a*ltibimp;
    c3a = x3a*ftibimp + y3a*ttibimp + z3a*ltibimp;
    c4a = x4a*ftibimp + y4a*ttibimp + z4a*ltibimp;

    c1b = x1b*ftalimp + y1b*ttalimp + z1b*ltalimp;
    c2b = x2b*ftalimp + y2b*ttalimp + z2b*ltalimp;
    c3b = x3b*ftalimp + y3b*ttalimp + z3b*ltalimp;
    c4b = x4b*ftalimp + y4b*ttalimp + z4b*ltalimp;

    end

    if size(A,2) > 1
      % initialize error matrix, which summarizes the transformation
errors
      ERR = ones(size(A,1),3);

      %initialize displacement and angle matrices
      DISPL = ones(size(A,1),3);
      ANGLE = ones(size(A,1),3);
        if imp > 1

        ERR = ones(size(A,1),6);

      %initialize corner coordinate arrays
      C1tibb = ones(size(A,1),3);
      C2tibb = ones(size(A,1),3);
      C3tibb = ones(size(A,1),3);
      C4tibb = ones(size(A,1),3);

      C1tibi = ones(size(A,1),3);
      C2tibi = ones(size(A,1),3);
      C3tibi = ones(size(A,1),3);
      C4tibi = ones(size(A,1),3);

      C1talb = ones(size(A,1),3);
      C2talb = ones(size(A,1),3);
      C3talb = ones(size(A,1),3);
      C4talb = ones(size(A,1),3);

      C1tali = ones(size(A,1),3);
      C2tali = ones(size(A,1),3);
      C3tali = ones(size(A,1),3);
      C4tali = ones(size(A,1),3);

%      %initialize transform arrays
%       TR_tal = ones(4,4,size(A,1));
%       TR_talimp = ones(4,4,size(A,1));
%       TR_tib = ones(4,4,size(A,1));
%       TR_tibimp = ones(4,4,size(A,1));

        %initialize relative displacement magnitude arrays
```

```
        TIB_CORNERS = ones(size(A,1),4);
        TAL_CORNERS = ones(size(A,1),4);
        end
      for k = 1:(size(A,1))

         %BASE = mark_mat(A(k,:), baseframe);
         CAL = mark_mat(A(k,:), calca_m);
         TIB = mark_mat(A(k,:), tibia_m);
         if imp > 1
         TAL = mark_mat(A(k,:), talus_m);
         TIBIMP = mark_mat(A(k,:), tib_implant_m);
         TALIMP = mark_mat(A(k,:), tal_implant_m);
         end

         if size(CAL,1) > 2 && size(TIB,1) > 2
            % Calculating Calcaneus Position/Orientation with respect
to Tibia
            [calpt,            Trcal,            Errcal]            =
trs(calrefpt,CAL,S_CALCA,errthresh,2);
            [tibpt,            Trtib,            Errtib]            =
trs(tibrefpt,TIB,S_TIBIA,errthresh,2);

            if Errcal > maxthresh || Errtib > maxthresh
               caltibang = [NaN NaN NaN];
               tibpt = [NaN NaN NaN];
               calpt = [NaN NaN NaN];
            else

               caltibang                                             =
ankle_angles(Trtib,Trcal,ftib,ltib,ttib,fcal,lcal,tcal);  %here  tib  is
the reference and cal is the target segment

            end

            ANGLE(k,:) = caltibang;      %ANGLE is an array of the JCS
defined angles (alpha, beta, gamma)

            caltibvec = calpt - tibpt;

            %  rotate  vectors  from  tibial  and  calcaneal  coordinate
systems
            % to the current position according to JCS convention
            f_jcs = rot(Trtib,ftib');
            l_jcs = rot(Trcal,lcal');
            t_jcs = ucross(l_jcs,f_jcs);

            % determining components of caltibvec along the axes of
the JCS (ie. q1 - lateral, q2 - anterior, q3 - compression/superior
translation)
            DISPL(k,1) = dot(caltibvec',f_jcs);
            DISPL(k,2) = dot(caltibvec',t_jcs);
            DISPL(k,3) = dot(caltibvec',l_jcs);
```

```
        if imp > 1

                if k ==1
                    %translate the reference point for the tibia/talus
to the starting point of the implant to eliminate previous
migration/subsidence effects
                    [tib2refpt,          N1,          Errn1]          =
trs(tibimprefpt,TIBIMP,S_TIBIM,errthresh,2);
                    tibimprefpt = tib2refpt;
                    S_TIBIM = TIBIMP;
                    S_TIBIA2 = TIB;

                    [tal2refpt,          N2,          Errn2]          =
trs(talimprefpt,TALIMP,S_TALIM,errthresh,2);
                    talimprefpt = tal2refpt;
                    S_TALIM = TALIMP;
                    S_TALUS = TAL;
                end

%TIBIAL IMPLANT
            if size(TIB,1) > 2 && size(TIBIMP,1) > 2

               [tib2pt,           Trtib,           Errtib]           =
trs(tib2refpt,TIB,S_TIBIA2,errthresh,2);
               [tibimppt,         Trtibimp,        Errtibimp]        =
trs(tibimprefpt,TIBIMP,S_TIBIM,errthresh,2);

               if Errtib > maxthresh || Errtibimp > maxthresh

                   tibpt = [NaN NaN NaN];
                   tibimppt = [NaN NaN NaN];

               else

%                    TR_tib(:,:,k) = Trtib;
%                    TR_tibimp(:,:,k) = Trtibimp;

                  % determining corner position in current frame
                    C1tibb(k,:) = rot(Trtib,c1a') + tib2pt';
                    C1tibi(k,:) = rot(Trtibimp,c1a') + tibimppt';
                    C2tibb(k,:) = rot(Trtib,c2a') + tib2pt';
                    C2tibi(k,:) = rot(Trtibimp,c2a') + tibimppt';
                    C3tibb(k,:) = rot(Trtib,c3a') + tib2pt';
                    C3tibi(k,:) = rot(Trtibimp,c3a') + tibimppt';
                    C4tibb(k,:) = rot(Trtib,c4a') + tib2pt';
                    C4tibi(k,:) = rot(Trtibimp,c4a') + tibimppt';

                    % calculating relative displacement between tibial
implant and bone for each corner
```

```
                    TIB_CORNERS(k,1)   =   norm((rot(Trtibimp,c1a')   +
tibimppt') - (rot(Trtib,c1a') + tib2pt'));
                    TIB_CORNERS(k,2)   =   norm((rot(Trtibimp,c2a')   +
tibimppt') - (rot(Trtib,c2a') + tib2pt'));
                    TIB_CORNERS(k,3)   =   norm((rot(Trtibimp,c3a')   +
tibimppt') - (rot(Trtib,c3a') + tib2pt'));
                    TIB_CORNERS(k,4)   =   norm((rot(Trtibimp,c4a')   +
tibimppt') - (rot(Trtib,c4a') + tib2pt'));

                end
            end
% TALAR IMPLANT
            if size(TAL,1) > 2 && size(TALIMP,1) > 2

                [talpt,            Trtal,            Errtal]           =
trs(tal2refpt,TAL,S_TALUS,errthresh,2);
                [talimppt,         Trtalimp,         Errtalimp]        =
trs(talimprefpt,TALIMP,S_TALIM,errthresh,2);

                if Errtal > maxthresh || Errtalimp > maxthresh

                    talpt = [NaN NaN NaN];
                    talimppt = [NaN NaN NaN];

                else

%                     TR_tal(:,:,k) = Trtal;
%                     TR_talimp(:,:,k) = Trtalimp;

                    % determining corner position in current frame
                    C1talb(k,:) = rot(Trtal,c1b') + talpt';
                    C1tali(k,:) = rot(Trtalimp,c1b') + talimppt';
                    C2talb(k,:) = rot(Trtal,c2b') + talpt';
                    C2tali(k,:) = rot(Trtalimp,c2b') + talimppt';
                    C3talb(k,:) = rot(Trtal,c3b') + talpt';
                    C3tali(k,:) = rot(Trtalimp,c3b') + talimppt';
                    C4talb(k,:) = rot(Trtal,c4b') + talpt';
                    C4tali(k,:) = rot(Trtalimp,c4b') + talimppt';

                     % calculating relative displacement between talar
implant and bone for each corner
                    TAL_CORNERS(k,1)   =   norm((rot(Trtalimp,c1b')   +
talimppt') - (rot(Trtal,c1b') + talpt'));
                    TAL_CORNERS(k,2)   =   norm((rot(Trtalimp,c2b')   +
talimppt') - (rot(Trtal,c2b') + talpt'));
                    TAL_CORNERS(k,3)   =   norm((rot(Trtalimp,c3b')   +
talimppt') - (rot(Trtal,c3b') + talpt'));
                    TAL_CORNERS(k,4)   =   norm((rot(Trtalimp,c4b')   +
talimppt') - (rot(Trtal,c4b') + talpt'));

                end
```

```
            end
            ERR(k,:) = [k Errtib Errcal Errtal Errtibimp Errtalimp];
        else
            ERR(k,:) = [k Errtib Errcal];
        end


         else

             caltibang = [NaN NaN NaN];
             calpt = [NaN NaN NaN];
             tibpt = [NaN NaN NaN];


         end

      end

    else

      disp('No data at this position')

      Errcal = NaN;
      Errtib = NaN;

    end

         %fixing angle rotation direction for right foot
         if side == 'r'
            ANGLE(:,1) = -ANGLE(:,1);
            %ANGLE(:,2) = -ANGLE(:,2);
            ANGLE(:,3) = -ANGLE(:,3);
         end

%% Plotting JCS displacements and angles and the 4 corner relative
displacement magnitudes

    x = size(DISPL,1)/opto_freq;
    if imp == 1
        Proper_Output = [DISPL, ANGLE, ERR];
    clf; hold on
    plot((1/opto_freq):(1/opto_freq):x,DISPL(:,1),'k','linewidth',2)
    plot((1/opto_freq):(1/opto_freq):x,DISPL(:,2),'b','linewidth',2)
    plot((1/opto_freq):(1/opto_freq):x,DISPL(:,3),'r','linewidth',2)
    xlabel('Time (s)','fontsize',12)
    ylabel('Displacement (mm)','fontsize',12)
    leg = legend('q1 (flexion axis - lateral +ve)', 'q2 (floating axis
-    anterior    +ve)',    'q3    (long    axis    -    compression
+ve)','Location','Best');
    set(leg,'FontSize',9);
    title(['Intact    -    '    LOAD    ':    Translation    of    JCS
Origin'],'fontsize',14)
```

```
        set(gca, 'ygrid','on','box','on','fontsize', 12)
        saveas(gcf,['IntactJCSdispl' LOAD],'emf')

    clf; hold on
    plot((1/opto_freq):(1/opto_freq):x,ANGLE(:,1),'k','linewidth',2)
    plot((1/opto_freq):(1/opto_freq):x,ANGLE(:,2),'b','linewidth',2)
    plot((1/opto_freq):(1/opto_freq):x,ANGLE(:,3),'r','linewidth',2)
    xlabel('Time (s)','fontsize',12)
    ylabel('Angle (deg)','fontsize',12)
    leg = legend('\alpha (flexion axis - DF +ve)', '\beta (third axis
- INV +ve)', '\gamma (long axis - IR +ve)','Location','Best');
    set(leg,'FontSize',9);
    title(['Intact - ' LOAD ': Joint Rotation Angles'],'fontsize',14)
        set(gca, 'ygrid','on','box','on','fontsize', 12)
        saveas(gcf,['IntactJCSangles' LOAD],'emf')

    elseif imp == 2
        %               1-3     4-6     7-10        11-14       15-17
18-20   21-23   24-26   27-29   30-32   33-35   36-38   39-41   42-44
45-47   48-50   51-53   54-56   57-59   60-62   63-68
        Proper_Output   =   [DISPL,   ANGLE,   TIB_CORNERS,   TAL_CORNERS,
C1tibb,  C1tibi,  C2tibb,  C2tibi,  C3tibb,  C3tibi,  C4tibb,  C4tibi,
C1talb, C1tali, C2talb, C2tali, C3talb, C3tali, C4talb, C4tali, ERR];
    clf; hold on
    plot((1/opto_freq):(1/opto_freq):x,DISPL(:,1),'k','linewidth',2)
    plot((1/opto_freq):(1/opto_freq):x,DISPL(:,2),'b','linewidth',2)
    plot((1/opto_freq):(1/opto_freq):x,DISPL(:,3),'r','linewidth',2)
    xlabel('Time (s)','fontsize',12)
    ylabel('Displacement (mm)','fontsize',12)
    leg = legend('q1 (flexion axis - lateral +ve)', 'q2 (floating axis
-    anterior    +ve)',    'q3    (long    axis    -    compression
+ve)','Location','Best');
    set(leg,'FontSize',9);
    title(['STAR - ' LOAD ': Translation of JCS Origin'],'fontsize',
14)
        set(gca, 'ygrid','on','box','on','fontsize', 12)
        saveas(gcf,['STAR-JCSdispl' LOAD],'emf')

    clf; hold on
    plot((1/opto_freq):(1/opto_freq):x,ANGLE(:,1),'k','linewidth',2)
    plot((1/opto_freq):(1/opto_freq):x,ANGLE(:,2),'b','linewidth',2)
    plot((1/opto_freq):(1/opto_freq):x,ANGLE(:,3),'r','linewidth',2)
    xlabel('Time (s)','fontsize',12)
    ylabel('Angle (deg)','fontsize',12)
    leg = legend('\alpha (flexion axis - DF +ve)', '\beta (third axis
- INV +ve)', '\gamma (long axis - IR +ve)','Location','Best');
    set(leg,'FontSize',9);
    title(['STAR - ' LOAD ': Joint Rotation Angles'],'fontsize',14)
        set(gca, 'ygrid','on','box','on','fontsize', 12)
        saveas(gcf,['STAR-JCSangles' LOAD],'emf')

    clf; hold on
```

```
plot((1/opto_freq):(1/opto_freq):x,TIB_CORNERS(:,1),'k','linewidth',2)

plot((1/opto_freq):(1/opto_freq):x,TIB_CORNERS(:,2),'b','linewidth',2)

plot((1/opto_freq):(1/opto_freq):x,TIB_CORNERS(:,3),'r','linewidth',2)

plot((1/opto_freq):(1/opto_freq):x,TIB_CORNERS(:,4),'g','linewidth',2)
    xlabel('Time (s)','fontsize',12)
    ylabel('Displacement Magnitude (mm)','fontsize',12)
    leg    =    legend('Corner    1    (anterolateral)',    'Corner    2
(anteromedial)',    'Corner    3    (posterolateral)',    'Corner    4
(posteromedial)','Location','Best');
    set(leg,'FontSize',9);
    title(['STAR  -  '  LOAD  ':  Implant  Relative  Displacements  -
Tibia'],'fontsize',14)
        set(gca, 'ygrid','on','box','on','fontsize', 12)
        saveas(gcf,['STAR-TibRelDispl' LOAD],'emf')

    clf; hold on

plot((1/opto_freq):(1/opto_freq):x,TAL_CORNERS(:,1),'k','linewidth',2)

plot((1/opto_freq):(1/opto_freq):x,TAL_CORNERS(:,2),'b','linewidth',2)

plot((1/opto_freq):(1/opto_freq):x,TAL_CORNERS(:,3),'r','linewidth',2)

plot((1/opto_freq):(1/opto_freq):x,TAL_CORNERS(:,4),'g','linewidth',2)
    xlabel('Time (s)','fontsize',12)
    ylabel('Displacement Magnitude (mm)','fontsize',12)
    leg    =    legend('Corner    1    (anterolateral)',    'Corner    2
(anteromedial)',    'Corner    3    (posterolateral)',    'Corner    4
(posteromedial)','Location','Best');
    set(leg,'FontSize',9);
    title(['STAR  -  '  LOAD  ':  Implant  Relative  Displacements  -
Talus'],'fontsize',14)
        set(gca, 'ygrid','on','box','on','fontsize', 12)
        saveas(gcf,['STAR-TalRelDispl' LOAD],'emf')

    else
        Proper_Output  =  [DISPL,  ANGLE,  TIB_CORNERS,  TAL_CORNERS,
C1tibb,  C1tibi,  C2tibb,  C2tibi,  C3tibb,  C3tibi,  C4tibb,  C4tibi,
C1talb, C1tali, C2talb, C2tali, C3talb, C3tali, C4talb, C4tali, ERR];
    clf; hold on
    plot((1/opto_freq):(1/opto_freq):x,DISPL(:,1),'k','linewidth',2)
    plot((1/opto_freq):(1/opto_freq):x,DISPL(:,2),'b','linewidth',2)
    plot((1/opto_freq):(1/opto_freq):x,DISPL(:,3),'r','linewidth',2)
    xlabel('Time (s)','fontsize',12)
    ylabel('Displacement (mm)','fontsize',12)
    leg = legend('q1 (flexion axis - lateral +ve)', 'q2 (floating axis
-    anterior    +ve)',    'q3    (long    axis    -    compression
+ve)','Location','Best');
```

```
    set(leg,'FontSize',9);
    title(['Agility    -    '    LOAD    ':    Translation    of    JCS
Origin'],'fontsize',14)
        set(gca, 'ygrid','on','box','on','fontsize', 12)
        saveas(gcf,['Agility-JCSdispl' LOAD],'emf')

    clf; hold on
    plot((1/opto_freq):(1/opto_freq):x,ANGLE(:,1),'k','linewidth',2)
    plot((1/opto_freq):(1/opto_freq):x,ANGLE(:,2),'b','linewidth',2)
    plot((1/opto_freq):(1/opto_freq):x,ANGLE(:,3),'r','linewidth',2)
    xlabel('Time (s)','fontsize',12)
    ylabel('Angle (deg)','fontsize',12)
    leg = legend('\alpha (flexion axis - DF +ve)', '\beta (third axis
- INV +ve)', '\gamma (long axis - IR +ve)','Location','Best');
    set(leg,'FontSize',9);
    title(['Agility - ' LOAD ': Joint Rotation Angles'],'fontsize',14)
        set(gca, 'ygrid','on','box','on','fontsize', 12)
        saveas(gcf,['Agility-JCSangles' LOAD],'emf')

    clf; hold on

plot((1/opto_freq):(1/opto_freq):x,TIB_CORNERS(:,1),'k','linewidth',2)

plot((1/opto_freq):(1/opto_freq):x,TIB_CORNERS(:,2),'b','linewidth',2)

plot((1/opto_freq):(1/opto_freq):x,TIB_CORNERS(:,3),'r','linewidth',2)

plot((1/opto_freq):(1/opto_freq):x,TIB_CORNERS(:,4),'g','linewidth',2)
    xlabel('Time (s)','fontsize',12)
    ylabel('Displacement Magnitude (mm)','fontsize',12)
    leg    =    legend('Corner    1    (anterolateral)',    'Corner    2
(anteromedial)',    'Corner    3    (posterolateral)',    'Corner    4
(posteromedial)','Location','Best');
    set(leg,'FontSize',9);
    title(['Agility  -  '  LOAD  ':  Implant  Relative  Displacements  -
Tibia'],'fontsize',14)
        set(gca, 'ygrid','on','box','on','fontsize', 12)
        saveas(gcf,['Agility-TibRelDispl' LOAD],'emf')

    clf; hold on

plot((1/opto_freq):(1/opto_freq):x,TAL_CORNERS(:,1),'k','linewidth',2)

plot((1/opto_freq):(1/opto_freq):x,TAL_CORNERS(:,2),'b','linewidth',2)

plot((1/opto_freq):(1/opto_freq):x,TAL_CORNERS(:,3),'r','linewidth',2)

plot((1/opto_freq):(1/opto_freq):x,TAL_CORNERS(:,4),'g','linewidth',2)
    xlabel('Time (s)','fontsize',12)
    ylabel('Displacement Magnitude (mm)','fontsize',12)
```

```
    leg    =    legend('Corner    1    (anterolateral)',    'Corner    2
(anteromedial)',    'Corner    3    (posterolateral)',    'Corner    4
(posteromedial)','Location','Best');
    set(leg,'FontSize',9);
    title(['Agility  -  '  LOAD  ':  Implant  Relative  Displacements  -
Talus'],'fontsize',14)
        set(gca, 'ygrid','on','box','on','fontsize', 12)
        saveas(gcf,['Agility-TalRelDispl' LOAD],'emf')
    end

eval('ERRF = ERR;')

dlmwrite                                                ([name_of_output
'.csv'],Proper_Output,'delimiter',',','precision',16)
```

G.2 ANKLE_ANGLES.M

```
function [JCS]=ankle_angles(Trf,Trt,ff,lf,tf,ft,lt,tt)
% Modified Sept 12, 2011 by Kurt McInnes
% function spine_angles.m
% modified from find_angles.m, Oct. 21, 1997
%  by David Wilson
% this function finds the Cardan agles of flexion, ad/adduction and
% axial rotation of the spine as defined by the standardization
proposal
% of Cole et al, J. Biomech Eng. 115:344-349, Nov. 1993

% Input: t
% Output: the matrix CA: column 1: flexion; column 2: inv/ev;
% column 3: int/ext rot

i = 1;

% Determine the orientations of these axes in the reference and target
segments
% fi,li,ti refer to the axes in the reference segment: tibia
% fj,lj,tj refer to the axes in the target segment: calcaneus

     fj = Trt(2:4,2:4)*ft';
     lj = Trt(2:4,2:4)*lt';
     tj = Trt(2:4,2:4)*tt';

     fi = Trf(2:4,2:4)*ff';
     li = Trf(2:4,2:4)*lf';
     ti = Trf(2:4,2:4)*tf';

% Normalize these vectors

   fi = fi/norm(fi);
   li = li/norm(li);
   ti = ti/norm(ti);

   fj = fj/norm(fj);
   lj = lj/norm(lj);
   tj = tj/norm(tj);

% Determine the unit vectors e1,e2 and e3

  e1 = fi;

  e3 = lj;

  e2 = cross(e3,e1)/norm(cross(e1,e3));
```

```
%  Calculate the magnitude and direction of the Cardan angles

%plantarflexion/dorsiflexion
    v1 = (e3 - (e3'*e1)*e1)/norm(e3 - (e3'*e1)*e1); %projecting e3 and
initial  e3  position  (li)  onto  plane  normal  to  flexion  axis  and
normalizing
    v2 = (li - (li'*e1)*e1)/norm(li - (li'*e1)*e1);

    JCS(i,1) = 180/pi*acos(v1'*v2);

       if  e2'*li  >  0           %DF  is  +ve  according  to  Wu  2002  JCS
convention

          JCS(i,1) = -JCS(i,1);

       end

%inversion/eversion
    v3  =  (li  -  (li'*e2)*e2)/norm(li  -  (li'*e2)*e2);  %projecting
initial e3 (li) onto plane normal to inv/ev axis - by definition e3
belongs to this plane already

    JCS(i,2) = 180/pi*acos(e3'*v3);

       if cross(e2,e3)'*v3 > 0        %INV is +ve

           JCS(i,2) = -JCS(i,2);

       end

%internal/external rotation
    v4 = (e1 - (e1'*e3)*e3)/norm(e1 - (e1'*e3)*e3);
    v5 = (fj - (fj'*e3)*e3)/norm(fj - (fj'*e3)*e3);

    JCS(i,3) = 180/pi*acos(v5'*v4);


       if v5'*e2 > 0

            JCS(i,3) = -JCS(i,3);     %IR is +ve

       end

% remove complex parts of angles

JCS = real(JCS);
```

G.3 TRS.M

```
function [NOW, T, Err] = trs(THEN,REFNOW,REFTHEN,errthresh,option)
% trs.m
% [NOW, T, Err] = trs(THEN,REFNOW,REFTHEN,errthresh)
% this function transforms the coordinates of the
% points in the matrix THEN to the coordinate
% system defined by the reference points REFNOW
% that were in the system REFTHEN
%
% modified March 30, 2000: if option 2 is selected,
% then the points are considered to match exactly [1 2 3 4] in refthen
% corresponds to [1 2 3 4] in refnow

if size(REFNOW,1) < 3 | size(REFTHEN,1) < 3
   NOW = [NaN NaN NaN];
   Err = NaN;
   T = NaN .* eye(4);
   return
end

% determine order of points

if nargin < 4, errthresh = 1.5, end

[Or,Err,For] = best_order4(REFTHEN,REFNOW,errthresh);

% option 2 allows the order to be prescribed if points are
% known to correspond

if nargin > 4
if option == 2
   minsize = min([size(REFNOW,1) size(REFTHEN,1)]) ;
   For = 1:minsize;
   Or = 1:minsize;
end
end

% determine transformation matrix

[T,Err] = vwd(REFTHEN(For,:),REFNOW(Or,:));


% transform

NOW = transform(T,THEN);
```

G.4 VWD.M

```
function [T, err] = vwd(A,Q)
% vwd.m
% started June 30, 1995 by Dave Wilson
%
% based on the algorithm developed by Veldpaus, Woltring, Dortmans, J.
Biomechanics,
% V. 21, 1988, pp 45-54
% This takes as input the original positions of the reference markers
% and the final positions of the reference markers, and generates
% the rotation matrix R and the translation vector v between them
%
% The rows of A are the initial positions
% The rows of Q are the final positions



% n is the number of points defining the reference system

n = size(A,1);
G = zeros(3,3);

% a and p are the average vectors: row vectors

a = (1/n)*sum(A);
p = (1/n)*sum(Q);

% G is the average matrix

for i = 1:n

   g = (Q(i,:)-p)'*(A(i,:)-a);
   G = G+g;

end

G = 1/n*G;

ad = adj(G);

detg = det(G);

P = G'*G;

j1 = P(1,1) + P(2,2) + P(3,3);

pad = adj(P);

j2 = pad(1,1) + pad(2,2) + pad(3,3);
```

```
j3 = detg*detg;

% find beta1, beta2, beta3

eps = 10E-10;
x=1;
y=1;
h1 = sqrt(j2)/j1;
h2 = detg*sqrt(j1)/j2;

test = 1000;

while test > eps

Det = x*y - h1*h2;
help1 = 0.5*(1-x*x+2*h1*y);
help2 = 0.5*(1 - y*y + 2*h2*x);
dx = (y*help1 + h1*help2)/Det;
dy = (h2*help1 + x*help2)/Det;

test = (dx*dx/x*x + dy*dy/y*y);

x = x+dx;
y = y+dy;

end

x = x+dx;
y = y+dy;

beta1 = x*sqrt(j1);
beta2 = y*sqrt(j2);
beta3 = detg;

R = (beta1*G + ad)*inv(P + beta2*eye(3));

% v is the translation vector

v = p - (R*a')';

% compute final position of the points predicted by calculated
transformation

for i = 1:size(A,1)

    F(i,:) = [v + (R*(A(i,:))')'];

end

% determine the error in the predicted position and the actual
position
```

```
point_error = F-Q;

total_error = 0;

max_error = 0.0000000001;

for j = 1:size(A,1)

    total_error = total_error+norm(point_error(j,:));
    if norm(point_error(j,:)) > max_error
    max_error = norm(point_error(j,:));
    end

end

% error can be the total difference between predicted and actual
position (total_error)
% or the maximum error

err = total_error;
%err = max_error;

% set up a 4X4 transformation matrix containing v and R

T(1,:) = [1 0 0 0];
T(2:4,1) = v';
T(2:4,2:4) = R;
```

APPENDIX H: JCS ANGLE PLOTS

L 15 N Intact PF-DF

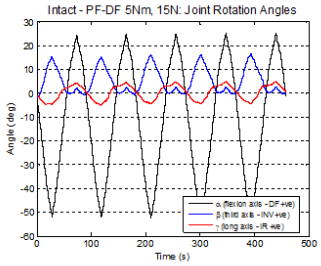

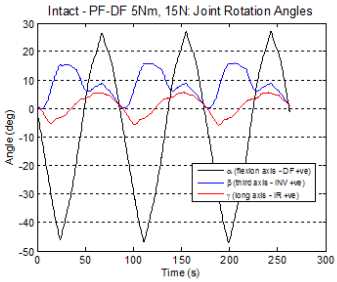

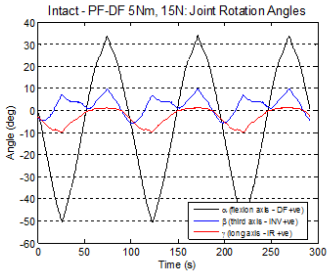

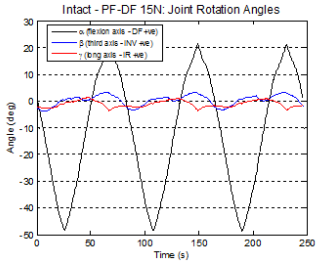

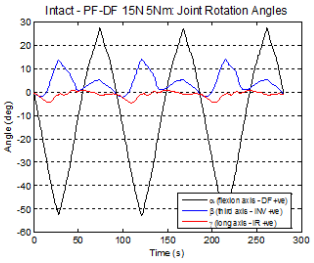

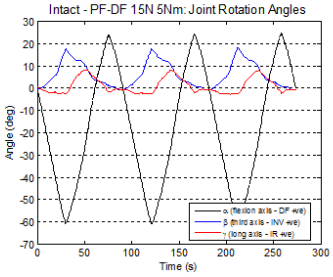

15N Agility PF-DF

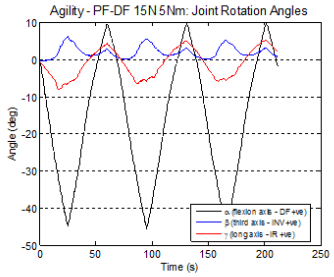

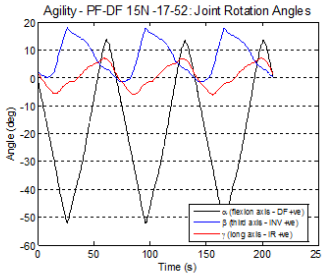

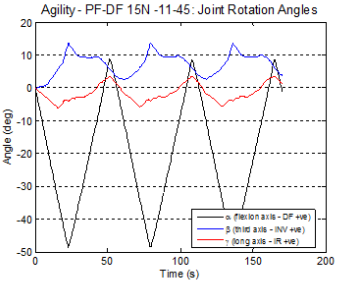

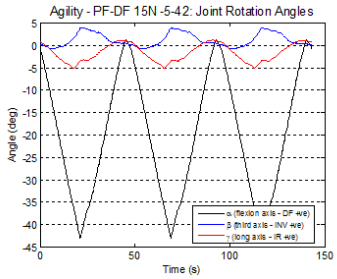

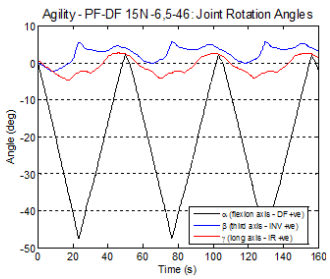

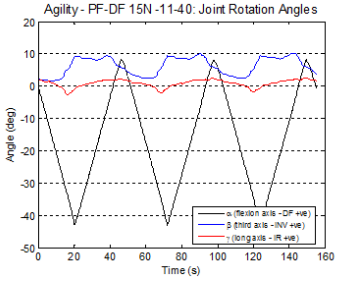

R 15N Intact PF-DF

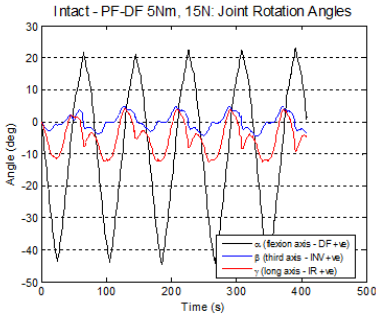

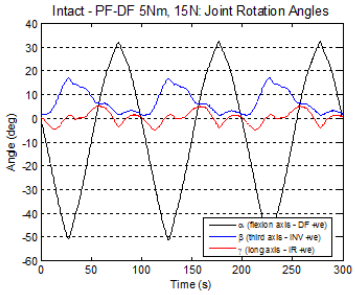

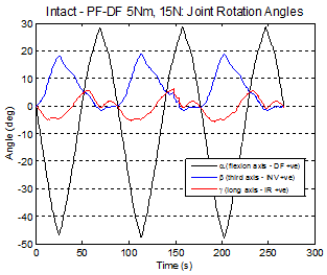

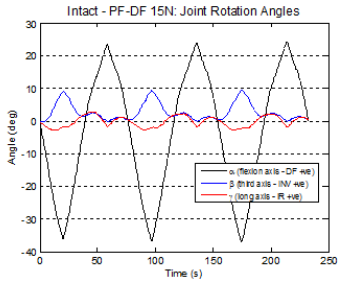

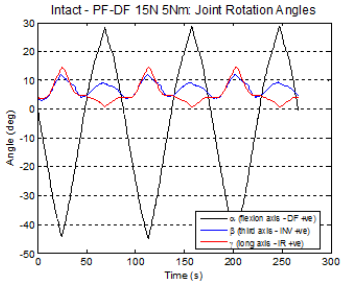

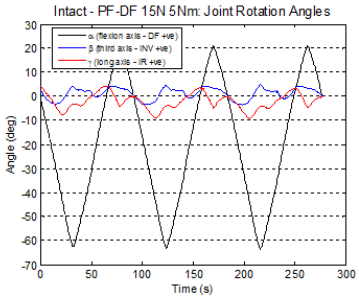

15N STAR PF-DF

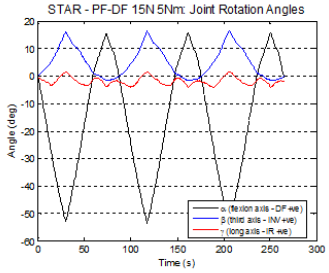

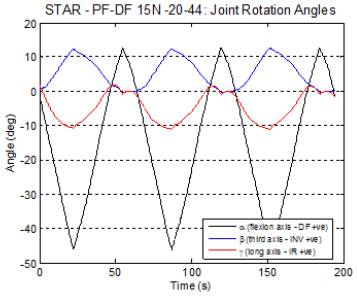

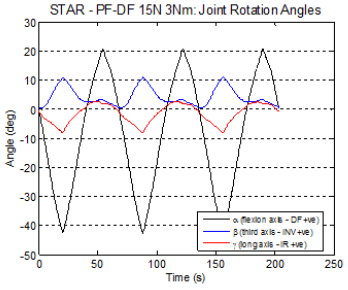

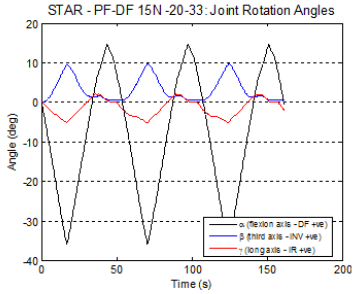

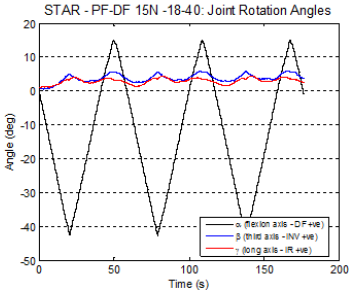

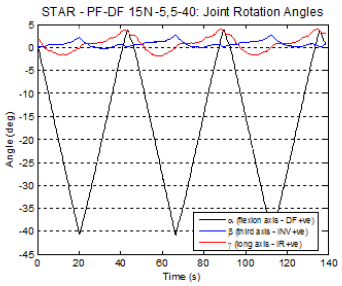

L 300 N Intact PF-DF

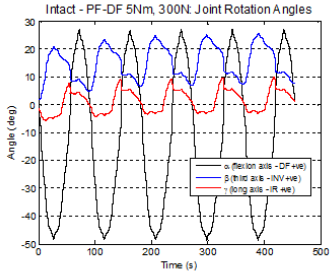

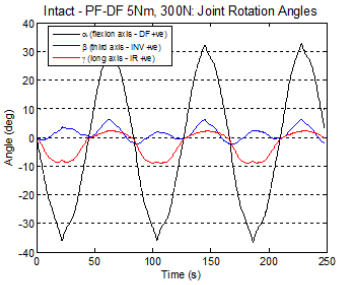

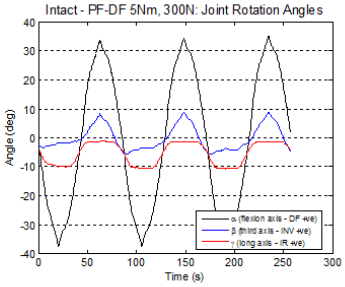

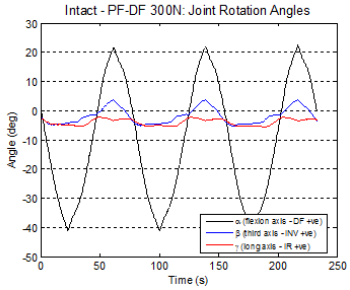

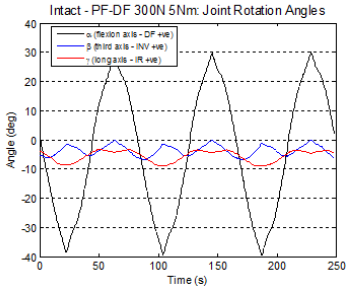

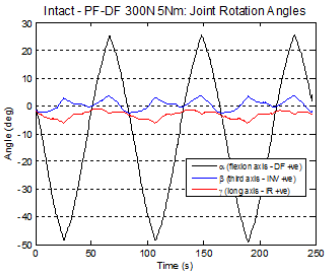

300N Agility PF-DF

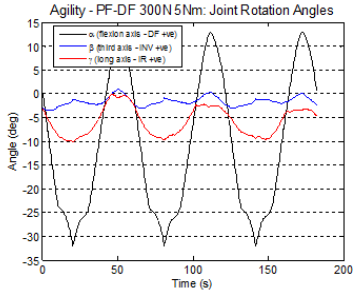

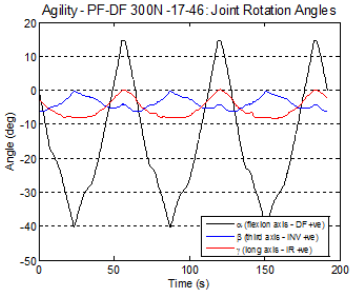

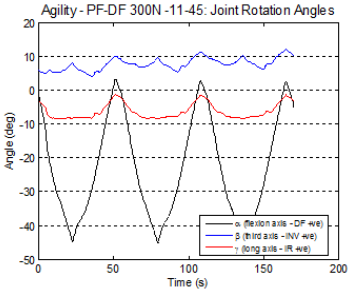

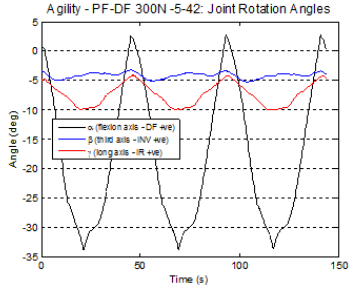

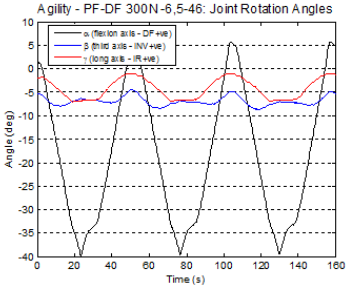

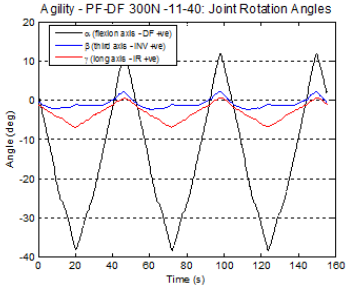

R 300N Intact PF-DF

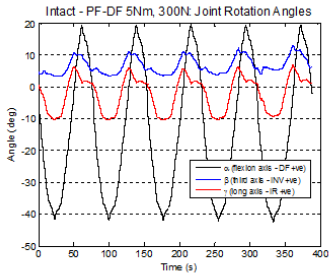

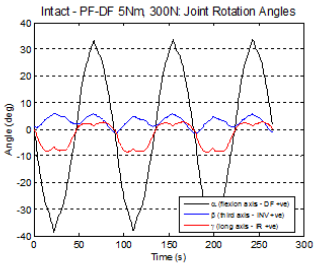

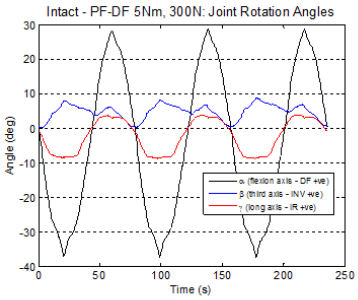

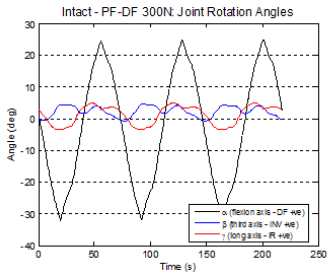

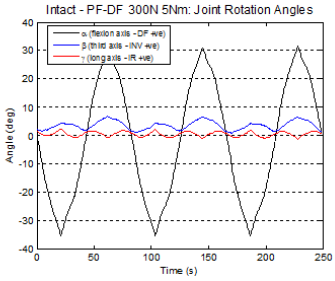

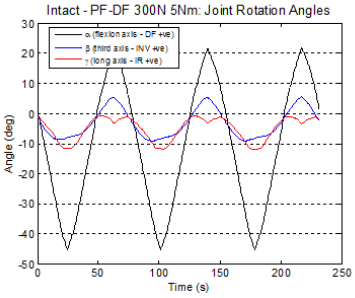

300N STAR PF-DF

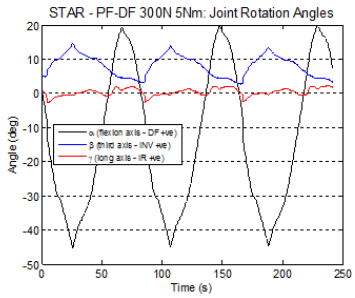

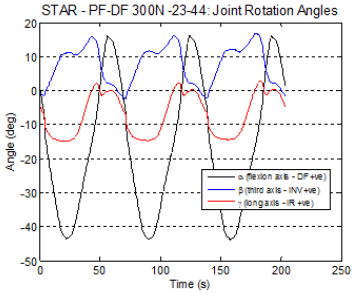

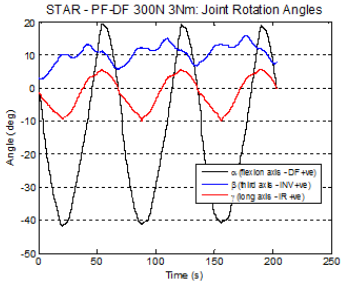

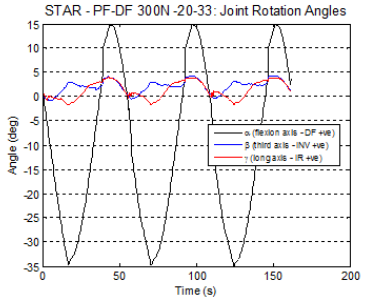

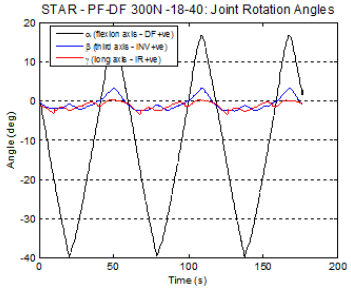

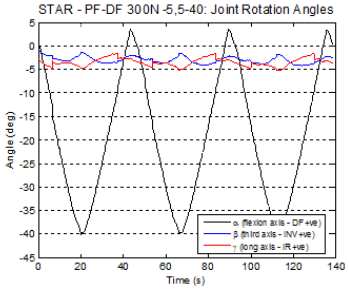

L 15 N Intact INV-EV

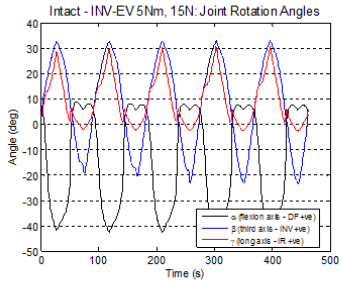
Intact - INV-EV 5Nm, 15N: Joint Rotation Angles

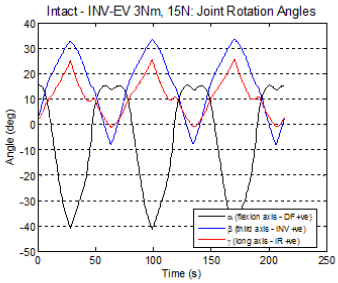
Intact - INV-EV 3Nm, 15N: Joint Rotation Angles

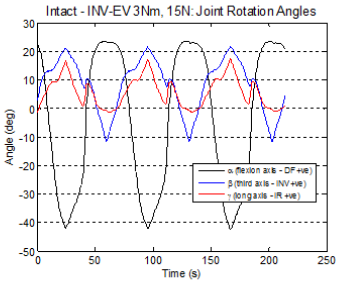
Intact - INV-EV 3Nm, 15N: Joint Rotation Angles

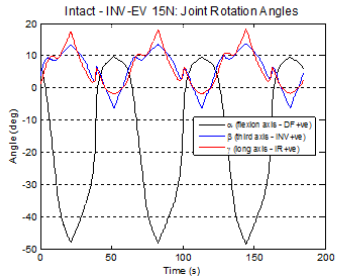
Intact - INV-EV 15N: Joint Rotation Angles

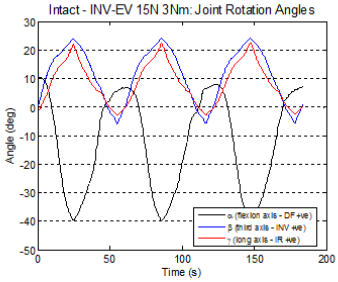
Intact - INV-EV 15N 3Nm: Joint Rotation Angles

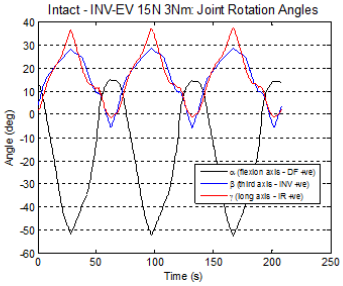
Intact - INV-EV 15N 3Nm: Joint Rotation Angles

15N Agility INV-EV

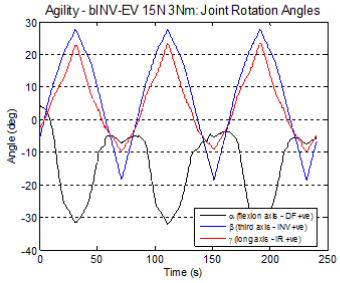
Agility - bINV-EV 15N 3Nm: Joint Rotation Angles

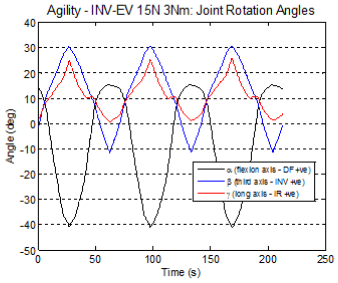
Agility - INV-EV 15N 3Nm: Joint Rotation Angles

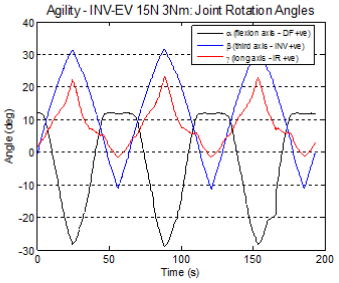
Agility - INV-EV 15N 3Nm: Joint Rotation Angles

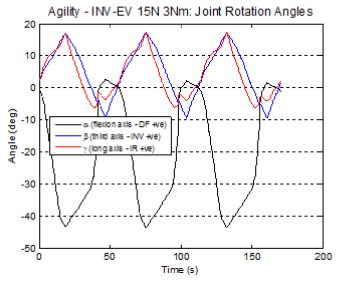
Agility - INV-EV 15N 3Nm: Joint Rotation Angles

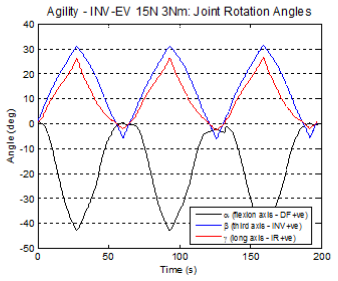
Agility - INV-EV 15N 3Nm: Joint Rotation Angles

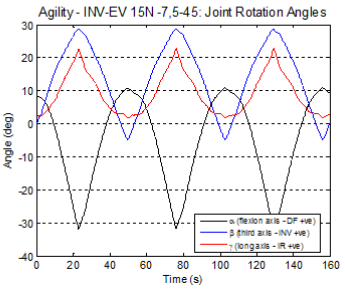
Agility - INV-EV 15N -7,5-45: Joint Rotation Angles

R 15N Intact INV-EV

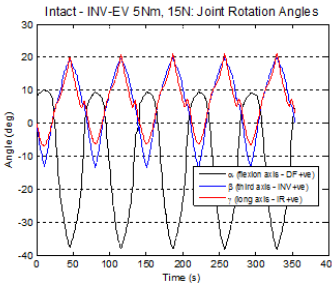

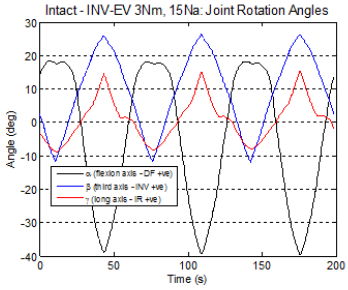

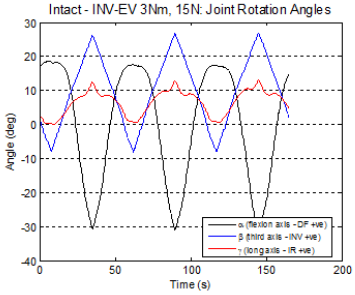

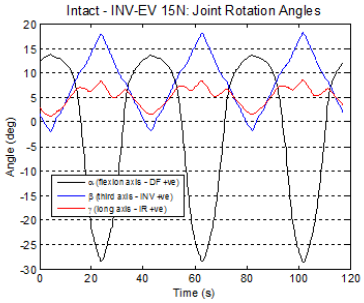

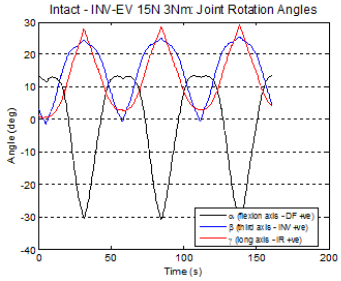

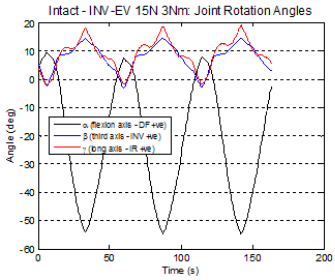

15N STAR INV-EV

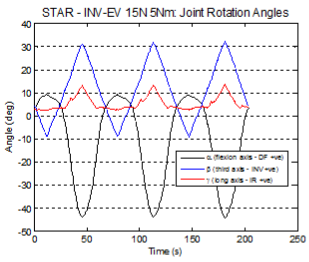

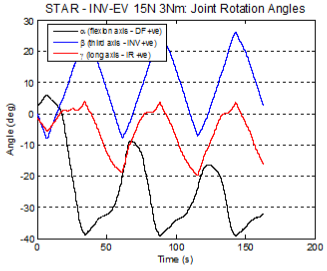

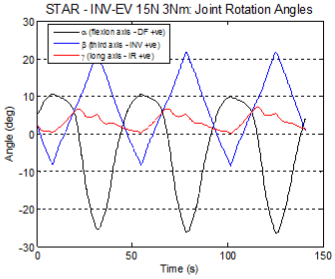

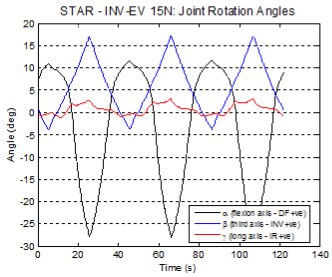

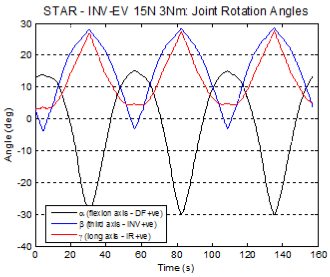

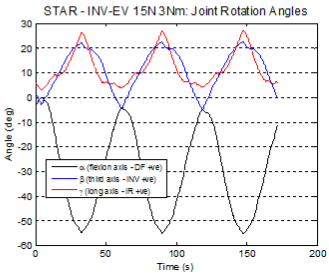

L 75N Intact INV-EV

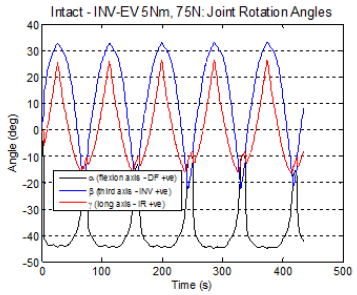
Intact - INV-EV 5Nm, 75N: Joint Rotation Angles

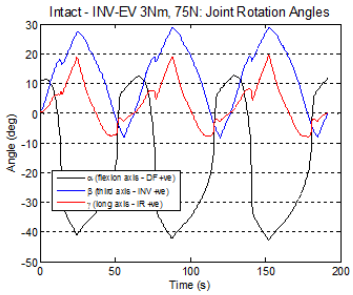
Intact - INV-EV 3Nm, 75N: Joint Rotation Angles

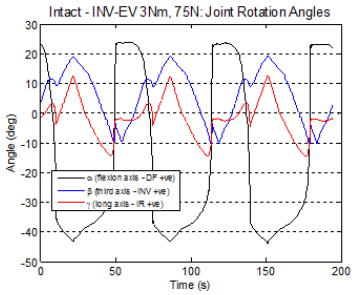
Intact - INV-EV 3Nm, 75N: Joint Rotation Angles

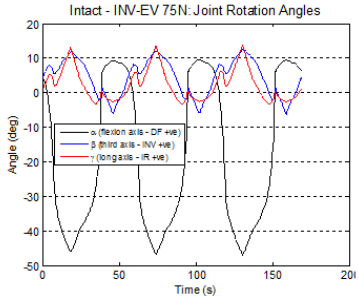
Intact - INV-EV 75N: Joint Rotation Angles

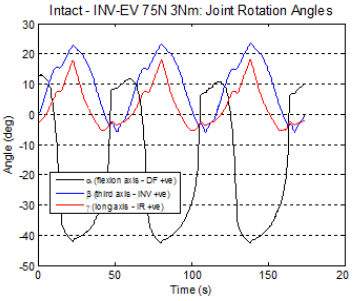
Intact - INV-EV 75N 3Nm: Joint Rotation Angles

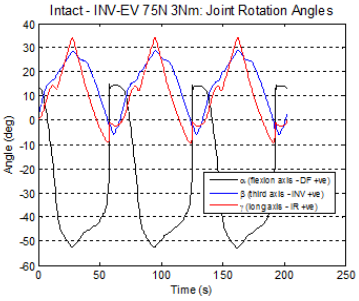
Intact - INV-EV 75N 3Nm: Joint Rotation Angles

75N Agility INV-EV

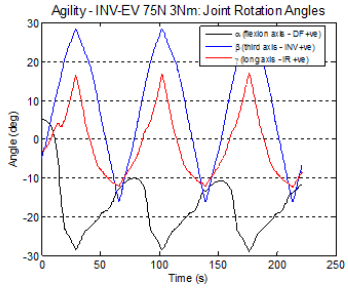
Agility - INV-EV 75N 3Nm: Joint Rotation Angles

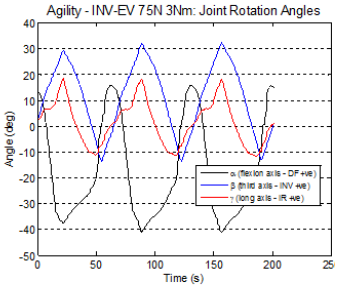
Agility - INV-EV 75N 3Nm: Joint Rotation Angles

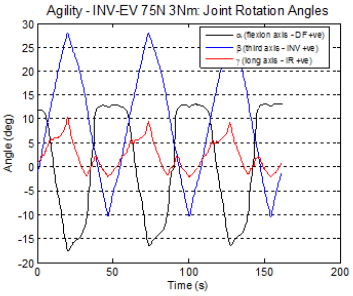
Agility - INV-EV 75N 3Nm: Joint Rotation Angles

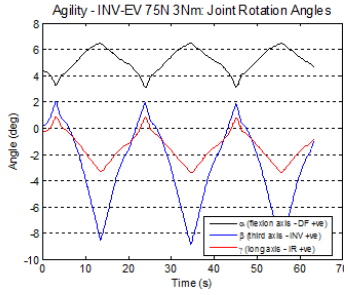
Agility - INV-EV 75N 3Nm: Joint Rotation Angles

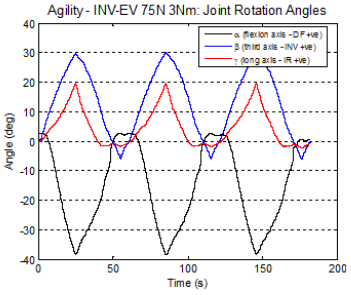
Agility - INV-EV 75N 3Nm: Joint Rotation Angles

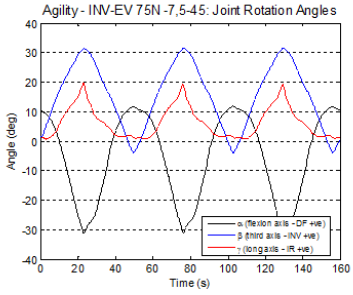
Agility - INV-EV 75N -7,5-45: Joint Rotation Angles

R 75N Intact INV-EV

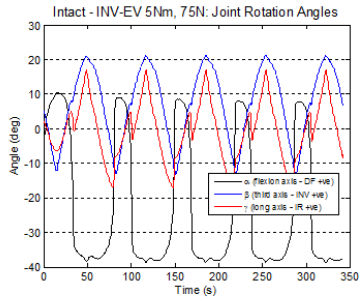

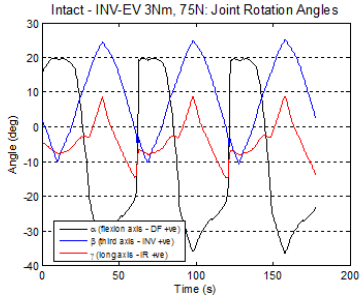

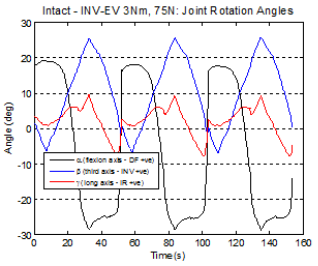

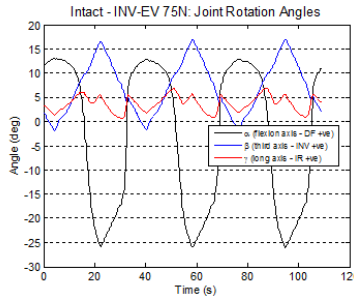

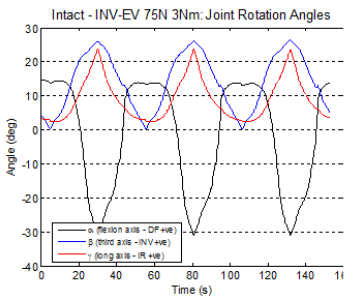

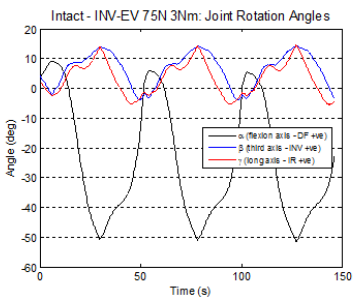

75N STAR INV-EV

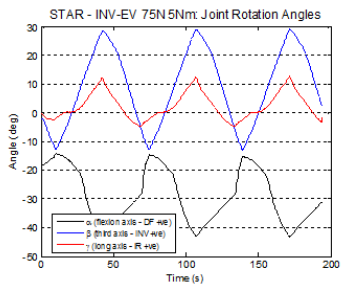

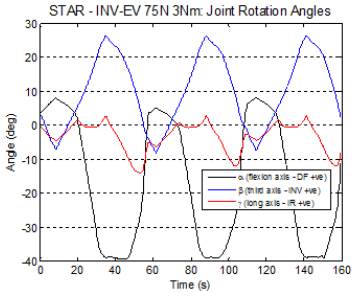

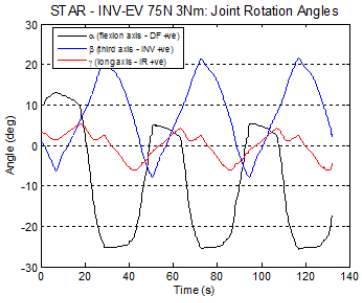

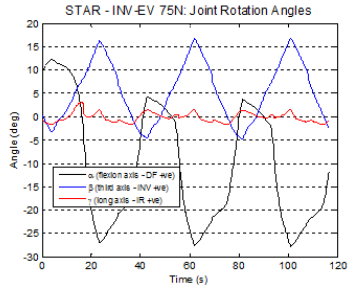

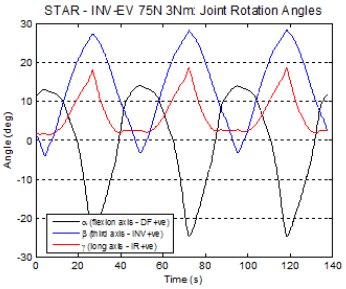

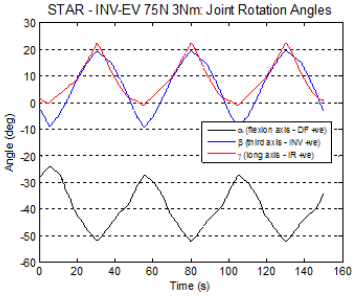

L 15 N Intact IR-ER

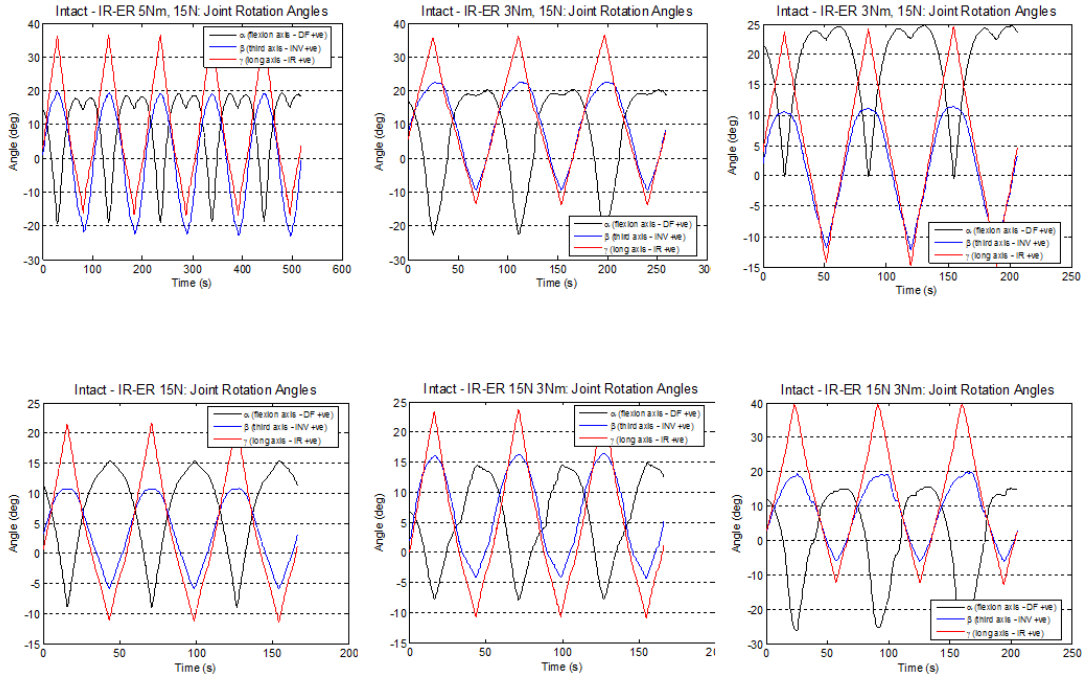

15N Agility IR-ER

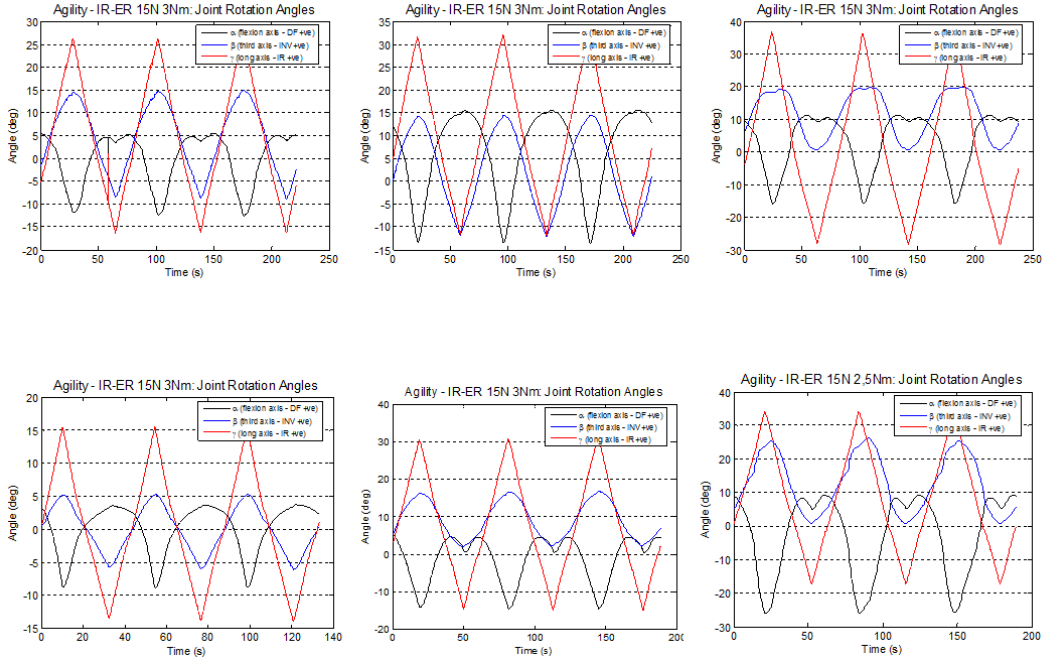

R 15N Intact IR-ER

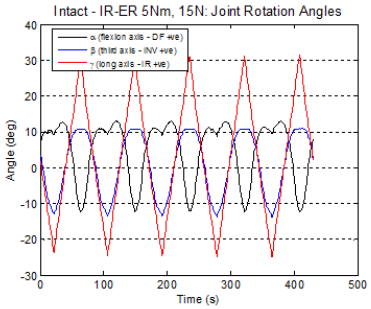
Intact - IR-ER 5Nm, 15N: Joint Rotation Angles

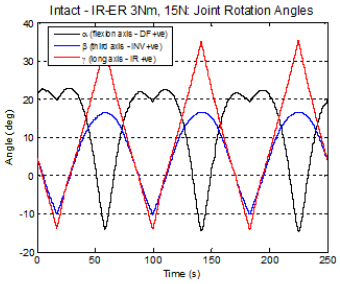
Intact - IR-ER 3Nm, 15N: Joint Rotation Angles

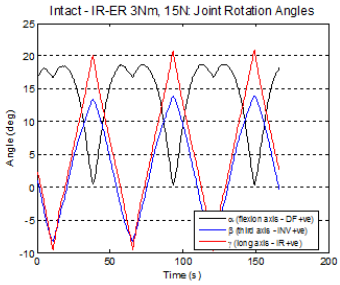
Intact - IR-ER 3Nm, 15N: Joint Rotation Angles

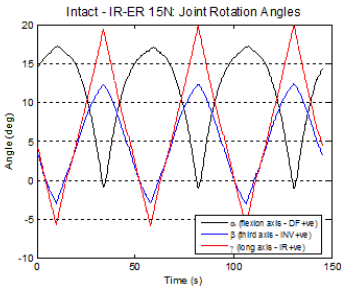
Intact - IR-ER 15N: Joint Rotation Angles

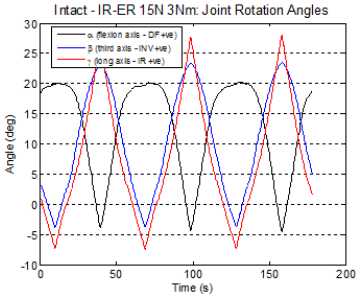
Intact - IR-ER 15N 3Nm: Joint Rotation Angles

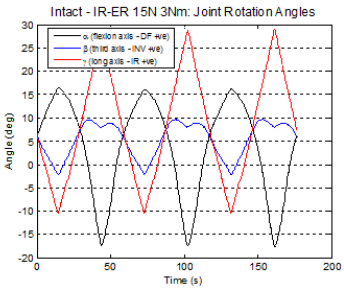
Intact - IR-ER 15N 3Nm: Joint Rotation Angles

15N STAR IR-ER

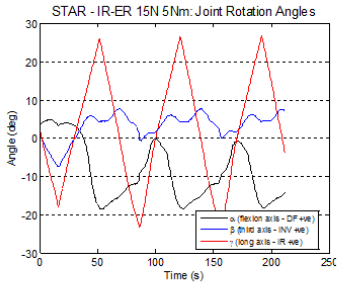
STAR - IR-ER 15N 5Nm: Joint Rotation Angles

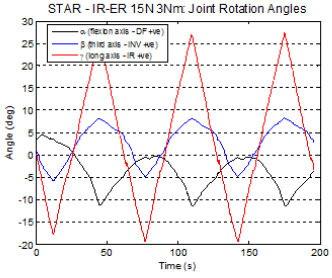
STAR - IR-ER 15N 3Nm: Joint Rotation Angles

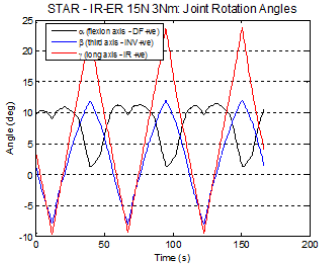
STAR - IR-ER 15N 3Nm: Joint Rotation Angles

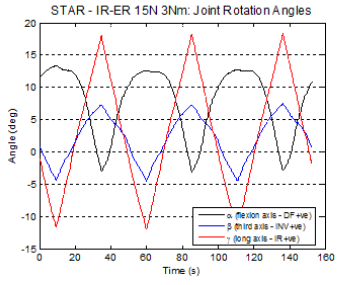
STAR - IR-ER 15N 3Nm: Joint Rotation Angles

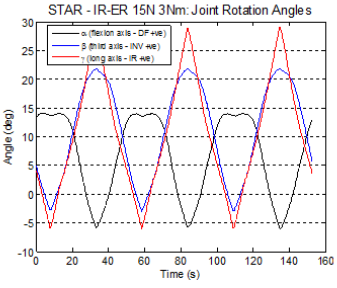
STAR - IR-ER 15N 3Nm: Joint Rotation Angles

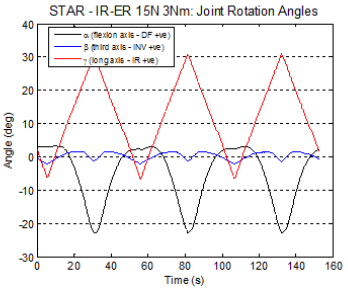
STAR - IR-ER 15N 3Nm: Joint Rotation Angles

L 300N Intact IR-ER

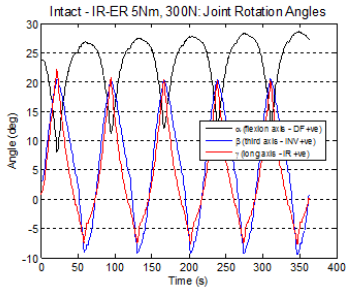
Intact - IR-ER 5Nm, 300N: Joint Rotation Angles

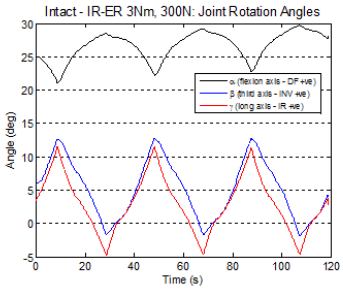
Intact - IR-ER 3Nm, 300N: Joint Rotation Angles

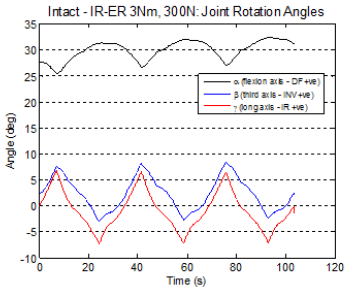
Intact - IR-ER 3Nm, 300N: Joint Rotation Angles

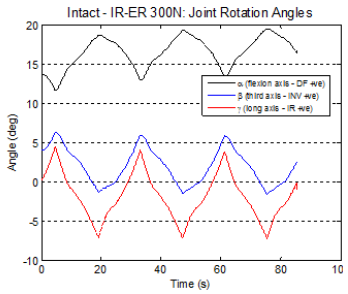
Intact - IR-ER 300N: Joint Rotation Angles

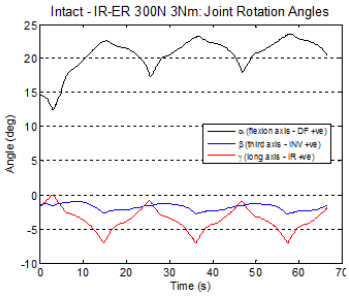
Intact - IR-ER 300N 3Nm: Joint Rotation Angles

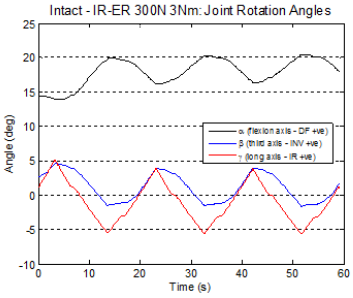
Intact - IR-ER 300N 3Nm: Joint Rotation Angles

300N Agility IR-ER

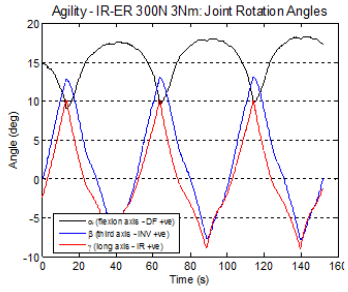
Agility - IR-ER 300N 3Nm: Joint Rotation Angles

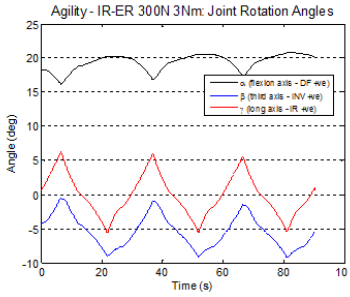
Agility - IR-ER 300N 3Nm: Joint Rotation Angles

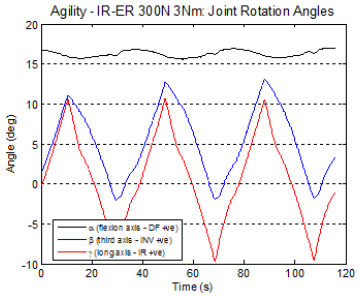
Agility - IR-ER 300N 3Nm: Joint Rotation Angles

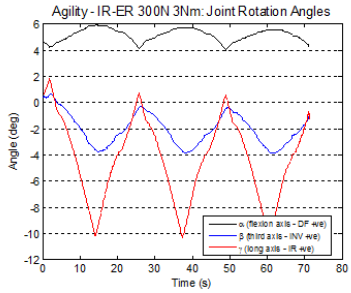
Agility - IR-ER 300N 3Nm: Joint Rotation Angles

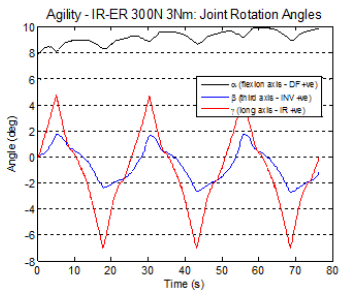
Agility - IR-ER 300N 3Nm: Joint Rotation Angles

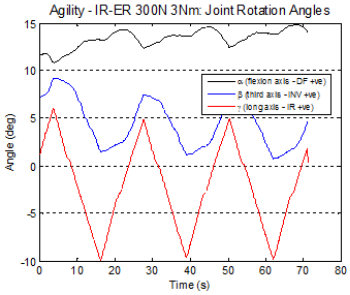
Agility - IR-ER 300N 3Nm: Joint Rotation Angles

R 300N Intact IR-ER

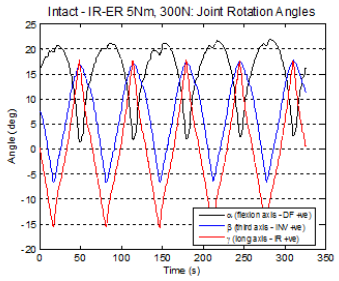

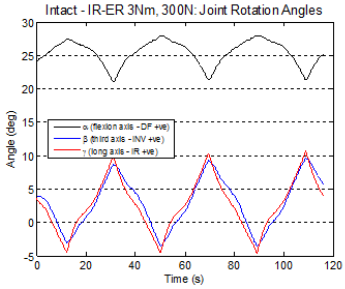

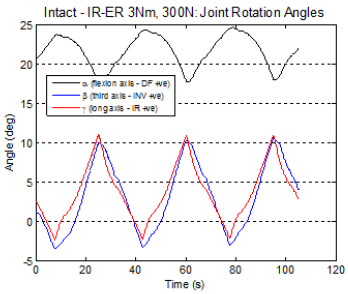

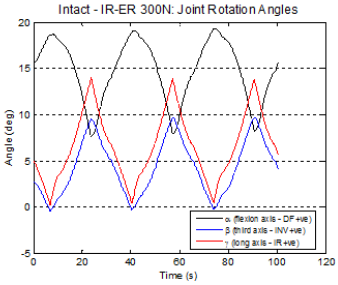

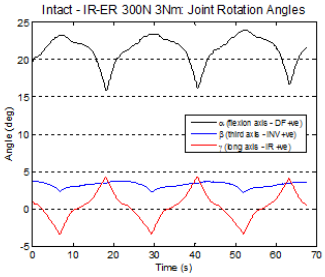

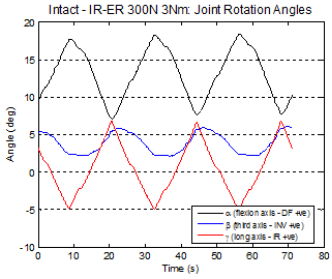

300N STAR IR-ER

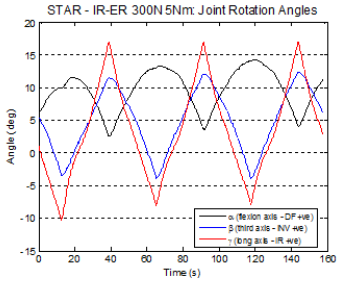

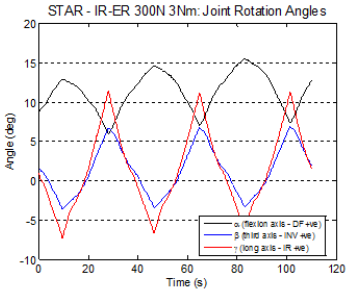

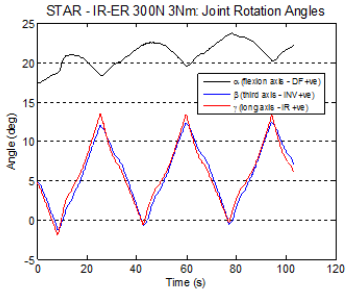

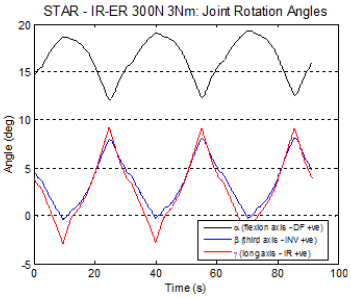

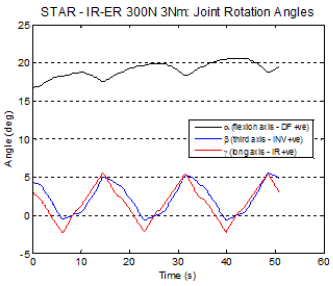

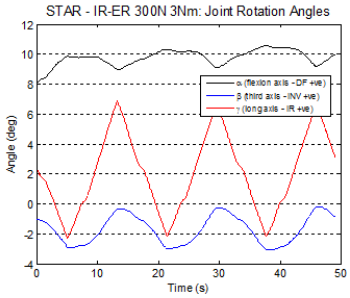

APPENDIX I: APPLIED LOADING: MOMENT-ANGLE PLOTS

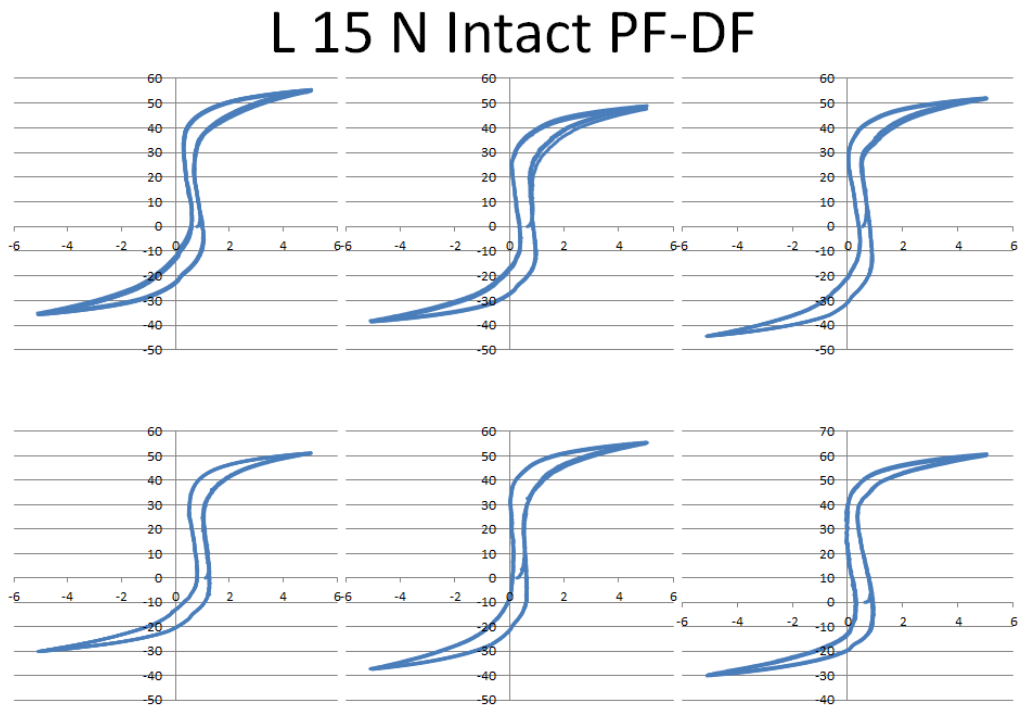

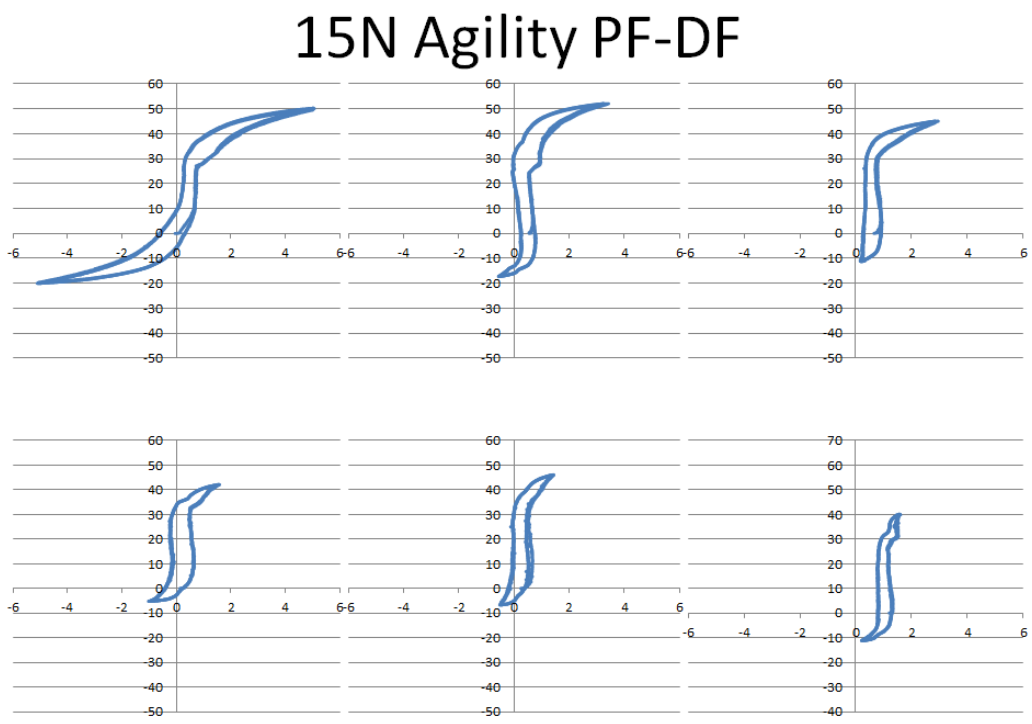

R 15N Intact PF-DF

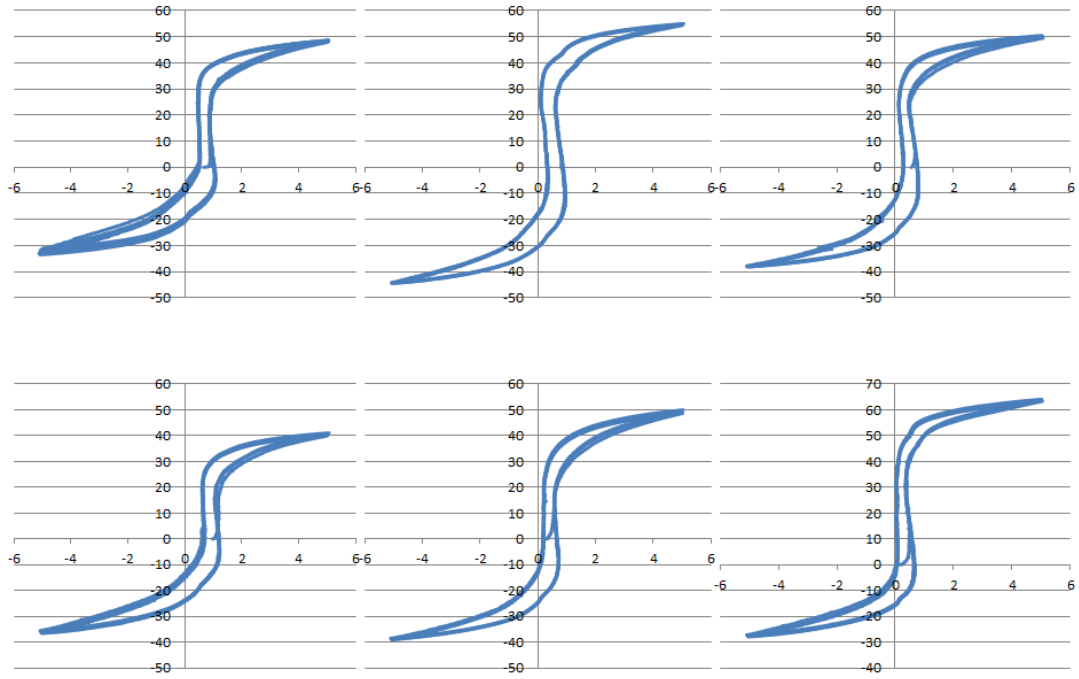

15N STAR PF-DF

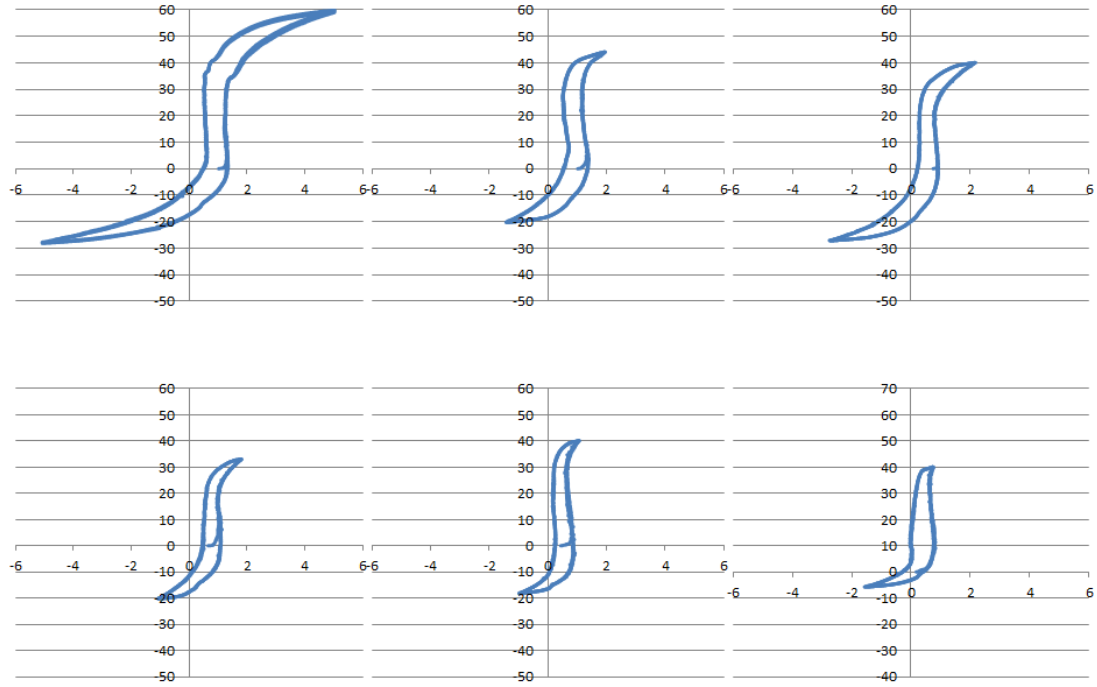

L 300 N Intact PF-DF

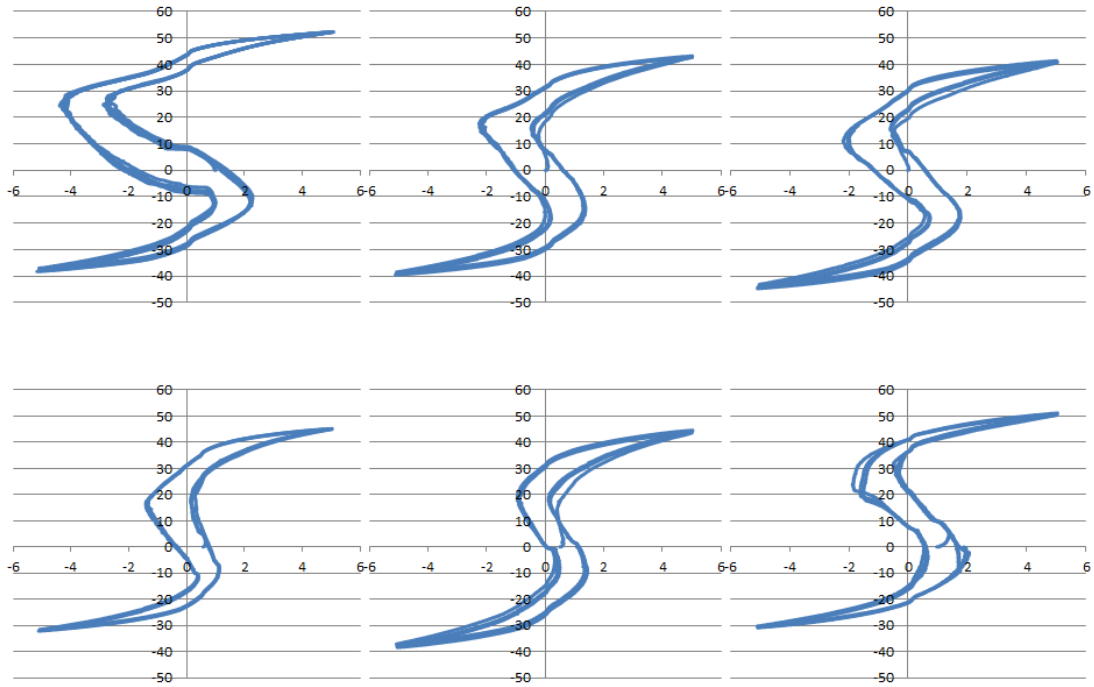

300N Agility PF-DF

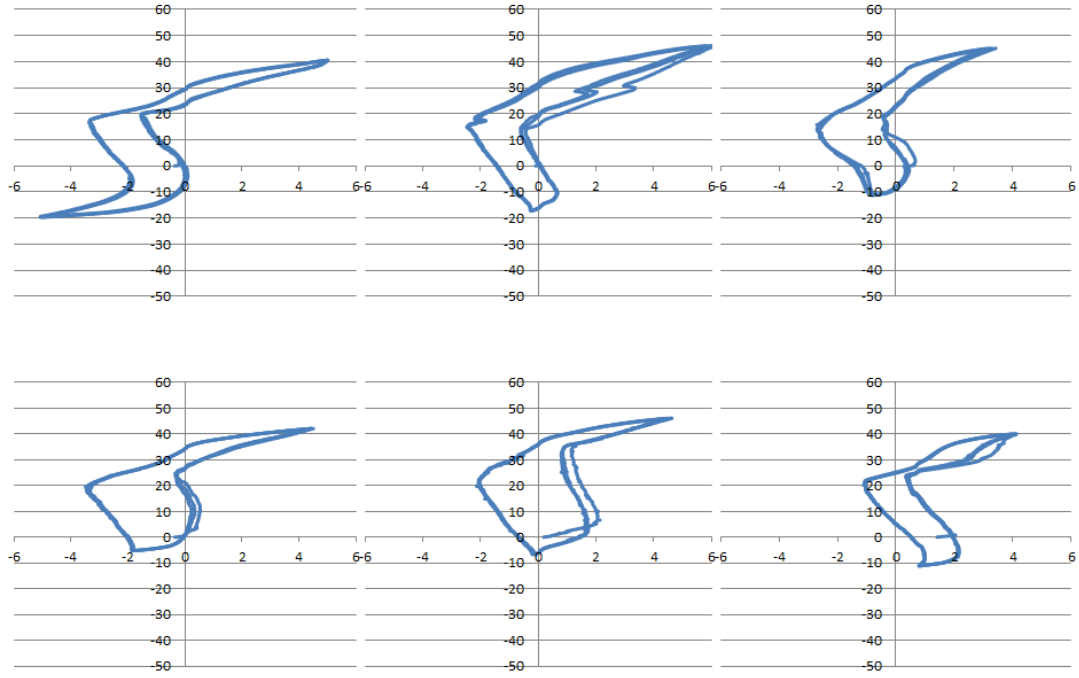

R 300N Intact PF-DF

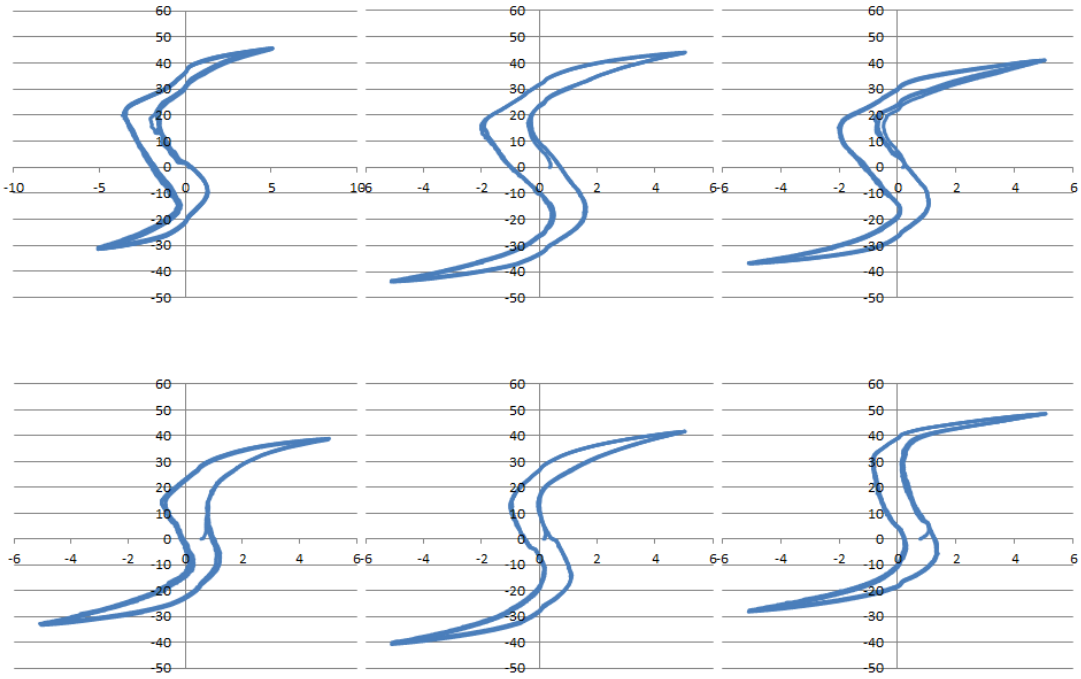

300N STAR PF-DF

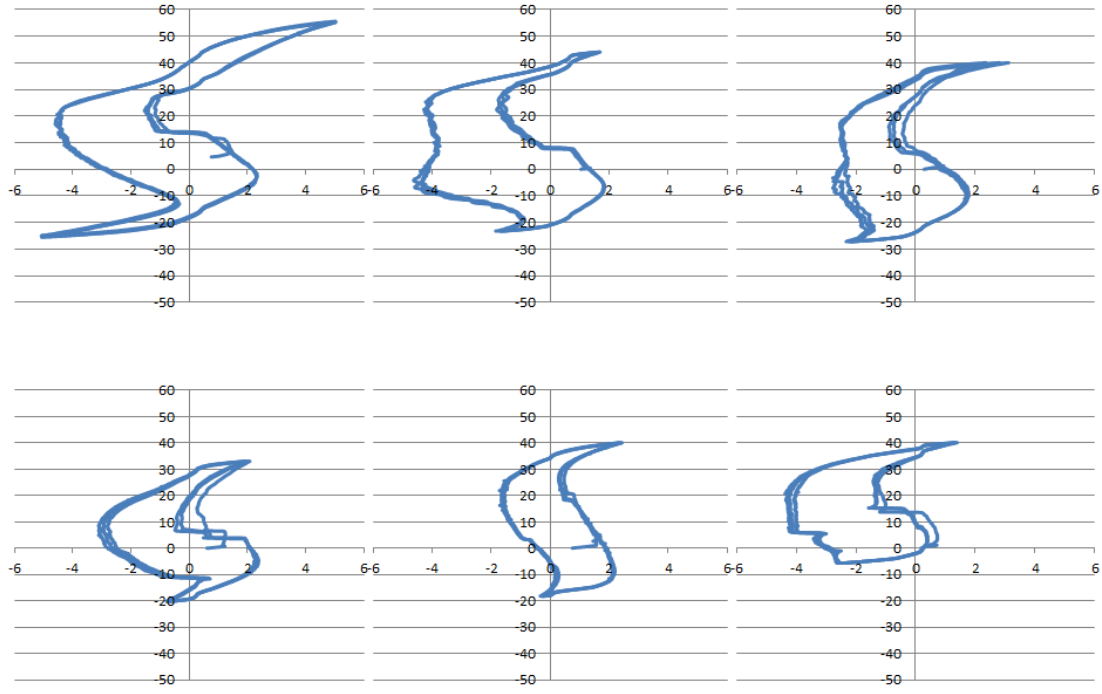

L 15 N Intact INV-EV

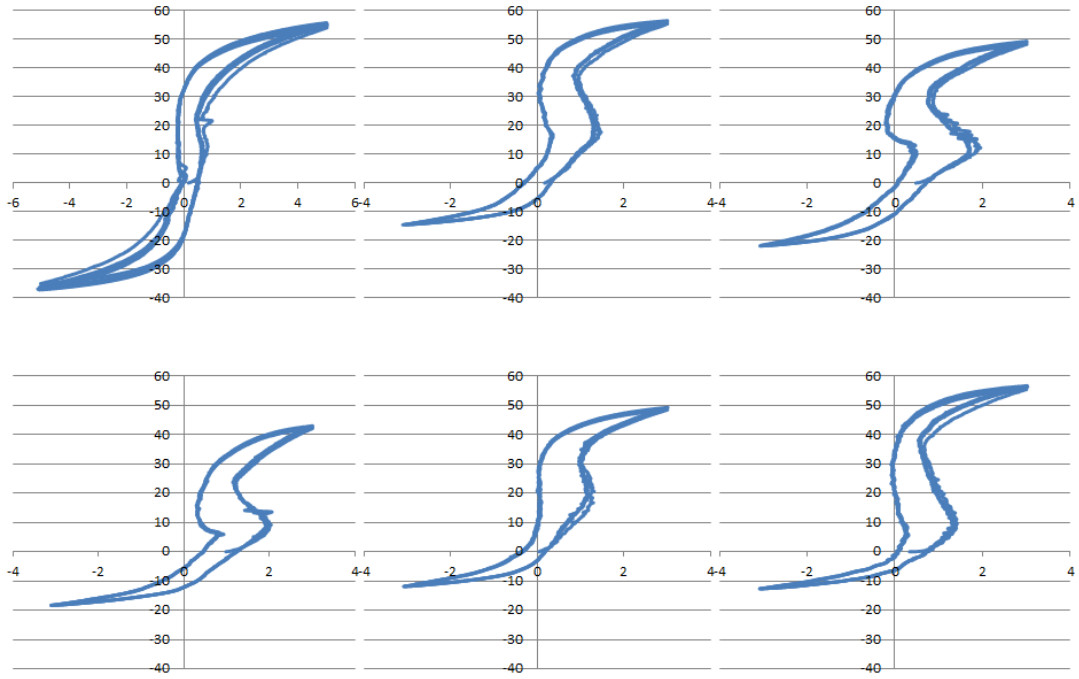

15N Agility INV-EV

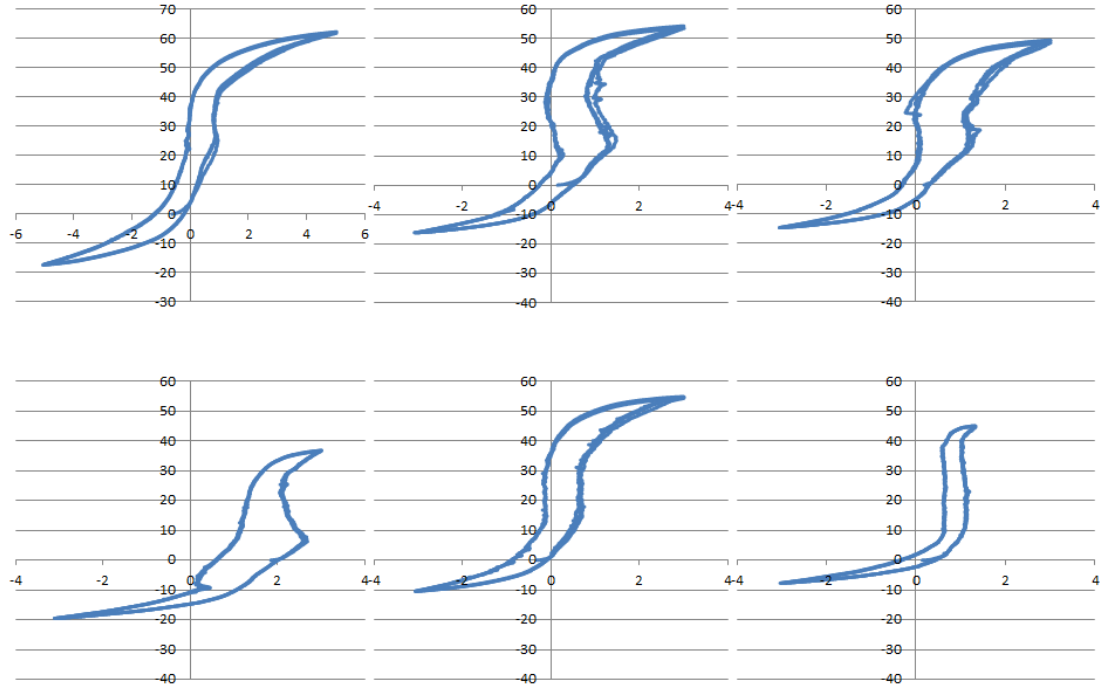

R 15N Intact INV-EV

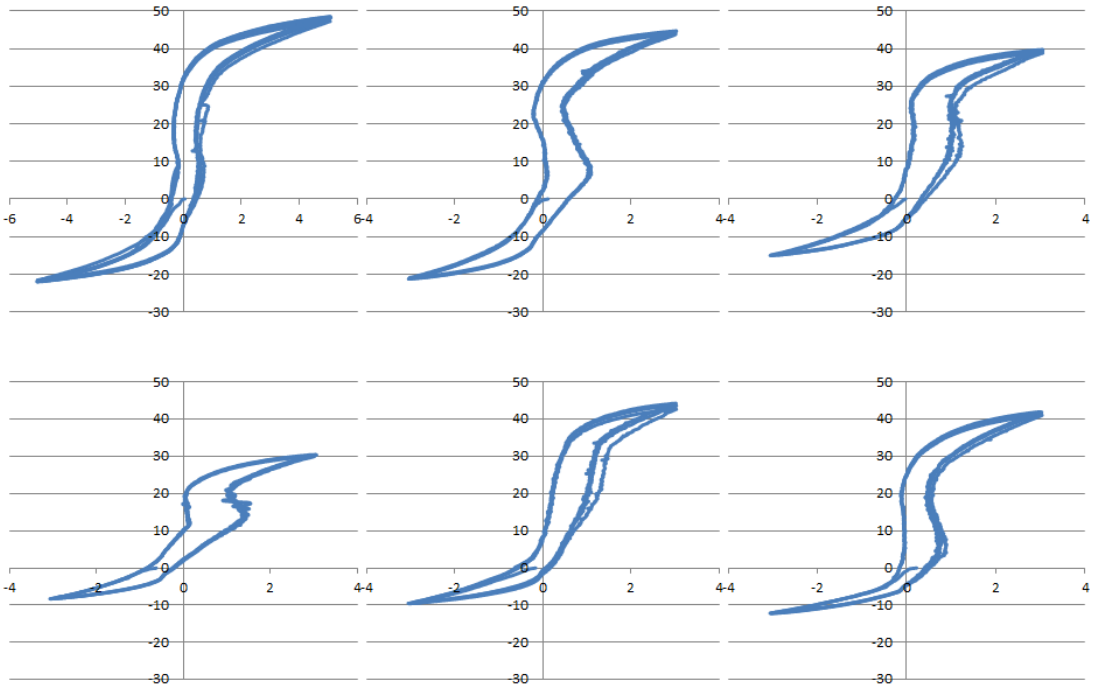

15N STAR INV-EV

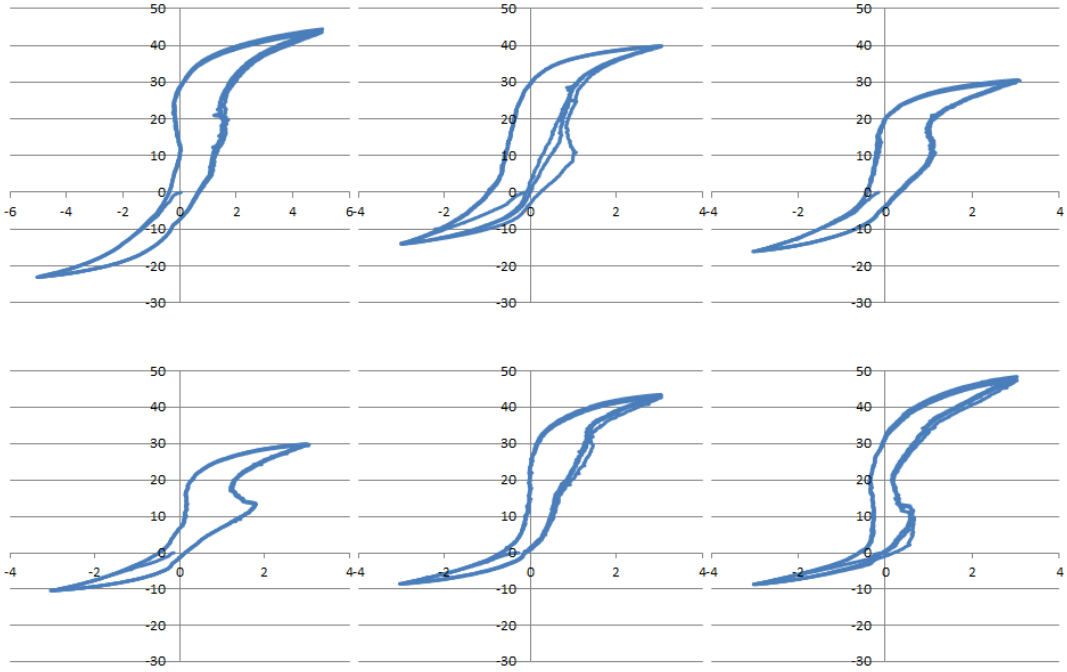

L 75N Intact INV-EV

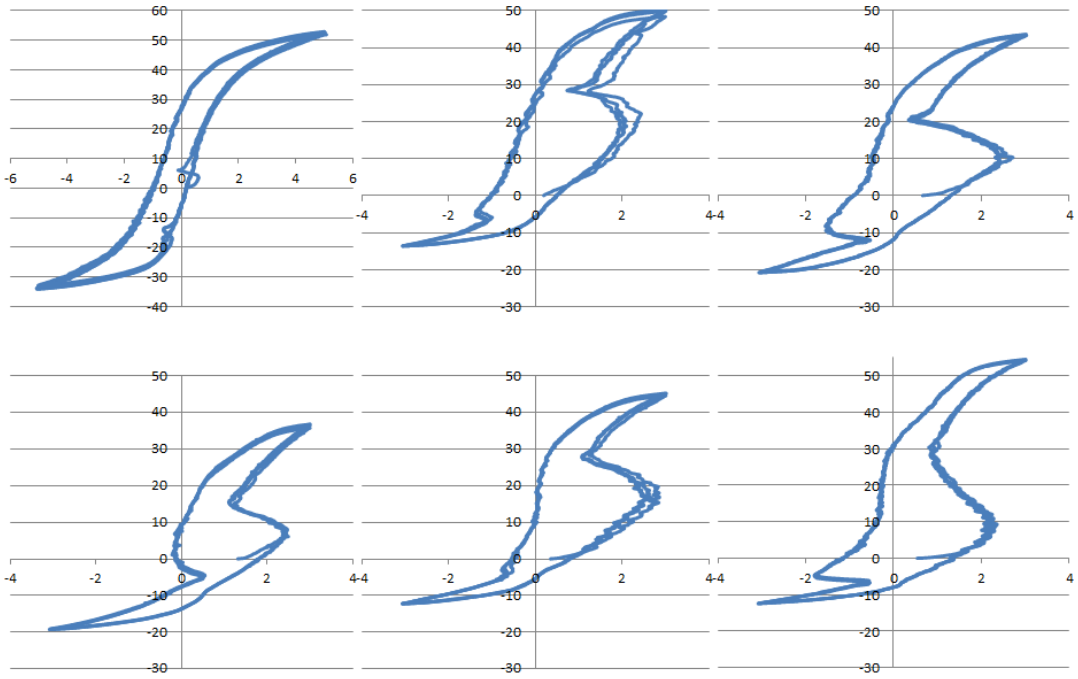

75N Agility INV-EV

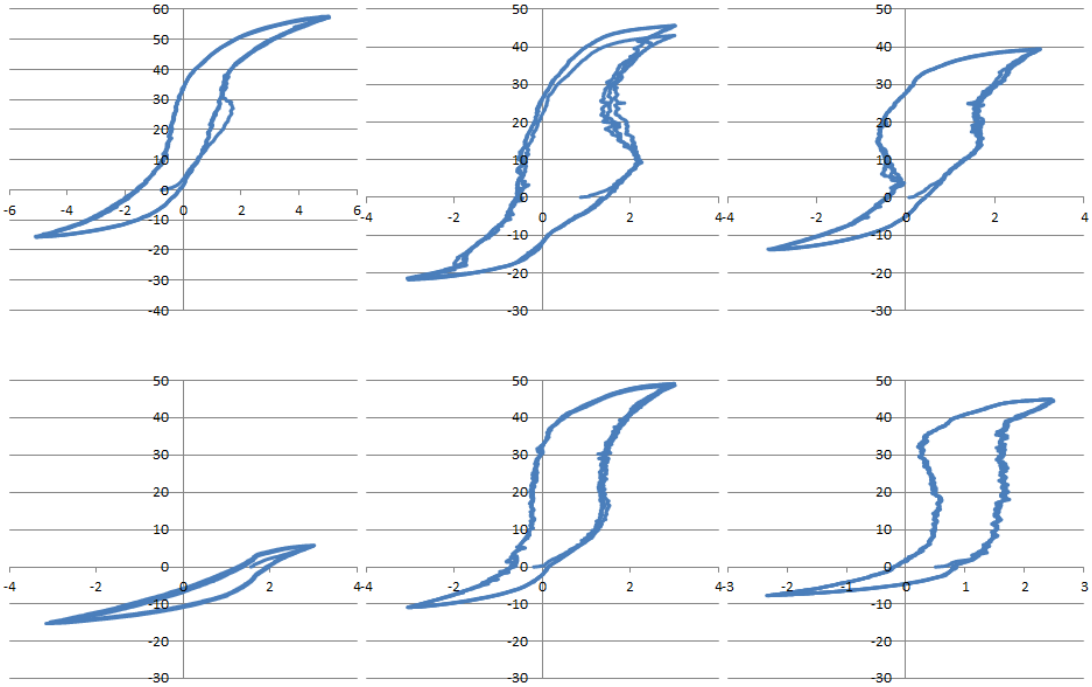

R 75N Intact INV-EV

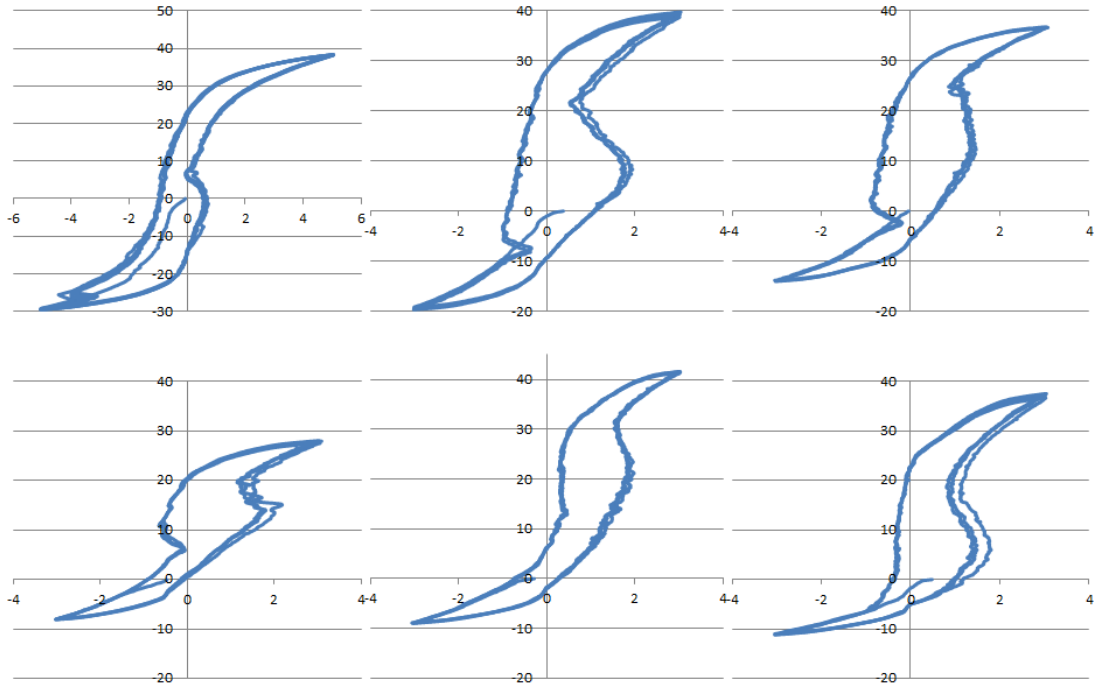

75N STAR INV-EV

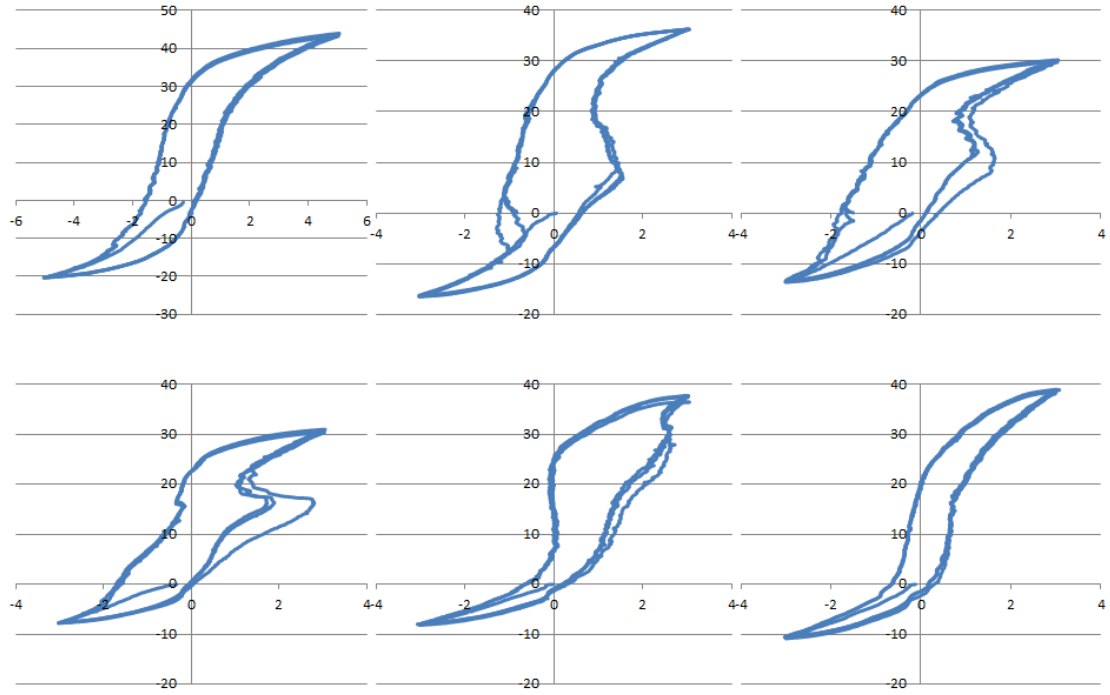

L 15 N Intact IR-ER

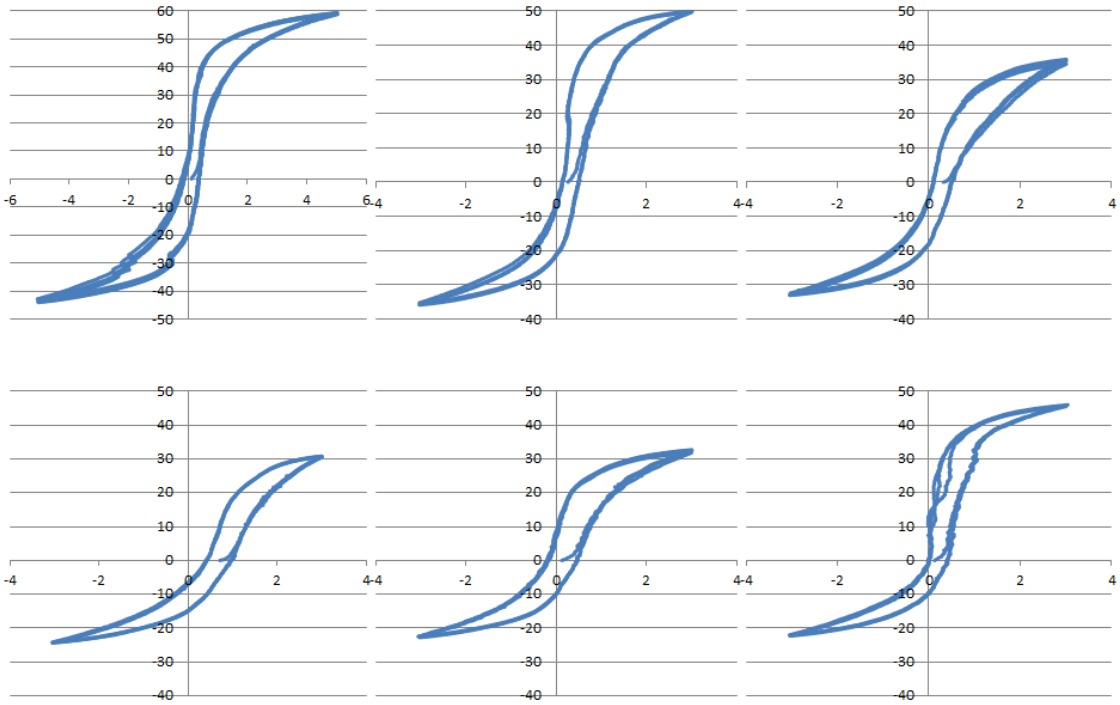

15N Agility IR-ER

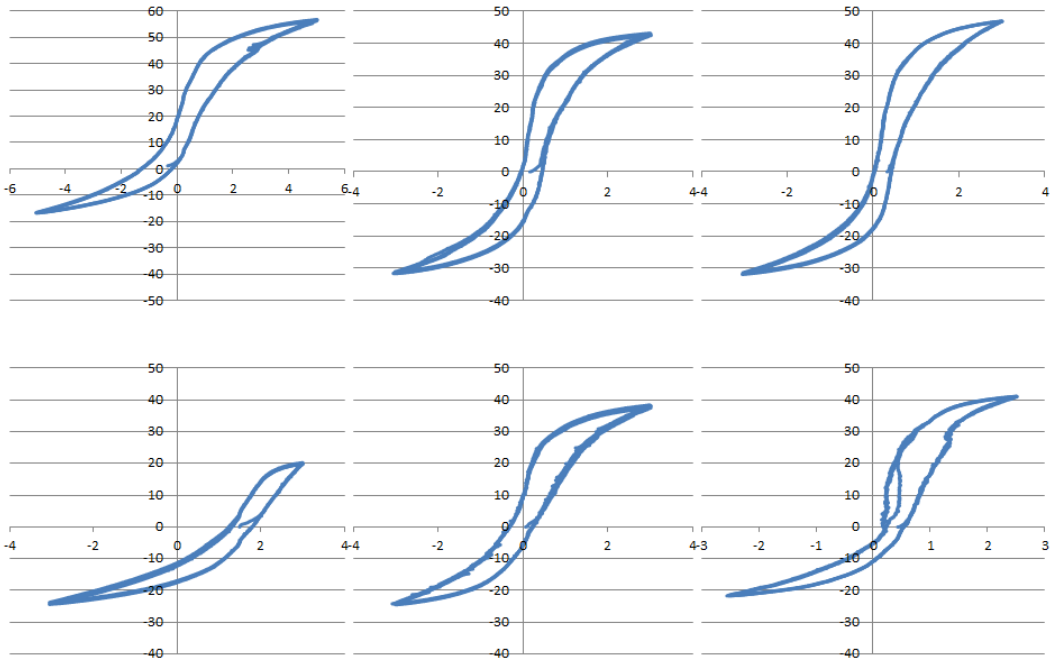

R 15N Intact IR-ER

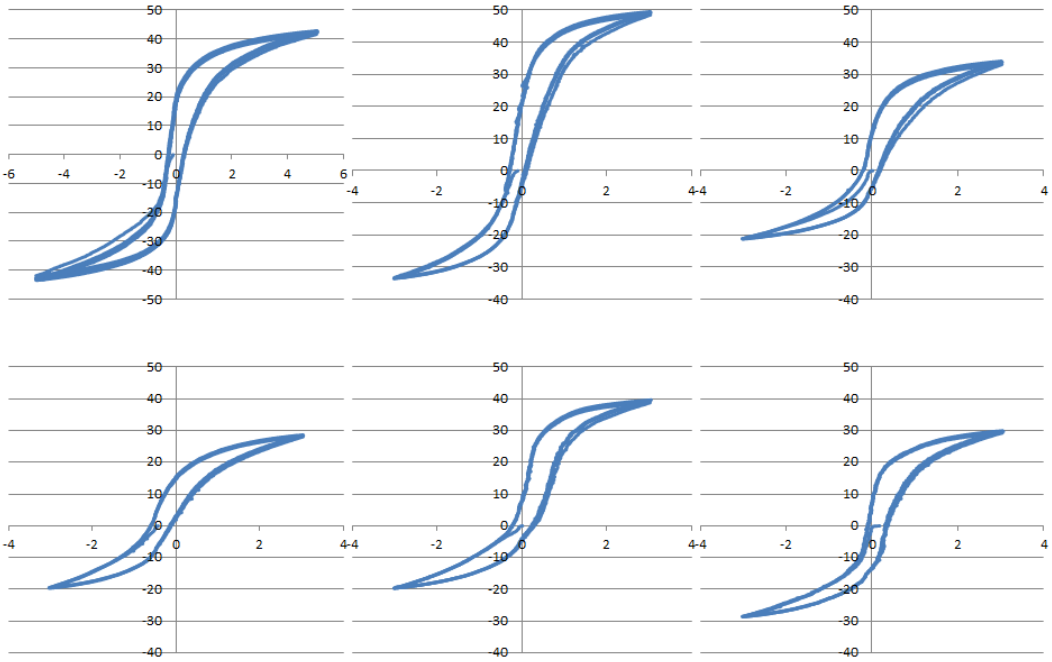

15N STAR IR-ER

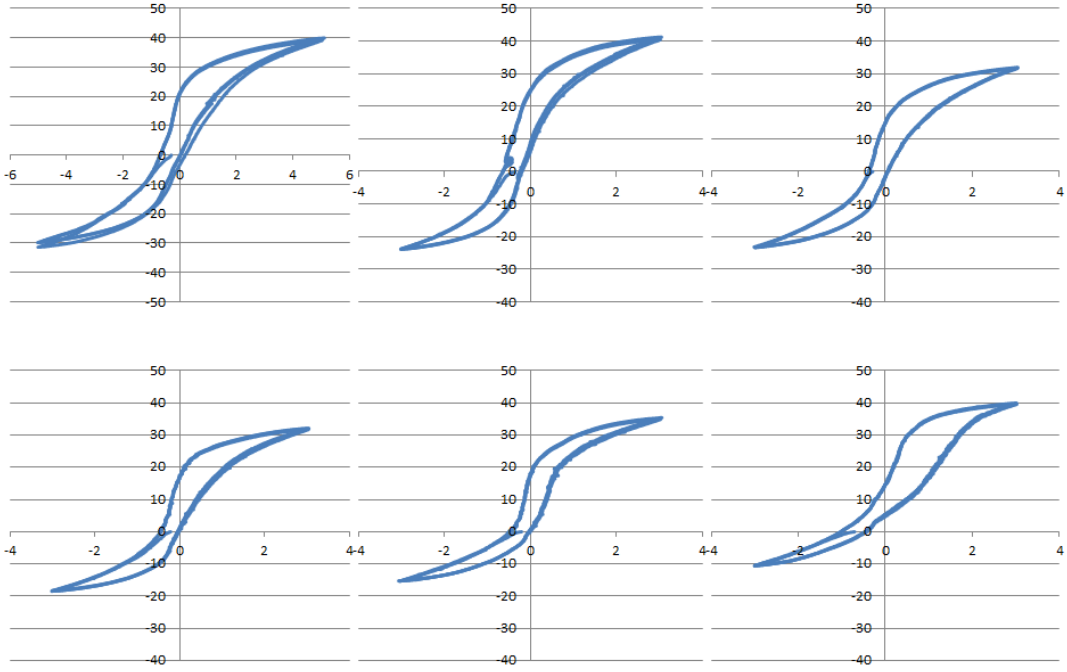

L 300N Intact IR-ER

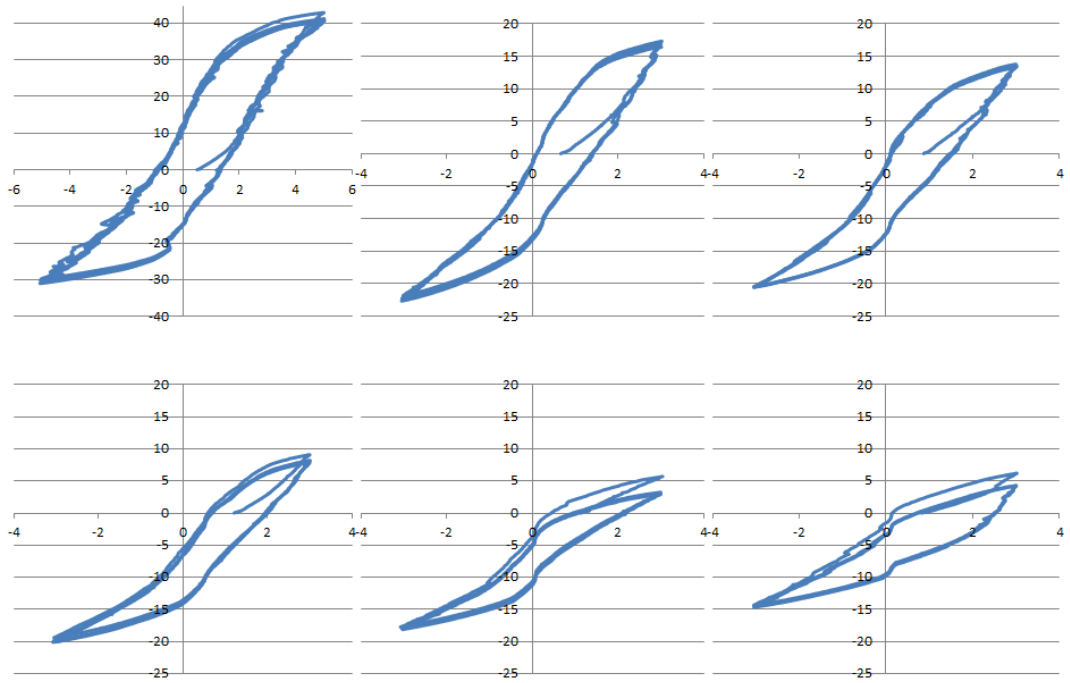

300N Agility IR-ER

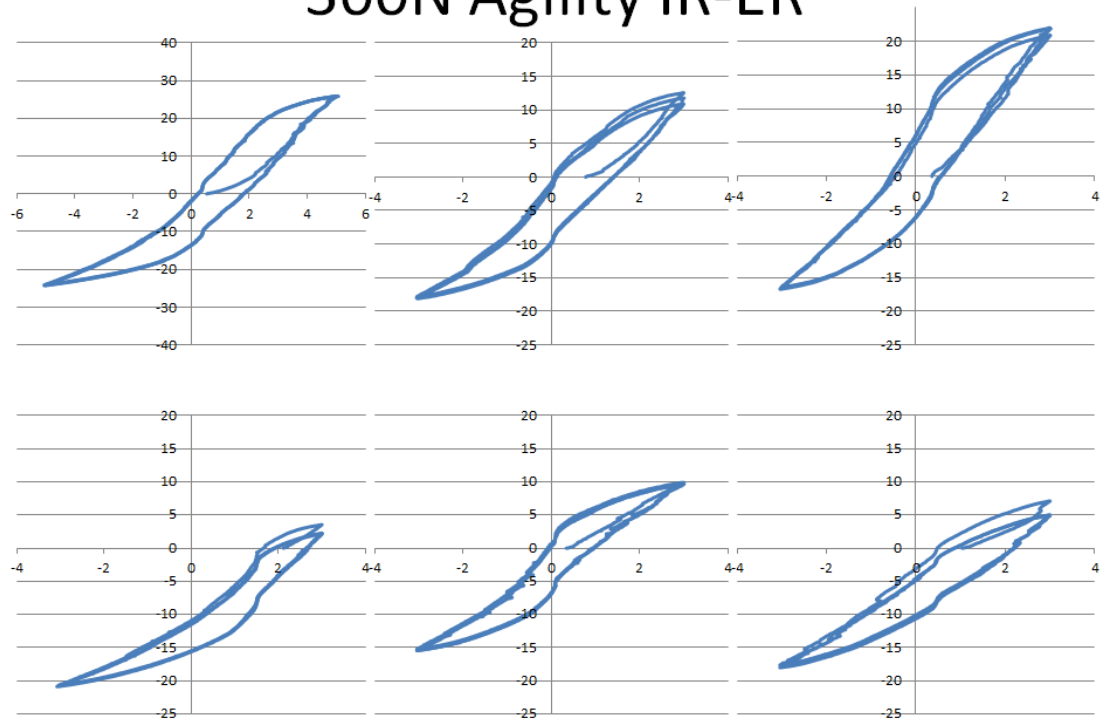

R 300N Intact IR-ER

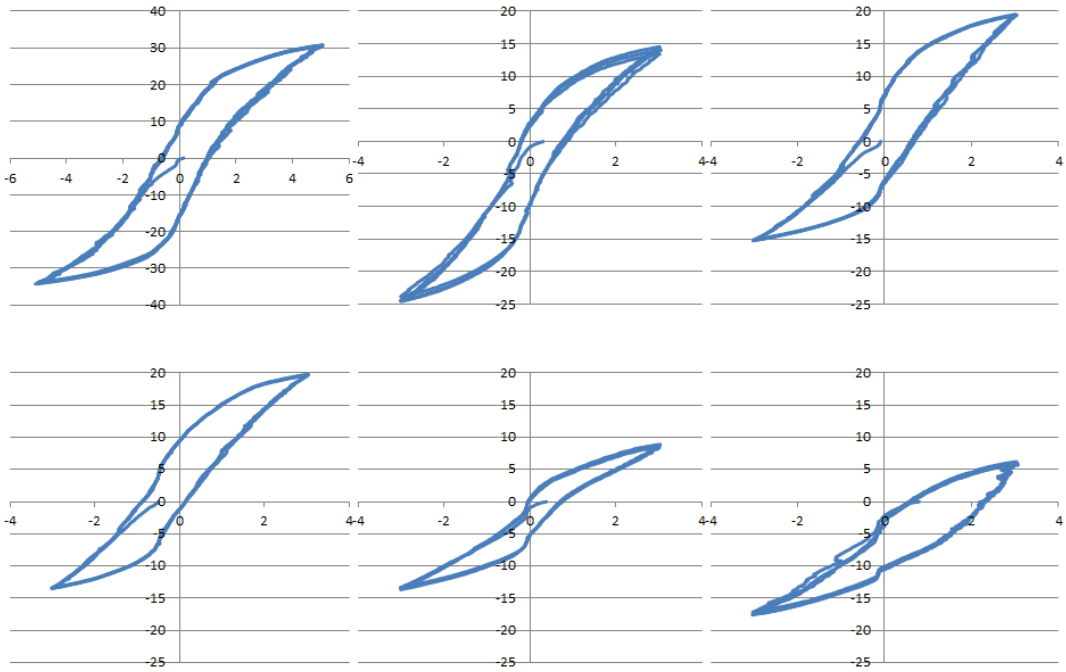

300N STAR IR-ER

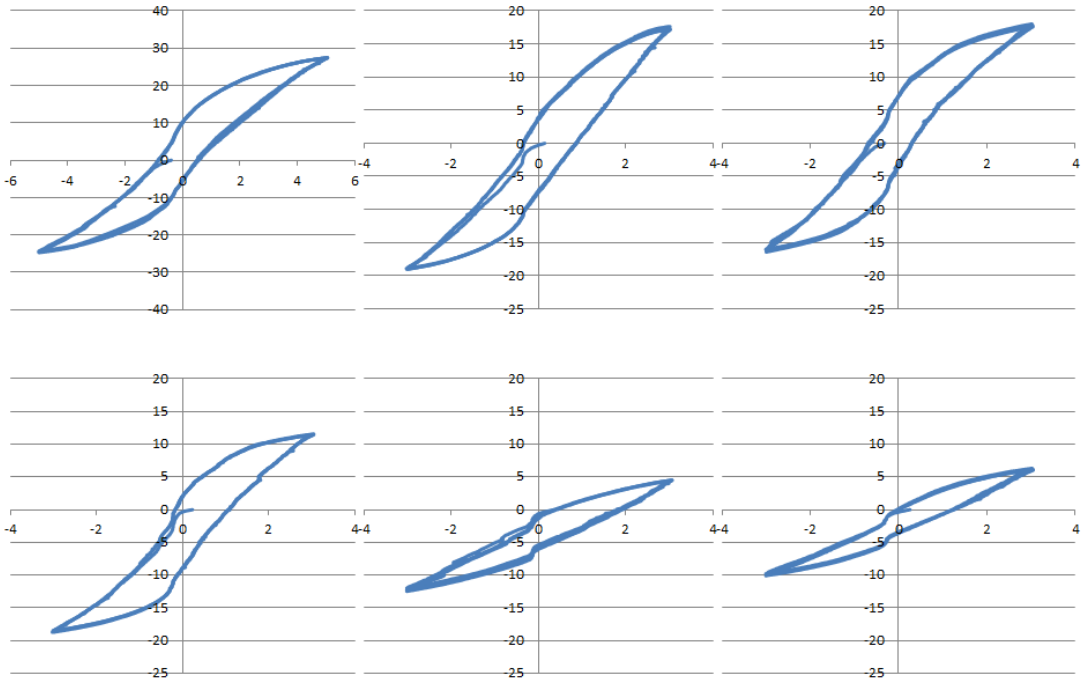

APPENDIX J: DATA TABLES

Table 18: Peak tibial micromotion magnitudes. Data given as mean values ± standard deviation (in mm).

		PF-DF	INV-EV	IR-ER
Uncompressed	Agility	0.436 ± 0.619	0.257 ± 0.172	0.344 ± 0.149
	STAR	0.214 ± 0.183	0.098 ± 0.025	0.200 ± 0.046
Compressed	Agility	0.222 ± 0.070	0.240 ± 0.115	0.240 ± 0.163
	STAR	0.484 ± 0.358	0.152 ± 0.049	0.129 ± 0.075

Table 19: Peak talar micromotion magnitudes. Data given as mean values ± standard deviation (in mm).

		PF-DF	INV-EV	IR-ER
Uncompressed	Agility	2.772 ± 1.363	1.460 ± 0.889	0.904 ± 0.322
	STAR	0.728 ± 0.269	0.643 ± 0.176	0.396 ± 0.188
Compressed	Agility	1.214 ± 0.505	1.020 ± 0.815	0.237 ± 0.145
	STAR	0.789 ± 0.328	0.633 ± 0.310	0.206 ± 0.130

Table 20: Motion Coupling Ratios for PF-DF loading direction. Ratios are shown as mean ± SD

	Compression	Intact	Agility	STAR
INV-EV	15	0.175 ± 0.055	0.159 ± 0.075	0.158 ± 0.086
	300	0.138 ± 0.054	0.088 ± 0.027	0.161 ± 0.090
IR-ER	15	0.132 ± 0.051	0.155 ± 0.045	0.130 ± 0.060
	300	0.136 ± 0.065	0.145 ± 0.010	0.147 ± 0.101

Table 21: Motion coupling ratios for INV-EV loading direction. Ratios are shown as mean ± SD

	Compression	Intact	Agility	STAR
PF-DF	15	1.867 ± 0.730	1.170 ± 0.367	1.365 ± 0.418
	75	1.866 ± 0.696	0.843 ± 0.412	1.101 ± 0.318
IR-ER	15	0.756 ± 0.280	0.687 ± 0.123	0.498 ± 0.305
	75	0.815 ± 0.248	0.522 ± 0.150	0.453 ± 0.227

Table 22: Motion coupling ratios for IR-ER loading direction

	Compression	Intact	Agility	STAR
PF-DF	15	0.704 ± 0.112	0.505 ± 0.129	0.444 ± 0.174
	300	0.629 ± 0.217	0.200 ± 0.150	0.352 ± 0.158
INV-EV	15	0.584 ± 0.141	0.441 ± 0.127	0.374 ± 0.245
	300	0.686 ± 0.298	0.618 ± 0.293	0.672 ± 0.213

Table 23: Peak medial/lateral (q1) joint translations (mean ± SD in millimeters)

	Compression	Intact	Agility	STAR
PF-DF	15 N	3.29 ± 1.77	4.03 ± 1.84	1.78 ± 0.84
	300 N	6.34 ± 2.85	4.15 ± 1.35	3.29 ± 1.23
INV-EV	15 N	8.92 ± 6.19	13.65 ± 4.39	11.39 ± 6.36
	75 N	9.25 ± 6.26	14.25 ± 5.59	10.91 ± 6.51
IR-ER	15 N	5.19 ± 4.90	6.88 ± 3.26	4.74 ± 1.39
	300 N	5.10 ± 5.35	5.45 ± 4.13	4.68 ± 2.66

Table 24: Peak anterior/posterior (q2) joint translations (mean ± SD in millimeters)

	Compression	Intact	Agility	STAR
PF-DF	15 N	4.12 ± 1.58	2.72 ± 0.99	4.35 ± 1.17
	300 N	2.84 ± 1.40	2.99 ± 1.95	7.25 ± 2.25
INV-EV	15 N	5.75 ± 2.01	5.43 ± 1.50	6.71 ± 2.45
	75 N	6.53 ± 2.16	5.27 ± 2.64	5.74 ± 2.91
IR-ER	15 N	5.02 ± 2.60	6.66 ± 3.16	4.61 ± 2.65
	300 N	3.20 ± 3.01	2.74 ± 1.83	3.46 ± 2.72

Table 25: Peak compression/distraction (q3) joint translations (mean ± SD in millimeters)

	Compression	Intact	Agility	STAR
PF-DF	15 N	6.09 ± 2.28	5.94 ± 1.65	8.27 ± 4.13
	300 N	6.24 ± 3.12	6.27 ± 2.50	11.60 ± 5.69
INV-EV	15 N	5.33 ± 2.82	5.02 ± 1.26	7.36 ± 3.34
	75 N	5.54 ± 2.46	3.96 ± 2.18	5.87 ± 3.77
IR-ER	15 N	2.68 ± 1.76	3.00 ± 1.72	2.46 ± 1.77
	300 N	0.73 ± 0.45	1.01 ± 0.50	0.32 ± 0.23